Stony Brook University

IN-SITU KINETICS AND X-RAY COMPUTED MICROTOMOGRAPHY IMAGING STUDIES OF METHANE HYDRATES IN HOST SEDIMENTS

A Dissertation

by

Prasad B. Kerkar

To

The Graduate School

in Partial fulfillment of the

Requirements

for the Degree of

Doctor of Philosophy

In

Materials Science and Engineering

Stony Brook University

August 2010

Stony Brook University

The Graduate School

Prasad B. Kerkar

We, the dissertation committee for the above candidate for the
Doctor of Philosophy degree, hereby recommend acceptance of this dissertation.

Devinder Mahajan, Dissertation Advisor
Professor, Department of Materials Science and Engineering

Dr. Michael Dudley, Committee Chairperson
Professor, Department of Material Science and Engineering

Dr. Tadanori Koga, Assistant Professor
Department of Material Science and Engineering

Dr. Rudy Rogers
Professor, David C. Swam School of Chemical Engineering,
Mississippi State University

This dissertation is accepted by the Graduate School.

Lawrence Martin
Dean of the Graduate School

Abstract of the Dissertation

***IN-SITU* KINETICS AND X-RAY COMPUTED MICROTOMOGRAPHY IMAGING STUDIES OF METHANE HYDRATES IN HOST SEDIMENTS**

by

Prasad B. Kerkar

Doctor of Philosophy

in

Materials Science and Engineering

Stony Brook University

2010

Methane hydrates naturally occur in abundance in permafrost and marine environments. Methane hydrates are ice-like inclusion compounds in which water molecules form a framework through hydrogen bonding and encapsulate methane molecules under conditions of low temperature and high pressure. In natural settings, the sediment-hydrate interaction governs the mechanical strength and other geophysical properties of formations containing methane hydrates. In this study, methane hydrate formation/dissociation kinetics was studied with methane/water (both pure water and seawater) hosted in consolidated Ottawa sand-cores at pressure-temperature (PT) conditions (P: 9.2 MPa; T: 4^{o}C) mimicking sub-seafloor settings. The formation study was conducted by charging methane at different pore pressures followed by cooling. The hydrate formation was delayed with increasing pore pressure or consolidation of host sediment. The hydrate dissociation was achieved by incremental step-wise system depressurization during which time, gas output response, sediment cooling due to the reaction endothermicity and post-depressurization PT equilibrium were recorded. The dissociation events due to depressurization were short-lived. During depressurization, thermocouple monitoring showed that the temperature at the center of the core dropped more rapidly than at the middle radius and the boundary. Post-depressurization dissociation was thermally induced where sediments were allowed to warm up to a bath temperature. The post-depressurization PT equilibrium followed theoretical data for

methane hydrates on the higher pressure side due to an excess pore pressure generated within confined core. The post-depressurization PT equilibrium was used to calculate the enthalpy of dissociation value as 59.45 kJ/mol. The gas output during depressurization was fit to estimate hydrate dissociation constant.

A set of formation/decomposition runs was repeated with seawater. The formation kinetics of hydrates from seawater was found to be delayed with the degree of consolidation. The post-depressurization PT equilibrium values were utilized to calculate the enthalpy of dissociation of methane hydrates. The endothermic effect due to hydrate dissociation was recorded with the highest degree of cooling recorded at the center and the half-radius than that at the core boundary. The cooling responses during depressurization from three thermocouples placed at different lateral and radial positions within core were used as an indicative of presence of hydrates and their preferential dissociation positions. The post-depressurization dissociation was thermally induced, during which the sediments warmed up to the bath temperature. All post-depressurization pressure-temperature (PT) followed theoretical methane-seawater equilibrium on higher pressure side until all hydrates were dissociated. These post-depressurization PT equilibriums were used to estimate the enthalpy of dissociation of methane hydrates from seawater and a consolidated core as 54.774 kJ/mole.

The microscopic visualization of time-resolved 3-dimensional (3-D) growth of individual tetrahydrofuran hydrates and methane hydrates formed within a porous media was performed using synchrotron X-ray computed microtomography. Tomographic data were acquired where ~1200 X-ray images were recorded while rotating the sample tube from 0-180^{o} at the X2B beamline, National Synchrotron Light Source (NSLS), Brookhaven National Laboratory (BNL). Each tomogram was reconstructed for 2-dimensional cross-sectional images which were compiled to generate 3-D volume. The images of hydrate patches, formed from excess tetrahydrofuran in aqueous solutions, show random nucleation and growth concomitant with grain movement but independent of container-wall effect. Away from grain surfaces, hydrate surface curvature was convex showing that liquid, not hydrate, was the wetting phase, similar to ice growth in porous media. The time-resolved 3-D images show methane hydrate as pore-filling that is well represented by a model reported by Dvorkin et al. (1999). The observed methane hydrate

(sI) growth in porous media is similar to that observed for tetrahydrofuran hydrate (sII) reported previously in this study. The contact angle for the methane hydrate system was measured to be 154.25^{o} from the CMT data. A combination of patchy and pore-filling microstructure properties could lead to sediment instability, in the event of methane release by hydrate decomposition.

TABLE OF CONTENTS

LIST OF FIGURES

LIST OF TABLES

ACKNOWLEDGEMENTS

This dissertation has become possible due to many who helped me along the way. So please do not take offense if somehow I have forgotten to mention you here. First of all, I want to thank my advisor Dr. Devinder Mahajan for providing me an opportunity to be a part of his methane hydrate group. I firmly believe that the best moments come from the best opportunities. It is hard to put into words how proud I am to be a part of his group and proud as well to play a part in the pursuit of establishing X-ray computed microtmography technique for revealing hydrate microstructure. I want to express my gratitude to him for challenging me with a variety of projects as a great mentor and for his kindness, understanding, and support. I hope that I also have been able to contribute some things during my stay to his group and the chemical and molecular engineering program of which I share his vision and resolve. I want to thank everyone on my reading and exam committee for making this a better thesis – Professors Michael Dudley, Tadanori Koga and Rudy Rogers. I want to acknowledge Dr. Keith Jones, Brookhaven National Laboratory (BNL) for all work that was done at the National Synchrotron Light source (NSLS). I saw his conviction and want to salute his unwavering commitment to the science. I want to acknowledge everyone at Brookhaven National Laboratory and Stony Brook University who assisted me with laboratory facilities. I am also grateful of Al Tobin for choosing me as his TA where I got to revise, apply chemical engineering thermodynamics concepts and shape-up my teaching skills. I have been here far too long to thank all my lab members but it will be a remiss if I don't mention Mike Eaton, Mojgan Anjom, Suarabh Patel and Kristine Horvat. My time in Stony Brook was made enjoyable by many friends/apartmentmates including Apoorva Mehra, Unmesh Kulkarni, and Arash Ghabchi. I want to thank Santosh Kulkarni for his help with coding to fit methane output data from hydrate decompositions. I also want to acknowledge Aleya Kaushik for helping me with seawater salinity measurements. I appreciate the time and help of Claire Burrows and Kristine Horvat in proof-reading my writings and providing invaluable suggestions throughout. Lastly, my biggest thanks go to my mom and dad for their love, support and encouragement to pursue chemical engineering. It is their belief in me that sustains me and summons my energy and determination. I also owe a great deal

to my sister, Pradnya and my girlfriend, Shweta for keeping me focused, balanced and putting up with my endless complaints about grad school.

Chapter 1

Introduction

The United States currently consumes about 23.2 trillion cubic feet (Tcf) natural gas per year which is about 23% of total energy used. The Energy Information and Administration (EIA) forecasts that the world oil demand will rise from 81 million barrels per day (bpd) this year to 121 million bpd by 2025 with the US, China and the rest of developing Asia consuming up to 60% of those extra barrels. The limited oil resources, overall growth in global energy demand, geopolitics of oil, and need to achieve power generation through inexpensive and less polluting means has renewed interest in natural gas.

The U.S. Geological Survey (USGS) estimates that methane hydrates buried under the U.S. waters alone hold some 200 Tcf of natural gas, which would be enough methane to supply the entire nation's energy needs for over a decade at its present rate of consumption. Taken collectively from all sources, there is enough recoverable methane in the form of hydrates- methane locked in ice- to supply energy for hundreds, maybe thousands, of years. This leads to the hope for methane hydrates to be a solution to our dwindling fossil fuel supply only if an environmentally benign method to extract methane is developed.

The previous methane hydrate research was driven by the quest for an unconventional resource to meet the growing energy challenge. However there are several technological hurdles to commercialize gas hydrates. The most known marine gas hydrates are in fine-grained, clay-rich sediments with little or no permeability. Flow of gas to a well bore requires effective paths of fluid flow, but establishing such paths in low permeability sediments may be exceedingly difficult.[1] There is certainly a serious safety hazard involved during drilling operations, since hydrates can decompose into gas under well bore conditions. Pumping hot oil from great depths through drill pipes can cause warming of sediments and dissociation of hydrate, liberating large amounts of methane, weakening sediments, and perhaps generating pockets of highly pressured gas. The result might be gas blowouts, loss of support for pipelines, and sea-floor failure that could lead to underwater landslides and the release of methane from hydrates.

Researchers have documented the presence of gas bubbles from dissociating methane hydrates in the Gulf of Mexico (GoM), Blake Ridge (BLR), and the Cascadia margin regions. The observations at the GoM site show that gas hydrates on the seafloor form and decompose in cycles over the course of weeks to many months (Kastner, 2006). The hydrates at BLR occur as layers (up to 15 cm thick) of white, crystal-like "bubbles" resembling upside-down ice cream cones. Large (~1 cm) bubbles were seen floating up through the water from a seafloor discharge site (Van Dover et al., 2003). Suess et al. (2001) presented evidence of methane bubbling from porous hydrate mounts and floating hydrates at the sea surface of the Cascadia margin.

Commercial production of gas from hydrate is expected to have a long time on the horizon (20-30 years) (White, 2004) due to substantial technological and economical challenges (Boswell, 2009) involved such as proxy bottom simulating reflector (BSR) evidence, inability to calibrate electric logs due to dissociation of hydrates when brought to the surface, free gas beneath the gas hydrate stability zone (GHSZ), the presence of gas vents, inconsistent occurrence, uncertain methane origin (biogenic, thermogenic) and hence unreliable molecular and isotopic composition, and periodic release of large chuck of hydrate from the sea floor.

[1] US Department of the Interior, US Geological Survey, Fact Sheet 021-01

Many of the technological challenges with respect to sea-floor stability in the event of production/dissociation of methane hydrates are due to their unknown microstructural model and the effect of overburden. The hydrates under shallow seals exhibit more expansion and ice or gas hydrate supported texture which leads to unstable dissociation due to the absence of overburden pressure as opposed to the same at considerable depth resulting in framework-supported textures (Mikami et al., 2000). Thus the connecting pores of the gas hydrate or ice supported texture can undergo texture changes and reduce the permeability during production. At a grain-size scale, hydrates in sediments are classified as cementing at grain contacts, grain coating, grain supporting, pore filling, or massive. The microstructural growth model for hydrates within the porous media governs the elastic properties and the mechanical strength of the seafloor.

The goal of this study is to address aspects that will aid in understanding the sediment-hydrate interaction. The specific problems on which this work focused are as follows:

<u>Goal 1</u>. Quantification of methane saturation at known natural gas hydrate sites by establishing (macroscopic) methane hydrate formation/decomposition kinetics in host sediments.

Most marine hydrate accumulations are several meters thick below the seafloor though hydrate mounds are also found on the seafloor through gas seepage. There is paucity of data on the formation/dissociation kinetics of methane hydrates in natural sediments. A unit, Flexible Integrated Study of Hydrates (FISH), at the Brookhaven National Laboratory is suitable for studying methane hydrate formation and dissociation kinetics in a laboratory setting. The earlier FISH configuration consisted of a Jerguson see-through high-pressure cell (volume: ~200 mL) that was previously used to form samples of unconsolidated methane hydrate in host sediments at pressures of up to 10 MPa at temperatures of 2-4^{o}C. The unconsolidated system is an excellent representation of hydrate mounds on the seafloor. Below the seafloor, the effect of overburden pressure is dominant as a function of depth and may affect methane saturation in a hydrate deposit, The accurate representation of such a natural system will be the application of overburden pressure on a sediment sample. The kinetic data can provide hydrate

saturation as a function of depth. The following tasks are associated with methane hydrate formation/dissociation kinetics.

Modifications of the FISH Unit

The formation of both unconsolidated and consolidated methane hydrate samples are needed to mimic seafloor systems. The capability to form unconsolidated methane hydrate samples exists in the present configuration of the FISH unit. The following modifications were performed to add capability to form consolidated methane hydrate samples and make the unit more versatile.

- Add a customized Temco high-pressure (up to 34 MPa) cell to the FISH unit to form consolidated methane hydrate samples (2 inch in diameter and 6 inch long). The overburden pressure could be varied to simulate methane hydrate reservoirs at seafloor depths.
- Add a stainless steel poppet check valve below the fixed retainer in Temco cell to confine sediment within the cell and prevent water gravity-drainage.
- For precision temperature control, add three type J thermocouples spaced along the Temco cell length.
- Add an Omega mass flow meter (accuracy: ±1%) with LCD display to precisely measure methane gas output during hydrate decomposition.
- Add an Overburden pressure Isco syringe pump than can deliver constant gas flow and constant overburden pressure (maximum pressure: 70 MPa) on the core sample.

Methane Hydrate Formation in Host Natural Sediments and Data Acquisition

The modified FISH unit fitted with Jerguson see-through cell and Temco cell can operate in high-pressure mode to form methane hydrates in natural sediments. The automated Labview data collection system from National Instruments (NI) records temperatures, pressures and flow rates throughout the unit. The tasks carried out for formation and dissociation kinetics of methane hydrates in natural sediments are as follows:

- Calibration of both cells, pressure sensors, thermocouples in the FISH unit.

- Effect of effective pressure on methane hydrate formation kinetics in consolidated Ottawa sand.
- Effect of effective pressure on methane hydrate dissociation kinetics and methane gas quantification of methane gas output upon dissociation by depressurization to retrieve hydrate dissociation constant.

Goal 2. Microstructure investigations of methane hydrate in porous media to predict hydrate site stability.

The approach was to utilize various spectroscopic techniques described under the following operational tasks.

Computed Microtomography (CMT) technique

- CMT data collection and reconstruction procedure development

  The CMT data collection is an established procedure but 2-dimensional and 3-dimensional (3-D) data reconstruction is a challenge. A method was developed that involves the following steps for data acquisition and 3-D volume construction and rendering. The goal was to generate a reproducible data processing procedure.

  - Collect a total of 1200 views in an assembled file (.prj) in IPLab software for a region of interest (ROI) keeping the sample container within the ROI from angle 0 to 180^{o}. Scan several tomograms with time.
  - Interactive data language (IDL) based convert_x2b_netcdf_display.sav routine for converting filename.prj to filename.volume
  - IDL based tomo_display.sav routine for converting filename.prj to filenamerecon.volume
  - Converting image sequence into raw data in ImageJ
  - Raw data processing in Drishti
  - Volume rendering and applying transfer function in Drishti

- Design of an ambient pressure and low temperature CMT cell.

For characterization of depleted sediments or surrogate system which would also act as reference does not require high pressure. The sample holder used was a typical 1 mL polypropylene syringe fitted with a cooling jacket.

- Characterization of natural depleted sediments

  Characterize natural sediment samples from GoM, BLR sites and reference sediment sample (Ottawa sand) using the simple CMT cell that operates at ambient pressures. Reconstruct data using a developed procedure. The data from CMT would be complimented by a suite of other spectroscopic techniques to characterize these sediment samples. It involved measurement of particle size, morphology, surface characteristics, elemental composition through scanning electron microscopy (SEM) and energy dispersive X-ray (EDX) analysis.

- Design of high-pressure (7 Mpa) and low temperature (2-5^{o}C) CMT cell

  The requirements for methane hydrate formation cell are complex with respect to high pressure, low temperature and low attenuation. Pure methane hydrate systems (devoid of sediments) have been studied in small cells (~1 mL) such as the one by Oak Ridge National Laboratory (ORNL). Such systems have limited use for extrapolation in natural settings where host sediments are known to play significant role. This task was to design and construct a cell that could accommodate about ~5 mL of sediment-water mixture at high pressures of methane. Since no such off-the shelf cell existed, the challenge was to select a material of construction for high pressure, effective cooling, and less absorption to utilize 6-35 keV beam energy at beamline X2B, National Synchrotron Light Source (NSLS), Brookhaven National Laboratory (BNL).

- Characterization of surrogate tetrahydrofuran (THF) hydrate system – Baseline study

  The goal of this experiment was to establish feasibility of the CMT technique for hydrate microstructure determination. It is known that the THF-water system forms structure II hydrate at ~278 K and ambient pressure. Gas hydrate formation had never been observed using the CMT technique. Since methane hydrate requires high pressures to form and the presence of sediments complicates the situation as they act as x-ray absorbers thus lowering the attenuation, a simple THF-water-glass beads

system was first used as a baseline for time-resolved methane hydrate growth imaging.

- Methane hydrate formation and their microstructure determination

  The ultimate goal was to investigate the microstructure of methane hydrates (structure I) by performing their time-resolved X-ray CMT while they were formed in porous media loaded in the proposed high-pressure cell.

Chapter 2

Background: Gas Hydrates, Structure, Stability, Occurrences, Laboratory Studies, X-ray CMT and its Application for Hydrates

2.1 What are Hydrates?

Gas hydrates are naturally occurring ice-like solids in which water molecules form a framework through hydrogen bonding and trap gas molecules in cage-like structures known as clathrates. Although many gases form hydrates in nature, methane hydrates are by far the most common; methane is the most abundant natural gas. The volume of carbon contained in methane hydrates worldwide is estimated to be twice the amount contained in all fossil fuels on Earth, including coal and conventional natural gas. Estimates of the global resources of natural gas hydrates range from 100,000 to almost 300,000,000 trillion cubic feet (Tcf). To put these quantities in context, estimates of the remaining global reserves and undiscovered resources of conventional natural gas total are about 13,000 Tcf.

2.2 Structure

Gas hydrates are solid crystalline compounds in which gas molecules are encaged inside the lattices of ice crystals. These light non-polar gases are referred to as guests,

whereas the ice crystals are called hosts. Hydrocarbon gas hydrates are of particular interest. A hydrocarbon gas M will induce water to form hydrates under low temperature and high pressure conditions.

$$M + N_H H_2O \leftrightarrow M.N_H H_2O$$

where N_H is the hydration number.

The water molecules through hydrogen bonding form a lattice structure with interstitial cavities. These cavities are occupied by gas molecules with molecular size smaller than the diameter of the cavities, thereby stabilizing the crystal lattice framework. It has been established that a majority of hydrates crystallize into two types of structures, commonly known as sI and sII, which have been investigated with X-ray diffraction methods by von Stackelberg and Müller (1954). They found that the unit cell of sI is a 12 Å cube, consisting of 46 water molecules, which has two types of cavities. The two small cavities are pentagonal dodecahedra (5^{12}), whereas the six large cavities are tetradecahedra ($5^{12}6^2$) and have two opposite hexagonal faces and twelve pentagonal faces, giving an average coordination number for the hydration shell in the crystalline state of 22 water molecules at a radius of about 3.91 Å (Table 2.1). The smaller cavities are almost spherical, whereas the larger cavities of sI are slightly oblate. The unit cell of sII, which is a 17.3 Å cube with 136 water molecules, also contains two types of cavities. The 16 smaller cavities are distorted pentagonal dodecahedra and the 8 larger cavities are hexadecahedra ($5^{12}6^4$), having 4 hexagonal faces and twelve pentagonal faces. The latter cavities are almost spherical in shape.

Ripmeester et al. (1987*)* reported a new hexagonal hydrate structure, known as sH which requires both large and small molecules to stabilize the structure. According to the authors, the unit cell oh sH hydrate has 34 water molecules forming a hexagonal lattice. The sH has three different types of cavities, three 5^{12} cavities which are common to all known hydrate structures, two new 12 face $4^3 5^6 6^3$ cavities and one new large $5^{12}6^8$ cavity. The $4^3 5^6 6^3$ cavity has three square faces, six pentagonal faces, and three hexagonal faces, whereas the $5^{12}6^8$ cavity has 12 pentagonal faces and eight hexagonal faces. The first two cavities accommodate the small gas molecules. The large cavity in this structure can accommodate even larger molecules, so molecules in the size range of 7.5 to 8.6 Å can potentially form gas hydrates.

The structure formed is a function of the molecular size of the gas molecules, with smaller molecules such as methane, ethane, nitrogen, and carbon dioxide forming sI and larger gas molecules such as propane and isobutene forming sII. The sH is formed from components of the light naphtha fraction or components of gasoline, thus indicating a hydrate structure that can participate in petroleum as well as natural gas processes. The arrangement of molecules in sI, sII, and sH are shown in Fig. 2.1.

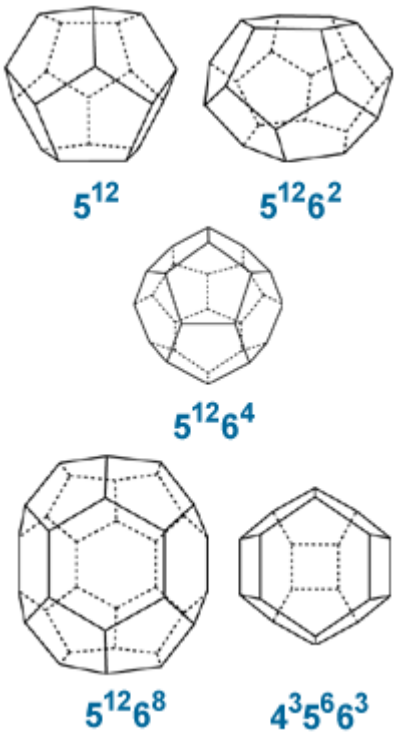

FIG. 2.1. Types of cavities in Structures I, II and H hydrate (Sloan, 1998).

Table 2.1. Physical properties of the three types of gas hydrates (Sloan, 1998).

	Structure I	**Structure II**	**Structure H**
Cavity Types	5^{12}, $5^{12}6^2$	5^{12}, $5^{12}6^4$	5^{12}, $4^35^66^3$, $5^{12}6^8$
Radius (Å)	3.91, 4.33	3.902, 4.683	3.91, 4.06, 5.71
Cages / Unit cell	2, 6	16, 8	3, 2, 1
Co-ordination number	20, 24	20, 28	20, 20, 36
Crystal Type	cubic	cubic	hexagonal

Vast amounts of hydrocarbons are trapped in hydrate deposits (Sloan; 1998). Such deposits exist in distinct geologic formations such as permafrost and deep marine sediments, where the thermodynamic conditions of low temperature and high pressure allow hydrate formation. The lower depth limit of hydrate deposits is controlled by the geothermal gradient. Current estimates of worldwide quantity of hydrocarbon gas hydrate range between 10^{15} to 10^{18} m^3. Even the most conservative estimates of the total quantity of gas in hydrates may surpass by a factor of two the energy content of the total fossil fuel reserves recoverable by conventional methods (Sloan, 1998).

2.3 Methane Hydrate Occurrence and Stability

Formation of gas hydrates requires the presence of hydrate-forming gases and water under appropriate pressures and temperatures. In natural environments, low temperature and high pressure conditions could occur in sedimentary deposits offshore in shallow depths below the ocean floor in outer continental margin and onshore beneath the permafrost (Kvenvolden and McMenamin, 1980). Figure 2.2 shows the potential onshore and marine hydrate accumulations. The geologic occurrence of gas hydrates has been known since the mid-1960s when gas-hydrate accumulations were discovered in Russia (Makogon, 1981). Cold surface temperatures at high latitudes of earth are conducive to the development of onshore permafrost and gas hydrates in the subsurface. Gas hydrates are known to be present in the western Siberian platform (Makogon, 1981) and are believed to occur in other permafrost areas of northern Russia, including the Timan-Pechora province, the eastern Siberian craton, and the northeastern Siberian and Kamchatka areas (Cherskiy et al., 1985). Permafrost associated gas hydrates are also present in the Northern American arctic. Direct evidence for gas hydrates on the North Slope of Alaska comes from core tests and indirect evidence comes from drilling and open-hole industry well logs, which suggest the presence of numerous gas-hydrate layers in the area of the Prudhoe Bay and Kuparuk River oil fields (Collett and Ehlig-Economides, 1983). Well-log responses attributed to the presence of gas hydrates have been obtained in about one-fifth of the wells drilled in the Mackenzie Delta and in the Arctic Islands, more than one-half of the wells are inferred to contain gas hydrates (Bily

and Dick, 1974). In permafrost regions, gas hydrates may exist at subsurface depths ranging from approximately 150 to 2000 m. Samples from the Leg 146 Cascadia margin (sites 889/890 offshore Vancouver and 892 offshore Oregon) have been characterized to contain small pellets of hydrates disseminated in silty clay and occasional massive hydrates underneath free gas cap (Suess et al., 2001). The hydrates have been traced in the form of small crystals dispersed in sediments at Blake Ridge (BLR) Ocean Drilling Program (ODP) Leg 164 on the Atlantic continental rise between depths of 190 to 450 m (Dickens et al., 1997). Massive hydrates were found in intervals of fractured claystones and siltstones and in the form of thin sheets offshore Costa Rica at a 3300 m water depth (Kimura et al., 1998). The organic matter buried about one meter beneath the seabed undergoing biogeochemical changes leads to gassy sediments found in river deltas, estuaries and harbors, but also in deeper waters on continental shelves and slopes (Best et al., 2004). Shallow gassy sediments have been an issue of concern as a contribution to global warming, earthquakes, increased rainfall and unstable drilling platforms. In Gulf of Mexico where the ocean is at least ~1300 m deep, methane hydrates exist at depths of about 0-375 meters below sea-floor (mbsf).

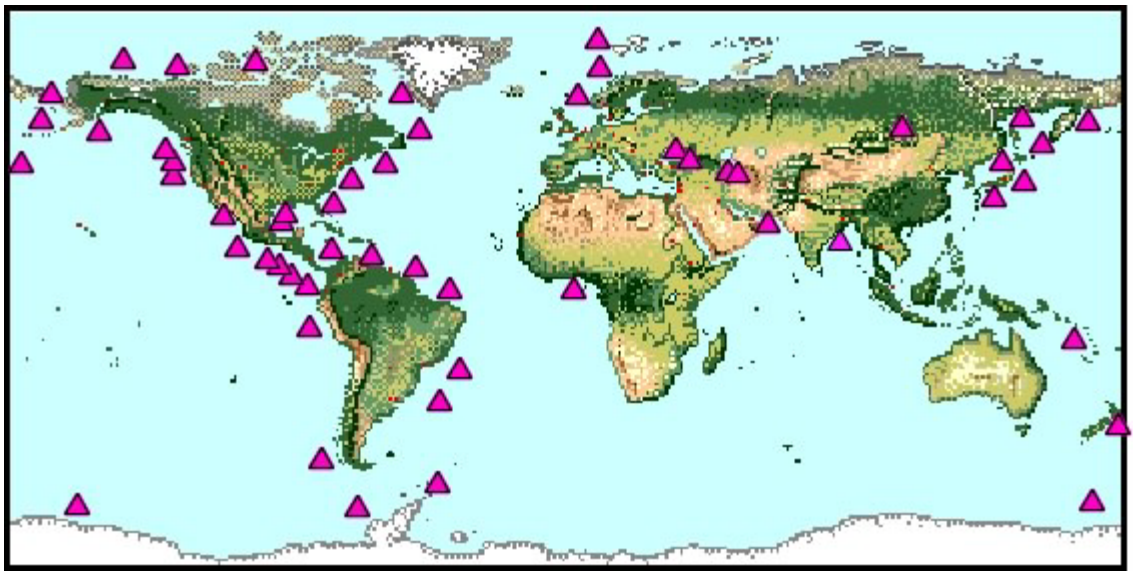

FIG. 2.2. Worldwide distribution of methane hydrate sites (shown in triangles) (Courtesy: Naval Research Laboratory).

The gas hydrate stability zone (GHSZ) is a subsurface depth range within which gas hydrates are stable or may crystallize from the gas phase. The thickness of GHSZ depends mainly upon water depth, bottom water temperature, pressure, thermal gradients in sediment pores, pore water chemistry, gas composition and sediment geochemistry. The geothermal gradient of the earth increases the pressure requirement for the stability of the hydrate at a much greater rate than the pressure increases due to the hydrostatic gradient. Therefore, there is a depth interval where hydrates may be stable. Figures 2.3(a) and (b) are examples of the depths of hydrate phase stability in permafrost and in oceans, respectively. In each figure, the dashed lines represent the thermal gradients as a function of depth. The slopes of dashed lines are discontinuous both at the base of the permafrost and the water/sediment interface, where new sediment thermal conductivities cause new thermal gradients. The solid lines are drawn from hydrate phase equilibrium data, with pressure converted to depth. As shown in the figure, in permafrost regions, where surface temperatures are well below freezing, gas hydrates can be present at depths between 150 and 2000 m (Kvenvolden and Lorenson, 2001). Under offshore conditions, gas hydrate stability conditions usually extend to depths of 100 to 500 mbsf (Collett et al., 2000), although gas hydrates have been recovered from the ocean floor in some cases. In all these regions, there is a rapid accumulation of organic detritus from which bacteria generate biogenic methane. Carbon isotope analysis show that most of the methane in hydrates is of microbial origin. The methane in clathrates typically has a bacterial isotopic signature and highly variable $\delta^{13}C$ (-40 to -100‰), with an approximate average of about -65‰ (Kvenvolden, 1993; Dickens et al., 1995). However thermogenic sources have also been identified in the Gulf of Mexico (GoM).

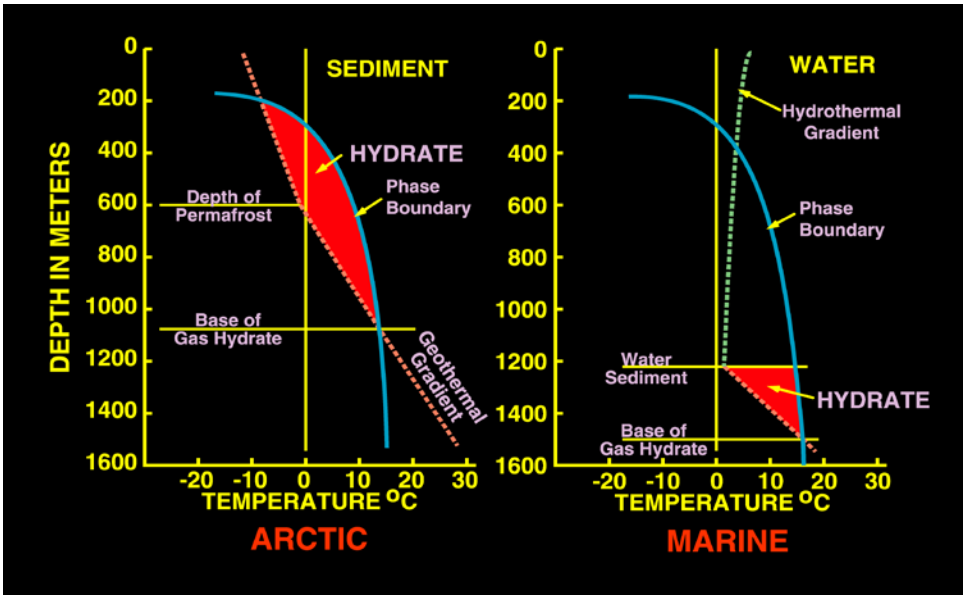

(a) **(b)**

FIG.2.3. Hydrate stability zone for (a) arctic and (b) marine environments (http://www.usgs.doe.gov/). The geothermal/hydrothermal gradients (shown in a dotted lines) and methane hydrate phase boundary curve (shown in blue) enclose a region (shown in red) in which hydrates are stable. In the marine model, the seafloor is shown at ~1300 m as an example of Gulf of Mexico site.

Although massive gas hydrates containing only about 6% mass sediment have been reported (Kvenvolden and McDonald, 1985), they have often been found dispersed in coarse-grained sediment or in geostrata, trapping the natural gas by cementing (Brooks et al., 1985). Sloan (1998) and Collett (2000) have illustrated the possible configurations of hydrates such as disseminated, nodular, layered and massive (Fig. 2.4). The recent coring operations offshore Japan and in the Mackenzie Delta of Canada reveals 80-90% gas hydrate saturation in sand sections.

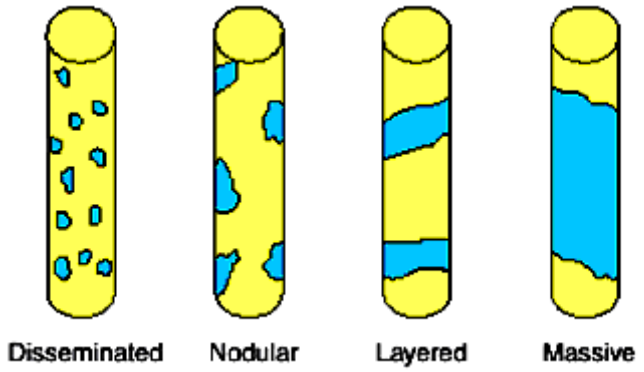

FIG. 2.4. Potential gas hydrate configurations in sediments (Sloan, 1998; Collett, 2000).

2. 4 U.S. Gas Hydrate Potential

Methane hydrates are found abundantly below seafloor in Gulf of Mexico (GoM) (Milkov and Sassen, 2001), Blake Ridge (BLR) (Dickens et al., 1997) and Cascadia margin (Suess et al., 2001), or in permafrost environments on the North Slope of Alaska (Collett and Ehlig-Economides, 1983), Mackenzie Delta regions of northern Canada (Bily et al., 1974) and Russian Siberia (Makogon, 1981). U.S. off-shore gas hydrates sites such as the Blake Ridge, Gulf of Mexico, Cascadia margin and a permafrost site on the North Slope of Alaska are discussed in detailed below.

2.4.1 Blake Ridge

During the ODP (Leg 164) in the Atlantic Ocean, 400 km east from the coast of South Carolina (November and December 1995), hydrate coring was done at BLR 994, 995, 997 and 991, 992, 993, 996 sites (Fig. 2.5) up to 700-750 mbsf and 50-67 mbsf respectively for sediment characterization and gas migration investigations (Paull et al., 2000). The average seafloor depth and water saturation between 210-450 mbsf at 994, 995, 997 sites are 2750 m and 85-100% respectively. The methane hydrate is present between ~212-429, ~193-450 and ~186-451 mbsf at site 994, 995 and 997 respectively (Collett and Ladd, 2000). The sediment consists of silty clays and calcareous oozes and it was found to contain between 0.5-1.5% organic carbon, while gas was ~99% methane, ~1% CO_2 and trace amounts of ethane and other hydrocarbons. The volumetric evolved gas to water ratio of 130-160 indicated 70% cage filling of sI methane gas hydrates

(Sloan, 1998). The mercury injection method revealed the pore diameters range from a few nanometers to a few microns, the mode being 80-150 nm (Clennell et al., 1999). The acoustic velocity values in the well logs of less than 1500 m/s below 450 mbsf (base of gas hydrate stability) pertains to the presence of 200 m thick free gas with 17% gas saturation at site 997B. The free gas zone is thin at site 995 and way below 450 mbsf at site 994 (Wood and Ruppel, 2000).

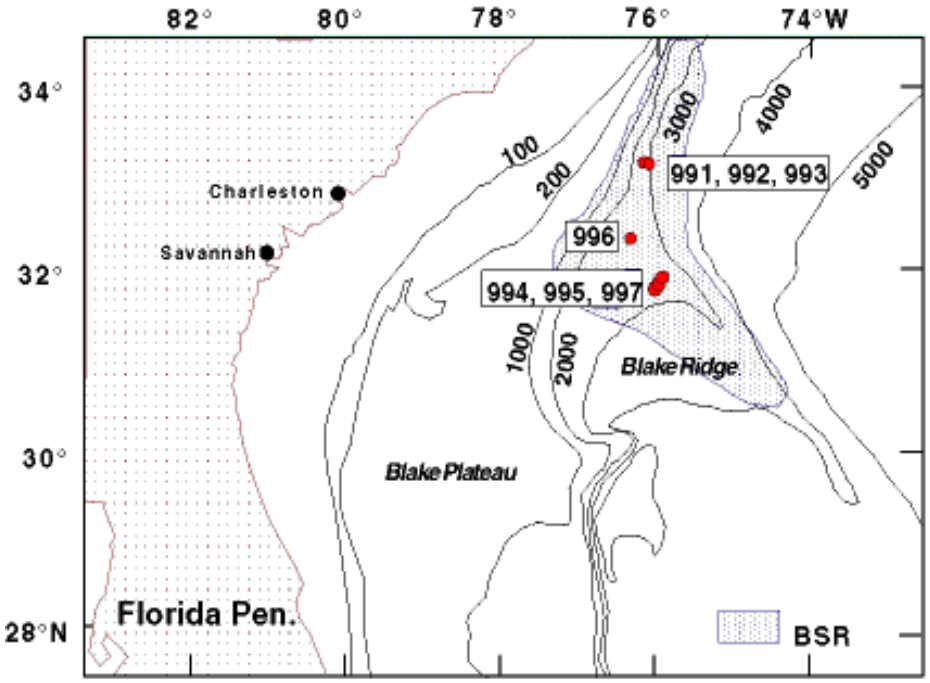

FIG. 2.5. Blake Ridge 996 Site in the Atlantic ocean off the coast of South Carolina (NETL).

The BLR 996 site has a small fault extending downwards which helps fluid migration. The cores from the uppermost sediment column contained gas hydrates. Moreover, hydrogen sulfide gas concentration (>100 ppm in shallow (<20 mbsf) cores) although decreased with depths, is a result of an anaerobic methane oxidation reaction with sulfate. The shear sonic velocity and other geophysical logs acquired at site 996 have shown that the sediments are overconsolidated above the BSR at 440 mbsf because of the presence of hydrates. BLR methane hydrates have appeared as intergranular cement and increase the rigidity and the bulk modulus of the host sediment. Below the

bottom of the thermodynamic hydrate stability zone at ~520 mbsf, the high compressibility of the formation and the attenuation of the monopole sonic waveforms also show the presence of free gas. Between these two depths, gas hydrate and free gas may coexist. The existence of free gas and gas hydrates below the BSR may be explained by capillary effects in the smaller pores or by remaining crystalline structures after partial hydrate decomposition.

Guerin et al. (1999) has given a comparison between sites 994, 995 and 997. The low seismic amplitudes to ~530 mbsf at site 994 indicate the presence of gas hydrates at this depth. However the free gas either rising from a deeper source or resulting from gas hydrate dissociation is driven past the southwest edge of the BSR through numerous faults (Dillon et al., 1996). At site 997, a high concentration of free gas is responsible for the attenuation of the monopole waveforms occurring from 440 to 480 mbsf. Moreover, the porosity decreases sharply in first 100 mbsf from 85 to 65% and slowly in 100-600 mbsf (65-47%) at site 997 (Flemings et al., 2003). Between 480 and 550 mbsf, hydrates and free gas coexist as at site 995. A higher concentration of free gas increases the dipole waveform amplitudes in this interval, despite the presence of hydrates. At higher depths, and most notably below 600 mbsf, high concentrations of free gas are indicated.

The transmission microscopy of the sediments from ODP Leg 164 (997A, 510 mbsf) immediately after core recovery revealed the existence of foraminifera[1], diatoms[2], accumulations of spicules, sand-like microfossile debris and pods and lenses of framboidal pyrite[3] (Lorenson, 2000). Since capillary forces within fine or constricted pores reduce gas hydrate formation temperature by as much as $4^{o}C$ at a particular pressure (Handa and Stupin, 1992), hydrates are primarily found in highly porous or coarse grained sediments as opposed to smaller, constricted pores within fine grained sediments. The gas hydrate concentrations at BLR are found to be lesser than 15% of the bulk volume of the host sediment (Ginsburg et al., 2000). The average concentrations of gas hydrates are 3.9, 5.7 and 3.8% at sites 994, 995 and 997 respectively from core

[1] Foraminifera – Foraminifer are large subset of amoeboid, cells that move or feed by means of temporary projections, called pseudopods (false feet).
[2] Diatoms – Diatoms are major group of eukaryotic (with complex cell structure and nucleus) algae and are one of the types of phytoplankton (plankton or drifting organism which produces complex organic compounds from simple inorganic compounds and an external source of energy such as light.
[3] Framboidal pyrite – Framboidal pyrites (Iron Sulfide, FeS_2) are solitary spherules or irregular masses of organic matter preserved in the pores of sedimentary deposits.

porosities and acoustic logs (Lee, 2000). These values are about 2.2, 3.3 and 2.2% of the total sediment volume (vol%) and very similar to the ones from resistivity logs (Collett and Ladd, 2000). Moreover, the downhole well logging at Leg 164 found gas hydrates as disseminated deposits (Paull et al., 1996; Kumura et al., 1997) in coarse-grained sediments with high porosity.

2.4.2 Gulf of Mexico (GoM)

The northwestern GoM (Fig. 2.6) is a unique and well-studied location with faults, folding and buoyant salt deposits where hydrates occur in shallow sediments (5-20 m) as seafloor mounds. Although more than 160 high gas flux sites occur on the GoM slope, only ~50 sites on the GoM are believed to contain gas hydrates in sediment due to their decomposition from shallow deposits (Milkov and Sassen, 2003). This distribution of hydrates in the GoM contrasts with other continental margins viz: BLR, Costa Rica, Cascadia and Nankai Trough, where hydrate zone is from ten to hundred meters below seafloor.

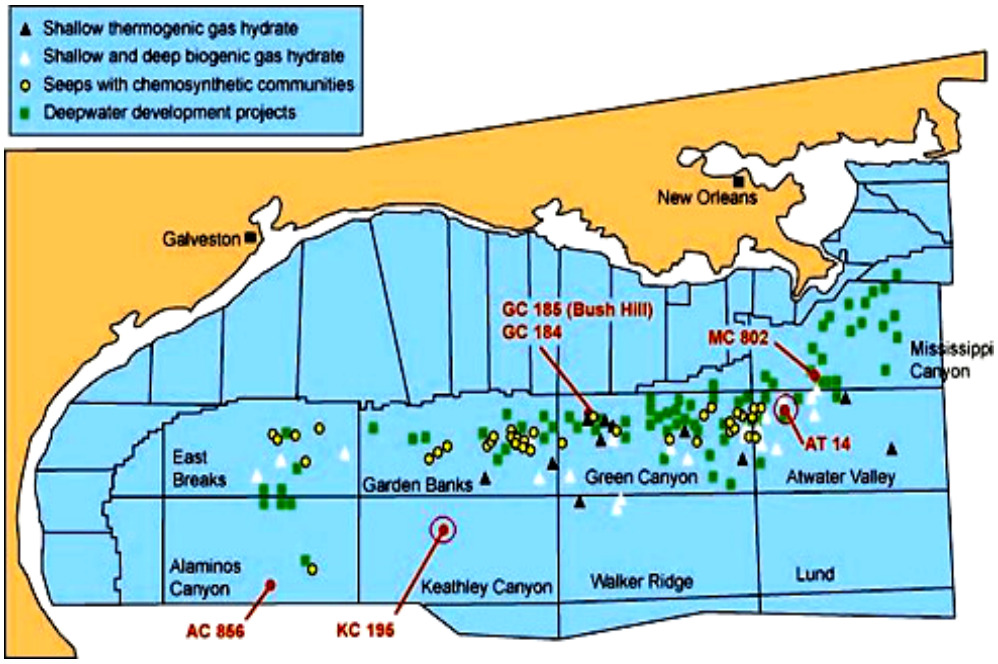

FIG. 2.6. Gulf of Mexico drilling locations relative to lease blocks (NETL).

Based upon derived GHSZ thickness and assumption of 5-10 vol% gas hydrate concentration, Milkov and Sassen (2003) estimated the volume of hydrate-bound gas at Green Canyon (GC) blocks 184/185, GC 234/235, Garden Banks (GB) 388, Mississippi Canyons (MC) 798/842, GC 204, MC 852/853 and Atwater valley (AT) 425/426 sites in GoM. The MC 852/853 (~1050-1060 m water depth) where hydrate of C1-C5 hydrocarbon gases (sII) occur within deformed and gassy sediments containing biodegraded crude oil, appear to have the highest economic potential, whereas, GC 204, GB 388 and AT 425/426 sites were ranked as "average". The GC 234/235, GC 184/185 and MC 798/842 sites contain only small amount of gas hydrate-bound gas and have less economic potential.

Francisca et al. (2005) reported the comparison of physical properties such as visual observations of gas hydrate, grain size, specific surface area, pH, percentage of carbonate, gravimetric water content, porosity, mechanical properties and electromagnetic properties of GC185, GB425 and MC852. The average water depth at these lease blocks is ~540 m, ~620 m, ~1080 m respectively. The hydrate-bearing sediments recovered in October, 2002 from top ~2 m and ~3.5 m at GC185 and MC852 respectively were found to be within oil seam and with specific surface area of 57-79 and 30-64 m^2/g respectively. The percentage sand fraction (>75 μm) and clay fraction (<2 μm) at these sites were 4.9 and 3.5, and 55 and 48.5 respectively. The gravimetric water content varies significantly with depth 125% at mudline to 50% at 2 mbsf at GC185 whereas from ~145% at mudline to 100% at 3.56 mbsf for MC852. The water content (w), specific gravity (Gs) of 2650 kg/m^3 and 100% water saturation (S) yield porosities (ø) between 50-80% using the following equation.

$$Gs.w = S\frac{\phi}{1-\phi} \tag{1}$$

Chevron Exploration and Production Technology Company executed the drilling of 7 wells including two out of five short wells (24.4 and 31.4 mbsf) in AT valley and two wells in Keathley Canyon (KC) in April and May of 2005, for *in-situ* measurements and characterization purposes (Jones, 2006). The wells AT13#1, AT14#1, AT13#2 were drilled up to 246, 286.8, 199.9 mbsf respectively, whereas KC151#2, KC151#3 were drilled through 1310 and 1333.5 m water depth respectively and up to 459 and 440 mbsf

respectively. As much as 20% of pore space hydrate concentration was estimated within sediment consisting of mostly silts and clays with only a small thickness of sand.

The sediments in the northern GoM overlie enormous reservoirs of liquid and gaseous hydrocarbons that rest upon Jurassic-age salt deposits (Kennicutt et al., 1988; Roberts et al., 1999). GoM gas hydrates are sII hydrates, containing methane (44%), ethane (11%), propane (32%), iso-butane (9.5%), butane (3%) and pentane (0.5%) (Sassen and Macdonald, 1997; Orcutt et al., 2004). Sediments in and around areas of active seepage are characterized by elevated concentrations of simple (C1–C5) and complex (oils) hydrocarbons and hydrogen sulfide (H_2S). Complex chemosynthetic communities comprised of a variety of microorganisms and bacteria-metazoan symbioses thrive around hydrocarbon seeps in the GoM (Fisher, 1990). The magnitude of spatial and temporal variation in fluid flow at GoM seeps is presently unknown.

2.4.3 Cascadia Margin

Leg 146, including sites 889/890 around 100 km off the coast of Vancouver Island and 892 offshore Oregon, has been a part of ODP. The sediments at both sites are undeformed and fine gained (clayey silts) with occasional sand layers. However, the underlying accreted material is highly tectonized and has varying texture and physical properties (Clennell et al., 1999). The small pallets of gas hydrates are found disseminated in silty clay and occasional massive pieces in shallow subsurface HSZ at site 892 (Westbrook et al., 1994). The “soupy” or mousse-like layers which are interleaved with overconsolidated sediment found have on average a coarser texture than non-hydrated sediments at these sites (Kastner et al., 1996).

The International Ocean Drilling Program (IODP) conducted an expedition 311 in the northern Cascadia region (Fig. 2.7) in September-October of 2005 (Expedition 311 Scientists, 2005). The logging while drilling (LWD)/measurement while drilling (MWD) and wireline logging discovered different stages in the evolution of gas hydrates at sites U1325, U1326, U1327 and U1329 (Fig. 2.8) along a margin-perpendicular transect, from the earliest occurrence at the westernmost site U1326 to the final stage at easternmost shallow water site U1329. The amount of methane in the pore fluid exceeds the local

methane solubility at sites U1326 and U1327, where more than 80% of the pore volume hydrates occur in several tens of meters thick regions at a shallow depth of ~100 mbsf. The cold vent site U1328 represents massive gas hydrates at ~40 mbsf with the concentration exceeding 80% of the pore space. The bathymetry data shows water depths of ~2200, ~1827, ~1306, ~1265 and ~950 m at sites U1325, U1326, U1327, U1328 and U1329 respectively. The site U1325 is characterized as coarse grained sand layers within fine-grained (clay and silty clay) detrital interlayers (0-52.5 mbsf) and fine grained detrital sediments with intervals of silty/sandy interlayers of turbidite deposits (below 52.23 mbsf). The LWD/MWD suggests that hydrates are concentrated in thin sand layers between 173-240 mbsf. The degassing of core indicates small amount of gas hydrates (0.4%) or free gas (0.3%) depending upon the base of GHSZ (BGHSZ). The gas composition is entirely of methane with ~0.1-0.5% of CO_2 and <5 and <15 ppm of C_{2+} hydrocarbons at 230 mbsf and higher depths respectively. The site U1326 is characterized as fine-grained detrital sediment with thin silty/sandy interlayered turbidite sequences. The 40% gas hydrate saturation occurs within 50-100 mbsf with inferred water saturation as low as 20% and gas being predominantly methane.

The five holes viz: A, B, C, D, E were drilled at site U1327 (maximum depth of 1322 meters below sea level) to characterize it as mainly fine-grained detrital sediment with abundant coarse-grained layers up to 6 m thick indicating turbidite deposits. The deepest (246 mbsf) and ~25 m below BSR core from U1327-D hole yielded 0.9% of pore space free methane gas. The shallowest core from ~80.5 mbsf at U1327-E hole contained 0.2% gas hydrate, whereas gas hydrate in the core sample from 155.6 mbsf at U1327-D was found to be ~8% of the pore space. The methane was found to be the predominant gas with increasing concentration of ethane near the BSR. The LWD/MWD confirmed as much as 18 m thick zone of gas hydrate (120-138 mbsf) with >50% of the pore volume in the U1327-A hole by increased electrical resistivity and acoustic velocity and decreased density.

The site U1328 represents an area of active fluid flow due to at least four vents with near surface faults. The sediment at this site is characterized by fine-grained detrital sediment with abundant coarse-grained layers up to 6 cm thick indicating turbidite deposits. The LWD/MWD GeoVision tool inferred gas hydrate or possibly free gas in the

interval 0-46 mbsf with as high as 95% saturations and 90-100 mbsf in U1328-A hole. The seafloor temperature of ~3.5^{o}C and the geothermal gradient of ~5.4^{o}C/100 m predict BGHSZ from 222 to 247 mbsf. The gas hydrate saturation varied from ~15% to 2% in core samples from 15 and 26.5 mbsf in U1328-B hole. The gas hydrate saturation also significantly varied from 22 to 0.7% in U1328-C and U1328-E hole at same depth of 92 mbsf. The core sample (U1328-E) from 233 mbsf, very close to BSR depth, contained methane or methane hydrate with 58% or 50% of the pore space respectively.

The easternmost site U1329 (Fig. 2.7) on the southwest-northeast-trending margin has water depth of ~946 mbsl and BSR depth of ~125 mbsf. This site is characterized by fine-grained detrital sediment, locally interbedded with coarse-grained sediment from 0-37.18 and 135 mbsf– total depth. The intermediate depth, 37.18-135.60 mbsf is characterized by biogenic silica (mainly diatoms). The porosity decreases to from ~65 at the seafloor, 55% at 25 mbsf to ~23% at 220 mbsf, whereas the grain density varies from ~2.8 g/cc at the seafloor to ~2.6 g/cc at 175 mbsf. The degassing of the core from 56.1 and 74 mbsf from U1329E hole resulted into gas hydrate of <1% of pore volume. However, the deepest core (188.5 mbsf i.e. much below BGHSZ), suggested a potential pore volume free gas saturation of 2.4%. As at site U1327, methane was found to be a predominant gas with increasing concentration of ethane near the BSR.

Torres et al. (2002) analyzed *in-situ* gas samples and pore water from the northern (HRN) and southern summit (HRS) of hydrate ridge in Cascadia margin. These peaks of the ridge at depths of 600 and 800 m are covered by carbonate deposits representing a more mature stage in the evolution and sediment exhibiting preserved and localized carbonate respectively. The entire ridge showed three provinces viz: (a) methane gas discharge at discrete release points, at HRN due to pressure changes on a deep gas reservoir and at HRS by more localized phenomena destabilizing massive gas hydrates at the seafloor, (b) extensive bacterial mats overlaying sediments capped with methane hydrate crusts at both HRN and HRS and (c) sites colonized by vesicomyid clams where bottom of seawater changes the methane content from the sediment. Milkov et al. (2005) reported molecular and isotopic properties of HRN of Leg 204 where shallow (0-40 mbsf) gas hydrate are of allochthonous mixed microbial and thermogenic methane with a small portion of thermogenic C_{2+} gases migrating vertically and laterally from 2000-2500

mbsf, whereas deeper (50-105 mbsf) hydrates may have crystallized from microbial methane and ethane generated dominantly. It is important to note that non-hydrocarbon gases such as CO_2 and H_2S are not abundant in hydrate samples.

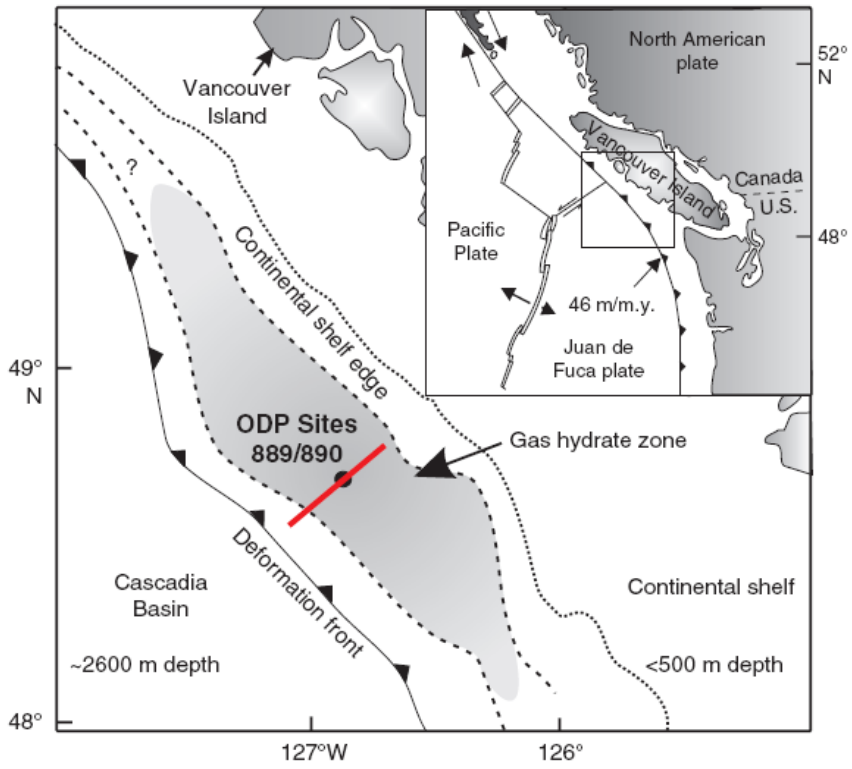

FIG. 2.7. Northern Cascadia Margin offshore Vancouver Island (Expedition 311 Scientists, 2005).

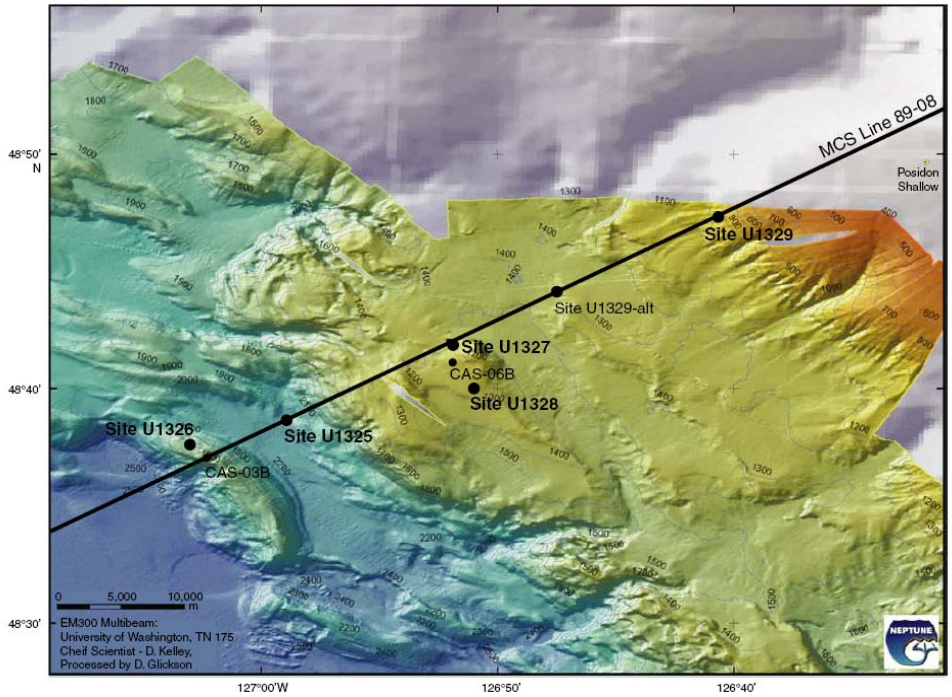

FIG. 2.8. Bathymetry map of IODP Sites U1325, U1326, U1327, U1328 and U1329 from expedition 311 (Expedition 311 Scientists, 2005)

Recently, Lu et al. (2007) characterized the structure, gas content and composition and distribution of guest molecules in the oil-stained natural hydrate sample recovered from a water depth of ~855 m in Barkley canyon, about 80 km off the west coast of Vancouver island, on the northern Cascadia margin. This characterization provides the first confirmation of the existence of natural sH hydrate associated with sII hydrate, both containing more than 13 guest hydrocarbons. The complex hydrate is more stable than methane hydrate and lies between sII and sH on the pressure-temperature (PT) plot, which makes it more potential in oceanic sediments as shallow as 200-500 mbsf.

2.4.5 The North Slope of Alaska

The Prudhoe Bay Unit (PBU), Kuparuk River Unit (KRU), Milne Point Unit (MPU), National Petroleum Reserve- Alaska (NPR-A) and the Beaufort Sea Shelf and Slope, Bering Sea Slope and Rise, North Pacific Aleutian Ridge and Gulf of Alaska are onshore and off-shore Alaska sites where gas hydrates are inferred or identified. Figure

2.9 depicts the distribution of the Eileen and Tarn gas hydrate accumulations in the area of the PBU, KRU and MPU oil fields on the Alaska North Slope (ANS). This area may contain as much as 1.24 Tcf (44 Tcf of gas in place) (Collett, 1993).

The occurrences of gas hydrates on the ANS was confirmed in 1972 with core and production test data from the Northwest Eileen State-2 well located in the northwest part of the PBU field (Collett, 1993). Studies of pressurized core samples, downhole logs, and the results of formation production tests indicate three phase gas-hydrate bearing stratigraphic units in the Northwest Eileen State-2 well. Gas hydrate presence was also confirmed in an additional 50 exploratory and production wells in Northern Alaska based on downhole log responses. Most of these inferred gas hydrates occur in six laterally continuous sandstone and conglomerate units; all of these "Eileen" gas hydrates are geographically restricted to the area overlying the western part of the PBU, the eastern part of the KRU and most of the MPU. Seismic surveys and well logs in the western part of the PBU indicate the presence of several large free-gas accumulations stratigraphically trapped down-dip of four of the log inferred gas hydrate units.

Recently, data from wells along the southwestern margin of the KRU revealed the presence of at least two distinct, relatively thick "Tarn" gas hydrate accumulations overlying the recently developed Tarn field. Cirque-2 well studies suggest at least two distinct gas hydrate accumulations occur within the depth interval from approximately 150 to 720 meters (500 to 2,360 feet) within Tabasco Companion sands. The upper gas hydrate-bearing stratigraphic interval in the Cirque wells appears to be the up-dip equivalent to the West Sak and Ugnu sands. Shallow data collected in a Tarn development by the USDOE/USGS in September, 2000 confirmed the occurrence of a thick hydrate gas in the up-dip portion of Ugnu and West Sak sand. Preliminary analysis of area wells and regional seismic data suggests that the lower free-gas interval within Tabasco Companion sands may be trapped up-dip by a second as yet undrilled gas-hydrate accumulation.

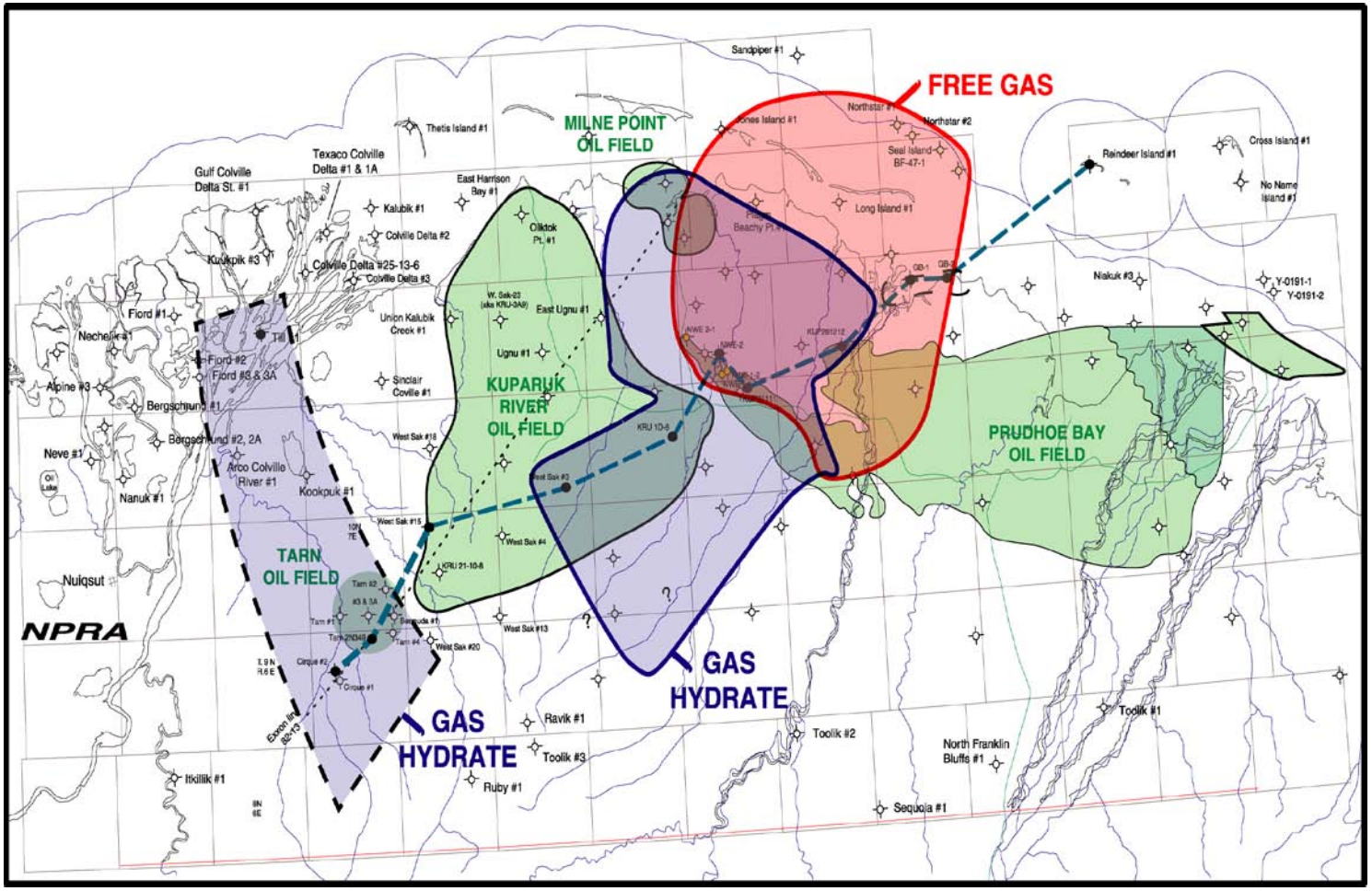

FIG. 2.9. Distribution of gas hydrates on the north slope of Alaska (Collett, 2004). The distribution of the Eileen and Tarn gas hydrate accumulations in the area is shown with a dotted line and that in the Prudhoe Bay Unit, Kuparuk River Unit, and Milne Point Unit is shown with blue boundary. The accumulation of free gas is shown with a red boundary.

2.5 Laboratory Methane Hydrate Formation Studies in Porous Media

Handa and Stupin (1992) published the pressure-temperature profiles for the hydrate-ice-gas and hydrate-liquid water-gas for methane and propane hydrates in 70 Å radius silica gel pores. In the porous sediments, water is in a finely dispersed state and hydrates form quite readily. Thermodynamically, pore hydrates are less stable than bulk hydrates; they are present in a finely dispersed state because of the confinement of pores.

Uchida et al. (1999, 2002) measured dissociation conditions in a 30 mL high-pressure vessel containing Vycor glass sediment (100 Å, 300 Å and 500 Å.) and water. After twenty-four hours of equilibrium time, dissociation curves were compared with bulk hydrate formation data. The hydrate dissociation in pores smaller than 300 Å differs from bulk hydrates. The dissociation data for different sediment sizes underlines the effect of pore-size on dissociation temperature. The magnitude of the inhibition of decomposition conditions in small pores was determined by the reduction of water activity, a measure of the chemical potential normalized by the bulk state.

Seshadri et al. (2001) and Anderson et al. (2001) have recorded this shift for hydrates in media with pore radii between 20 and 251 Å. Ostergaard et al. (2002) and Anderson et al. (2003a,b) compiled experimental studies on hydrate equilibrium in artificial porous media and discussed the quantitative effect of fine pores on hydrate stability. Anderson et al. (2003b) found the equilibrium conditions to be a strong function of pore diameter for methane, carbon dioxide and methane-carbon dioxide hydrates within mesoporous silica glass with mean pore diameters of 9.2, 15.8 and 30.6 nm. The modified Gibbs-Thomson relationship and plotted experimental data to determine interfacial tension for the methane clathrate-water system to be 32 ± 3 mJ/m^2 from the slope of following equation.

$$\frac{\Delta T_{m,pore}}{T_{m,bulk}} = \left(\frac{-2\gamma_{sl}}{\rho_s \Delta H_{m,s}}\right)\left(\frac{1}{d}\right) = cons\tan t\left(\frac{1}{d}\right) \qquad (2)$$

where, $\Delta T_{m,pore}$ – Temperature change during hydrate formation

$T_{m,bulk}$ – Bulk hydrate melting temperature

γ_{sl} – Interfacial energy

$\Delta H_{m,s}$ – Specific enthalpy of transition

d – Pore diameter

ρ_s – Specific density of hydrate

Smith et al. (2002) established methane hydrate equilibrium in silica gel pores of 2, 3, 5 and 7.5 nm nominal radii. Glass beads of 5 mm diameter were coated with silica gel with a liquid nitrogen, silica gel and water slurry in a 30 mL high-pressure cell. The cell was exposed to experimental temperature and methane pressure after vacuuming out air and cooling the cell in liquid nitrogen for 30 minutes. The equilibrium pressure was found to be higher than that for bulk methane hydrates and inversely proportional to the nominal pore radii, the highest being 2 nm. Later, Smith et al. (2004) extended their work on equilibrium conditions for propane, CO_2 hydrates, along with methane in 15 nm radii pores of glass.

Oak Ridge National Laboratory (ORNL) (Elwood Madden et al., 2006) has designed 72 L seafloor process simulator (SPS) (Fig. 2.10) and determined the effect of methane flux on hydrates within 60 cm long, 4.8 cm diameter column with Ottawa sand containing Snowmax, Black sand (<500 μm gain size) and permafrost sediments from the Hot Ice-1 GIP, Alaska at 1500 psi (10 MPa) and 275-277 K. Methane saturated water at ~10 mL/min flow showed no visible sign of hydrates till 3-6 hours, even with 200 mg of Snowmax, while free methane gas with or without water flow took 10-40 minutes for hydrate formation, which emphasizes the relevance of methane bubbles within sediments or at the water-gas interface on induction time. Riestenberg et al. (2003) also investigated the effect of colloids on the equilibrium conditions for methane hydrate by bubbling methane gas through pure water, 200 mg/L bentonite solution and 34 g/L silica suspension at 441 psi (3 MPa) and ~5^{o}C. The hydrate formation pressures were found to be significantly lower for 200 mL/lit bentonite solution than that for pure water, where dissociation conditions were unchanged by colloids.

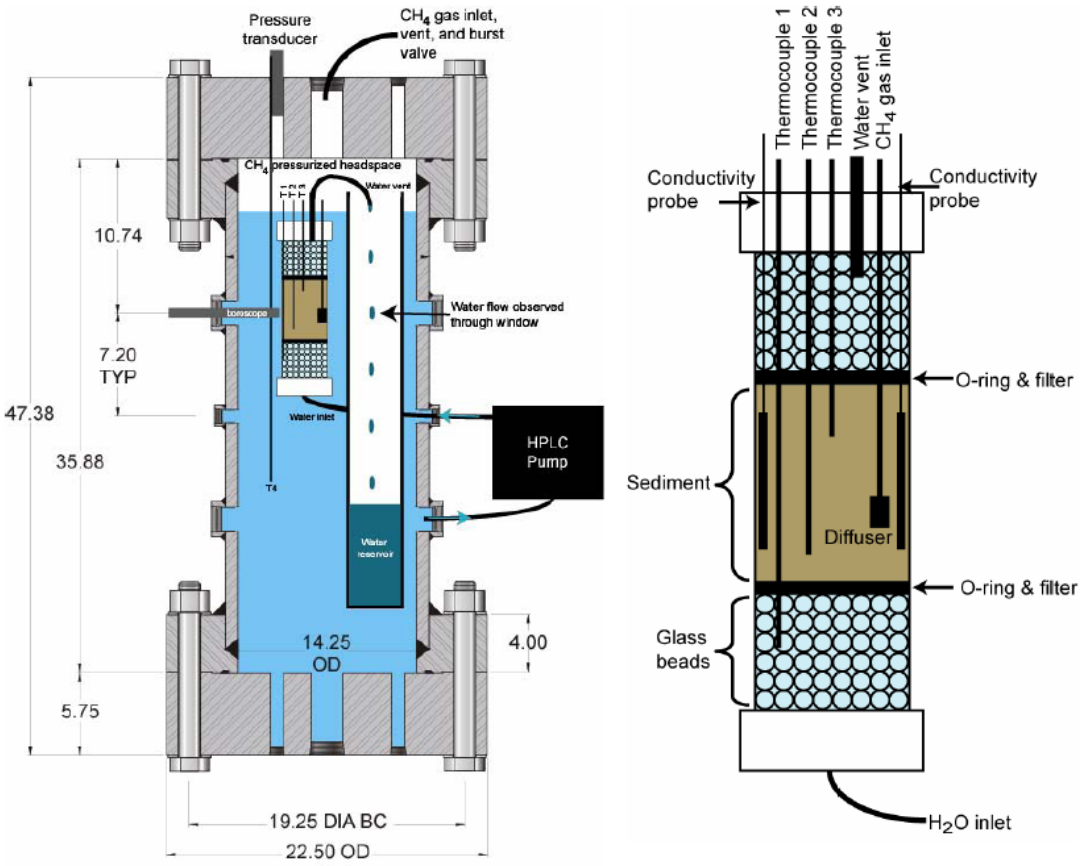

FIG. 2.10. Schematic of seafloor process simulator (SPS) and sediment column at Oak Ridge National Laboratory (Elwood Madden et al., 2006).

Waite et al (2004) compared compressional wave speed (Vp) of hydrates formed with 58, 31, 16% water saturations within 7 cm diameter and 14 cm high Ottawa sand column with predicted Vp, bulk modulus and shear modulus for hydrate distribution models (Dvorkin et al., 1999) viz: hydrate floating in pore fluid, load bearing hydrates, hydrate covering and cementing grains, and hydrate cementing grain contact. Methane hydrates were formed at a confining pressure of 1800 psi (12.4 MPa) and constant pore pressure and temperature of 1764 psi (12 MPa) and 279K respectively. The compressional wave speed measurement after hydrate formation matched those predicted for hydrate coating and cementing grains.

Turner et al. (2005) performed hydrate equilibrium experiments in an Adriatic sandstone (3.8 cm diameter, 8.9 cm length) with an average pore radius of 550 Å (0.055 μm). The hydrate PT equilibrium shift was not observed from that that for bulk hydrates.

The hydrate equilibrium temperature shift with pore radii was computed to be negligible with radii larger than ~600 Å (0.06μm). However the sensitivity analysis assumed the wetting angle of the interface between hydrate crystal and water to be 0^o (perfectly wetting).

Kneafsey et al. (2007) performed X-ray computed tomography (CT) to determine local density changes during methane hydrate formation and dissociation in a partially saturated core-scale sand sample in an X-ray transparent aluminum vessel of 1211 mL internal volume. A sand (100-200 μm)/water (244 g) mixture of 2219 g was packed to a porosity of 38.7% and water saturation of 52%. CT scan showed increased density throughout the sample with the largest increases occurring where the density was initially lowest due to poor packing during hydrate formation.

Methane Hydrate Formation in Sandstone

Yousif et al. (1991) developed and validated the first three-phase 1-dimensional model to simulate the process of gas production, by means of a depressurization of methane clathrate from Berea sandstone. A 6 inch (15.2 cm) long and 0.5 inch (1.3 cm) diameter Berea sandstone sample (100 md permeability and 18.8% porosity) was saturated with 1.5 wt% aqueous sodium chloride solution and methane gas at 1130 psi (7791 kPa) pore pressure, 1180 psi overburden pressure and temperature of 273.7 K. The measurement of electrical resistances provided an additional method to check for hydrate formation, besides the pressure drop in the core sample, for a period of 5 to 34 hours until no change in resistance and pressure drop was observed. A pressure drop of 406 psi after 41 hours and a change in resistance confirmed hydrate formation, although it was not uniform along the core length, causing the permeability to vary.

Sung et al. (2003) validated the experimental model with previous hydrate equilibrium studies by Sloan (1998), measuring the equilibrium conditions of methane hydrate in Berea sandstone (24% porosity and 218 md permeability) saturated with 1.5 wt% sodium chloride and 99.99% methane at 870 psi gas and 33.8^oF (1^oC) isochoric conditions. The confining pressure was about 200 psi higher than the internal pressure. The decrease in pressure to 464 psi in 8 hours and increase in resistivity from 40 kΩ to 73 kΩ signified hydrate formation in Berea sandstone. An excellent match was observed

between the measured equilibrium conditions of hydrate formation in porous medium, such as Berea sandstone and those obtained by Sloan (1998) for bulk hydrates formed in a tank reactor. This might be related to the core being homogeneous with high porosity and permeability.

Kleinberg et al. (2003) mimicked the gas hydrate stability zone (GHSZ) moving down through free gas that has accumulated under the original GHSZ in Berea sandstone, of 2 inch diameter and 11.8 inch in length, in acrylic tubes. The dried samples were initially filled with 100% methane gas at 19 psia. At 2952 ft (900 m) depth (1319 psia), the gas lines were cut and 160 mL pore volume seawater was made to compress the gas (3280 ft (1000 m) depth). No further gas was supplied during the seven weeks after which NMR measurements were performed. In the fast preparation method, which mimicked the transport of free methane to coarse-grained sediments far from thermodynamic equilibrium, the gas flow through the sample was impeded at about 4593 ft (1400 m). NMR measurements were made at 6561 ft (2000 m). The samples were moved to 3280 ft (1000 m) depth, with no addition of gas, for measurements. A second descent to 6561 ft (2000 m) with the attempted addition of gas was followed by ascent to 1968 ft (600 m). The hydrates were formed where the gaseous methane reactant is most abundant: in the largest pore spaces. The methane hydrates were primarily pore-filling, not grain cementing.

Uchida et al. (2004) measured the decomposition conditions of methane hydrates in silica sand, sandstone, clays (kaolinite and bentonite) and glass beads with pore diameters ranging from 1.5 to 44 μm during formation-decomposition cycles. The water saturated Berea sandstone sample, of 1.5 inch diameter and 0.4 inch length with 17% porosity, was placed in the high-pressure vessel, and then degassed before introducing methane gas at 826 psi and 48^{o}F in an amount such that at completion of the reaction there would be enough gas left over to stabilize hydrates. The hydrate reaction was complete within one week, reaching equilibrium pressure and temperature conditions (595 psi and 32^{o}F). At this point in time, the temperature was increased at rate of 0.1^{o}F/h to observe the pressure increase due to the release of gas from hydrates. Variations in the surface texture or pore size, among sand, silica, sandstone, clay and glass beads, did not significantly affect the equilibrium conditions of gas hydrates. However, the equilibrium

lines of hydrates within porous glasses, which had small pores ranging from 0.01 to 0.05 μm in diameter, shifted to lower temperature or higher pressure because of changes in the water activity in smaller pores (Uchida et al.; 1999).

In recent successful attempts at forming methane gas hydrate in Berea sandstone and detecting it with a resonant ultrasound spectrometer (RUS) instrument at the Pacific Northwest National Laboratory (PNNL) (Zhu and McGrail, 2004), the saturated sandstone sample with deionized water was pressurized to 1000 psig (7 MPa) with methane gas, at a temperature of 1°C. Following six days of equilibration time, the temperature was lowered to -3°C for 2 days to assist in complete conversion to gas hydrate. The temperature was then returned to 1°C, where the sample was held for an additional 2 days. A series of resonance spectra were then obtained over the course of 7 days, as the temperature was increased in steps up to 9°C. A minimum equilibration time of 4 hours was allowed after a temperature change, before a RUS spectrum was collected. A reduction in resonance peak amplitude and frequency as a function of temperature is clearly seen in the spectra, demonstrating that RUS is a sensitive detection method for the presence of gas hydrate in porous sediments. At 950 psi (6.6 MPa), the bulk equilibrium gas hydrate temperature is approximately 49.1^{o}F (9.5°C). However, the RUS data clearly show a continuous change in the amount of gas hydrate in the sample between 33.8 and 48.2^{o}F (1 and 9°C). This behavior cannot be explained by the Gibbs-Thomson effect, which describes the depression in equilibrium temperature (or elevation of pressure) as being caused by an interfacial energy contribution in small pores. Pore sizes in the sandstone are much too large to show a significant Gibbs-Thomson effect. Other physicochemical mechanisms appear to have a significant effect on gas hydrate equilibrium in this sample.

2.6 X-ray Computer Microtomography

While Stock (1999) describes X-ray computer microtomography (CMT) as “learning more and more about less and less”, CMT has emerged as a non-invasive and non-destructive tool in the areas of medicine, biology, petroleum, and material technology that has been preferred now more widely than ever before. X-ray absorption

differs due to various substructures, phases, or density gradients, and reconstructed sample interior provides the solution to numerous engineering problems of interest.

2.6.1 The Concept

In 1917, Johan Radon, Czech mathematician became a pioneer in establishing mathematical solution behind CMT. Ever since Allan Cormack, a South African physicist in 1964, put forward an algorithm to reconstruct a finite number of radiographic viewing directions to determine the variation of X-ray attenuation within a cross-section of an object. Since the first CT scanner built by Godfrey Hounsfield in 1972, tomography has become a revolution in medical imaging. The word "tomography" is derived from the Greek tomos (slices) and graphein (to write).

If I_o is the intensity of the incident X-ray beam and I is the intensity of the beam once it transverses through a homogeneous object of thickness x (cm), the attenuation, the reduction either through absorption or refraction, is given by the following equation:

$$\frac{I}{I_0} = \exp(-\mu x) = \exp\left(\left(-\frac{\mu}{\rho}\right)\rho x\right) \tag{3}$$

where μ is linear attenuation coefficient (cm^{-1}), μ/ρ is mass attenuation coefficient (cm^2/g) and ρ (g/cc) is the density of the sample. The mass attenuation coefficient depends upon X-ray energy and the type of absorber or the material. As shown in Fig. 2.11, lower energy X-ray photons have a higher interaction probability or higher mass attenuation coefficient. For composite materials, the attenuation is given by summing the individual contribution of each chemical element as shown in following equation:

$$\frac{I}{I_0} = \exp\left(-\sum_i \mu_i x_i\right) = \exp\left(-\sum_i \left(\frac{\mu_i}{\rho_i}\right)\rho_i x_i\right) \tag{4}$$

Denison et al. (1997) derived the following relationship between linear attenuation coefficient and the electron density (the number of electrons per unit volume) of a material.

$$\mu_{cm^{-1}} = n\left(a + \frac{bZ^{3.8}}{E^{3.2}}\right) \tag{5}$$

where, a is a constant with a relatively small energy dependence, b is a constant, Z is the effective atomic number and E is the energy of the incoming X-ray beam. The effective atomic number for a mixture of the total number of materials can be computed using following equation for each fraction (f_i) of the total number of electrons contributed by element *i* with atomic number Z_i.

$$Z^{3.8} = \sum_i f_i.(Z_i)^{3.8} \tag{6}$$

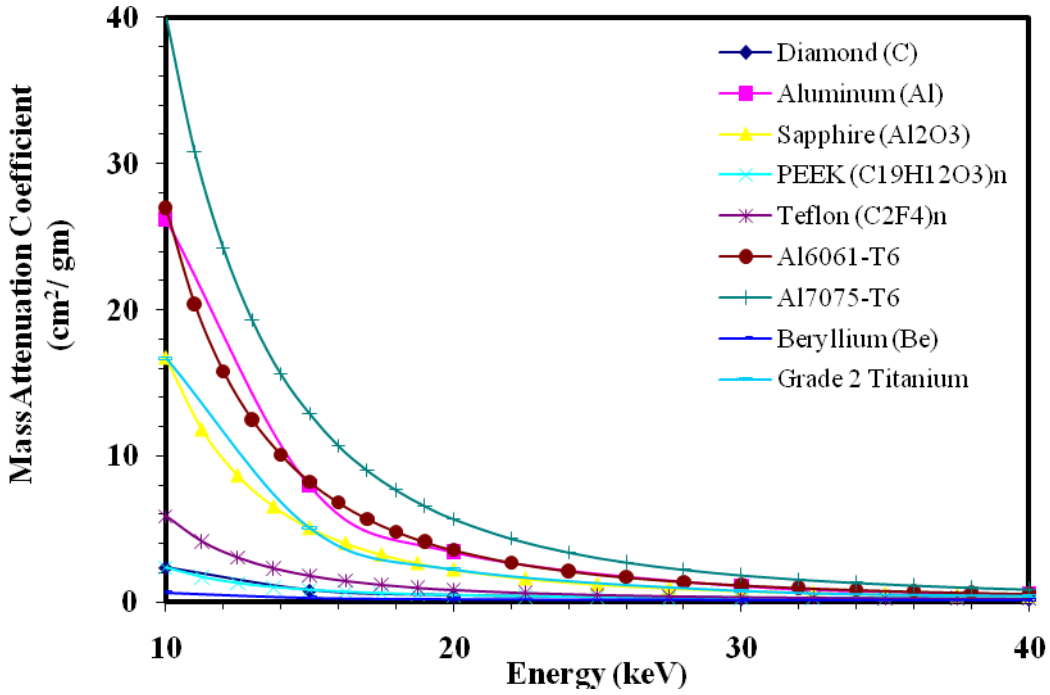

FIG. 2.11. Mass attenuation coefficient of different materials against photon energy[1]

The X-ray CMT provides an accurate map of variation of X-ray absorption within a sample, irrespective of its structure, phases involved, or density gradients. High resolution (50-100 µm) CMT reconstructs a sample's interior with micro-structural features of interest and their shapes. During tomographic imaging, the interaction between the specimen and photons can be classified as bright field or in-line technique and dark field or off-axis technique, both of which include rotation of the sample.

[1] The mass attenuation coefficient values are generated using NIST XCOM program which takes element, compound or wt% of each element in a mixture as an input along with energy range of an interest.

The specimen is placed directly between the X-ray source and detector in bright field techniques e.g. absorption and phase contrast. The spatial resolution is obtained by using either a small rastered probe beam or a position sensitive detector which provides significant speed advantages over serially sampled dark field methods viz: diffraction and fluorescence contrast, involving a detector inclined to the beam.

Medical X-ray CAT (computed axial tomography) or CT scan captures 2-dimensional (2-D) cross-sectional projections by placing the patient between a conventional X-ray source-linear array detector pair and by rotating it about the patient to collect projections from several angles. The reconstruction is accomplished by a variety of algebraic, statistical Fourier techniques, also termed as filtered back projection. X-ray absorption CMT is an extension of CAT fundamentals to a specimen between 1 mm to 1 cm in size, varying X-ray energy through a synchrotron and with spatial resolution up to 1 micron. Most importantly, tuning a synchrotron source below the absorption edge of many elements allows 3-dimensional (3-D) images of the concentration of those elements.

In a typical tomography scan, X-ray beam is passed through the specimen and the resulting images are recorded as a function of angle, θ from 0 to 180 degrees. The X-ray transmission detection usually limits the spatial resolution to the detector size. However, if the resulting beam is made to impinge on a thin high resolution scintillator, it converts each X-ray attenuation map to a magnified visible image which not only can be reimaged with conventional optics onto the cooled charged coupled device (CCD) area array, but it also allows flexibility to achieve higher magnification by simply changing the lens.

The raw fluorescence tomography data consists of elemental fluorescence (uncorrected for self-absorption) as a function of position and angle in the form of sinogram. The sinogram is reconstructed as a virtual slice through the sample by the coordinate transformation of (x,θ) to (x,y). This process is repeated at different z positions to give stack of closely spaced cross-sectional images of the sample. The cross-sectional images from a stack are later combined in 3-D rendering software to assign a depth-value to the pixel, thus creating a voxel within the stack of images. Besides x, y, z coordinates, a voxel also defines a point by a given attribute value i.e. density which is a

function of the sample's transmission. The density values are coupled with a color spectrum while a range of intensities control the opacity of a voxel on a computer screen.

2.6.2 Microstructure Models of Gas Hydrates in Sediments

There are a number of rock physics models in the literature that attempt to describe occurrence of gas hydrate on a grain scale (Fig. 2.12). The cementation models of Dvorkin and Nur (1996) treat the grains as randomly packed spheres where the gas hydrates occur at the contact point (model 1) or grow around the grains (model 2). These models predict increase in stiffness due to hydrates and decrease in porosity which alters elastic properties of the mineral phase. However, only a small amount of gas hydrate can lead to a large increase in elastic properties which stay relatively flat as the concentration of gas hydrate increases further.

Models 3 and 4 are variations of the cementation models, but consider the gas hydrate as either a component of the load-bearing matrix or filling the pores (Dvorkin et. al., 1999; Helgerud et. al., 1999). A pore-space hydrate fills intergranular porosities of sands and sandstones and is expected to be interconnected in their pore systems, which clearly contrasts with nodule and disseminated types (Model 6). A pore filling hydrate is small-sized and ranges up to 10 mm without any changes in porosity, however, it is considered to decompose continuously and effectively from the pore walls followed by their shrinkage in the pore space.

Model 5 is an inclusion-type model that treats gas hydrate and grains as the matrix and inclusions respectively, solving for the elastic moduli of the system by iteratively solving either the inclusion-type or self-consistent type equations. Models 1-5 all consider gas hydrate as homogeneously distributed in the sediments. However, evidence of gas hydrate coring within the DSDP, ODP (Booth et. al.,1998) and Mallik 2L-38 gas hydrate project (Dallimore et. al.,1999) reveals that hydrates often exist as pure aggregations (massive bodies, nodules, layers) and disseminate as fracture fillings in the shallow shaly sediments. This geometry is illustrated in model 6. A layered hydrate and

massive hydrate are extensively continuous horizontally and concordant to strata, whose thickness should exceed 100 mm.

Gas hydrates forming conventional gas reservoirs are likely to be pore-space gas-hydrates (Fig. 2.13(a) and 2.13(c)). Little expansion of the frozen texture would be expected if gas hydrates were formed at reasonable to considerable depth. Moreover, when buried to greater depths, an ice or gas-hydrate supported texture would develop (Fig. 2.13(b)). Gas from gas hydrates within framework supported textures is likely to be produced without any changes in texture, implying stable gas productivity. On the other hand, gas hydrates formed under shallow seals could grow and expand since they would not have to overcome excessive overburden stress conditions. Subsequently, the production from gas hydrates within an ice or gas hydrate supported texture (Fig. 2.13(b)) would be unstable, due to possible changes occurring in the texture with production. That is, the connecting pores of the gas hydrate or ice supported texture could collapse and reduce the permeability during gas extraction from the formation.

There have been two opposing composite models proposed viz: compaction model (the gas hydrate disseminated in the sediment pore space) and cementation model (the gas hydrate as a cementing agent on the grain boundaries). Gas hydrate saturation increases the elastic properties of the sediments. Dvorkin and Nur (1996) have treated the grains as randomly packed spheres where hydrates can grow at the contact point or around the grain. Hydrates have also been modeled as a load-bearing matrix, pore filling, or hydrate-grain inclusion. These models consider gas hydrates as homogeneously distributed in the sediment. However, they often exist as nodules and fracture filling in the shallow shaly sediments. The elastic properties against hydrate saturations for the cores recovered from Mallik 2L-38 well from Northern Canada match those by physical model of hydrate supporting grain matrix.

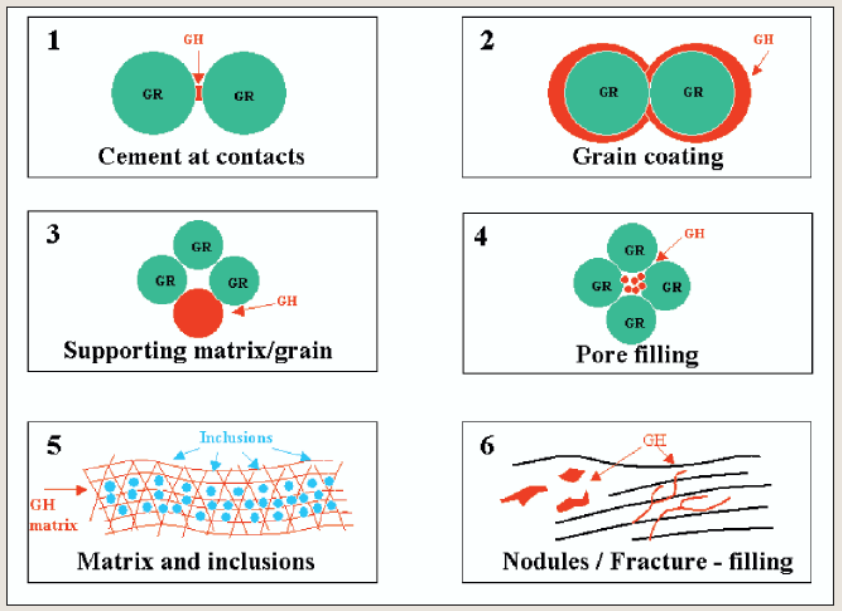

FIG. 2.12. Existing microstructural models of gas hydrate bearing sediments (Dai et. al., 2004).

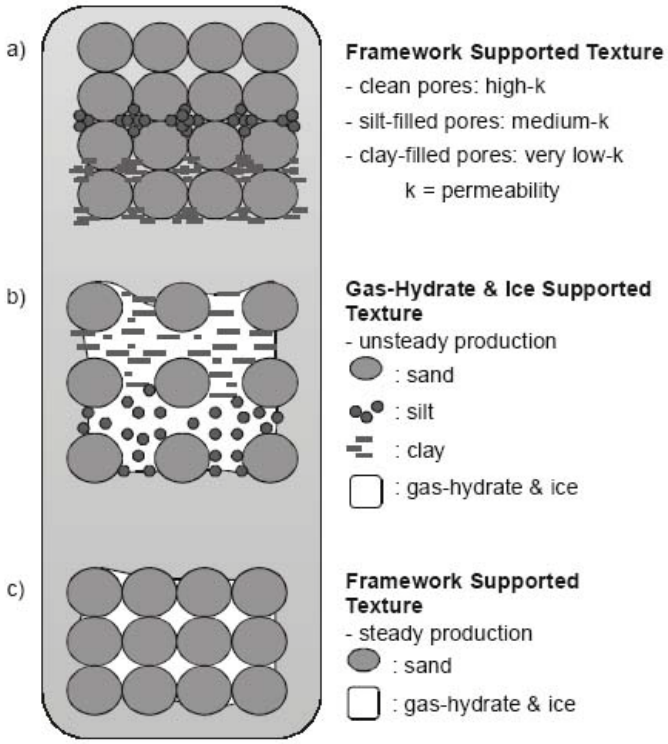

FIG. 2.13. Sediment texture models for (a) framework supported texture of various sizes, (b) ice or gas-hydrate supported texture, and (c) framework supported texture coarse grained (sand) material (Katsube et. al, 2004).

Contact Angle Relevance

The Young-Laplace equation relates the capillary pressure (Pc), and pressure difference between wetting (Pw) and non-wetting (Pnw) phases with surface tension (γ), radius of curvature (r), and contact angle (Θ).

$$Pc = Pnw - Pw = \frac{2\gamma \cos\theta}{r} \tag{7}$$

Figure 2.14(a) shows zero contact angle between the water meniscus and ice particle surface, whereas Fig. 2.14(b) depicts a non-zero contact angle of hydrate formed at grain contacts. Clennell et al. (2000) published a capillary model of pore freezing (Fig. 2.15) which clarifies the concept of contact angle for an ice-water system in pores.

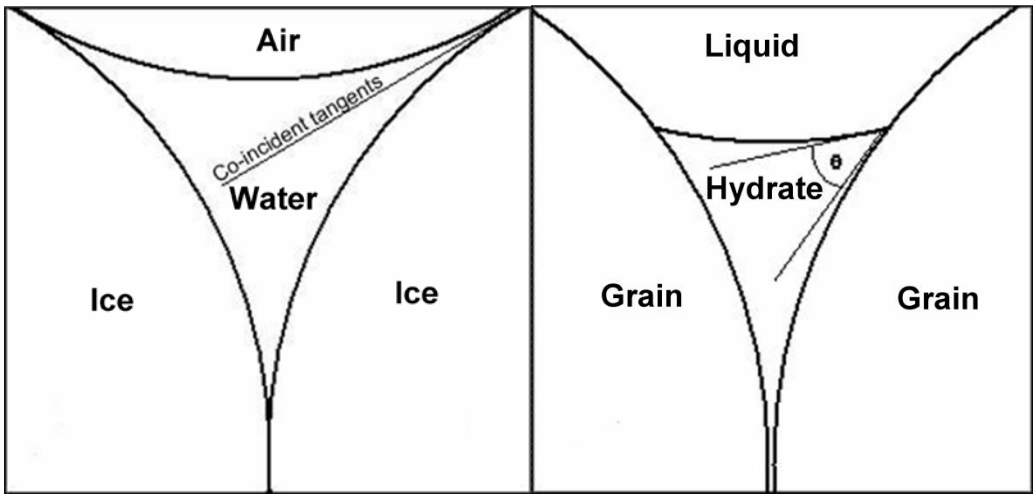

FIG. 2.14. Zero contact angle between the water and the ice surface (a) and non-zero contact angle between hydrate and the grain (b).

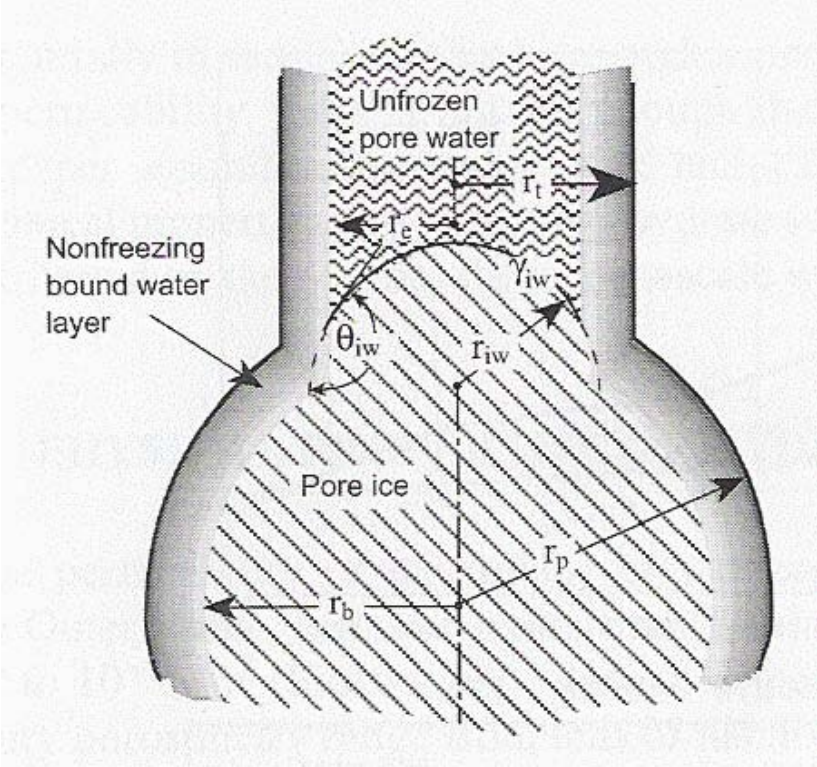

FIG. 2.15. Capillary model for pore freezing of water (Clennell et al., 2000).

Gibbs-Thomson equation is modified (Uchida et al., 1999) to have the effect of pore size and the curvature of solid surface on the temperature depression of melting temperature in pores below the bulk melting temperature in bulk.

$$\Delta T_{i,\,pore} = \frac{2\gamma_{iw} T_{bulk} \cos\theta_{iw}}{\rho_i \Delta H_f r_e} = \frac{\frac{N}{m}.^{o}K}{\frac{kg}{m^3}.\frac{J}{kg}.m} \tag{8}$$

where, γ_{iw} – surface energy between ice and water (0.0267 J/m^2 or N/m)

T_{bulk} - bulk melting temperature (^{o}K)

Θ_{iw} - contact angle for ice (180^o if water wets the pores and ice is non-wetting)

ρi - density of ice (916.7 kg/m^3)

ΔH_f - enthalpy of melting (latent heat) per unit mass (e.g. Ice, 334 kJ/kg)

r_e - effective pore size (m)

Thus, the finer the sediment, the smaller the effective pores and the higher the capillary pressure and the specific surface energy of ice-water interface, and hence, the liquid phase will be thermodynamically favored down to lower temperatures than that for bulk conditions. In sediments with larger pore size distribution, water freezes over the range of temperatures and water-ice freezing front moves through smaller pores.

Figure 2.16 can be adapted to describe hydrate formation within pores and equation 9 can be rewritten for hydrate-water properties. The surface energy of methane hydrate-water is assumed similar to that of ice-water, 26-30 mJ/m^2 in many instances (Henry et al., 1999). However, enthalpy of formation of methane hydrate has been found significantly different for bulk and small-pore conditions. In porous media, the higher capillary pressure of free gas bubble increases the fugacity of methane and its concentration in water. This stabilizes the methane hydrate.

$$\Delta T_{h,pore} = \frac{2\gamma_{hw} T_{bulk} \cos\theta_{hw}}{\rho_h \Delta H_f r_e} = \frac{\frac{N}{m}.^o K}{\frac{kg}{m^3}.\frac{J}{kg}.m} \qquad (9)$$

where, γ_{hw} – surface energy between hydrate and water (~0.0267 J/m^2 or N/m)

T_{bulk} - bulk melting temperature (^{o}K)

Θ_{iw} - contact angle for ice (180^o if water wets the pores and ice is non-wetting)

ρ_h - density of hydrate (0.91 g/cc)

ΔH_f - enthalpy of melting of hydrate per unit mass (e.g. ~436.7 kJ/kg)

r_e - effective pore size (m)

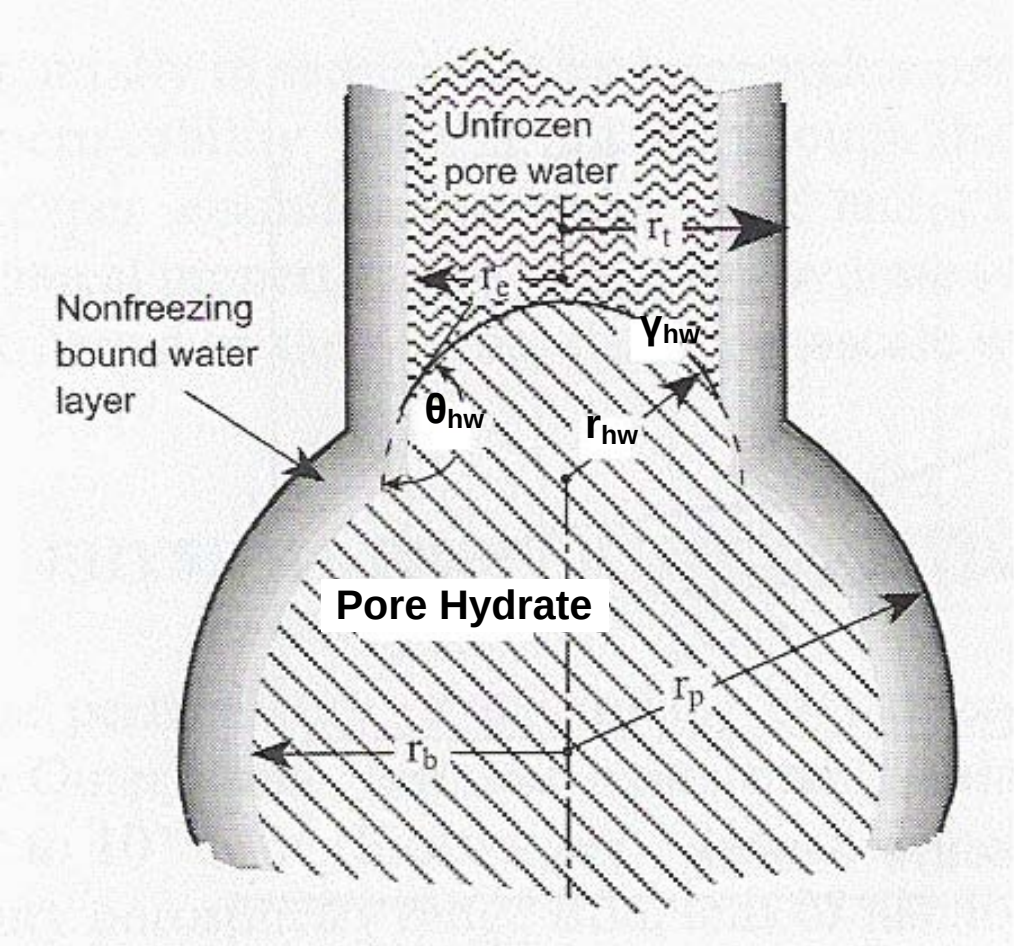

FIG. 2.16. Capillary model for hydrate in pores (Adpated from Clennell et al., 2000).

The van der Waals-Plateeuw thermodynamic model is one of the most commonly used models to predict methane hydrate equilibrium pressure as a function of the pore radius (Clarke et al., 1999; Wilder et al., 2001; Smith et al., 2002; Peddireddy et al., 2006) and to reconstruct pore volume distributions. Figure 2.17 provides taxonomy of the van der Waals-Plateeuw model which requires the pore radius, surface energy per unit area, and wetting angle as input for predicting equilibrium conditions.

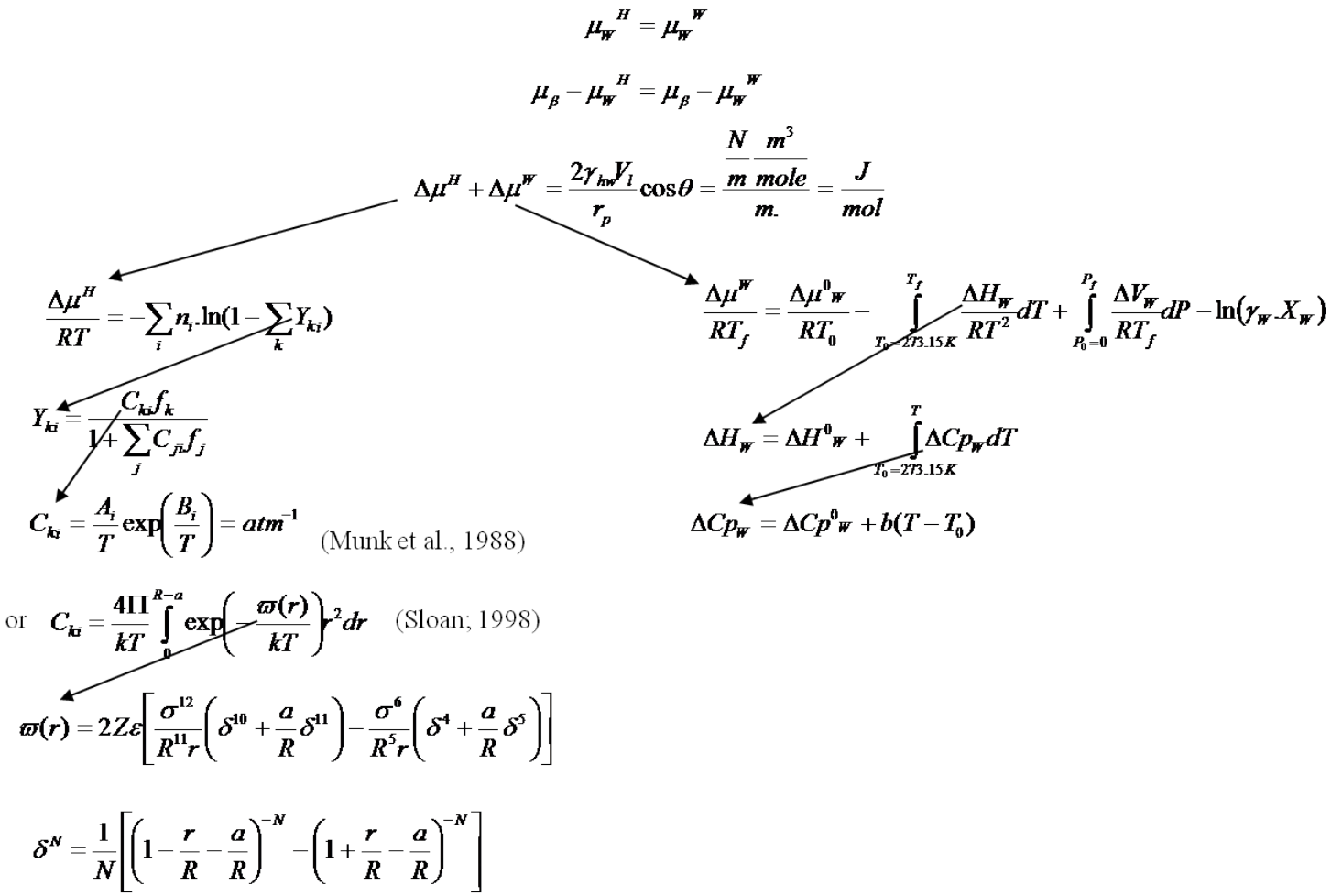

FIG. 2.17. Taxonomy of van der Waals and Plateeuw Model (van der Waals and Platteeuw, 1959).

where,

μ_W^H - Chemical potential of water in hydrate phase (J/mol)

μ_W^W - Chemical potential of water in water-rich phase or ice phase (J/mol)

μ_W^β - Chemical potential of water in a hypothetical empty lattice (J/mol)

γ_{hw} - Surface tension between water-hydrate phase

V_l - Molar volume of water in pure state

r_p - Radius of the pore (m)

θ - Wetting angle between pure water phase and the hydrate

R - Universal gas constant (J/mole^{o}K)

n_i - Number of cavities of type i in the hydrate lattice

Y_{ki} - Probability of a cavity of type i being occupied by the guest molecule, k

C_{ki} - Langmuir adsorption constant (atm^{-1}) of hydrate former k in cavity type i

f_k - Fugacity of hydrate guest in the gaseous state

j - Cavities which guest molecules can occupy

Ai - Experimental fit parameter for guest, methane in small (0.00007372) and large (0.025354) cavity (K/atm)

Bi - Experimental fit parameter for guest, methane in small (3267.99) and large (2782.94) cavity (K)

k - Boltzman constant ($1.3806503 \times 10^{-23}$ m^2 kg s^{-2} K^{-1})

$\hat{w}$ - Cell potential function of guest k in cell i

R - Radius of cell or cavity (Table 2.2)

Z - Co-ordination number of the cavity (Table 2.2)

r - Distance of gas molecule from the center of the cavity

a - Core radius of interaction for gas and water molecules (Table 2.3)

σ - Core-to-core distance between gas and water molecule (Table 2.3)

ε - Depth of intermolecular well (Table 2.3)

T_f - Temperature at which hydrate forms

P_f - Pressure at which hydrate forms

$\Delta\mu^0_W$ - Chemical potential difference for the reference state (1263 J/mol)

To - Standard reference state (273.15K)

ΔH_W - Enthalpy difference between the empty hydrate lattice and pure water (J/mol)

ΔH^0_W - Enthalpy difference between the empty hydrate lattice and pure water at reference temperature (J/mol)

ΔV_W – Volume difference between the empty hydrate and pure solid or liquid water

γ_w - Activity coefficient of liquid water (usually taken to be 1.0)

X_W - Mole fraction of water

Cp^0_W - Reference heat capacity difference (J/mol-K)

b - Constant fit to measure specific heat of water or ice

Table 2.2. Geometry of Structure I Gas Hydrates (Sloan, 1998).

Structure I	R (A^0)	Z
Small Cavity	3.95	20
Large Cavity	4.33	24

Table 2.3. Kihara Parameters for CH_4 and CO_2 (Sloan, 1998).

	ε/K (K)	σ (A^0)	a (A^0)
CH_4	154.54	3.165	0.3834
CO_2	168.77	2.9818	0.6805

2.6.3 Application of CMT for Hydrates

CMT holds tremendous potential for geoscientists revealing fascinating reservoir topologies and intricate oil or gas frameworks. In previous studies on hydrate X-ray CMT, Soh (1997) reported a plume-shaped, fluidized structure with gas bubbles in CT images indicating the dissociation of a relatively large nodule of gas hydrates from the sample cores at ~47 mbsf of the Amazon Fan on the Brazilian continental margin.

Mikami et al. (2000) presented gas hydrate dissociation simultaneously both on exposed surfaces and within the pore spaces of granular sand cores collected from JPAEX/JNOC/GSC Mallik 2L-38 exploratory well. Mork et al. (2000) observed NMR images to confirm hydrate formation in many interior points of quartz sand from the stoichiometric tetrahydrofuran (THF)-water mixture in quartz sand although attempts of CMT were not successful due to the negligible density difference between the stoichiometric THF-water mixture (0.978 g/cc) and THF hydrate (0.971 g/cc). However, Tohidi et al. (2001) found clathrates forming within the center of pores, rather than on grain surface with methyl blue enhancing the contrast between phases. Following 48 hours after the pore-centered hexagonal shaped THF hydrate formations from 40% mass THF aqueous solution, they undergo a rearrangement to develop hexagonal faces around the liquid film on the larger grains (0.313 mm) and encapsulation around smaller grains (0.070 mm).

Kunerth et al. (2001) performed acoustic laboratory measurements during the formation of a THF-Hydrate in unconsolidated porous media. As temperature is decreased, initial THF hydrate formation in the main pore body increases the bulk modulus followed by the freezing of remaining fluid water in the pores, which welds the grains increasing the shear strength of the sediment. Staykova et al. (2003) performed field-emission scanning electron imaging of gas hydrates formation stages up to 2 weeks from spherical ice Ih grains (average diameter of 40-80 μm) obtained by spraying technique at 882 psi (6 MPa) and 268 K. The hydrate film fills ice grain's crack and covers the ice grains after an hour, and the process further depends upon the clathration reaction at the ice-hydrate interface and the gas and water diffusion through hydrate shells surrounding the shrinking ice cores. The reaction rates were higher for the same sample with smaller initial ice grains and for same excess fugacity with CO_2 than with

CH_4. However, there was no difference between H_2O and D_2O from the reaction kinetics point of view indicating negligible deuteration effect.

Jin et al. (2004) characterized 10 mm thick cylinders cut from artificial methane hydrate sediments produced at -30^oC and 1448 psi (10 MPa). The porosity measurement from the 2-D image as the area ratio of pore space to total area was found to be within 3% of that from mass and volume measurement. Freifeld and Kneafsey (2004) carried out X-ray studies with a portable CT scanner of 130 keV beam energy and 200 μm of synthetic methane hydrate in 12/20 mesh Ottawa sand (30% porosity) packed in 28.6-mm diameter and 32-mm long pressure vessel. Periodical 2-D CT data during dissociation revealed that the initial dissociation occurs in hydrate nodules near walls of the pressure vessel and then progresses inwards.

Freifeld and Kneafsey (2004) presented the local temperature and density changes in 2-D during methane hydrate formation and dissociation in a partially saturated core-scale sand sample formed in an X-ray transparent aluminum vessel of 1211 mL volume. CT scan showed an increased density throughout the sample with the largest increases occurring where the density was initially lowest on account of poor packing during hydrate formation. The dissociation caused the density to decrease near the vessel wall and became larger and larger over time. During the second hydrate formation, hydrates were not found to form in the precise locations where dissociation occurred but occurred preferentially in a broad ring around the center, decreasing the density. The depressurization front moved inward from vessel wall, caused by thermal stimulation, giving increased density at the center due to water release.

Sato et al. (2005) investigated the density and hydrate saturation distribution of methane hydrate with high-speed X-ray CMT and at 1470 psi (10.1 MPa) and -30^oC within Toyoura sand with an average grain size of 0.2 mm. Best et al. (2004) classified methane gas bubbles in pressure-sealed cores as encompassing several adjacent void spaces (i.e. patchy gas saturation) in sand and as deforming the surrounding water-saturated sediment as they grow in mud, indicating gas migration through small gas bubbles move through connected void space, slower molecular diffusion of gas dissolved in the water filling the voids, or rapid gas movements through existing cracks in the mud.

Abegg (2006) imaged gas hydrate cores recovered from varying sub-seafloor

depths in the ODP at Leg 204 at the Cascadia margin (Abegg, 2006) using X-ray CMT. Results indicate that veinlet structures are predominantly found within samples obtained from deeper formations, whereas massive, dispersed, and bubble fabric structures are found at shallower depths. This may be due to the absence of overburden stress conditions at shallower depths. On the other hand, when buried deeply, an ice or gas-hydrate supported texture may give off gas without any changes in texture, implying stable gas seepage. However, the connecting pores of the gas hydrate or ice supported texture could fall apart and trap the gas in formations. Commonly, seismic sensing from BSR is used to detect and estimate hydrates below the seafloor. A high acoustic impedance difference from BSRs is inverted to estimate elastic properties, porosity, and hydrate saturation from sediments. The existing models assume uniform hydrate distribution within sediments. Hence, it is critical to understand hydrate growth and sediment-hydrate interaction.

Recently, Takeya et al. (2007) performed experiments with 19 wt% THF solution (stoichiometric ratio of THF (1 mole) to H_2O (17 mol)) at 35 keV monochromatic synchrotron X-ray beam line to reveal the density difference of THF hydrate in 3-D image.

Chapter 3

Experimental Set-Ups

3.1 Flexible Integrated Study of Hydrates (FISH) Unit - Model for Mimicking Marine Hydrate Occurrence

3.1.1 High Pressure Cells

Temco Cell vs Jerguson see-through Cell - Mounds vs Downhole

The previously studied Jerguson see-through Cell mimics seafloor conditions with water and sediments filled to half the volume of the cell, allowing the sediment column to expand upon hydrate formation. Temco DCHR-2.0 core holder allows simulating the geothermal conditions much further below the seafloor with the application of confining pressure. The radial confining pressure is applied on the rubber sleeve which surrounded sediments.

3.1.1.a Jerguson see-through Cell

The stainless steel high pressure cell manufactured by Jerguson Gage and Valve company, OH, has outer dimensions of 4 inch x 3 inch x 14 inch and an internal volume of 198 mL (Fig. 3.1). The cell has two 1 inch thick glass windows on two opposite sides sealed against the surrounding steel body with a precision die cut Teflon gasket and "black oxide" treated bolts and nuts to prevent rust. The tempered borosilicate glass is

rated for 600°F (315°C) and 3000 psi (20.7 MPa). Two 1/16 inch thermocouples are inserted from top and bottom to measure gas and sediment temperature.

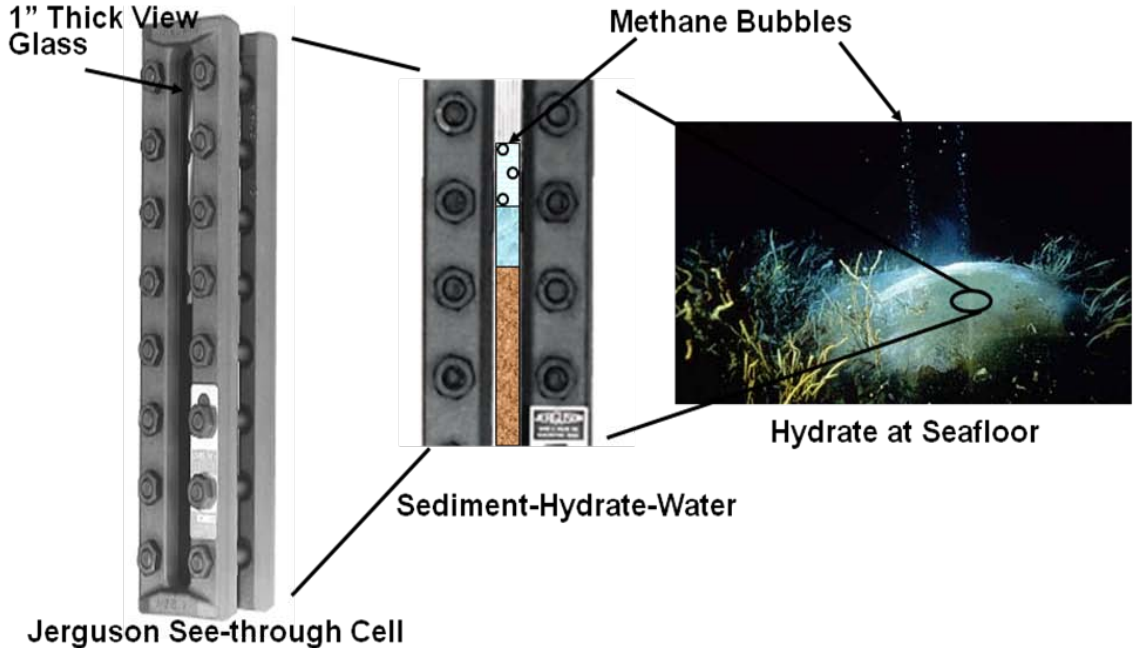

FIG. 3.1. Jerguson flat glass see-through cell (Jerguson Gauge and Valve).

3.1.1.b Temco DCHR Cell

The Temco DCHR series core holder (D-1357-4) shown in Fig. 3.2 is a hassler-type core holder with radial loading. These types of core holders are very common in petroleum research for permeability waterflooding, surfactant-polymer, and reservoir-fluid interaction studies. The core sample (maximum diameter 2 inch and length 6 inch) is held in a Viton 70 rubber sleeve. The annulus gap around the rubber sleeve is filled with a fluid which applied radial pressure on the sleeve and sample, simulating reservoir overburden pressure. The core sample can be removed with a pusher rod after releasing the overburden pressure and unscrewing the retainer. The oversized cores in diameter were can be fit by opening the sleeve with the vacuum in the annulus gap. The undersized cores in length can be adjusted with spacers. Three 1/8 inch pressure taps are located at 1, 3 and 5 inch along the core length.

Flexible metal hoses and quick-connects with and without valves have been employed to disconnect the cell without venting out methane or confining pressure. The

whole cell unit can be taken out of the coolant reservoir within a few moments to recover the core. The relief valve with changeable 1500-2250 psig spring has been mounted directly on the cell as a safety feature.

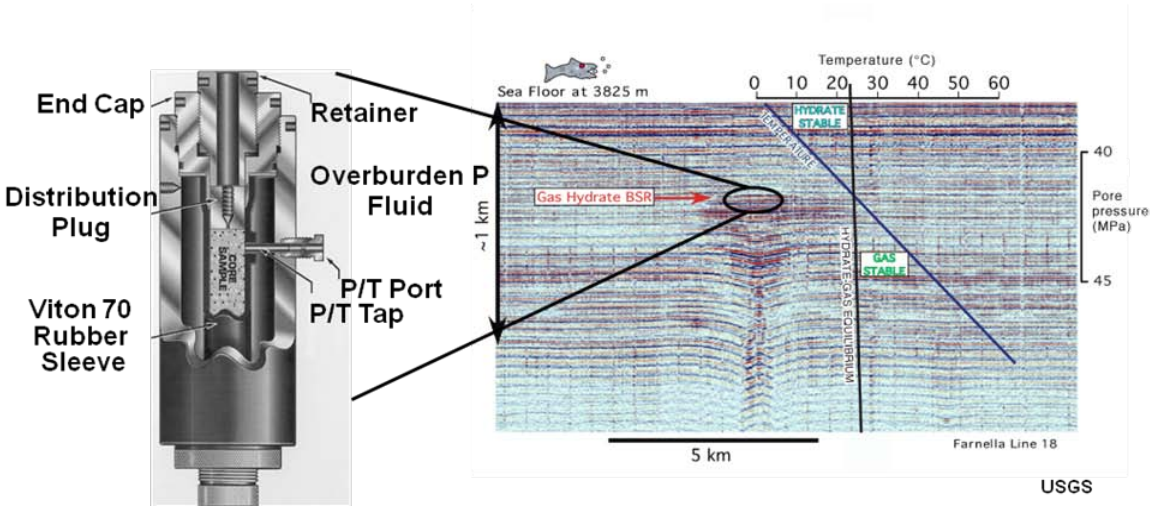

FIG. 3.2. Temco DCHR-series core holder.

3.1.2 Gas Metering

Brook's model 5850TR flow controller is used to measure or control the input methane gas. It provides direct flow measurements with ±1% FS accuracy (including linearity) from 0 to 2 SLPM at maximum operating pressure of 1500 psi (10.3 MPa). The output gas is metered with an Omega mass flow meter (FMA-A2317-SS-CH4-500PSI-70F) with LCD display and linear 0-5 VDC or 4-20 mA output. The flow meter is calibrated to NIST standard for methane gas, pressure range from 0 to 500 psi and 70^{o}F. It offers ±1% full scale (FS) accuracy (including linearity). The 0-5 VDC output is drawn into a Labview system with low loss, braided RG174 coaxial cable from pins 4 (positive) and 8 (negative).

3.1.3 Overburden Pressure Isco pump

Isco D Series Syringe Pump (100 DM) which works in both, constant flow or constant pressure mode is used to apply the overburden pressure on the core sample. The pump controller can operate up to three syringe pumps independently or in several coordinated configurations. The 100D module has 103 mL capacity and the highest pressure (0 – 10000 psi with 0.5% FS accuracy) and flow (10 mL/min - 30 mL/min with 0.3% accuracy) resolution.

3.1.4 Sediment and Water Control within Cells

The Jerguson see-through cell is fitted with all welded 0.5 µm pore size in-line stainless-steel filter with 0.25 inch Swagelok tubing (SS-4FWS-05) to trap the sediment in the confined volume. The stainless-steel poppet check valve with 0.25 inch Swagelok tube fitting and PTFE O-Ring has been installed below fixed retainer of Temco cell through which methane gas is introduced. The one-way opening of the check valve at 1 psig (0.11 MPa) prevents water gravity-drainage through the bottom retainer. Moreover, porous disks (2 inch diameter and 1/4 inch thickness) of ceramic (CoorsTek®) or ultra high molecular weight polyethylene (UHMWPE) (Genpore®) with ~50 µm pore size placed above and below core sample ensure the sediments are trapped within the rubber sleeve.

3.1.5 Temperature and Pressure Measurement, Gas Delivery and Cell cooling

Two perfluoroalkoxy (PFA) coated Omega's SS 1/16 inch diameter type J (TJ36-CC Series) thermocouples are mounted at the top and bottom of Jerguson see-through cell measuring gas and sediment-water temperature respectively. Three type J, 1/16" diameter and 24 inch long stainless-steel sheath with 1/16 inch long PFA coated lead wire (TJ84-ICSS-116U-24) are installed at different redial and lateral core (2 inch in diameter and 6 inch long) locations (Fig. 3.3). Moreover, several braided fiberglass insulated type J thermocouples have been installed to measure air, refrigerated circulator bath, cell water bath and outlet water bath temperature.

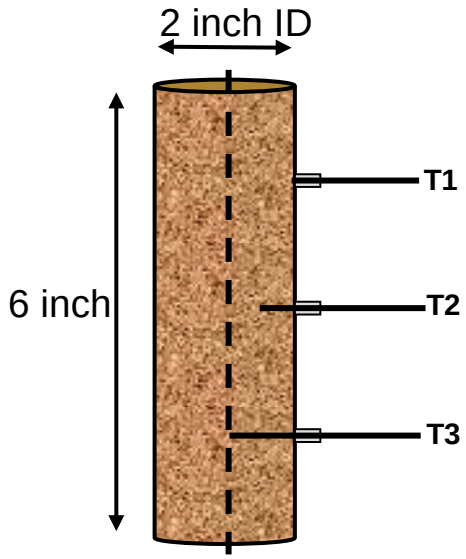

FIG. 3.3. Thermocouple locations (edge-T1, half-radius–T2 and center–T3) within sand-core.

Gas delivery line pressure and both cell pressure are measured and displayed with Omega's strain gage pressure transducers (PX4100-1.5KGV) and display unit (DP-25B-S-A) respectively. The overburden pressure of Temco cell is measured with similar pressure transducer which is utilized for cell pressure but have a higher maximum pressure (PX4100-3KGV). The linear output of 0-20 mV for 0-1500 or 0-3000 psi pressure range is drawn into a Labview unit. Both cells are submerged into a 26 inch (L) x 18 inch (W) x 26 inch (H) water bath which holds continuously stirred ~17.4 gallons of that which is cooled with cooling coils through which ethylene glycol is pumped from a RTE211 Neslab refrigerated circulator bath.

3.1.6 Data Acquisition System

National Instrument's (NI) SCXI-1000 (Signal Conditioning Extension for Instrumentation) chassis houses, powers, and controls the NI SCXI-1303 module and conditioned signals. The NI SCXI-1000 which transfers data and passes timing signals is a 4-slot chassis with standard AC power. The SCXI-1303, a terminal block inserted into the chassis, has 31 channels that can accept analog and digital signals. The signals from each thermocouple and pressure gauge are acquired in time loops, are transferred to pc

(filename.lvm), and are displayed on waveform graph through DAQ assistant in Labview program. Figure 3.4 shows the labview front panel window.

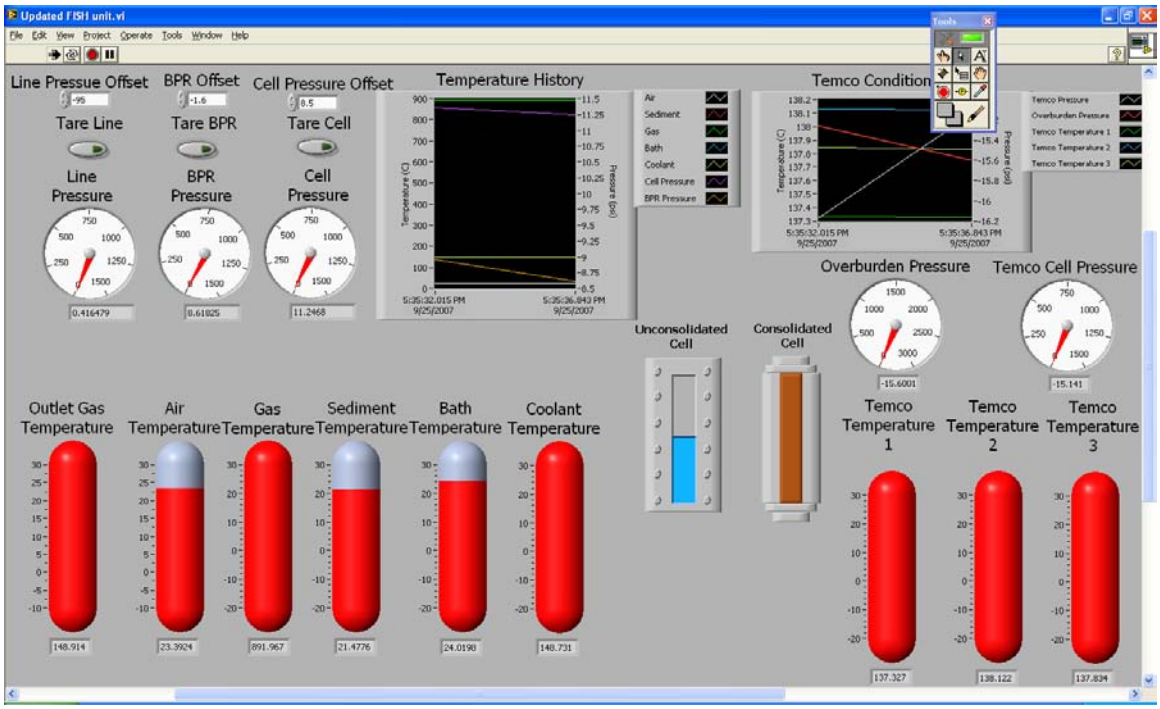

FIG. 3.4. Labview real time data acquisition layout window.

3.2 FISH Operation

3.2.1 Sediment, Preparation and Loading

3.2.1.a Initial Temco Assembly

i. In a typical core-holder assembly, the rubber sleeve was installed into the core holder body, ensuring pressure taps were within the ports. The loading bar was inserted through the sleeve and the ferrule-end cap assemblies with a slight amount of grease around the ferrule outer diameter were screwed equally until they bottom out from both ends to maintain equal force on each end of the sleeve. This not only keeps the sleeve stems aligned in the core holder body but also prevents the stems from locking and tearing the sleeve.

ii. Once the sleeve stems were ensured to be aligned in the body ports and no adjustment was required for ferrule-end cap assemblies, the o-rings were put flat around the stems.

iii. The connectors were installed around the stems and into the body with silver goop on their threads. An adjusting screw which provides an adjustable stop for the stem and avoids its rise tearing the rubber sleeve during pressurization was tightened into each connector until it stopped against the stem.

iv. The distribution plug and a bottom-fixed retainer (longer in length) assembly was screwed into the end cap until it bottoms out. After removing the loading bar, the bottom porous disk was lowered onto the bottom distributor. Three 1/16 inch thermocouples each with male national pipe thread (NPT) were installed in connectors.

3.2.1.b Core Sample Installation

i. The dried and weighed sediment sample was loaded into the rubber sleeve using a long funnel to avoid sediments into the inside end cap threads. The core sample was compacted gently first to avoid thermocouple misalignment and with the loading bar later.

ii. In the case of shorter cores, spacers could be used next to the core after lowering top porous disk but before screwing in the distribution plug and a top-adjustable retainer assembly.

3.2.1.c Pressurization

i. The quick-connects for reservoir fluid as well as for overburden fluid were installed.

ii. The vacuum was applied through the top port to remove air from the annulus between the outer diameter of the sleeve and the inner diameter of the body. With closed top port, the water was filed into the annulus from the bottom port and pressurized using the Isco syringe pump.

iii. The Isco syringe pump holds 103 mL water so annulus-gap filling and overburden pressurization took around 5-6 cycles of refilling the pump. The desired core

overburden pressure was achieved in 250 psi increments with regular leak-checks. The final overburden pressure was allowed to stabilize overnight.

iv. If the leak occurred around the end cap, the assembly of core sample was repeated after examining the sleeve and o-rings for the failure.

v. After overnight stabilized overburden pressure, the core was saturated with water/seawater using another Isco syringe pump in a constant flow mode where 5-6 times core- pore-volume liquid was injected through the core against gravity at low flow rate.

3.2.2 Parallel Operation of Jerguson see-through Cell and Temco DCHR

Figure 3.5 gives the schematics of the FISH unit where both Jerguson and Temco cells can be operated individually or in parallel.

3.2.2.a Methane Charging and Hydrate Formation

The hydrate formation was achieved by either (a) gradual charging of methane through a pre-cooled sand-core or (b) gradual charging of methane followed by cooling the sand-core to an experimental temperature. Before methane charging, the cell temperature was achieved over a day or two to the desired value by circulating glycol through the cooling coils. The temperature of glycol was adjusted by a set-point on a refrigerated circulator. The unique arrangement of valves in the gas delivery system allows by-passing mass flow controller in the shock charging of methane. However, in the steady gas flow hydrate formation, mass flow controller was used with down-stream back-pressure regulator. Brook's 5850TR series gas flow controller works best with 100-200 psi pressure drop. Hence the pressure of ~ 1200 psi at the back-pressure-regulator (BPR) inlet was maintained while methane charging via gas flow controller. Moreover, an additional pressure regulator placed in a gas charging system provided a secondary control to adjust the line pressure displayed on DP25B-E unit mounted on the panel to the desired value. Once the line pressure was stabilized, the gas was charged into the cell with the needle valve at the entrance of each cell. Since there is one gas delivery system, the pressurization of each cell was achieved sequentially rather than simultaneously. The hydrate formation was observed by monitoring cell pressure and temperature in Labview.

After a week of hydrate formation, gas was replenished into the cell with steady line pressure and through the gas flow controller which gave an estimate of methane consumed during hydrate formation.

3.2.2.b Hydrate Dissociation

Hydrate dissociation was initiated by charging N_2 to the inlet of back-pressure regulator to a pressure slightly lower than that of cell pressure. It is important to note again that the hydrate dissociation from both cells was carried sequentially due to single downstream gas collection system (left hand side of Fig. 3.5). The steady N_2 pressure at the BPR was followed by discharging the unreacted methane gas excess of BPR inlet pressure. Once the outlet mass flow meter stabilized and no gas was evolved out of the cell, the cell outlet valve was closed and BPR pressure was lowered by another 100-200 psi. This unreacted methane gas was bled off in the steps of 100-200 psi was continued until cell pressure reaches at least 50 psi more than the theoretical equilibrium pressure computed from CSMGem software for the experimental temperature. The dissociation at a desired constant pressure drop was achieved by lowering the BPR inlet pressure to the lower limit with cell outlet valve closed. The dissociation was very rapid process and its data was acquired at a faster rate (~1 sample per second in a separate file) as opposed to the formation (~1 sample per 15 seconds i.e. 40320 data points).

3.2.3 Individual Operation of Jerguson see-through Cell or Temco DCHR

3.2.3.a Methane Charging and Hydrate Formation

The individual cell operation procedure was very similar to one explained in section 3.2.2.a except the undesired cell can be by-passed using an appropriate valve.

3.2.3.b Hydrate Dissociation

The dissociation procedure discussed in section 3.2.2.b could be applied for an individual cell with care taken for not allowing the outlet gas from one cell into another unless desired.

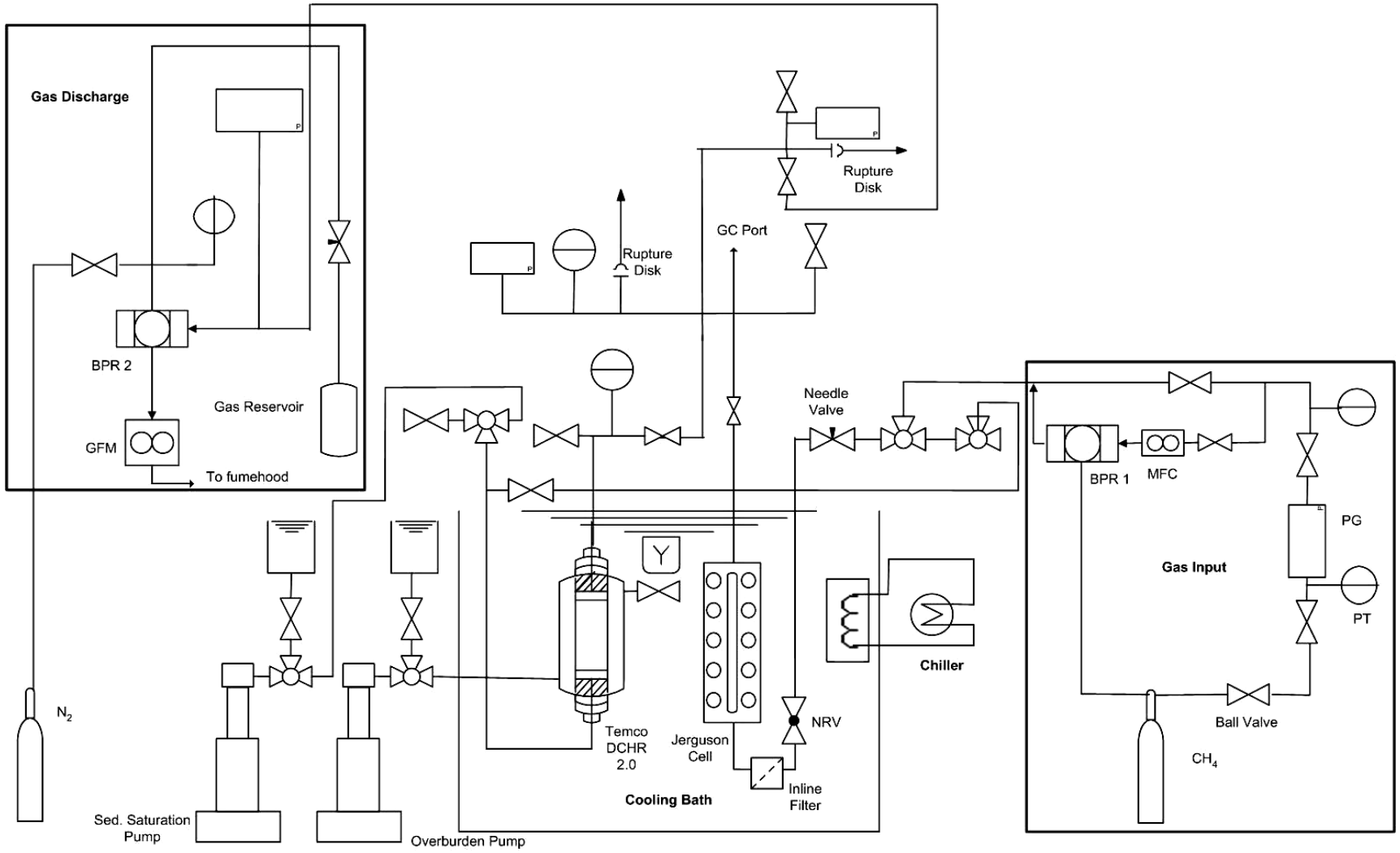

FIG. 3.5. Schematic of the Flexible Integrated Study of Hydrates (FISH) Unit.

3.3 X-ray Computed Microtomography (CMT) Setup and Analysis for Microstrcture Investigation of Hydrates and Natural Depleted Sediments

3.3.1 Beamline X2B Specifications and CMT Data Acquisition

The crucial parts of a beamline equipped with X-ray CMT technique are the beam, the filter, the sample and stage, the scintillator, the mirror, and the CCD camera. At the beamline X2B (Fig. 3.6), National Synchrotron Light Source (NSLS), Brrokhaven National Laboratory (BNL), the X-ray beam with an energy range of 6.5 to 35 keV, produced at a bending magnet, is used as a filtered white beam and made monoenergetic with a flat single crystal Si(111) Bragg spectrometer in He purged enclosure. A beam of 5 mm width and 1 mm height passes through a sample and impinges on a thin high resolution cesium iodide (CsI) scintillator. The X-ray transmission detection usually limits the spatial resolution to the detector size. But the CsI scintillator converts each X-ray attenuation map into a magnified visible image which not only can be reimaged with conventional optics onto the cooled CCD 1340 x 1300 array but also allows flexibility to make a simple lens change to view larger samples with lower magnification. The 2.5X lens provides ~7.5 μm resolution and keeps the entire 7 mm inside diameter sample container in the field of view, whereas 5X lens provides ~4 μm resolution and allows investigating the wall effects in detail. The flat mirror at 45^o to the beam folds the visible image produced by scintillator into camera optics and the detector placed 90^o to the incident beam to avoid its direct expose to X-rays. The stepping motor under the stage translates the sample horizontally through the beam during sampling the X-ray attenuation. The vertical translator is used to select the slice to be imaged. The IPLab software developed at ExxonMobil Research & Engineering allows controlling the alignment stage for focusing and attenuation purposes, as well as changing the beam energy, region of interest (ROI), angular increment, exposure time for each image etc. The typical data acquisition included around 1200 images with 3000-5000 msec of exposure for each image at every 1.5^o increment from 0 to 180^o. The output file, filename.prj (~1 GB) contained all 1200 tomographic image slices each composed of a rectangular array of reconstructed linear attenuation coefficient values, each

corresponding to a specific voxel of the sample. Typical data acquisition parameters are listed in Table 3.1.

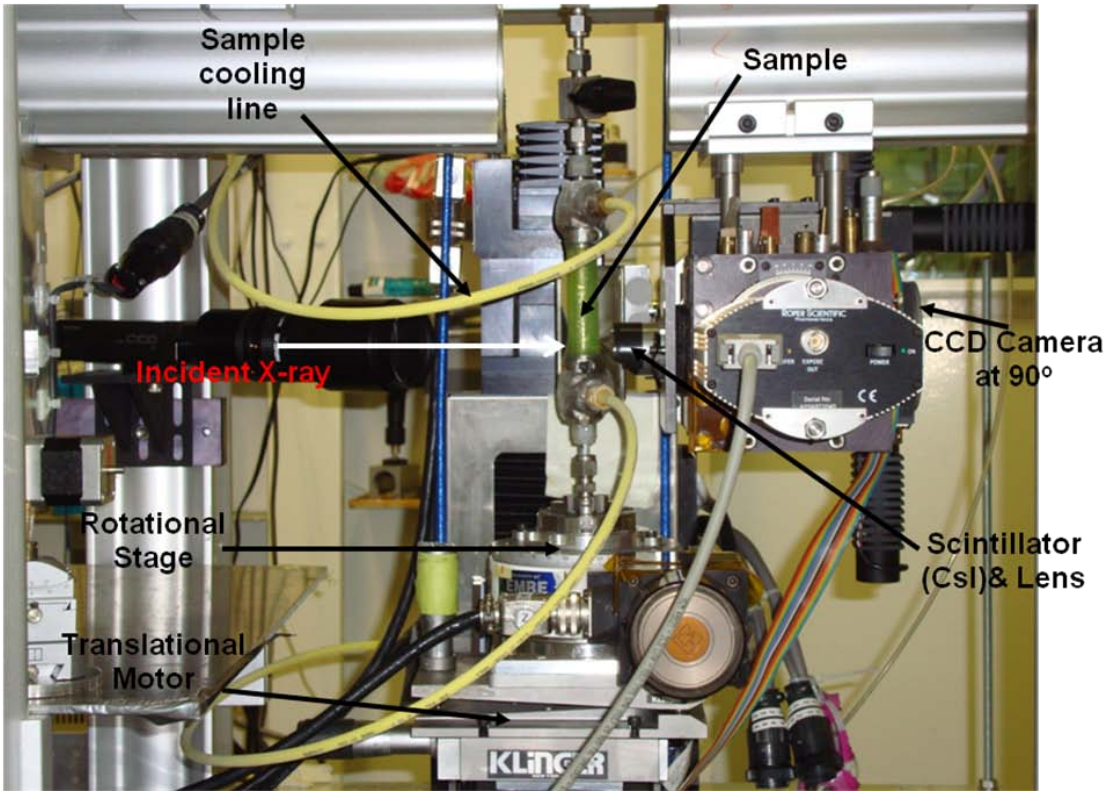

FIG. 3.6. X-ray CMT set up at beamline X2B, NSLS BNL.

3.3.2 CMT Data Analysis – Reconstructions

Around 300-400 slices from each of the .prj files were constructed into a .volume file using a routine (convert_x2b_netcdf_display.sav) (Fig. 3.7) by Mark Rivers in IDL tomography software. The excess air in the X-direction was thrown out and all 1200-1800 angular images were reconstructed. The .volume file was converted into a recon.volume file format using another routine (tomo_display.sav) (Fig. 3.8) to get horizontal cross-section of the sample. The vertical axis was optimized while running tomo_display.sav for each reconstruction to reduce the artifacts in the images. Table 3.2 summarizes both of these reconstruction steps.

Table 3.1. X2B data acquisition parameters.

Software	IPLAB™
Pre-tomoscan Image parameters	Type – Image Use maximum size of camera Exposure time: 3000-5000 msec
Energy	25-30 keV (Keeping $\tau = \mu.\rho.x = \sim 2.0$)
Band width	50 eV
Exposure or Calibration time	3000-5000 msec (Keeping ~55000 counts on blank image)
Rotational axis	670
Pixel size	3.98 μm (5X lens) or 1.99 μm (10X)
Number of views	1200
Rotational angle increment	0.15
Number of views/calibration	150 or 120 (for 8 to 10 calibrations)
Movement per calibration	-10000 to -15000 μm
Output file format	Filename.prj

Table 3.2. Image reconstruction parameters.

Routine	**IDL[1] (The Data Visualization and Analysis Platform)**
"convert_x2b_netcdf_display.sav" (Mark Rivers)	Command: idl –vm=/usr/local/cmt-lib/convert_x2b_netcdf_display.sav
	Input file format: filename.prj
	Output file format: filename.volume (~ 1GB)
	Volume options: ROI (Xmin, Xmax, Ymin, Ymax (# of slices = Ymax-Ymin), Zmin (angle), Zmax (1200)

[1] http://www.ittvis.com/idl/

"tomo_display.sav" (Brent Lindquist)	Command: idl –vm=/usr/local/cmt-lib/convert_x2b_netcdf_display.sav
	Input file format: filename.volume
	Output file format: filenamerecon.volume (~ 1GB)or movie format or jpg or tiff
	Reconstruction options: Rotational angle

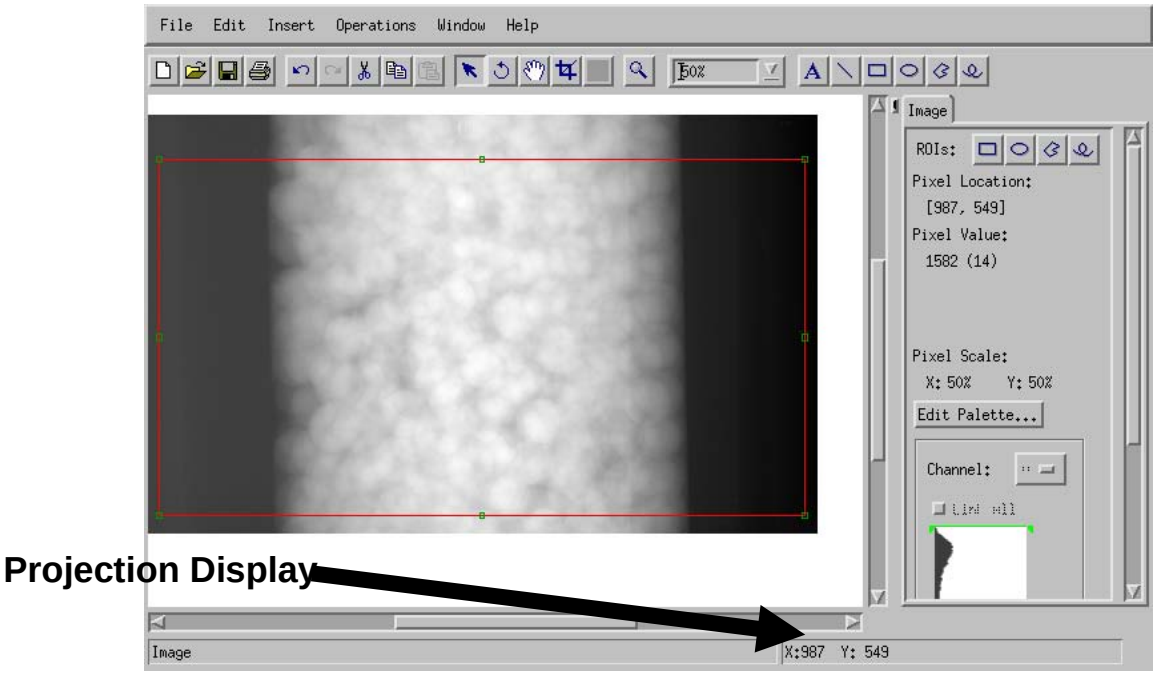

FIG. 3.7. Layout of IDL based convert_x2b_netcdf_display.sav routine for converting filename.prj to filenamerecon.volume.

3.3.3 Contact Angle Measurements

In the present analysis, the contact angle was measured with an angle tool located in a toolbar of ImageJ. After zooming over a ROI, a tangent was drawn at a desired point (point selection tool) with a straight line tool. The contact angle measurement can also be performed with several plug-ins available for ImageJ or with other commercially available image-analysis and processing softwares such as Leica Qwin (Leica QWin, Leica DMLB, Leica Microskopie and Systeme GmbH, Germany).

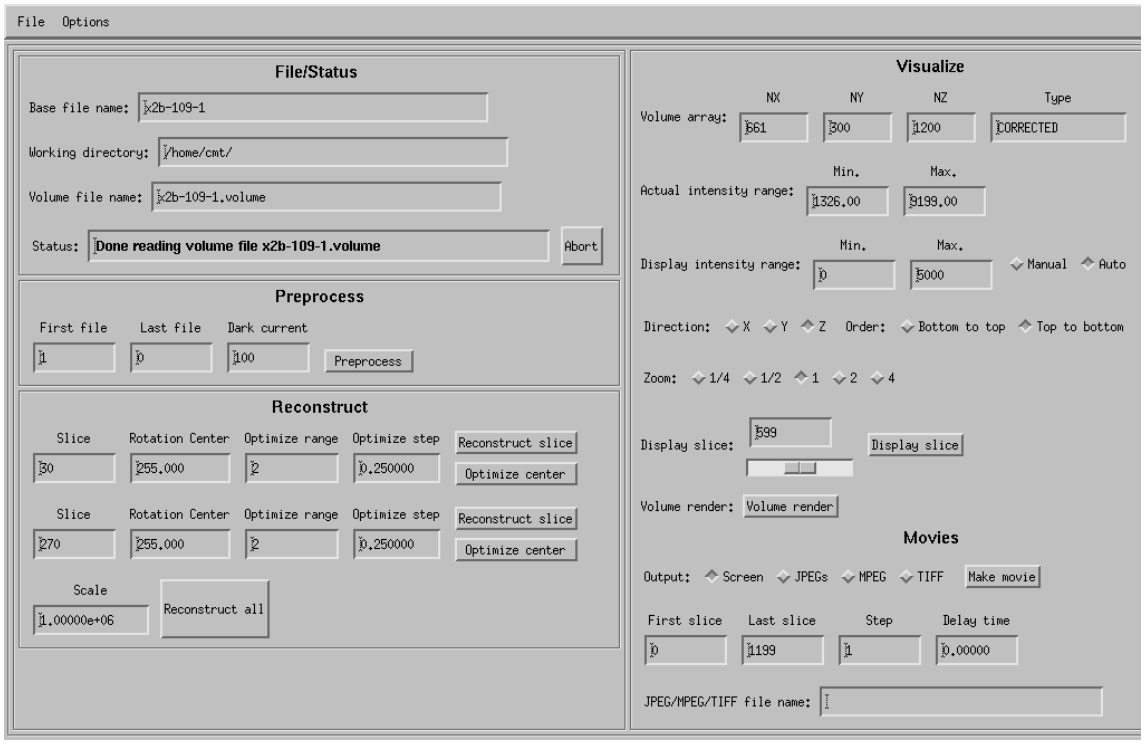

FIG. 3.8. Layout of IDL based tomo_display.sav routine for converting .volume file into a recon.volume file. Once .volume file was loaded into a shown routine, an individual slice was reconstructed around a defined or an optimized center. Once the reconstruction center was established, all slices were reconstructed and saved as the recon.volume file which could be opened in a same routine and saved as series of jpeg, tif files or mpeg movie format with options embedded on a visualization section of the window.

3.3.4 Estimation of Phase Saturation (%)

The individual phase saturations for a stack of 2-D images (jpeg or tif) were estimated with ImageJ and calculations in excel. The entire series of 2-D images was imported into ImageJ using an “Image Sequence” tool. The exterior of sample was cropped by defining a shape (an oval with x- and y- coordinates) for a region of interest and clearing outside (Fig. 3.9(a)). The histogram data (Fig. 3.9(b)) in an ASCII format for the entire stack was obtained in the ImageJ with an option under image analysis. The ASCII data was imported into excels and any commercially available software can be used to calculate the area under the peak and saturation for an individual phase. In the

present analysis, PeakFit4 was used to obtain a cumulative area curve for an imported histogram data in ASCII format.

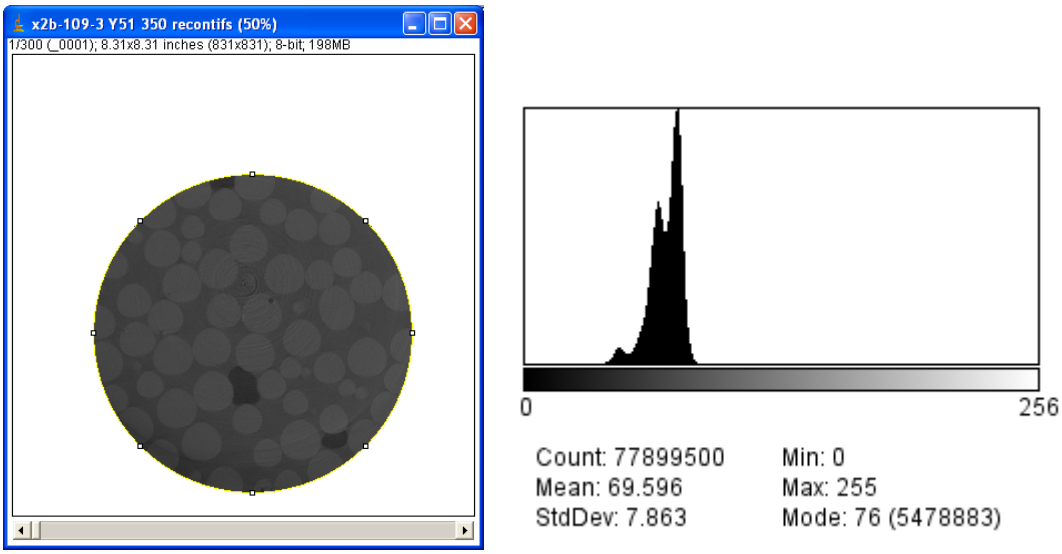

(a) **(b)**

FIG. 3.9. (a) ImageJ layout for a stack of 300 images (each of 8-bit and 831 x 831 pixels) of a sample containing THF hydrate (black) and aqueous solution of THF (grey) hosted in glass beads (white spheres). The sample container was rendered by defining an oval and clearing outside of it in ImageJ. (b) Histogram obtained for an entire stack in the ImageJ clearly shows three peaks corresponding to each phase arranged as per their mass attenuation coefficients from lower on the left to higher on x-axis.

3.3.5 Volume Construction and Rendering

A 3-D volume from the stack of images was created using number of softwares such as Drishti (Limaye, 2006), Cmtvis (Tomov and McGuigan, 2003) or with commercially available plug-inns for ImageJ (Rasband, 2005) developed at the Australian National University, University of Tennessee, Knoxville and National Institute of Health (NIH) respectively. The conversions of each stack of jpegs into volume in this analysis involved ImageJ and volume rendering software Drishti (Limaye, 2006). The first image of the stack was opened as an 8 bit image sequence in ImageJ (Fig. 3.10) and saved as raw data (filename.raw). The .raw data file was opened in Drishti with inputs

such as grid size and voxel size. The grid size was entered in z x y format as shown in Fig. 3.11 i.e. number of files (usually ~300-400) followed by x and y pixels with spacing between each. The voxel size was the resolution of the original image which depended upon the lens used during tomography. The 2.5X lens gave ~7.4 µm resolution whereas 5X lens offered ~3 µm resolution. The processed .raw data file was saved as filename.pvl.nc which was later re-opened several times for different rendering geometries and applying several transfer functions as shown in Fig. 3.12. The final rendered image was firstly converted into high resolution which lets user to save it as filename.jpeg.

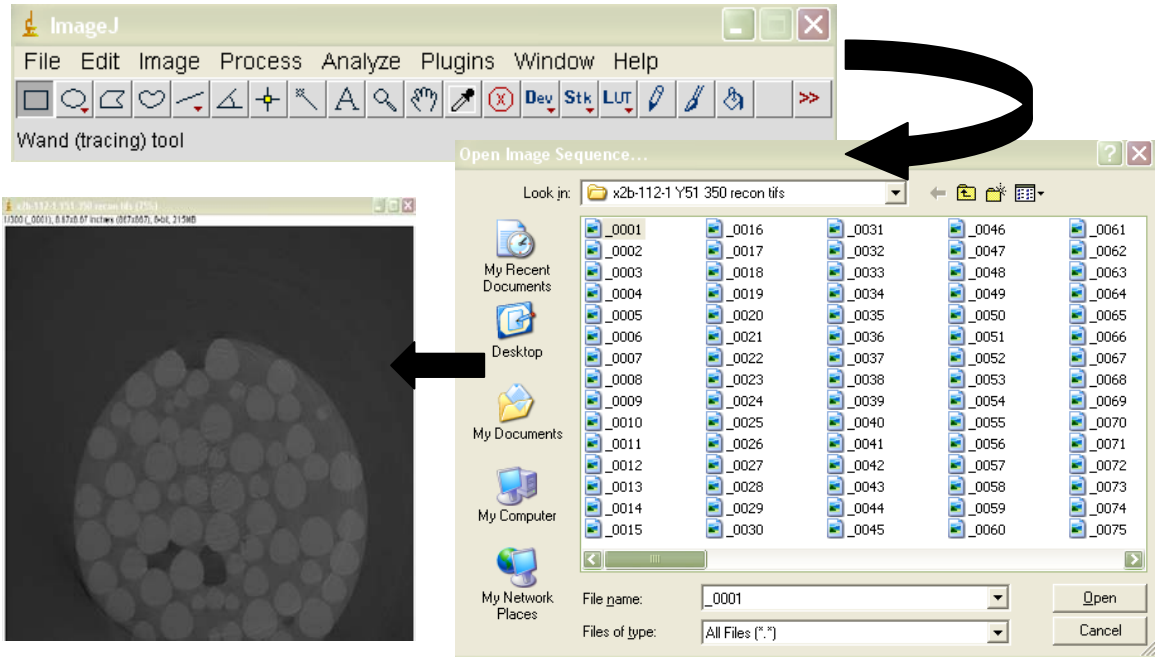

FIG. 3.10. Layout of ImageJ to convert image sequence into raw data. A series of images were opened with an import-image sequence tool under file menu. The imported data was saved in .raw format.

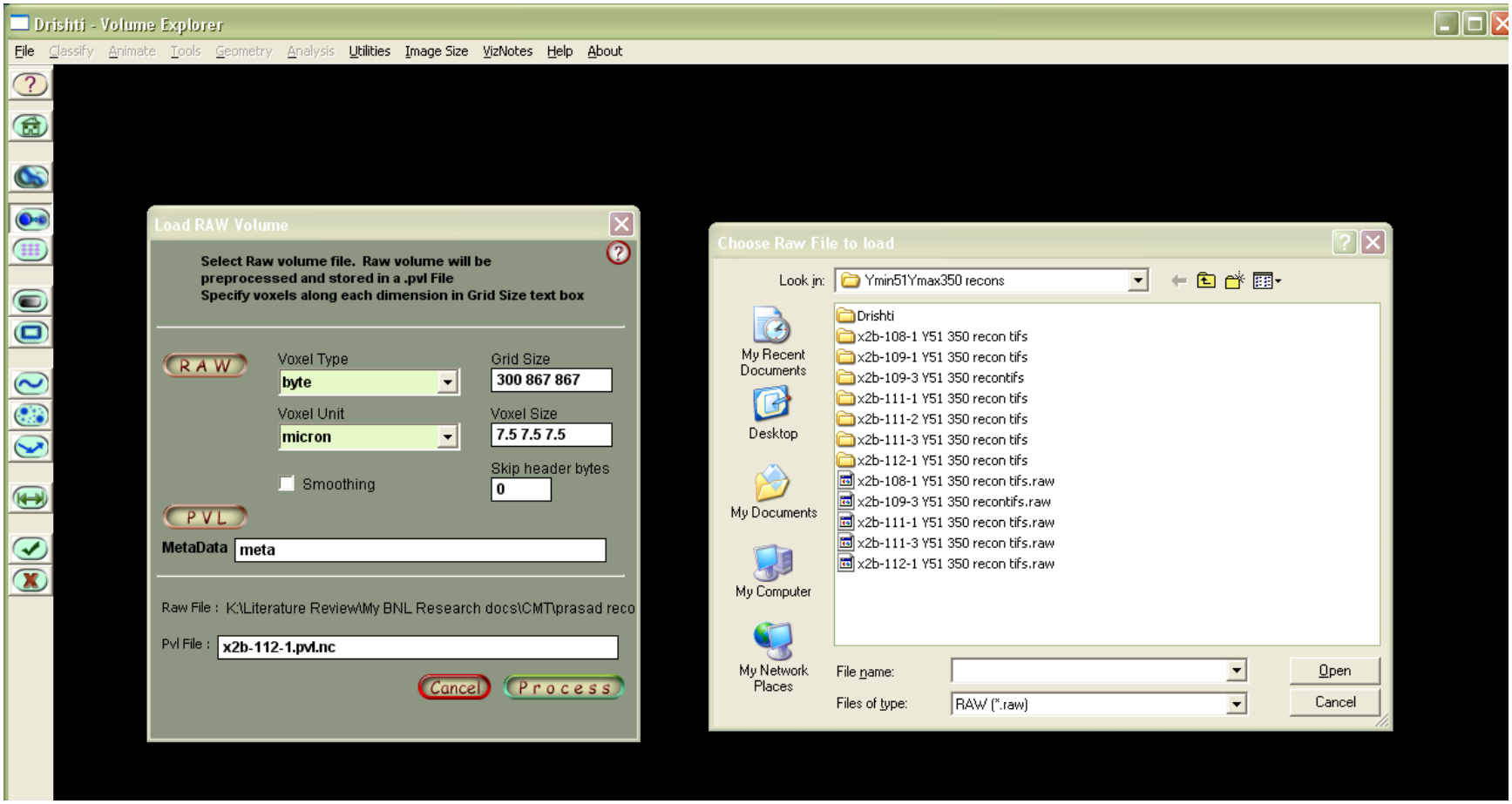

FIG. 3.11. Layout of raw data processing in Drishti. The *load raw volume* window was brought up with an option under file menu in Drishti. Upon selecting a .raw file to be processed, the raw volume parameters such as grid size, voxel size, voxel unit were entered. The resultant processed volume was saved with a filename with .pvl.nc or .pvl extension.

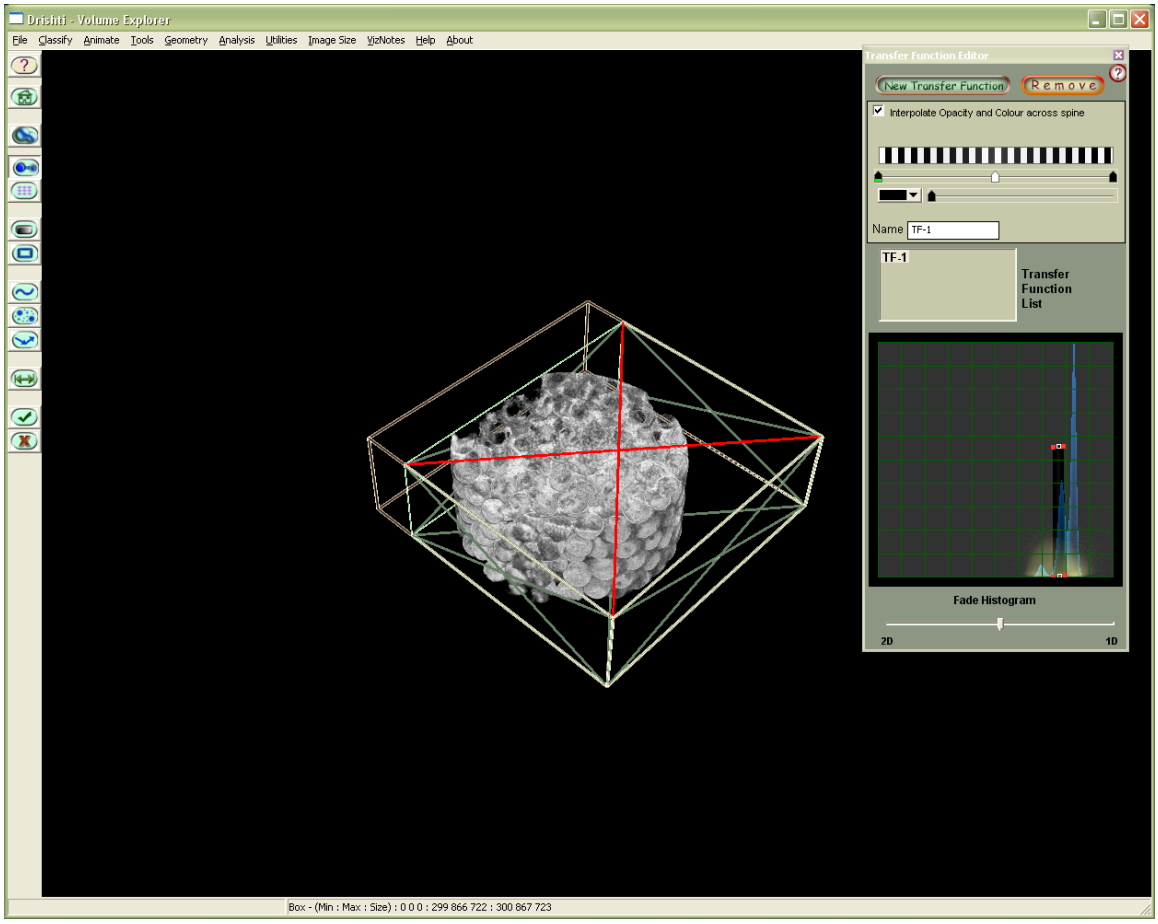

FIG. 3.12. Layout of volume rendering and application of transfer function in Drishti. The pre-processed .pvl.nc volume was loaded and an individual phase can be displayed in 3-D volume by selecting a transfer function to highlight a corresponding peak in 2-D histogram window. The volume was rendered to obtain a desired geometry in LowRes (low-resolution) mode. The resultant subvolume was saved as any image format after switching into a Hi-Res (high-resolution) mode.

Chapter 4

Sediment Characterization for Laboratory-Scale Methane Hydrate Formation and Dissociation

4.1 Ottawa Sand

Ottawa sand is standard reservoir sand in oil and gas research. The F-110 foundry sand is one of the fine grades, and it is commonly preferred in experiments due to its uniform size and shape that falls between rounded and subangular grains. The physical properties of Ottawa sand are summarized in Table 4.1.

Figures 4.1 and 4.2 show scanning electron microscope (SEM) images of dried Ottawa sand on double sided carbon tape placed on the stub. The images were taken from 2-7 mm working distance, at 20 kv accelerating voltage, and with Robinson backscattered electron detector to reveal sample's topography. The angular shape of individual particles can be seen from SEM images. This is also supported by sphericity, a measure of how round a grain is, for Ottawa sand as 0.7 (Santamarina, 2008).

Table 4.1. Physical properties of Ottawa sand.

Property	**Value**	**Reference**
Composition	99.8% Silicon Dioxide	U.S Silica
Shape	Round	U.S Silica
Color	White	U.S Silica
Grain Size	110 μm	U.S Silica
Permeability	92 darcies	U.S Silica
Grain Density	2.6476 g/cc	U.S Silica
Bulk Density	1.625 g/cc	U.S Silica
Hydraulic Conductivity	7.851 10^{-5} cm/sec	U.S Silica
Average(Bulk) Porosity	39.70%	U.S Silica
pH	7	U.S Silica
Sphericity	0.7	Santamarina, 2008
Specific Surface	0.019 m^2/g	Santamarina, 2008
Bulk Compressibility	1.72321x10^{-5} psi^{-1}	Wong, 2007
Pore size	48.28 μm	Kozney's eqn.

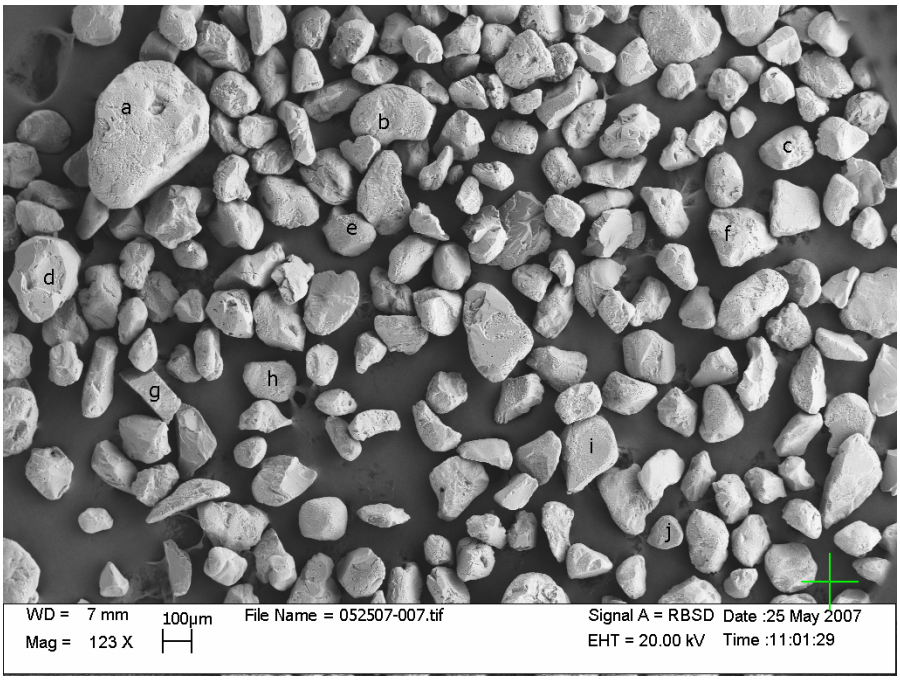

FIG. 4.1. Scanning electron micrograph of Ottawa Foundry F-110 sand.

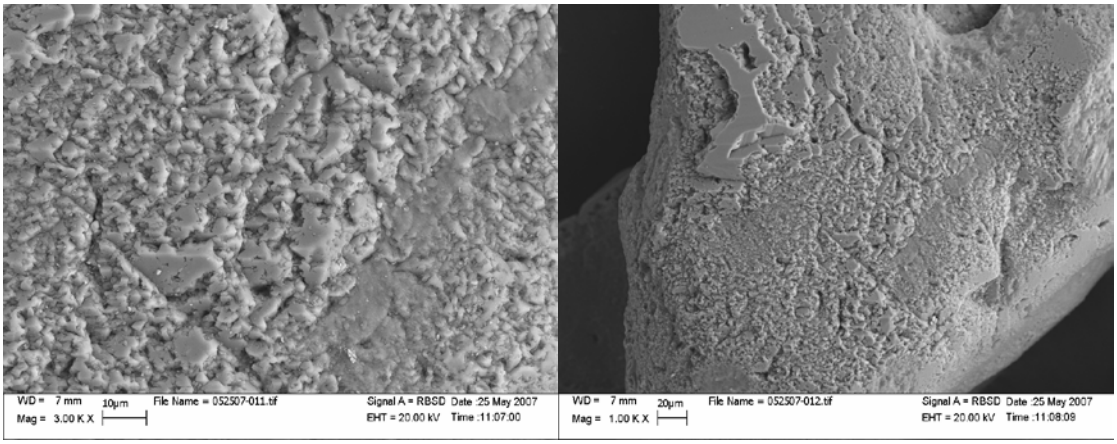

FIG. 4.2. Magnified scanning electron micrograph of Ottawa Foundry F-110 sand particle.

Figure 4.3 shows an energy dispersive X-ray (EDX) spectroscopy analysis of Ottawa sand. EDX analysis relies on the fact that each element in the periodic table has unique structure and response to an electron beam which excites the ground shell electron, causing an electron hole that ultimately gets filled by an electron from higher energy shell that gives away excess energy in the form of X-rays. EDX spectrum selection software enables the analysis of possible families of X-ray lines to avoid the misidentification of low intensity family members as belonging to some other element at a minor or trace concentrations. The chemical characterization from EDX analysis of Ottawa sand is consistent with the composition provided by US Silica Co (Table 4.2).

An amount of 700 g of F-110 Ottawa sand after overnight drying at 105^{o}C occupied ~455 mL volume in a measuring cylinder. However, upon compaction, the volume was reduced to 417 mL which gives ~1.678 g/cc bulk density. US Silica also reported porosity and bulk density for Ottawa sand to be 38.47% and 1.625 g/cc respectively. The particle density of Ottawa sand (2.6476 g/cc) is sufficiently closer to that of quartz (2.65 g/cc). In US Silica analysis, the particle volume was measured by Helium displacement, whereas porosity was computed by 3-dimensional (3-D) images. Figure 4.4 gives the particle size distribution of F-110 in the form of cumulative percentage retained on the sieve against the sieve opening. The average particle size of the sand comes out to be 110 µm.

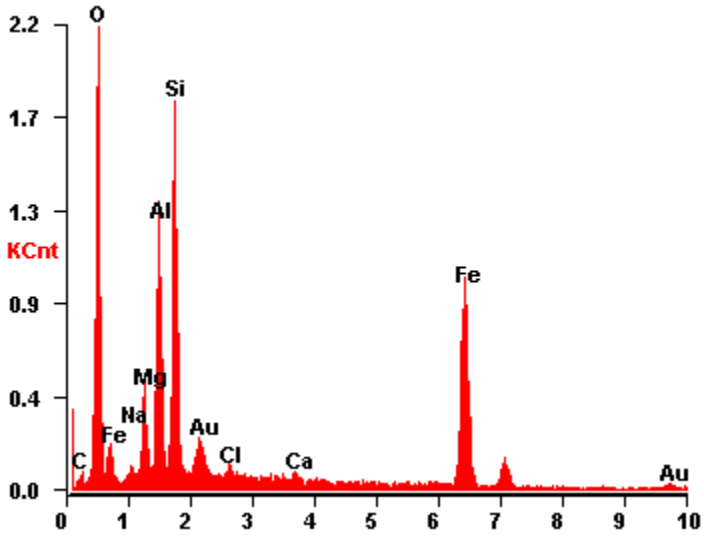

FIG. 4.3. EDX Analysis of Ottawa Sand.

Table 4.2. Chemical composition for crystal Ottawa sand (US Silica, IL).

Compound	**%**
SiO_2 (Silicon Dioxide)	99.8
Fe_2O_3 (Iron Oxide)	0.019
Al_2O_3 (Aluminum Oxide)	0.05
TiO_2 (Titanium Dioxide)	0.01
CaO (Calcium Oxide)	<0.01
MgO (Magnesium Oxide)	<0.01
Na_2O (Sodium Oxide)	<0.01
K_2O (Potassium Oxide)	<0.01
LOI (Loss on Ignition)	0.1

As discussed in Chapter 2, the northwestern Gulf of Mexico (GoM) is a unique location where hydrates occur in shallow sediments (5-20 m) as seafloor mounds when compared to other continental margins viz: Blake Ridge (BLR), Costa Rica, Cascadia and Nankai Trough, where the hydrate zone is from ten to a hundred meters below the seafloor (mbsf) due to the combined effect of gas solubility and limited gas supply.

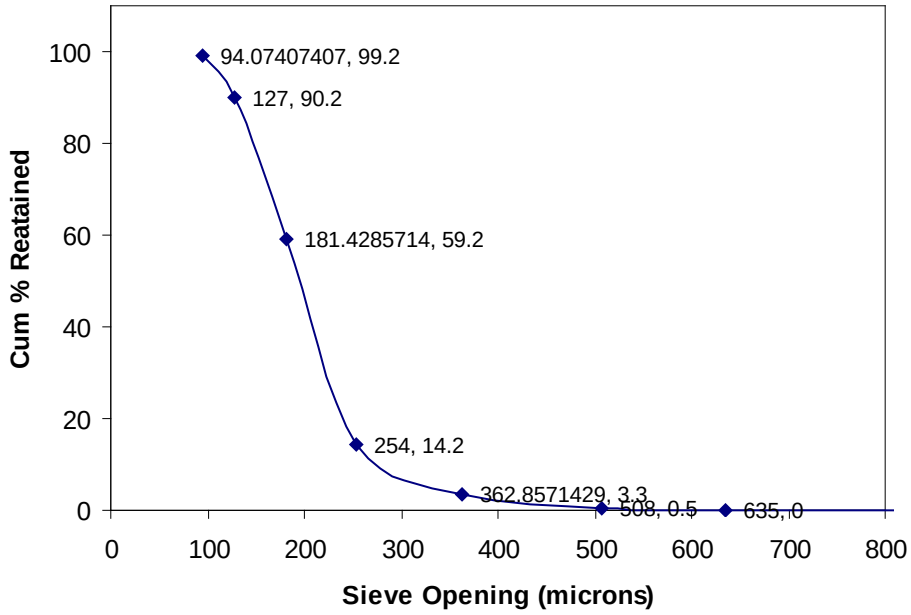

FIG. 4.4. Particle size distribution of Ottawa F-110 sand.

The lowered gas hydrate formation temperature at a particular pressure due to capillary forces within fine or constricted pores makes hydrate occurrence more likely in highly porous or coarse grained sediments (Handa and Stupin, 1992). The gas hydrate concentrations at BLR are found to be lesser than 15% of the bulk volume of the host sediment (Ginsburg, 2000) and the downhole well logging at Leg 164 has confirmed their occurrence as disseminated deposits (Paull et al., 1996; Kumura et al., 1997) in coarse-grained sediments with high porosity. The disseminated nature of hydrates has also been observed by Eaton (2007) in BLR sediments as opposed to nodular or vein configurations for the GoM.

This indicates that the analysis with Ottawa sand (with average particle size of 110 μm), will be comparable to natural sediments from BLR. This may allow achieving more hydrate saturation than GoM sediments for a proposed week timeline of a hydrate formation run. Moreover, the analysis would mimic BLR sediments for their geochemistry.

4.2 Natural Depleted Host Sediments - Gulf of Mexico

Winters et al. (2008) measured physical properties of sediment cores recovered from Keathley Canyon (KC) and Atwater (AT) sites in the northern GoM. The properties of shallow sediments (<50 mbsf) were found to change with increasing overburden pressure/depth. The pore water salinity varies between 35 ppt at the seafloor to 54.1 ppt at 378.78 mbsf. The water saturation decreases initially from ~100% at the seafloor to 39.5% at 39.54 mbsf and remains stable between 32 to 37% until an odd exception at 378.78 mbsf. The grain density was found to vary between 2.670 and 2.747 g/cc while the bulk density increases from 1.491 g/cc at 4.25 mbsf to 1.993 g/cc at 313.66 mbsf as shown in Fig. 4.5(a). The sub-seafloor temperatures (Fig. 4.5(b)) were computed with a geothermal gradient of 3.8^{o}C/100m for seafloor temperature of 4^{o}C (Dai et al., 2008). The pore-water or seawater density values (Fig. 4.5(b)) were computed from salinity values reported by Winters et al. (2008) and respective sub-seafloor temperatures.

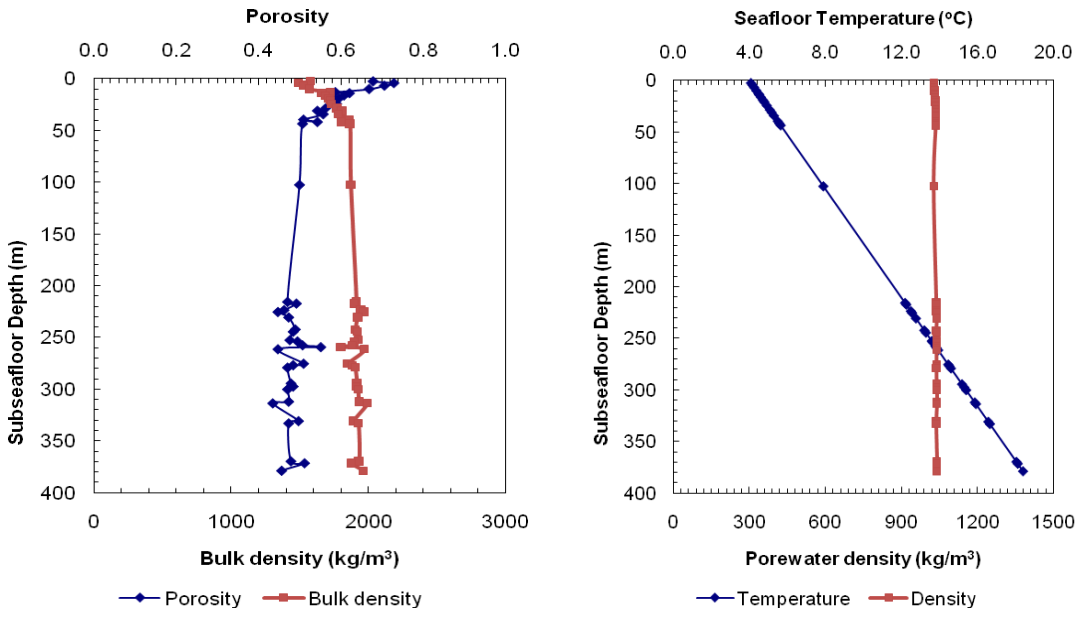

(a) **(b)**

FIG. 4.5. Porosity, bulk density (a), sub-seafloor temperature and pore-water density (b) of sediments with depth at Keathley Canyon site in Gulf of Mexico.

Kastner et al. (2008) reported salinity and solute constituents of pore water within cores recovered from the AT valley and KC 151#3 sites in the GoM (Table 4.3). Cook et al. (2008) analyzed logging-while-drilling (LWD) resistivity trends from KC151 site in the GoM and inferred the presence of hydrates in the form of (a) primarily within high-angle fractures and (b) saturating permeable beds. In an interval from 260 to 299.5 mbsf, porosity was found to increase with hydrate saturation unlike in an interval from 220.5 to 250 mbsf where it does not change with hydrate saturation. This indicates that gas dilation and hydrate-forced heave may force open sediments, increasing their bulk density. Yun et al. (2006) reported geophysical and geomechanical properties of core samples recovered from AT valley and KC sites in the GoM in April and May 2005. The specific surface (the ratio of grain surface area to their mass) for AT and KC sediments ranges between 89.3-143.1 m^2/g and 62.4-133.3 m^2/g respectively. Klapp et al. (2007) measured the mean grain size distribution of sediments recovered from the seafloor of Bush Hill region in the GoM and the hydrate ridge at 100.89 mbsf of Ocean Drilling Program (ODP) Leg 204 in the Cascadia margin as 301 and 517 μm respectively. The physical properties of the natural sediments analyzed in this study are compiled in Table 4.4.

Figure 4.6, 4.8 and 4.10 show SEM images of dry GoM sediments from KC151-3 site cores recovered from a depth interval of 230-265 mbsf (1394.5 m water depth). Figure 4.6(b) at 30kX magnification shows a majority of particles size less than 2 μm, which is consistent with Francisca et al. (2005) who found 55 and 48.5 percentage as clay (<2 μm) at sites GC185 and MC852 respectively. However the sediment grains are not seen as individual particles as in the case of Ottawa sand but in coagulated form even at 30kX magnification. An elemental characterization from EDX analysis shows that sediments primarily consists of Si, O, Al, Ca, Mg (Figs. 4.7, 4.9, 4.11).

Dry and wet (preserved) sediment samples from the GoM site, KC151-3 12C-2, 14C-3 and 1H-7 were placed in 1 mL polypropylene syringes for X-ray computed microtomography (CMT) analysis. For each sample, a tomoscan consisting of ~1200 projections, each with 3 sec of exposure of sample in X-ray beam and 7.42 μm pixel size (2.5X lens), was taken while rotating the sample tube from 0-180^o. Each tomogram was reconstructed for 2-D cross-sectional images, which were compiled to generate 3-D

volume. The 3-D volumes of 2315 x 4630 x 2968 μm^3 size for dry and preserved sediments are shown in Figure 4.12. The KC151-3 12C-2 and 14C-3 samples required an energy of 22 keV for a transmittance[1] of 13.5% as opposed to 19 keV needed for the same transmittance for sample KC151-3 1H-7, indicating that 1H-7 has a coarser structure. It is also evident from the 3-D grain pack of KC151-3 12C-2 and 14C-3 samples (Fig. 4.12), which is fine and more densely packed than that of 1H-7. However wet/preserved 1H-7 also required 19 keV photon energy, which implies that there is no effect of interstitial water. The coarser nature of the KC151-3 1H-7 sample arises from its shallow sub-seafloor depth (6.7 mbsf) as compared to 230-245 mbsf depth interval for 12C-2 and 14C-3 samples. A single peak in the histogram embedded in Fig. 4.12 for 1H-7 indicates the least voids due to the effect of compaction and water saturation.

Table 4.3. Solute chemistry of pore fluids at Keathley Canyon (KC) lease block 151, Hole 3 in the Gulf of Mexico (Kastner et al, 2008).

Hole Core-section (cm interval)	**14C-3 (80–100)**	**24C-1 (76–100)**	**12C-2 (0-25)**
Depth (mbsf)	244.9	370.3	231.3
Salinity	51	55	51
Cl^- (mM)	869	934	878
Alk (mM)	4.06	3.89	5.22
SO_4^{-2} (mM)	0	0	0.08
Ca^{+2} (mM)	21.33	21.95	21.76
Mg^{+2} (mM)	79.9	89.93	80.47
Sr^{+2} (mM)		305.7	215
K^+ (mM)	5.34	3.6	6.1
Na^+ (mM)	69	716	723
Li^+ (mM)		27.4	36
H_4SiO_4 (mM)	291	131	293

[1] Transmittance (T) = $I/I_0 = \exp(-\mu_{cm\wedge 2/g} . \rho_{g/cm\wedge 3} . t_{cm})$ where I is transmitted photon intensity, I_0 is incident photon intensity. The factor $\mu_{cm\wedge 2/g} . \rho_{g/cm\wedge 3} . t_{cm}$, commonly referred to as τ, is adjusted to ~2.0 to avoid image noise and reconstruction artifacts.

Table 4.4. Physical properties of core-sections recovered from Keathley Canyon (KC) lease block 151, hole 3 in the Gulf of Mexico.

KC151-3	14C-3	24C-1	12C-2	1H-7	Reference
Section of core (cm)	**(80–100)**	**(76-100)**	**(0-25)**	**(70-80)**	-
Depth (mbsf)	244.51	369.67	230.62	6.7	Winters et al., 2008
Salinity (ppt)	50.6	54.9	50.9	35.4	Winters et al., 2008
Grain density (kg/m^3)	2744	2747	2718	2721	Winters et al., 2008
Bulk density (kg/m^3)	1917	1931	1922	1525	Winters et al., 2008
Void ratio (e)	0.94	0.92	0.9	2.4	Winters et al., 2008
Water saturation (%)	35.6	34.8	34.5	-	Winters et al., 2008
Hydrate saturation (%)	>20%	>20%	>20%	-	Cook et al., 2008
Sea floor temperatures (^{o}C)	4.79	4.79	4.79	-	Lee and Collett, 2008
Seafloor depths (m)	1300	1300	1300	-	Kastner et al., 2008
Porosity (ø) = e/(1+e)	0.4845	0.4792	0.4737	0.7059	Terzaghi et al., 1996
Specific surface (m^2/g)	~100.3	-	-	-	Yun et al., 2006
% Sand	0.0007	0.0027	0.0145	0.0156	Winters et al., 2008
% Silt	0.2206	0.0715	0.2648	0.0901	Winters et al., 2008
% Clay	0.7787	0.9258	0.7207	0.8943	Winters et al., 2008
Grain diameter (µm)	5.7026	3.2912	8.9146	5.8735	http:/cru.cahe.wsu.edu
Pore diameter (µm)	3.5736	2.0186	5.3487	9.3975	Koxeny's equation

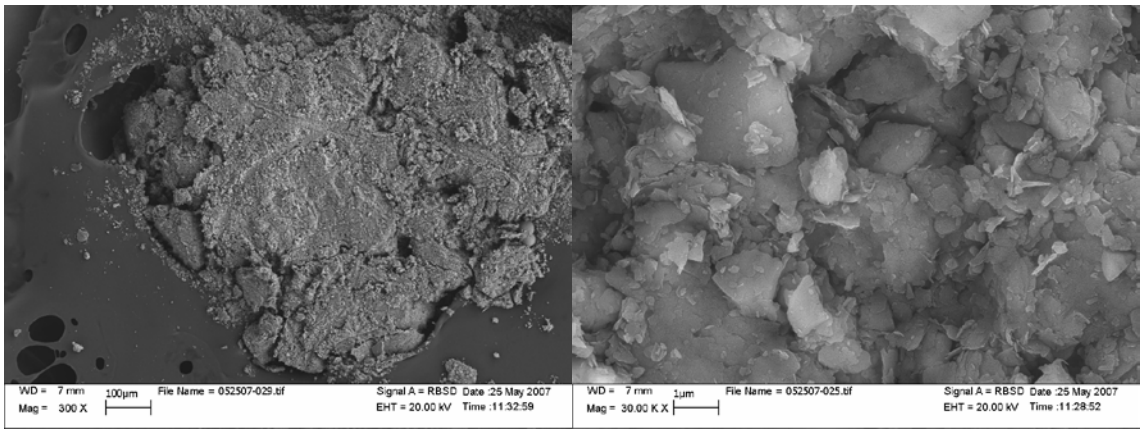

(a) **(b)**

FIG. 4.6. Scanning electron micrographs of Gulf of Mexico KC151-3 17H-4 sediments at (a) lower (300X) and (b) higher (30 KX) magnifications.

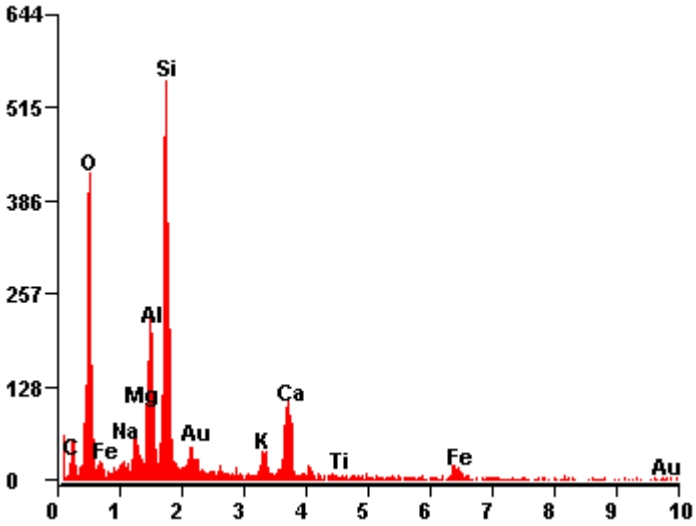

FIG. 4.7. EDX analysis of Gulf of Mexico KC151-3 17H-4 sediment.

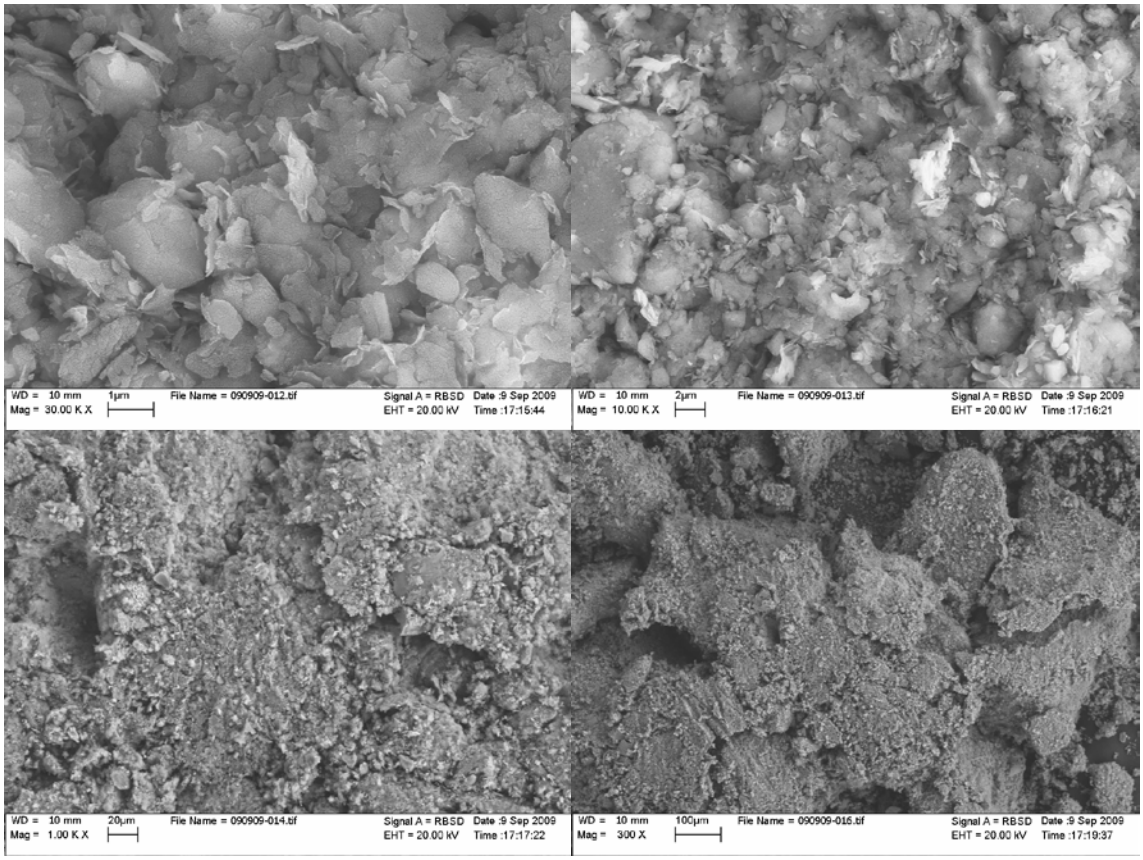

FIG. 4.8. Scanning electron micrographs of Gulf of Mexico KC151-3 1H-7 sand (6.7 mbsf) at various magnifications.

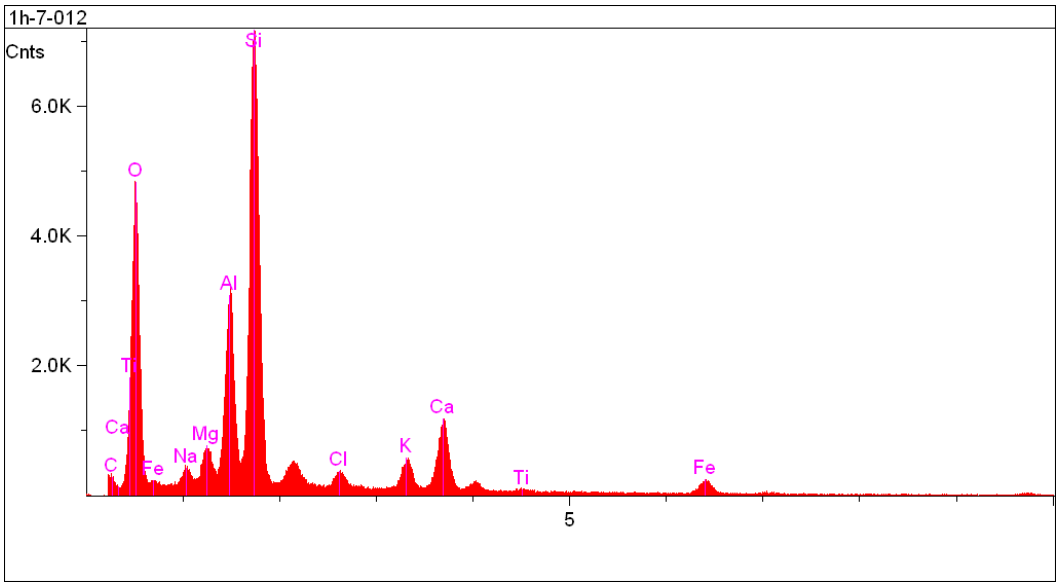

Fig. 4.9. EDX analysis of Gulf of Mexico KC151-3 1H-7 sand (6.7 mbsf).

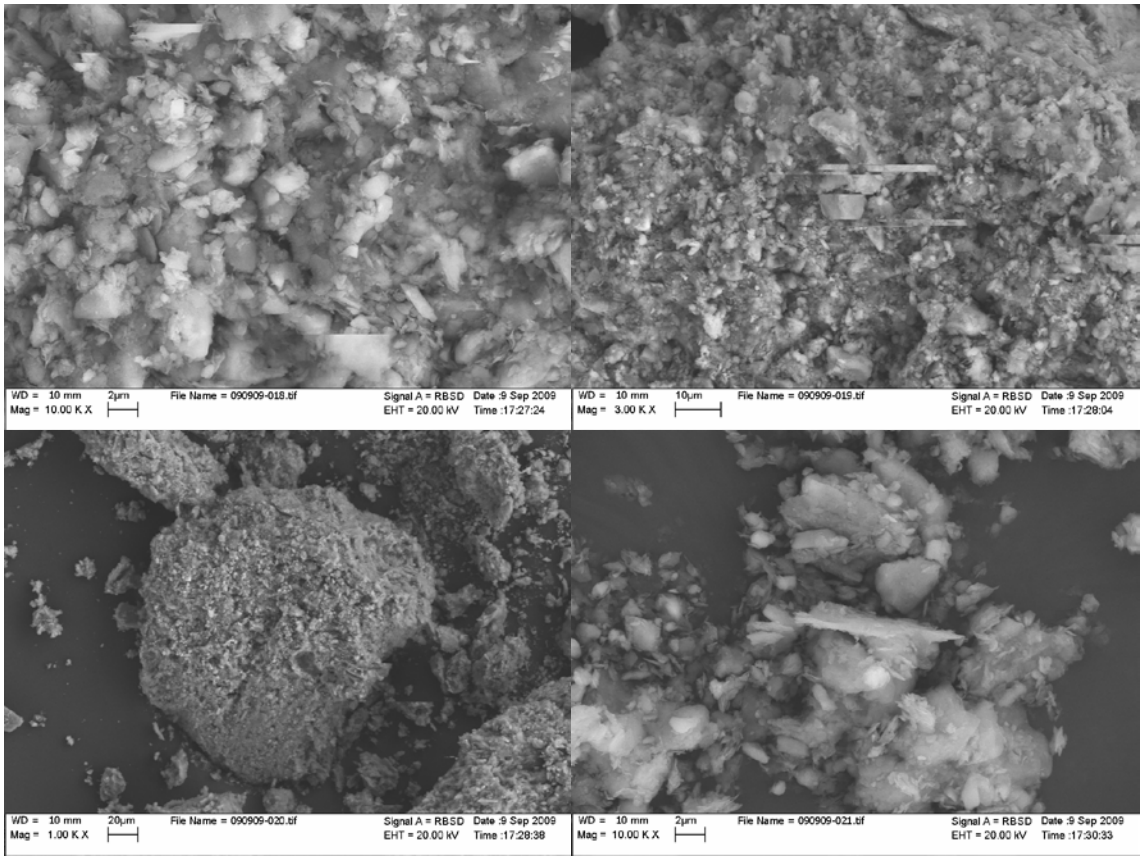

FIG. 4.10. Scanning electron micrographs of the mixture of Gulf of Mexico KC151-3 12C-2 (230.62 mbsf) and 14C-3 (244.51 mbsf) sands at various magnifications.

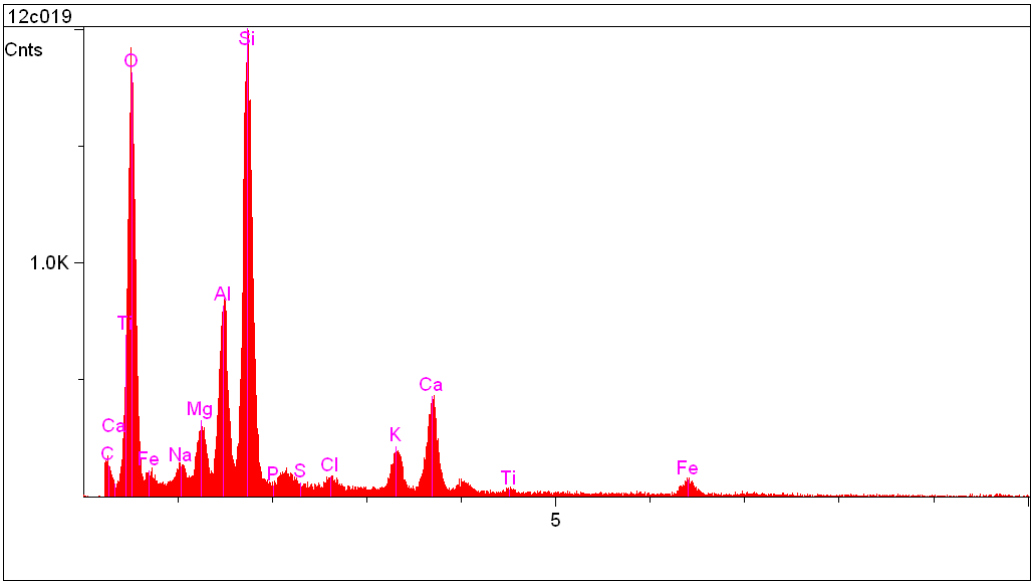

FIG. 4.11. EDX analysis of mixture of Gulf of Mexico KC151-3 12C-2 (230.62 mbsf) and 14C-3 (244.51 mbsf) sands.

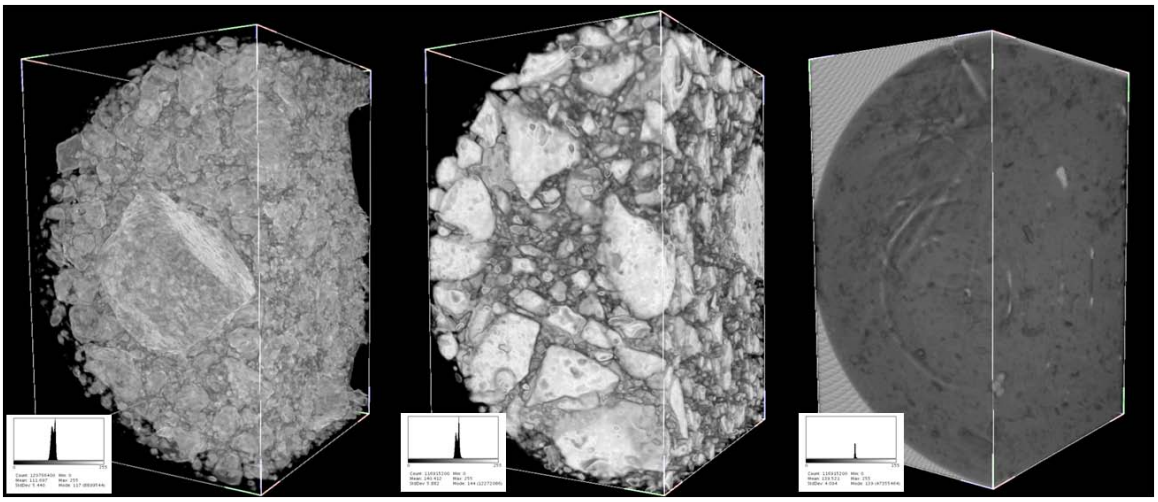

(a) **(b)** **(c)**

FIG. 4.12. X-ray CMT grain packs of 312 x 624 x 400 voxels of (a) dry mixture of Gulf of Mexico KC151-3 12C-2 & 14C-3 (b) dry Gulf of Mexico KC151-3 1H-7, 70-80 and (c) preserved/wet Gulf of Mexico KC151-3 1H-7, 70-80.

5.3 Natural Depleted Host Sediments – Blake Ridge

Collett and Ladd (2000) detected hydrate intervals, sediment porosities, water saturations at sites 994, 995, and 997 from Leg 164 of in the BLR. The gas hydrate interval between 185-450 mbsf was detected using electrical resistivity and acoustic transit-time downhole logs from sites 994, 995, 997. The physical properties of these sites are compiled in Table 4.5. Lee (2000) estimated gas hydrates amounts from acoustic logs at the Leg 164, BLR sites. The average gas hydrate saturation was found to be between 12.1%, using porosity from bulk density, and 3.8%, using core-derived porosity. The bulk density was computed using the matrix density value of 2.7 g/cc. Ginsberg et al. (2000) presented grain size distribution and pore-water chlorinity of sediments from cores recovered from various depths at site 994, 995, and 997 of BLR Leg 164. Table 4.5 shows weighted average grain size and pore-water chlorinity values at sites 994, 995, and 997 for hydrate intervals of 212-428.8, 193-450, and 186-451 mbsf respectively.

Table 4.5. Physical properties of core-sections recovered from Blake Ridge Site.

Site	994	995	997	Reference
Depth (mbsf)	212.0-428.8	193-450	186.4-450.9	Collett and Ladd, 2000
Thickness of hydrate region (m)	216.8	257	264.5	Collett and Ladd, 2000
Porosity (%)	57	58	58.1	Collett and Ladd, 2000
Water saturation (%)	95-100	95-100	95-100	Collett and Ladd, 2000
Bulk density (g/cc)	1.7	1.7	1.6	Collett and Ladd, 2000
Gas hydrate saturation (%)	3.3	5.2	5.8	Collett and Ladd, 2000
Seafloor temperatures (^{o}C)	3	3	3	Collett and Ladd, 2000
Seafloor depth (m)	2797.6	2774.6	2763.6	Collett and Ladd, 2000
Matrix density	2.7	2.7	2.7	Lee, 2000
Average chlorinity	494	495	490	Ginsberg et al., 2000
Average grain Size (µm)	6.96	9.99	7.22	Ginsberg et al., 2000
Average pore Size (µm)	6.15	9.20	6.67	Kozeny's eqn.

Lorenson (2000) performed light transmission and scanning electron microscopy of sediments recovered from ODP Leg 164 (BLR), and Leg 170 (Middle America Trench, offshore from Costa Rica) drilling sites. BLR sediments were found consisting of foraminifera, diatom, accumulations of spicules, sand-like microfossil debris, and pods or lenses of framboidal pyrite. SEM images of BLR sediments from our analysis (Fig. 4.13) show the coagulated nature of grains, even in the dry form, in contrast to Ottawa sand. However, our analysis does not show any presence of diatoms. An elemental composition of BLR sediments (Fig. 4.14) with an EDX technique is consistent with that observed for GoM sediments.

A dried sediment sample from ~250 mbsf ODP BLR Leg 164, Hole 995A, Core-section 31X-01, interval 110-120 cm was analyzed with an X-ray CMT tomogram acquired at a 19 keV energy for a necessary 13.5% transmittance as previously discussed. The 3-D image with a 7.42 µm pixel size is shown in Fig. 4.15. The coarse grain pack observed is consistent with earlier reported porosities in the order of 50-70% by Collett and Ladd (2000) and Jones et al. (2007).

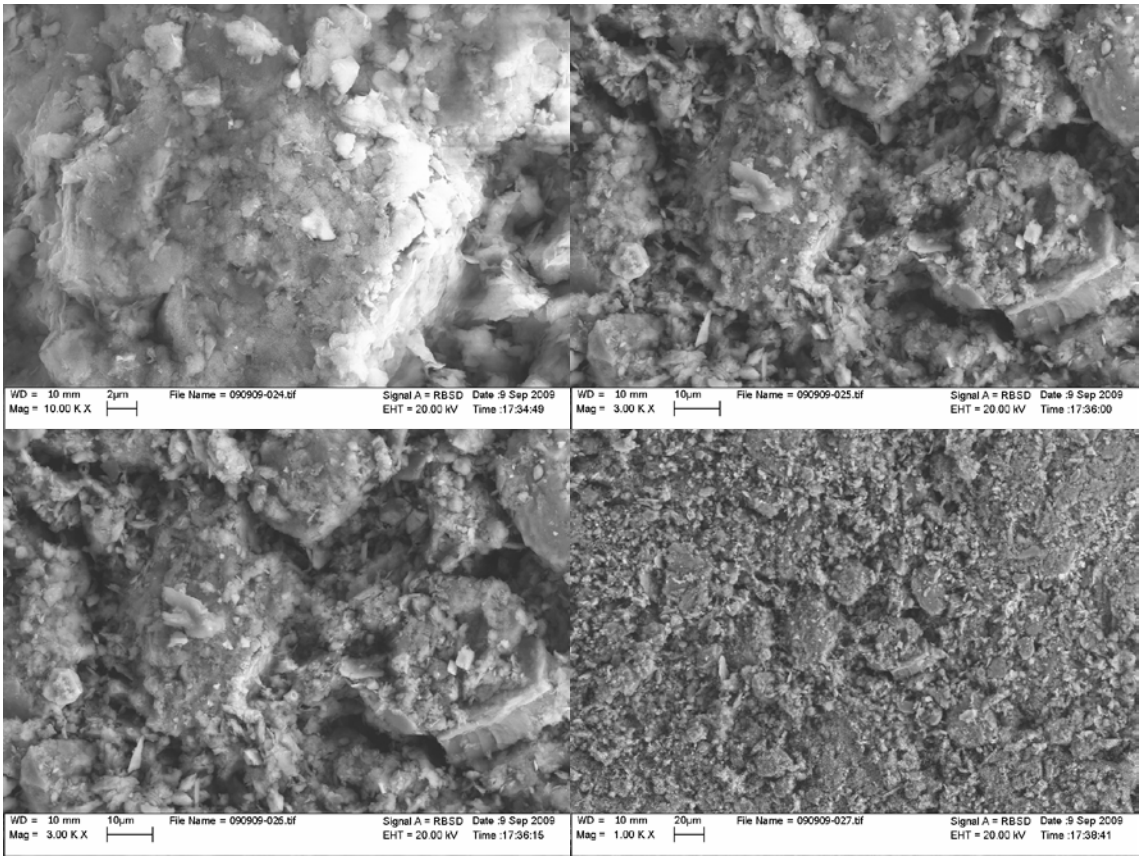

FIG. 4.13. Scanning electron micrographs of ODP Blake Ridge Leg 164, Hole 995A, Core-section 31X-01, interval 110-120 cm sand at various magnifications.

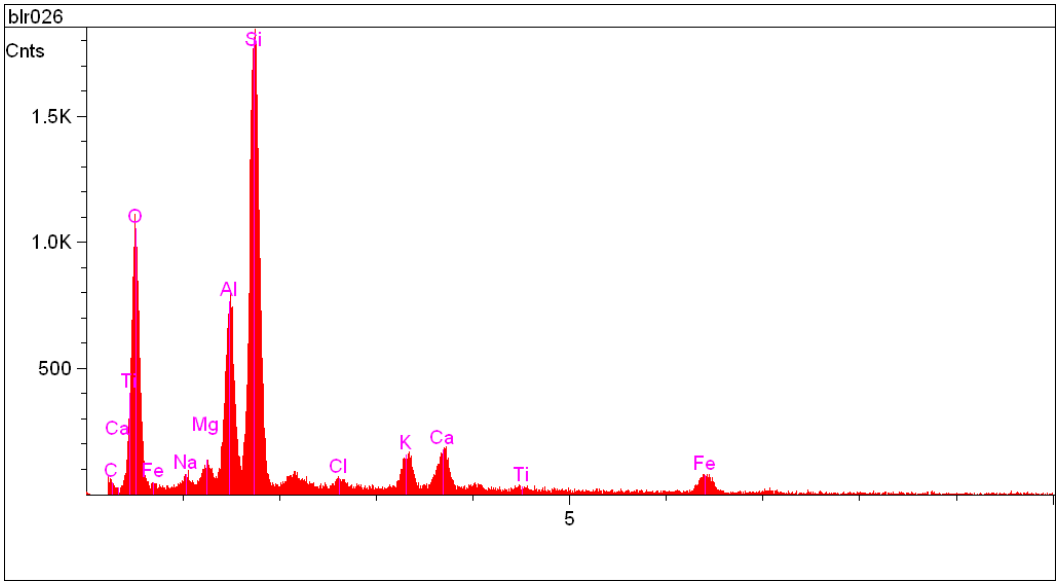

FIG. 4.14. EDX analysis of Blake Ridge Leg 164, Hole 995A, 31X-01, 110-120 sand.

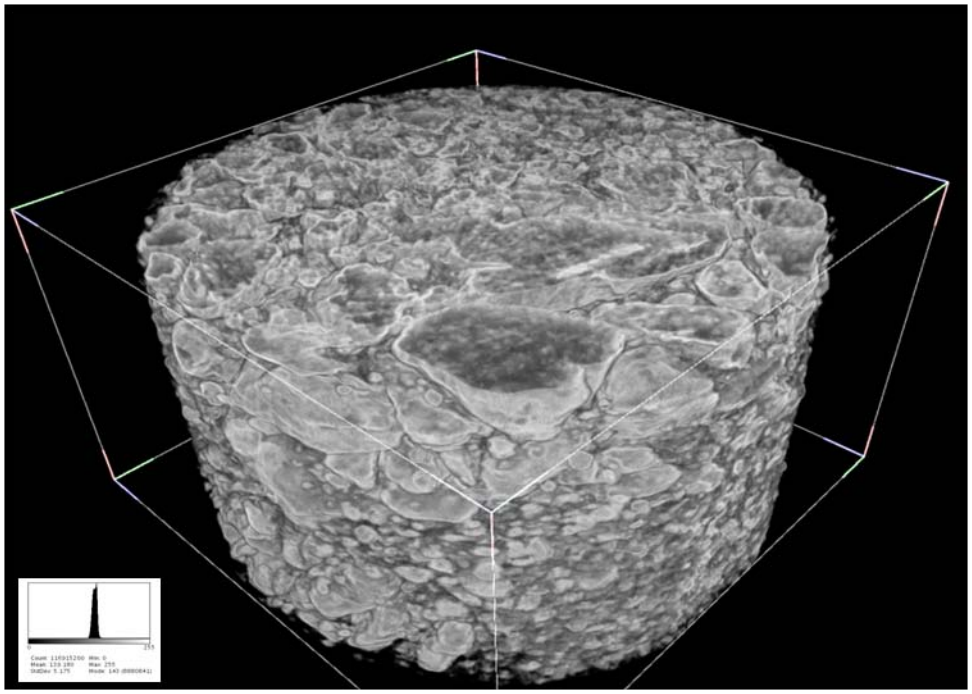

FIG. 4.15. X-ray CMT grain packs of 624 (l) x 624 (w) x 400 (h) voxels of dry Blake Ridge Leg 164, Hole 995A, 31X-01, 110-120 sand.

4.4 Water Saturation

The BLR gas hydrates at sites 994, 995, 997 are found at average depths of 200-425 mbsf. Collett and Ladd (2000) reported water saturations ranging from about 100% to a minimum of about 80% from Archie relation between 200 and 425 depths below sea floor. Moreover hydrate occurrence has been reported in sediment from 0.2 mbsf with 141% water content (222 m water depth) during the OC178 cruise near BLR and ~10-50 mbsf at the KC151-3 hole (water depth of 1333.5 m). Hence water saturation for later Ottawa sand-core analysis (Chapter 6, 7) was chosen to be 100% consistent with majority of hydrate intervals from BLR holes 994D, 995B, and 997B. Winters et al. (2009) reported GoM water saturations ranging from 30% to 100% at the KC151-3 site. The laboratory analysis with 100% water saturation will not only make core conditions more *in-situ* but also confirm uniform water distribution throughout the core.

4.5 Pure Water vs. Seawater

Kester et al. (1967) revised the previously reported composition of artificial seawater to bring it to within 1 mg/kg of natural seawater for all the major constituents. The revised salt composition for salinity of 35% is given in Table 4.6.

Table 4.6. Formula for 1 kg of artificial seawater with 35% salinity[2] (S) (Kester et al., 1967)

A. Gravimetric salts	
Salt	**g/ kg of distilled water**
NaCl	23.926
Na_2SO_4	4.008
KCl	0.677
$NaHCO_3$	0.196
KBr	0.098

[2] S = salinity (ppt or %); grams of salts per liter of solution

H_3BO_3	0.026
NaF	0.003
B. Volumetric salts	
Salt	**Moles/ kg of distilled water**
$MgCl_2.H_2O$ (MW: 203.33; ρ = 0.071 g/cc)	0.05327
$CaCl_2.2H_2O$ (MW: 147.03; ρ = 1.085 g/cc)	0.01033
$SrCl_2.6H_2O$ (MW: 266.64; ρ = 1.013 g/cc)	0.000009
MW – Molecular weight; ρ - Density	

Dickens and Quinby-Hunt (1994) established methane hydrate stability conditions in seawater (S = 33.5%) collected from Monterey Bay (off the California coast) and compared them with hydrate conditions for methane-pure water (Sloan, 1990). The hydrate stability conditions were consistent with previously reported thermodynamic conditions for a methane-synthetic seawater (S = 35%) system (Dholabhai et al., 1991). Makogon and Holditch (2001) performed several experiments in static and dynamic conditions with pure and natural gases mixed with distilled water, salt water, and freshwater or salt water containing thermodynamic and kinetic inhibitors. The salt water composition (41.953 g of mixture per liter of water) following American Material Standard D-1141-52 Formula A (1.025 g/cc density at 15^oC) used in the study is listed in Table 4.7. Wright and Dallimore (2004) measured the pore water salinity of the sediment sample cores from hydrate intervals between 921 and 1123 m of the Mallik 5L-38 research well in the Mackenzie Delta, Northwest Canada. The measured pore water salinity of the hydrate depleted cores ranged between ~7 ppt to 50 ppt. Duan and Sun (2006) extended the Pitzer model into a thermodynamic model to predict the phase equilibrium of methane and carbon dioxide hydrates in seawater (S = 35%) and aqueous electrolyte solutions. Figure 4.16 shows the methane hydrate pressure-temperature stability curves for methane-pure water and methane-seawater systems from various sources.

Table 4.7. Sea-salt composition for artificial sea water preparation (Makogon and Holditch, 2001)

Salt	% mass
NaCl	58.490
Na_2SO_4	9.750
KCl	1.645
KBr	0.238
H_3BO_3	0.071
$SrCl_2.6H_2O$	0.095
$MgCl_2.6H_2O$	26.460
$CaCl_2$	2.765
$NaHCO_3$	0.477
NaF	0.007
Brine pH	8.2

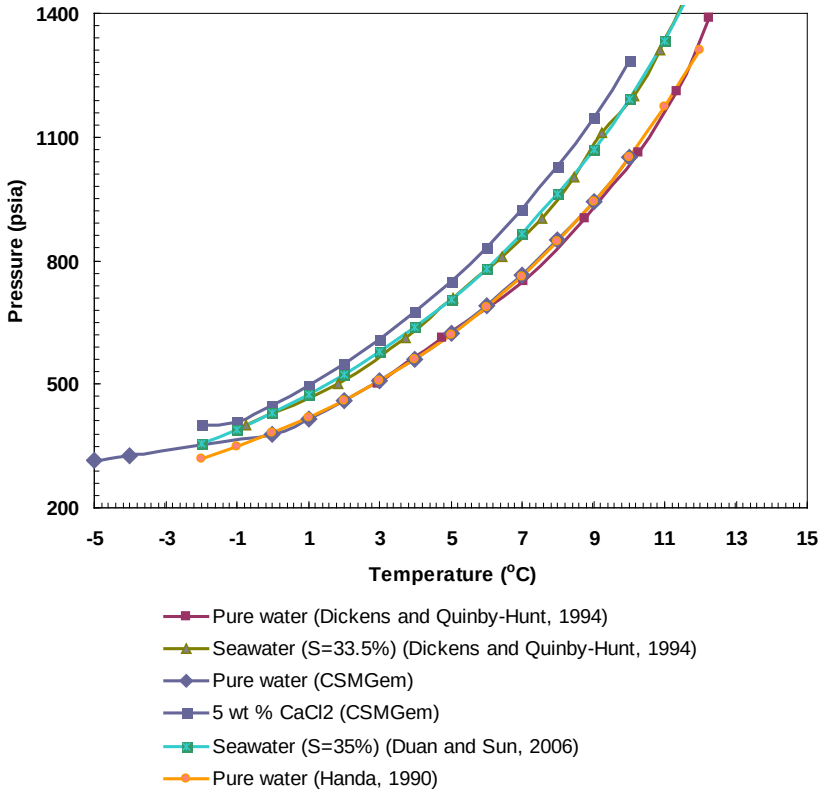

FIG. 4.16. Equilibrium pressures against temperature of methane hydrates from pure water, seawater and 5 wt% $CaCl_2$ solution

Fleischer et al. (2001) reviewed the origin of free methane gas in marine sediments from about 120 global occurrences including the GoM, BLR, Cascadia margin, and Long Island (LI) Sound. Salinity of the LI sound (~25-29% in central part of the sound) is slightly lesser than that of pure seawater (~35%). The water from the eastern end of sound and near the Atlantic Ocean has higher salinity. Salinity is lowest in spring when inflow of freshwater from Connecticut River meets the sound just across the northern fork of LI (Hammerson, 2004). In LI Sound the fresh water of rivers mix with the ocean water, thus reducing the salinity to about 29 ppm. Seawater for *in-situ* formation and dissociation kinetics experiments (Chapter 6) was collected from East Port Jefferson Beach in the Long Island Sound, NY. The salinity was measured by a chemical titration where all of the chloride content was precipitated out in a known volume of seawater. The seawater contains chloride as a major source of the negative ions and the relationship between chloride content and salinity was found to be a reasonably constant as shown in Eq. (1) (Knudsen, 1900). In three measurements, the chloride content in was found to be averaging about 15525 mg/liter (15.525%) of the seawater used in later Ottawa sand-core analysis (Chapter 6). This gives the salinity of seawater as 28.053% (28.053 g of salts per liter of seawater).

$$S\% = 1.805 \times Cl\% + 0.030 \quad (1)$$

4.6 Effective Pressure vs. Depth

Mimicking the sub-seafloor conditions in the presence of water, gas, hydrate phases requires the understanding of the variation of effective stress (difference between confining pressure and pore pressure) with sub-seafloor depth. Bryant et al. (1985) performed a consolidation test on sediments located at nine sub-seafloor depths at site 619 located in Pigmy basin, 206 km off the coast of Louisiana shoreline. Figure 4.17 displays the vertical effective stress (under hydrostatic conditions) and the preconsolidation stress (minimum, average and maximum). It is clear from Fig. 4.17 that a minimum of 1200 kPa (174 psi) effective stress would be necessary to mimic sub-seafloor depths up to 175m (574 ft).

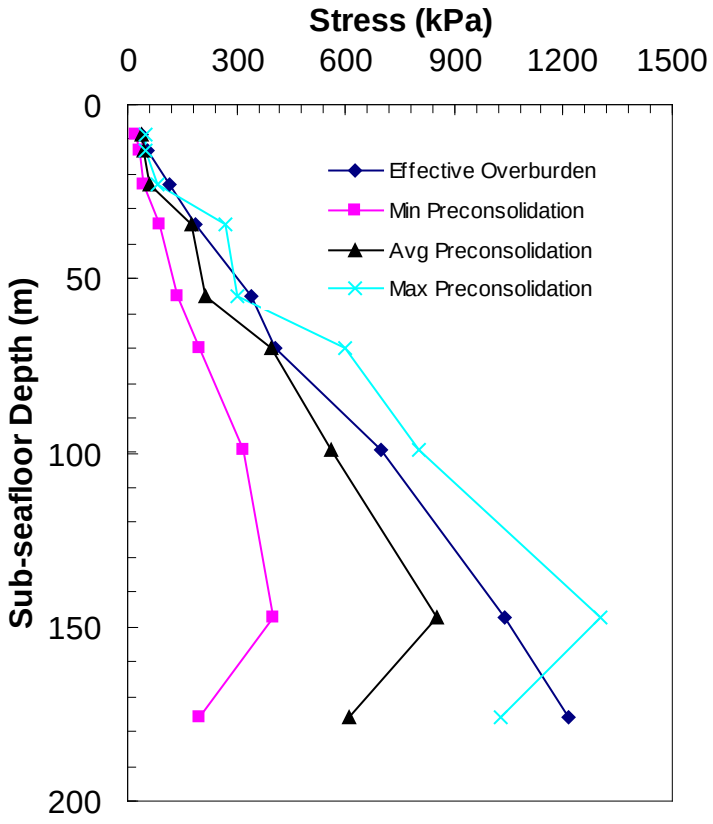

FIG. 4.17. Conditions of consolidation and excess pore-water pressure for Gulf of Mexico sediments from Leg 96, Site 619, Pigmy basin with water depth of ~2260 m (reproduced from Bryant et al., 1985).

The sediment porosity is greatly affected by rock/sediment compressibility and effective pressure. The effect of effective pressure on porosity can theoretically be computed with Eq. 2.

$$\phi = \phi_o . e^{-C_R . P_{eff}} \tag{2}$$

where $ø_o$ is the reference porosity (39.7% and 40.0% for Ottawa sand (U.S. Silica) and GoM (Hart, 1995) respectively), C_R is the rock/sediment compressibility (1.723×10^{-5} psi^{-1} and 4×10^{-5} psi^{-1} for Ottawa sand (Wong and Maini, 2007) and GoM ("Pitfalls," 2005) respectively), and P_{eff} is the effective stress. Figure 4.18 shows how porosity varies with effective stress for Ottawa sand and GoM sediments with and without interstitial water ($C_W = 1 \times 10^{-6}$ psi^{-1}). It is obvious from Fig. 4.18 that the porosity changes for

Ottawa sand or GoM sediments will be negligible for the effective stress of 1200 kPa (174 psi).

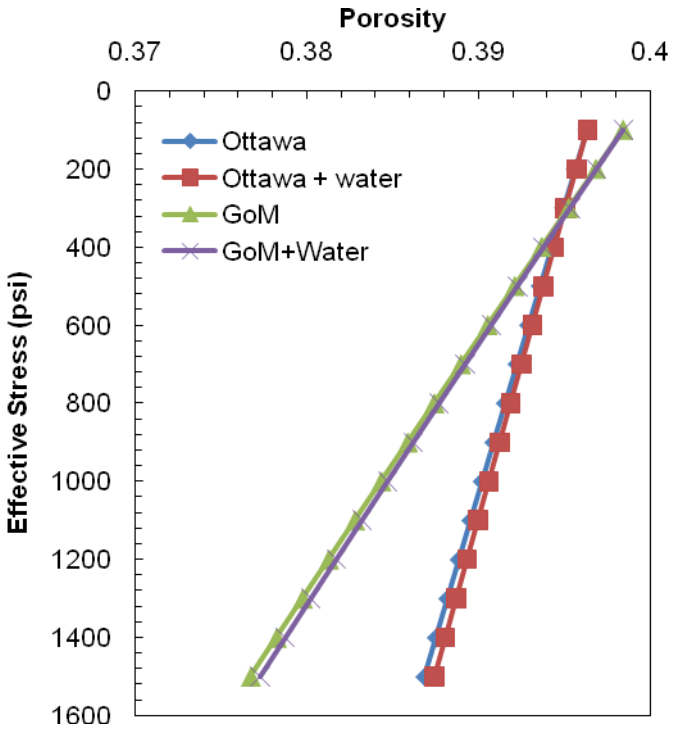

FIG. 4.18. Correlation between effective stress and bulk porosity for Ottawa sand and Gulf of Mexico sediments with and without interstitial water from their compressibility values.

Flemings et al. (2003) calculated the pore-water overpressure with depth at Site 994, 995, 997 using reference porosity ($ø_o$) of 71% from site 994 and bulk compressibility (C_R) of 1.73 x 10^{-3} psi^{-1}. The effect of overburden pressure on porosity of sediments from BLR was computed with Eq. (2) and shown in Fig. 4.19.

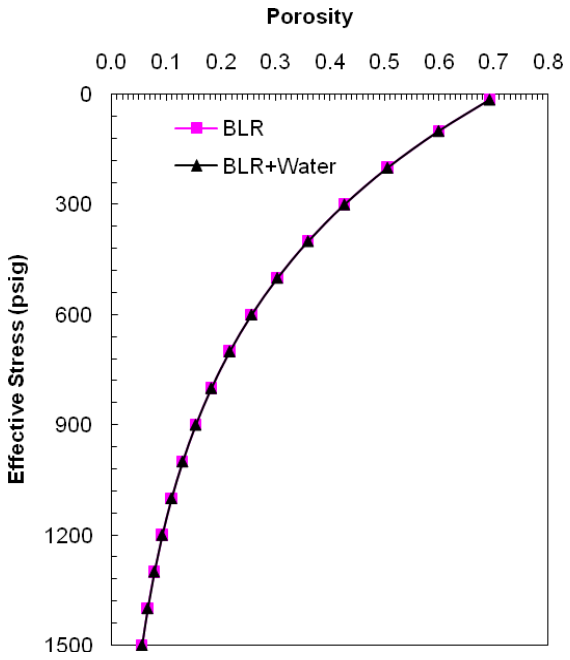

FIG. 4.19. Relation between effective stress and bulk porosity for Blake Ridge sediments with and without interstitial water from their compressibility values.

The effective pressure (P_{eff}) depends upon sediment porosity (ø) and the densities of pore fluids. It can also be computed using Eq. (3) (Ecker et al., 1998).

$$P_{eff} = (1-\phi).(\rho_s - \rho_f).g.h \quad (3)$$

where, ρs and ρf are the solid (grain) and fluid density respectively; h is sub-seafloor depth and g is the acceleration due to gravity. The sediment bulk density is given by Eq. (4).

$$\rho_b = \phi.\rho_f + (1-\phi).\rho_s \quad (4)$$

Upon substituting ρ_s from Eq. (4) into Eq. (3), P_{eff} can be written in terms of bulk density, porosity and pore-fluid density as in Eq. (5).

$$P_{eff} = (\rho_b - \rho_f).g.h \quad (5)$$

The pore-seawater density values were computed for sub-seafloor temperatures at each depth of the KC151 site in GoM. Using sediment bulk density values at KC151 site

reported by Winters et al. (2008), the sub-seafloor effective pressure was computed (Fig. 4.20).

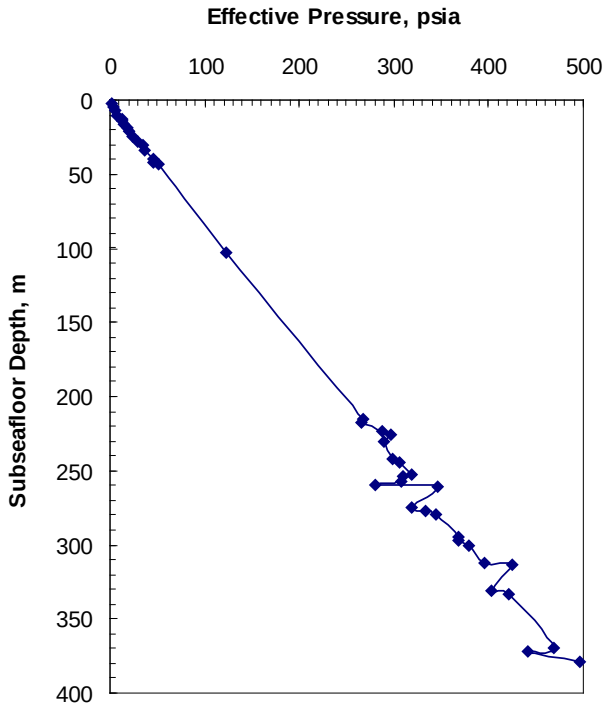

FIG. 4.20. Calculated effective pressure against sub-seafloor depth at Keathley Canyon site in Gulf of Mexico.

4.7 Effect of Confining Pressure on Gulf of Mexico Sediments

The behavior of sediments from GoM under radial compaction and their prospect of water saturation thereafter with a continuous flow system were tested in a Temco cell with a maximum core diameter of 2 inch and length 5.5 inch. For the available 296 mL volume, 568.34 g of a mixture of samples from KC151-3 12C-2 (231.3 mbsf) and 14C-3 (244.9 mbsf) was weighed using its bulk density of 1.92 g/cc. In a rubber sleeve with a 2 inch internal diameter, the packing of sand resulted in occupying 401.3 mL volume which corresponded to a packing density of 1.4154 g/cc. Hence 419 g of sand was loaded in the viton rubber sleeve, which was held in the Temco cell with an assembly of a distributor, a retainer, and an end cap. A radial confining pressure of 1000 psig was applied on the sleeve in 25-50 psi increments with a syringe pump. Once the confining

pressure was stabilized overnight, another syringe pump was utilized in a constant pressure mode to flow water through the sand-core against gravity. After flowing an initial ~5 mL of water through core, the water flow rate suddenly ceased to as low as 0.002 mL/min in spite of an upstream pressure of 200 psig. The upstream pressure as high as ~600 psig of water or even gas did not result into any permeability or cell pressure increase. The compacted and partially water saturated sand-core was removed from the cell and is shown in Fig. 4.21 (a). In another experiment, gravity assisted water drainage was examined through 419 g (301.8 mL) of KC151-3 24C-1 (370.3 mbsf) sediments taken in a 2 inch internal diameter PVC pipe. With 144.6 mL water added on the top of the sand necessary for 100% water saturation, water drainage was observed only up to a half and a 3/4 length of the core after 24 hours (Fig. 4.21(b)) and 48 hours respectively.

It is evident from Fig. 4.21(a) that the bottom part of the core is partially saturated with water. This is congruent with the argument that when sediments of low permeability are compacted, fluid (in this case water) gets trapped in pores (Sayers and den Boer, 2006). The water from fine pores may have exerted pressure on the surrounding hydrostatic pressure (overburden or confining pressure) commonly referred as pore pressure. Due to the limitation on the charging pressure of water/methane to not exceed a value ~100 psi lesser than confining pressure, the subsequent water saturation could not be performed.

This observation is consistent with the earlier reported nature of sub-seafloor sediments at the KC block in GoM from seismic analysis (Snyder et al., 2004). The sediments from 250-500 mbsf at KC site were found to be fine-grained with a low permeability for gas seepage, except in proximity to fault or fracture systems. Francisca et al. (2005) reported the grain diameter of sediments from Green Canyons (GC 185) and Mississippi Canyon (MC752) hydrate locations in GoM where 48% of the sediment is of clay size (<2 μm) or less than 5% of the sediment has a grain diameter >75 μm. Yun et al. (2006) also noted that sediments from KC are significantly more compressible (Cc = 0.735) than sediments at the AT valley (Cc = 0.292). The compressibility index (Cc) is related to the critical slate parameter (λ) as Cc = 2.303 * λ (Wood, 1990). The critical slate parameter (λ) is the slope of the plot of void ratio (e) and ln (P_{eff}'/kPa), where P_{eff}' is

the mean effective pressure. As Cc increases, the void ratio (e) decreases and hence porosity (ø= e/[1+e]) decreases.

Moreover, the KC and AT valley or AT valley mound sites are characterized as being predominantly fine-grained (4-1 μm), composed of mostly (66-85%) clay-sized particles (Hangsterfer et al., 2008). This is also supported by a characterization study of sediments from KC site where %clay composition ranged between 42.79 and 92.58 % (Winters et al., 2008). As the percentage of clay gets higher in sediments (average particle diameter: ~1.5 μm) - sand mixture, the hydraulic permeability decreases significantly due to the smaller pores. The higher percentage of clay (range: 43-65.3%) is also evidenced in sub-seafloor core samples from ODP Leg 204 in Cascadia margin (Pińero et al., 2007).

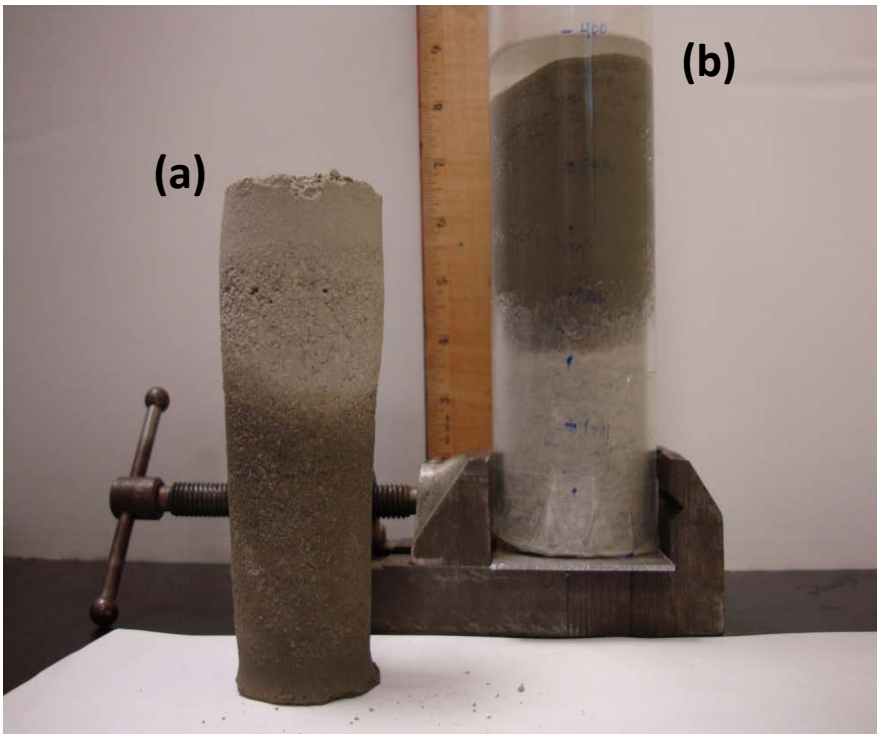

FIG. 4.21. (a) Gulf of Mexico KC151-3 1H-7, 70-80 after 1000 psig radial overburden and partial water saturation. (b) Gulf of Mexico KC151-3 24C-1, 419 g in 2 inch diameter PVC pipe, water drainage front after ~24 hours.

Chapter 5

Formation and Dissociation of Methane Hydrates from Pure Water in Consolidated Sand

5.1 Consolidated Core Studies with Pure Water – Experimental Conditions

Temco's DCHR-series hassler-type core holder was utilized to study the kinetics of methane hydrate formation/dissociation in consolidated sediments which simulated the geothermal conditions much below the seafloor. The core sample (2 inch in diameter and 0-6 inch long) was held within a rubber sleeve by radial confining pressure. The fluids and gases were injected through distribution plugs. The unique arrangement of pressure ports along the length of the core enabled the measuring of a radial and axial temperature profile within the core during hydrate formation/dissociation. During runs, conditions of overburden pressure (confining pressure) and pore pressure-temperature (PT) were varied.

In the hydrate formation/dissociation runs, 99.99% pure methane gas was charged at controlled flow rate (< 2000 mL/min) through a porous disk (2 inch diameter, 1/4 inch thick, 50 μm pore size) placed above and below the core. Three type J, 1/16 inch diameter thermocouples were installed at 1, 3, and 5 inch along the core length as shown

in Fig. 5.1. The effect of overburden pressure on hydrate formation and dissociation kinetics was investigated with Ottawa sand obtained from the US Silica Company. The operational conditions for runs (1-7) with Ottawa sand are listed in Table 5.2. With 1300 psig confining pressure on Ottawa sand-pack maintained at experimental temperature with a surrounding bath cooled; methane gas was charged up to desired pressure at flow rates <2000 mL/min. After charging methane gas, hydrate formation PT kinetics was monitored with time until pore pressure asymptoted at hydrate equilibrium pressure at the core temperature.

Table 5.1. Ottawa sand-core conditions for hydrate formation/dissociation Runs 1-13 with pure water.

Core holder	Temco DCHR-2.0 w/ 3 temperature ports
Core holder volume	308.9 mL
Core diameter	2 inch
Core length	6 inch
Sediment	462.42 g of Ottawa Sand F110 (average grain diameter – 110 μm)
Sediment density	1.625 g/cc
Volume of two ceramic filters	24.3 mL
Volume of sand	284.6 mL
Water saturation	~100%

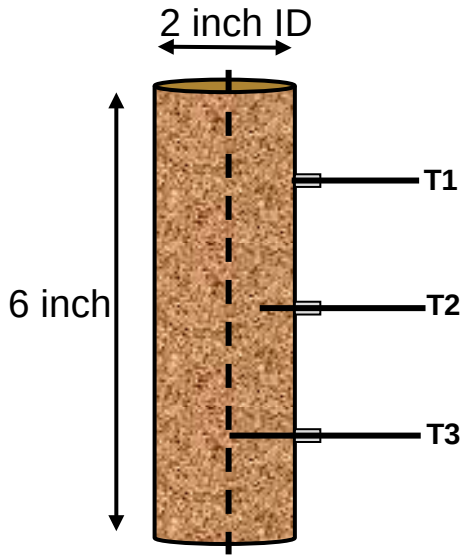

FIG. 5.1. Thermocouple locations (edge-T1, half-radius–T2 and center–T3) within the Ottawa sand-core for hydrate formation/dissociation Runs 1-10 with pure water.

Table 5.2. Summary of operational conditions (pressure, temperature, flow) of hydrate formation/dissociation Runs 1-7 with pure water and methane charging into a pre-cooled cell.

Run #	Core conditions P, psig	T,°C	Confining pressure psig	Methane flowrate mL/min	Formation events	Dissociation ΔP from equilibrium P psig
1	1200	4	1300	<1950	1	100-200
2	1200	4	1300	<2000	1	P_{eqm}
3	1200	4	1300	<1871	1	100-200
4	1200	4	1300	<1916	2	100
5	1200	4	1300	<1677	2	200
6	1200	2	1300	<1594	2	200
7	1200	2	1300	<1759	2	100

5.2 Results and Discussions

5.2.1 Formation and Dissociation Kinetics of Methane Hydrates Formed with Methane Charging into a Pre-cooled Sand-core

5.2.1.a Preliminary Runs (1-3) Outcome

Figures 5.2, 5.3, 5.4 show cell pressure and temperature profiles as a function of time during methane charging (a) and hydrate formation (b) events. The plots on the left are PT conditions that accompany the initial methane charging (first 100 minutes) followed by the entire hydrate formation event over 100 hours. The pressure for hydrate formation stabilized at 568, 552 and 565 psig, respectively for the three runs after ~60 hours of operation. The equilibrium pressure values for pure methane hydrate were calculated from the CSMGem at experimental temperatures of 4.02, 4.17, and 4.07^{o}C are 549, 557, and 552 psig, respectively. The exothermic temperature spikes observed by all thermocouples (Figs. 5.2(a), 5.3(a), and 5.4(a)) were due to a combined effect of pressurization and hydrate formation. As expected, the top thermocouple (T1) asymptoted first to the bath temperature (~4^{o}C) after charging. However, the bottom thermocouple (T3) showed a lower value than that for the middle thermocouple (T2) though the bottom one was placed at the center of the core. This was due to its proximity to higher conductive stainless-steel bottom distribution plug.

The hydrate dissociation was performed with stepwise depressurization. Figures 5.5(a) and 5.5(b) represent the decomposition runs associated with the formation Runs 1 and 3 respectively. Figure 5.5 depicts the amount of cooling due to hydrate dissociation reaching to a zero-slope at the point of maximum temperature depression. As observed during methane charging, the core surface temperature (T1) reached bath temperature first. Similarly, the proximity of bottom thermocouple (T3) to the distribution plug made it gain heat from the bath faster than the thermocouple at the half-radius of the core (T2). The temperature depression due to hydrate dissociation was highest for T3, which indicates higher hydrate saturation at the center of the core than that at the wall. Moreover, the lower slope of the temperature depression curve for the thermocouple

placed at the center of the core (T3) than that at the half-radius of the core suggests that the dissociation front moves outward from the center of the core.

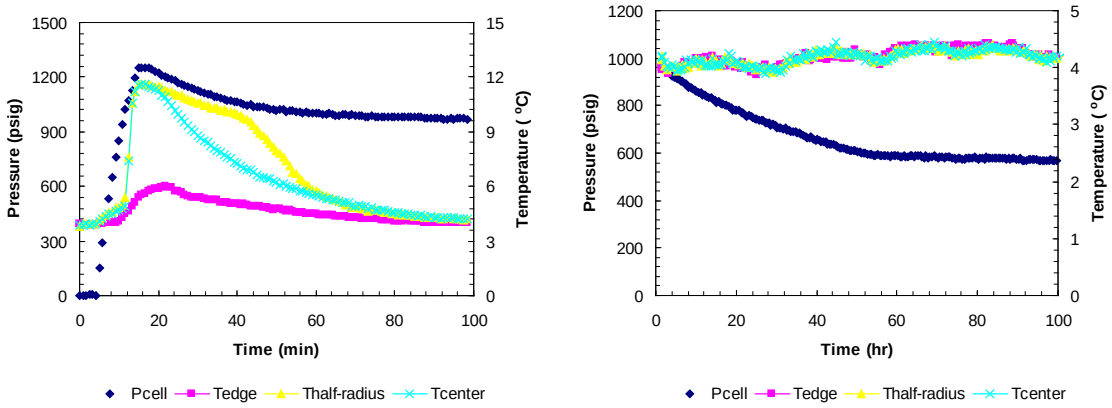

(a) **(b)**

FIG. 5.2. Cell pressure and temperatures within the sand-core (edge–T1, half-radius–T2 and center–T3) against time during (a) methane charging and (b) subsequent hydrate formation for Run 1.

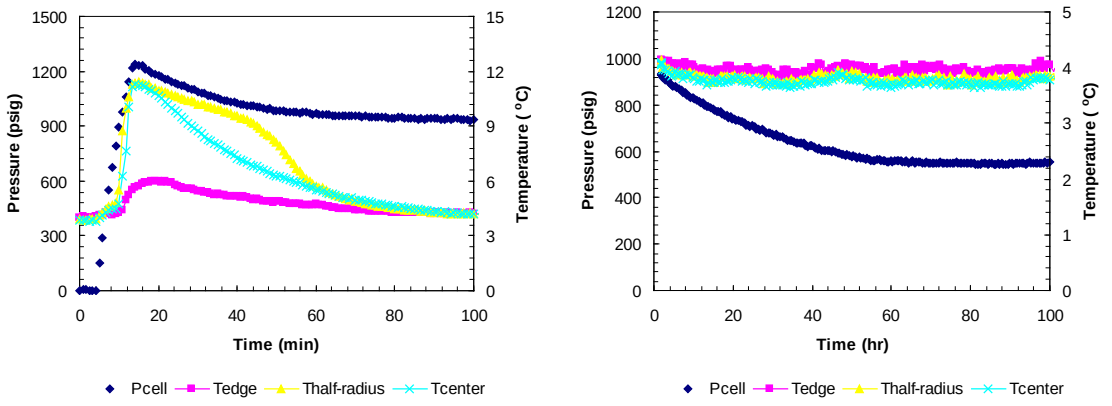

(a) **(b)**

FIG. 5.3. Cell pressure and temperatures within the sand-core (edge–T1, half-radius–T2 and center–T3) against time during (a) methane charging and (b) subsequent hydrate formation for Run 2.

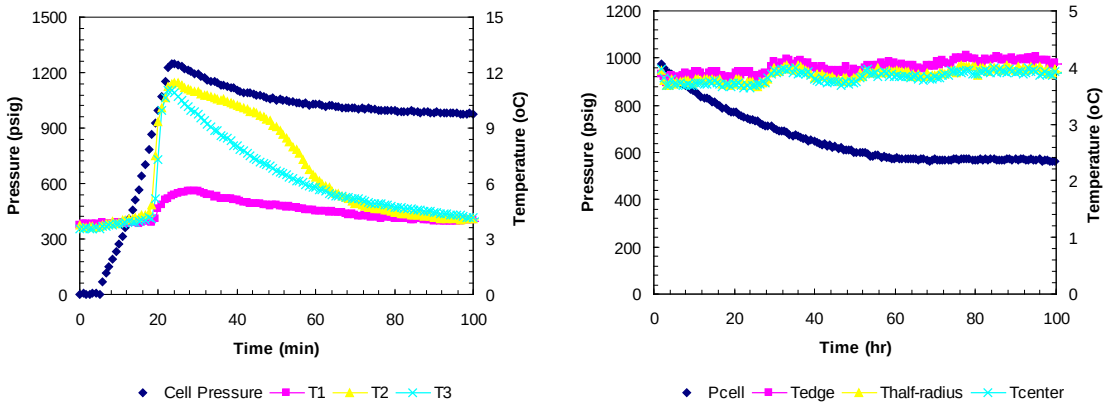

(a) **(b)**

FIG. 5.4. Cell and temperatures within the sand-core (edge–T1, half-radius–T2 and center–T3) against time during (a) methane charging and (b) subsequent hydrate formation for Run 3.

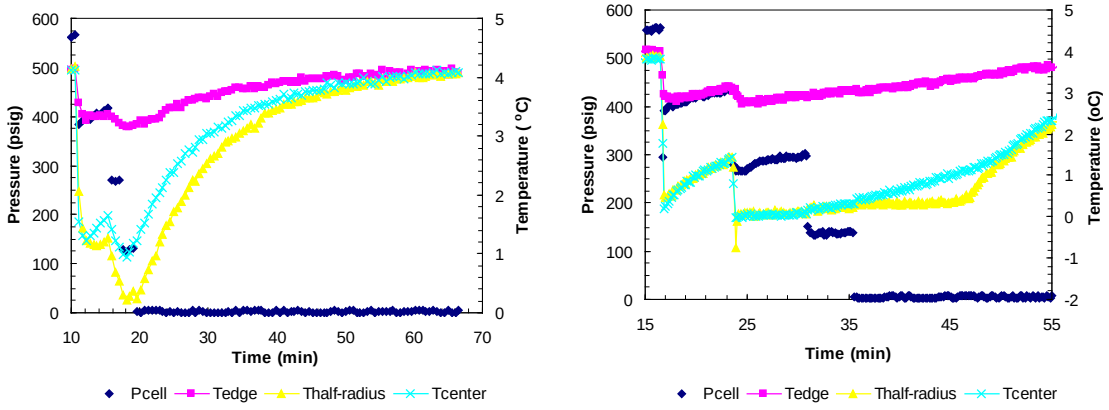

(a) **(b)**

FIG. 5.5. Cell pressure and temperatures within the sand-core (edge–T1, half-radius–T2 and center–T3) against time during hydrate dissociation for (a) Run 1 and (b) Run 3.

5.2.1.b Runs (4-7) Outcome

In the subsequent set of runs (4-7) as well, 462.42 g of Ottawa sand was utilized at similar experimental conditions as mentioned in Table 5.2, except the experimental temperature was varied to ~2^{o}C for Runs 6 and 7. During hydrate formation, the pore pressure asymptoted at equilibrium pressure (~547 psig) after 70 hours (Fig. 5.6). An

additional formation event (Fig. 5.7), which lasted another 140 hours, was carried out by re-pressurizing the cell from the equilibrium pressure to 1200 psig.

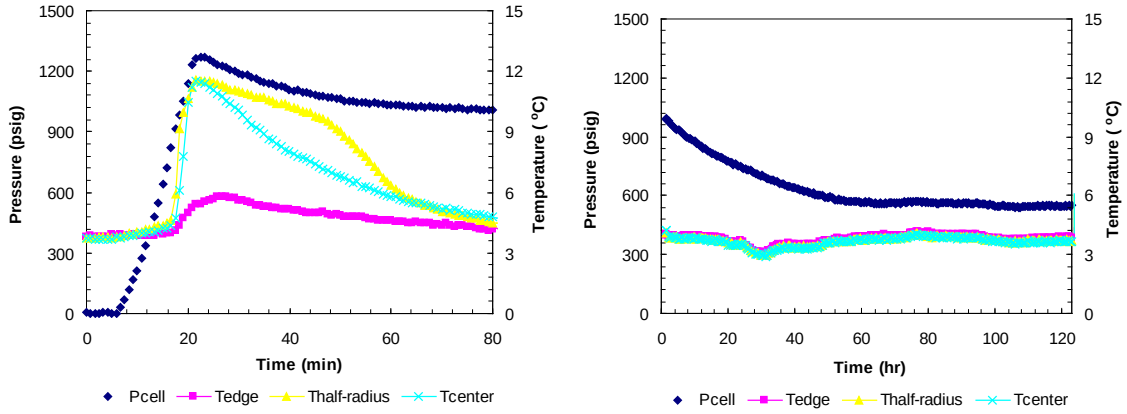

(a) **(b)**

FIG. 5.6. Cell pressure and temperatures within the sand-core (edge–T1, half-radius–T2 and center–T3) against time during (a) methane charging and (b) subsequent hydrate formation for Run 4.

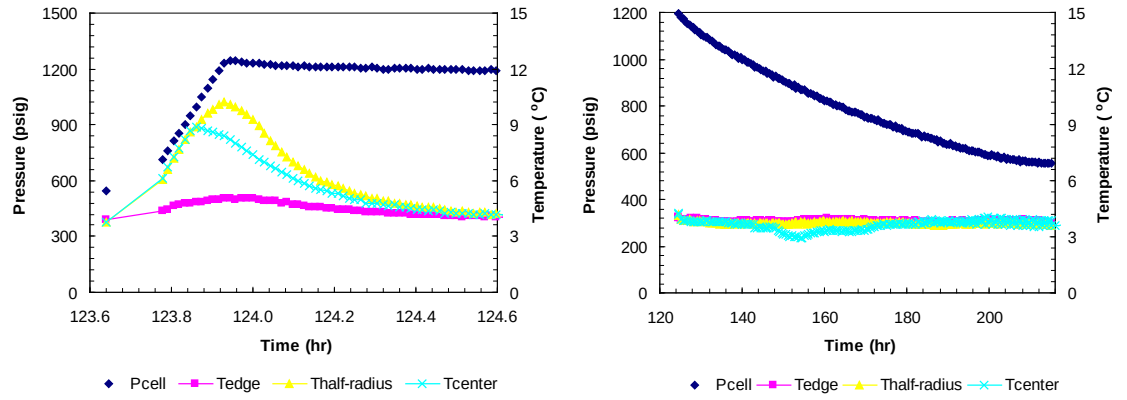

(a) **(b)**

FIG. 5.7. Cell pressure and temperatures within the sand-core (edge–T1, half-radius–T2 and center–T3) against time during (a) second charging and (b) subsequent hydrate formation for Run 4.

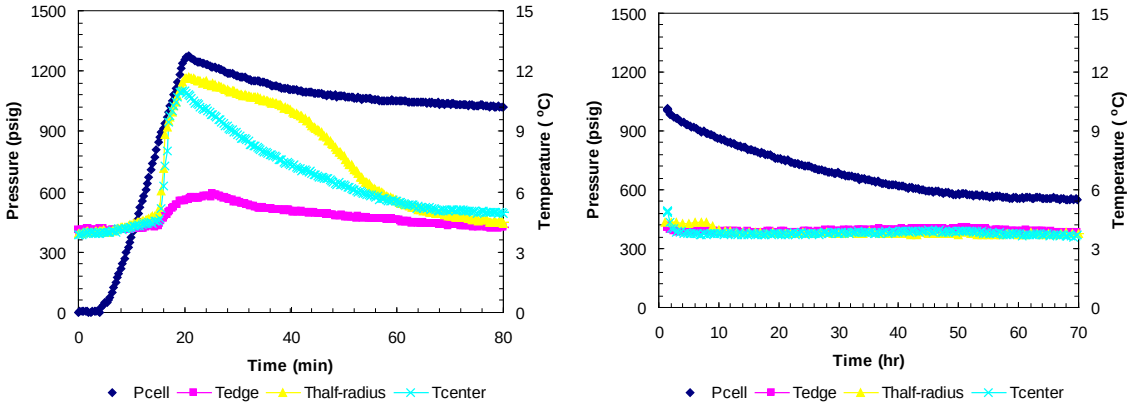

(a) **(b)**

FIG. 5.8. Cell pressure and temperatures within the sand-core (edge–T1, half-radius–T2 and center–T3) against time during (a) methane charging and (b) subsequent hydrate formation for Run 5.

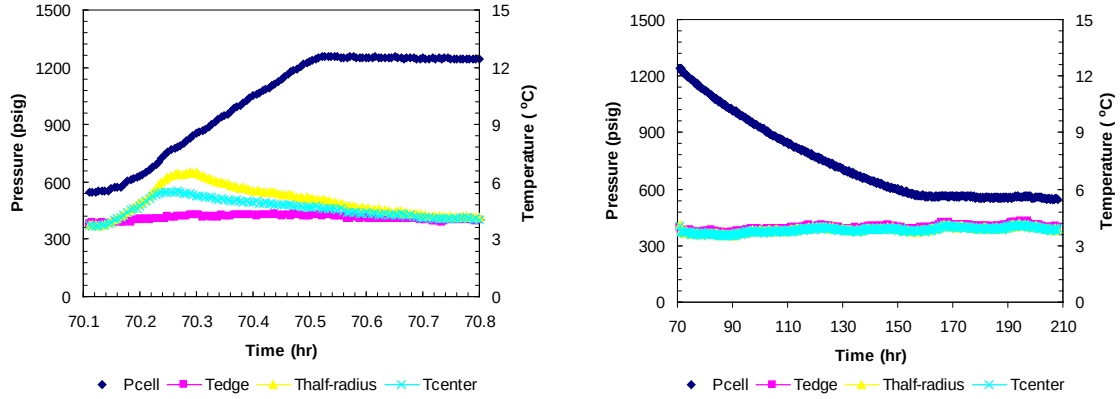

(a) **(b)**

FIG. 5.9. Cell pressure and temperatures within the sand-core (edge–T1, half-radius–T2 and center–T3) against time during (a) second charging and (b) subsequent hydrate formation for Run 5.

Following the second hydrate formation, the pore pressure was again raised above the hydrate stability region. This served as more control over the cell pressure and voided immediate hydrate dissociation as additionally charged methane filled the tubing between the cell outlet valve and downstream back-pressure regulator upon opening the

cell outlet. Once the cell PT equilibrated (after ~30 minutes), the dissociation was carried out by the step-wise depressurization technique.

Depressurization was achieved in a series of equal pressure drops (100 and 200 psi) from equilibrium pressure (~530 psig) at a bath temperature of 3.7^{o}C. The first pressure drop of 100 psi resulted in a cell pressure of 479 psig (Fig. 5.10(a)), and the sediment temperature dropped as low as 1.9^{o}C. The gas evolved during the dissociation was metered and plotted against time (Fig. 5.10(b)). Once gas output dropped to zero, the outlet valve was closed and the sample was allowed to equilibrate while the cell pressure gradually rose to the equilibrium pressure at the bath temperature (3.7^{o}C). The temperature at the outer thermocouple (T1) increased quickly towards the bath temperature along with the cell pressure. However, the temperature in the core center (T3) and the half-radius (T2) rose at much slower rate. Upon dissociation to 362 psig, the temperature in the sample (T2 & T3) dropped to -0.4^{o}C. Once again, after quantifying the output gas, the sample was allowed to equilibrate where all thermocouples followed a similar profile as in the first dissociation step. The next depressurization to 267 psig also lowered the sample temperatures (T2 & T3) near 0.01^{o}C. However the cell pressure rose only up to 282 psig. Furthermore, the pressure drops (153 and 0 psig) showed no endothermic behavior confirming complete methane hydrate dissociation in the first three steps. Figure 5.11 shows cumulative gas produced in each dissociation step, which lasted about 30 seconds.

After each dissociation step response, the outlet valve was closed and the sediment was allowed to warm up to bath temperature. This allowed dissociation at a constant sediment temperature. Figure 5.12 shows post-depressurization PT equilibrium for 3 pressure drops in Run 4. When compared with the PT equilibrium data for pure methane hydrate established with CSMGem (Ballard and Sloan, 2002), it is clear that the first two post-depressurization PT equilibrium curves follow the theoretical methane hydrate PT stability curve but on the higher pressure side (Fig. 5.12).

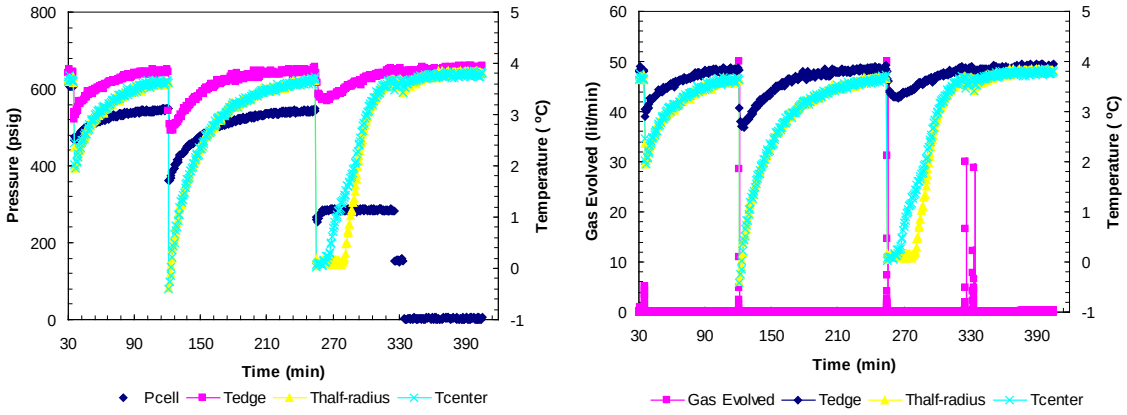

FIG. 5.10. (a) Cell pressure and (b) gas evolved with temperatures within the sand-core (edge–T1, half-radius–T2 and center–T3) against time during dissociation with increments of 100 psi pressure drops from equilibrium pressure in Run 4.

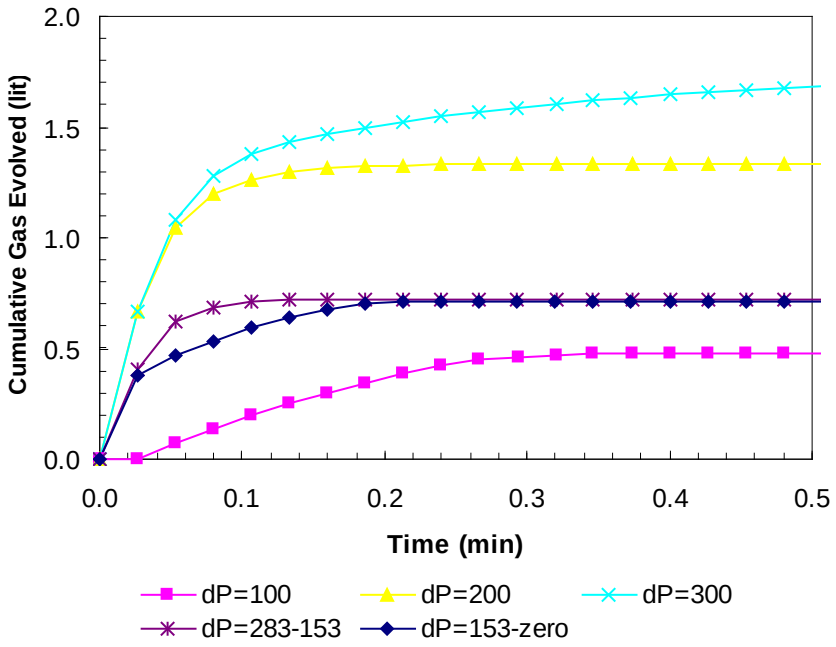

FIG. 5.11. Cumulative gas produced against time for incremental pressure drops during hydrate dissociation in Run 4.

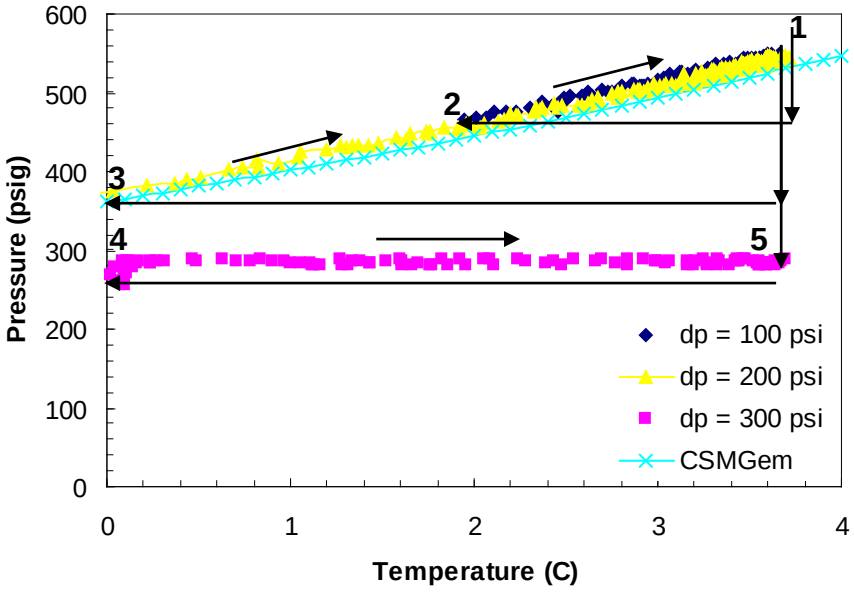

FIG. 5.12. Post-depressurization equilibrium pressure against core-center temperature conditions of methane hydrates in porous media for Run 4. Each plot corresponds to core conditions during thermally induced dissociations after each depressurization step. Equilibrium conditions of bulk methane hydrates were obtained from CSMGem.

For the present methane, water, and F110 Ottawa sand system, the Kozeny's equation (Eq. 1) for mean pore diameter (d_p) based on porosity (Ø) value of 39.70% at 1300 psig overburden pressure and the particle size (d_g) of 110 µm, yields an approximate mean pore diameter of 48.28 µm.

$$d_p = \frac{2}{3}.\frac{\Phi}{1-\Phi}.d_g \tag{1}$$

Myers et al. (1941) performed capillary rise experiments with sands and deduced the empirical relationship between mean grain diameter (d_g) in mm and effective pore radius (r_p) in mm as shown in Eq. 2. For Ottawa sand of 110 µm (0.11 mm) grain diameter, the effective pore diameter came out to be 58.65 µm.

$$r_p = \frac{1}{2}.\left(\frac{d_g}{2.4}\right)^{0.92} \tag{2}$$

The excess pore pressure for the first two post-depressurization PT equilibrium curves than that of the phase stability pressure of bulk methane hydrates was due to the confined pore spaces. The excess pore pressure observed for the present Ottawa sand-water-hydrate system (pore radii: 48-58 μm) was minimal when compared to the phase stability of methane hydrates in 14 nm pore radii sized silica gel (Hand and Stupin, 1992) (Fig. 5.13).

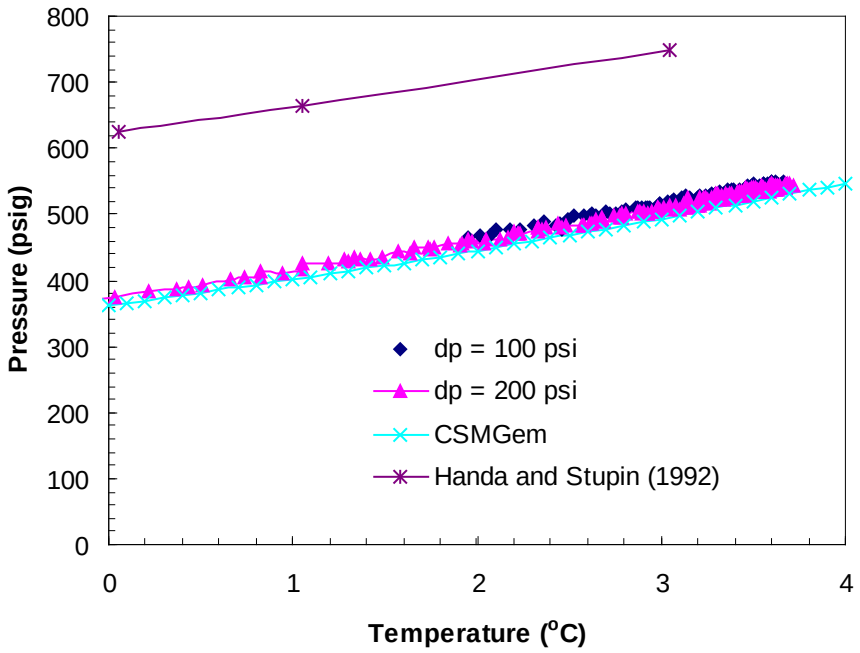

FIG. 5.13. Post-depressurization equilibrium pressure against core-center temperature conditions of methane hydrates in porous media for Run 4. Each plot corresponds to core conditions during thermally induced dissociations after each depressurization step. Equilibrium conditions of bulk methane hydrates were obtained from CSMGem.

The thermocouple readout profile during dissociation is shown in Fig. 5.14. The temperatures at the lateral and the radial positions within the sample were monitored with thermocouples placed at the outer core surface (T1), half-way radius (T2) and the center of the core (T3). The data in Figure 5.14 show that hydrates start to dissociate from the center of the sample towards the walls. This behavior differs from the previously reported thermal dissociation, which radially moves inwards from the vessel wall (Kneafsey et al., 2004).

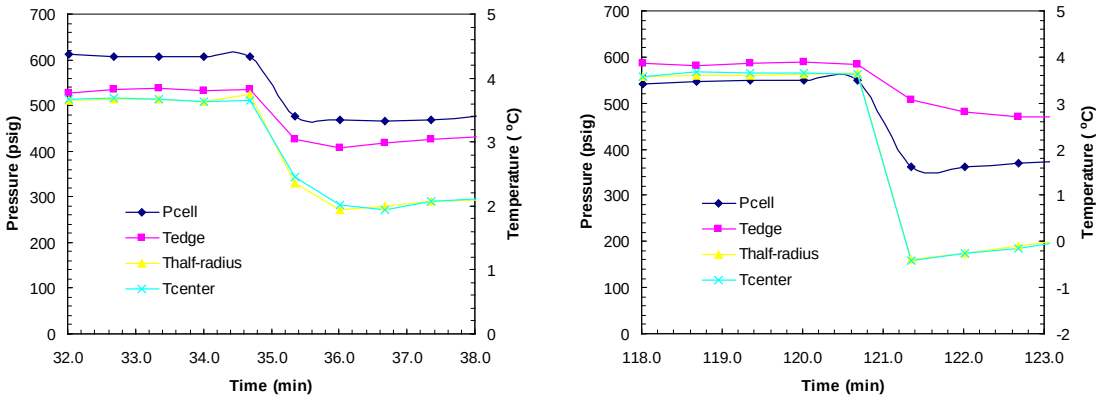

FIG. 5.14. Thermocouple responses at various core locations within the sand-core (edge–T1, half-radius–T2 and center–T3) during dissociation with (a) 100 psi and (b) 200 psi drops below hydrate equilibrium pressure in Run 4.

In the Run 5, with similar formation conditions, the dissociation was observed for 200 psig pressure drops once the cell reached PT equilibrium (523 psig, 3.92ºC) at the end of formation. The PT responses plotted against time (Fig. 5.15(a)) look similar to the one at 100 psi dissociation. The hydrate dissociation due to the first pressure drop resulted in a sediment temperature as low as -0.08ºC which is ~2^{o}C lower than that observed at the 100 psi pressure drop. Once the system reached equilibrium again at 545 psig at 4ºC after ~3 hours, the pressure was dropped to 120 psig and a temperature as low as -0.46ºC. Following the second dissociation step, the cell did not return to PT conditions, confirming complete hydrate dissociation. Subsequently, the cell pressure was lowered from 112 psig to 0 psig with negligible change in sediment temperature.

The cumulative gas evolved from the cell versus time is shown in Fig. 5.15(b). During the first and second depressurization of Run 4 (Fig. 5.10(b)) and the first depressurization of Run 5 (Fig. 5.15(b)), the instantaneous flow rate was recorded as high as 50 L/min, the maximum flow rate value for the outlet flow meter. Hence the cumulative gas output values reported may be under-stated.

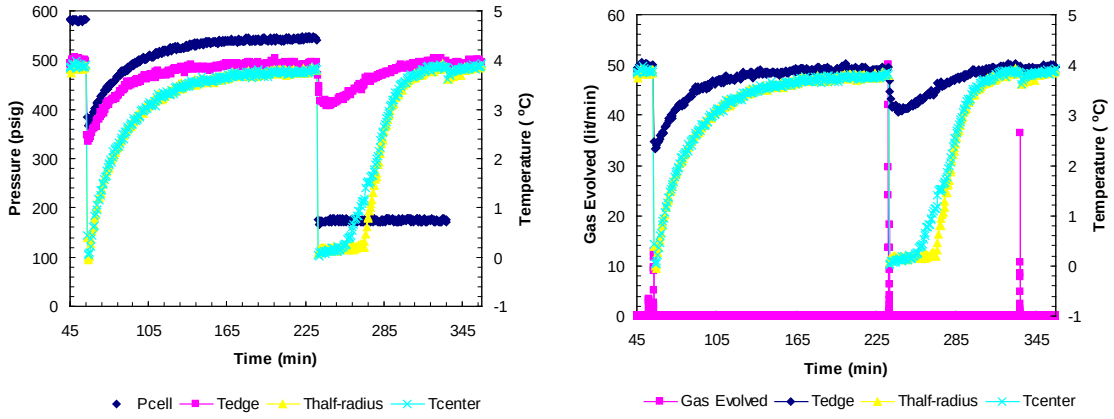

(a) **(b)**

FIG. 5.15. (a) Cell pressure and (b) gas evolved with temperatures within the sand-core (edge–T1, half-radius–T2 and center–T3) against time during dissociation with increments of 200 psi pressure drops from equilibrium pressure in Run 5.

The faster temperature drops at the center of the cell (T3) and half-radius (T2) (Fig. 5.16) than that at the core wall (T1) during dissociation due to the 200 psi pressure drop in Run 5 confirms that the hydrate dissociation front indeed starts from the center towards the wall.

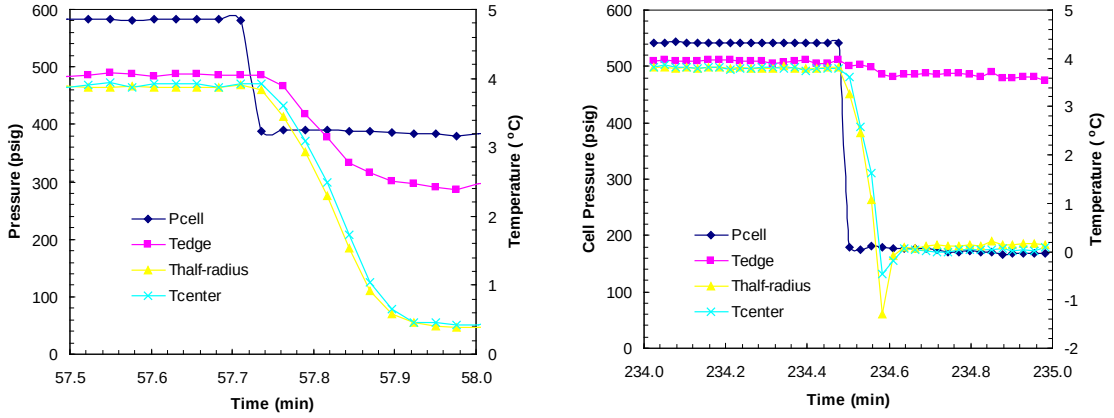

(a) **(b)**

FIG. 5.16. Thermocouple responses at various core locations within the sand-core (edge–T1, half-radius–T2 and center–T3) during dissociation with (a) 200 psi and (b) 400 psi drops below hydrate equilibrium pressure in Run 5.

Using the Clausius-Clapeyron equation (Eq. 3), the enthalpy of dissociation (ΔH_{hyd}) was calculated by plotting lnP against 1/ [TZR] where P is cell pressure, T is core-center temperature (core center), Z is compressibility of methane at PT estimated using the Redlich-Kwong-Soave equation of state and R is universal gas constant. The results are shown in Fig. 5.17 for each post-depressurization from Run 4 (49.14 kJ/mol, 58.524 kJ/mol) and Run 5 (59.134 kJ/mol). Although these values agree well with the theoretical enthalpy of dissociation value (62.6 kJ/mol) computed from equilibrium PT values derived with CSMGem, the effect of porous media on ΔH_{hyd} is evident. Porous media has been found to lower the enthalpy of dissociation for methane hydrates. Hand and Stupin (1992) found the enthalpy of dissociation of methane hydrates to be 45.19 kJ/mol in porous silica gel having a mean pore diameter of 14 nm.

$$\ln\left(\frac{P_2}{P_1}\right) = \frac{\Delta H_{hyd}}{Z.R}\left(\frac{1}{T_1} - \frac{1}{T_2}\right) \tag{3}$$

The methane hydrate formation conditions of Run 6 and 7 were identical to those employed in Run 4 and 5 except the core temperature was 2^oC. Table 5.2 summarizes the operational conditions of Runs 1-7. After initial charging (Fig. 5.18(a)), the pore pressure asymptoted at the hydrate equilibrium pressure of 463 psig at the core temperature of ~1.8^oC after 90 hours (Fig. 5.18(b)). Note that the previous run at 4^oC and 1200 psig initial pressure took 70 hours to reach the hydrate equilibrium. The second formation event (Fig. 5.19) lasted for 130 hours when the cell was re-pressurized to 1200 psig.

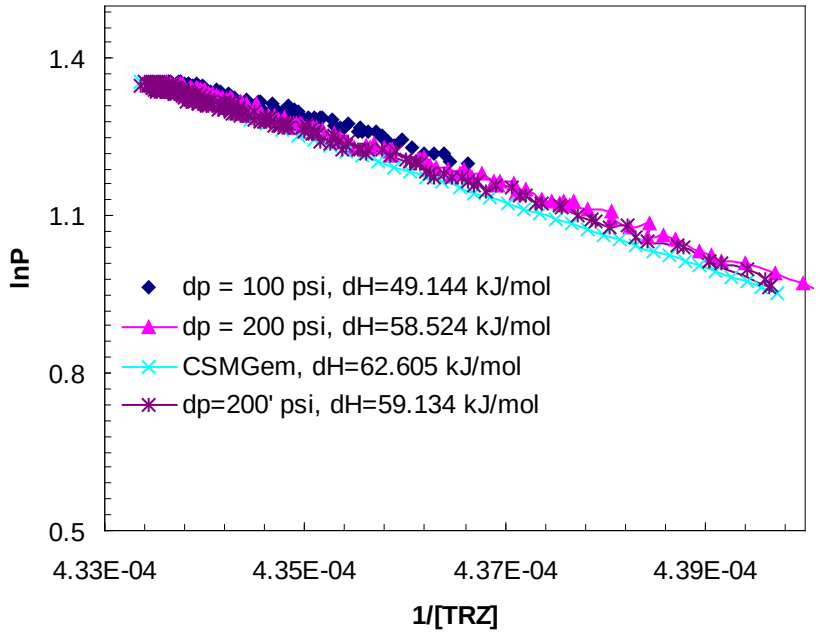

FIG. 5.17. Post-depressurization equilibrium pressure (lnP) against core-center temperature (1/[TRZ]) for Runs 4 (dp = 100, 200 psi) and 5 (dp = 200’ psi). The Clausius-Clapeyron equation was used to calculate the enthalpy of dissociation (ΔH_{hyd}) of methane hydrates in porous media at a confining pressure of 1300 psig. Equilibrium conditions of bulk methane hydrates obtained from CSMGem were used to calculate the theoretical ΔH_{hyd}.

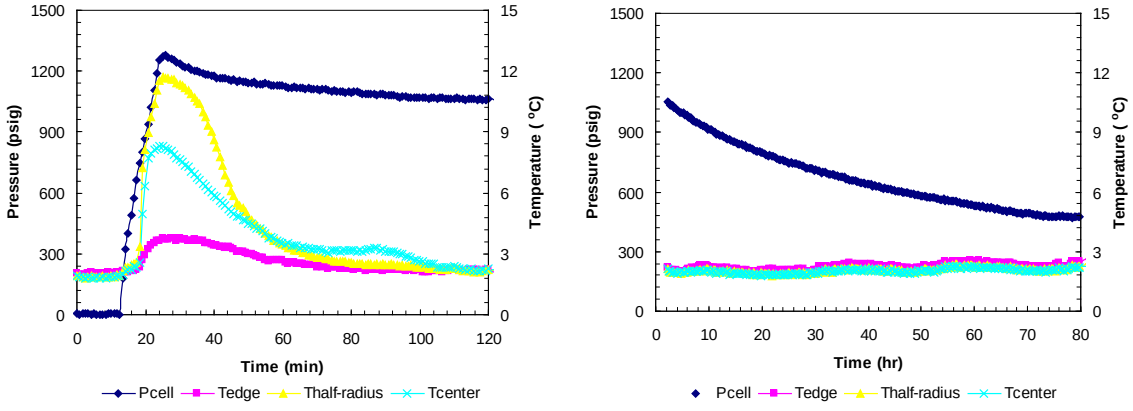

(a) **(b)**

FIG. 5.18. Cell pressure and temperatures within the sand-core (edge–T1, half-radius–T2 and center–T3) against time during (a) methane charging and (b) subsequent hydrate formation for Run 7.

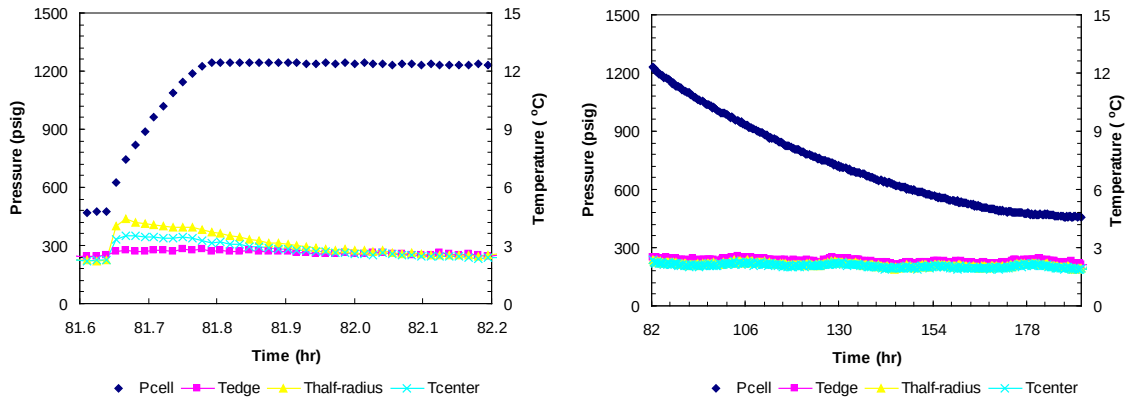

(a) **(b)**

FIG. 5.19. Cell pressure and temperatures within the sand-core (edge–T1, half-radius–T2 and center–T3) against time during (a) second charging and (b) subsequent hydrate formation for Run 7.

Following the second hydrate formation, additional methane (measured at 1734 mL) was charged to increase the pore pressure above the hydrate stability region. This gave more control over the cell pressure and avoided immediate hydrate dissociation as additionally charged methane filled the tubing between the cell outlet valve and downstream back-pressure regulator upon opening the cell outlet. However, in spite of having upstream line pressure as high as 1000 psig, the cell pressure did not rise above 580 psig during Run 7. This is due to a classical problem with methane hydrates- plugged lines near the cell entry.

The dissociation in Run 6 was carried out with 200 psig pressure drops once the cell reached the PT equilibrium after a second hydrate formation event. The hydrate dissociation due to the first 200 psi pressure drop resulted in a temperature as low as -0.88ºC (Fig. 5.20(a)), which is ~2^{o}C lower than that observed for the 70 psi pressure drop. Once the system reached equilibrium at 435 psig at 2ºC after ~2.5 hours, the pressure was decreased to 48 psig with a temperature as low as -0.46ºC. Following the second dissociation step, the cell did not return to equilibrium PT conditions. It is to be noted that the system was unable to return to methane hydrate equilibrium pressure at the bath temperature of ~2^{o}C, suggesting that all methane hydrates had already dissociated.

The instantaneous gas evolved from the cell for each pressure drops (200 and 400 psi) are plotted with time in Fig. 5.20(b).

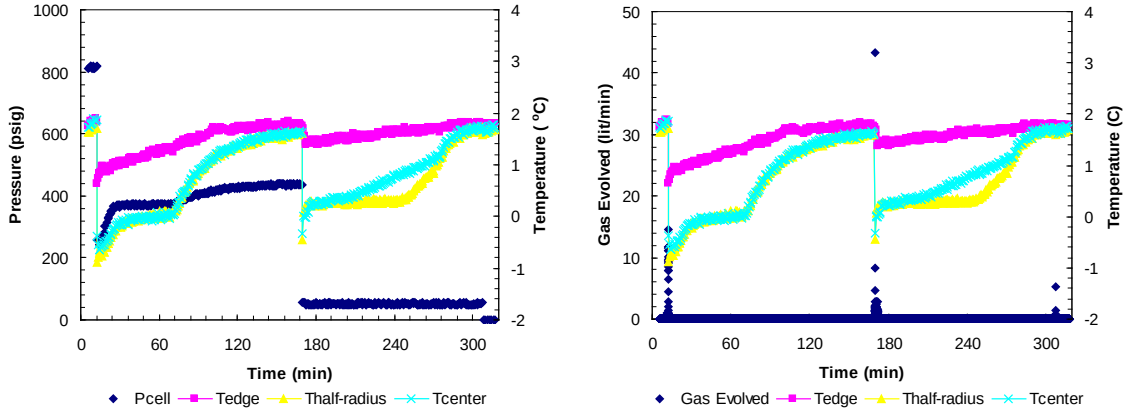

(a) **(b)**

FIG. 5.20. (a) Cell pressure and (b) gas evolved with temperatures within the sand-core (edge–T1, half-radius–T2 and center–T3) against time during dissociation with increments of 200 psi pressure drops from equilibrium pressure in Run 6.

The depressurization in Run 7 was achieved in a series of equal pressure drops (70 psi) from the equilibrium pressure (~449 psig) at the bath temperature of 2.1^{o}C. The first pressure drop of 70 psi resulted in the new cell pressure of 382 psig (Fig. 5.21(a)), and the sediment temperature dropped as low as -0.08^{o}C. The instantaneous gas evolved during the dissociation was metered and plotted against time (Fig. 5.21(b)). Once an instantaneous gas output dropped to zero, the outlet valve was closed and the sample was allowed to equilibrate where the cell pressure gradually rose while cell temperature rising up to the bath temperature (2.05^{o}C). However, as soon as the cell pressure increased above the hydrate stability region, additional gas (~1734 mL) charged caused momentary hydrate formation as noted by the exothermic temperature spike. The second pressure drop of 170 psi resulted in a temperature drop of up to -0.45^{o}C (Fig. 5.21(a)) and an instantaneous gas output of ~5 L/min (Fig. 5.21(b)). During subsequent dissociation, only the first pressure drop of ~270 psi (from P_{eqm} = 453 psig at 1.9^{o}C) exhibited an endothermic behavior due to hydrate dissociation. This confirms complete methane hydrate dissociation in the first three steps. The following dissociations were purely of the gas phase as there was no appreciable change in temperature during discharging.

During depressurization 4^{o}C, the instantaneous flow rates were recorded as high as 50 L/min. However the dissociations from 2^{o}C (Fig. 5.20(b), 5.21(b)) did not result into the instantaneous flow rates of >15 L/min.

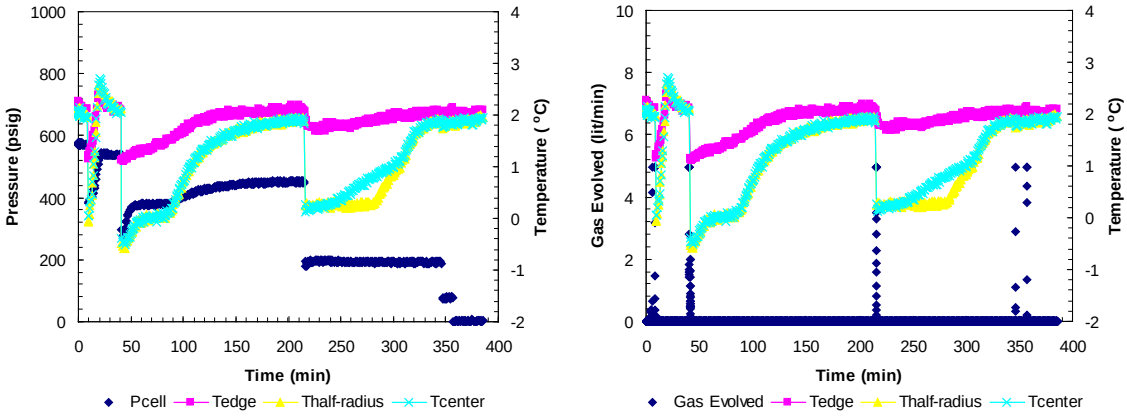

(a) **(b)**

FIG. 5.21. (a) Cell pressure and (b) gas evolved with temperatures within the sand-core (edge–T1, half-radius–T2 and center–T3) against time during dissociation with varying pressure drops from equilibrium pressure in Run 7.

Figure 5.22 shows post-depressurization PT equilibrium after each dissociation step for 3 pressure drops. When compared with the PT equilibrium for pure methane hydrate established with the CSMGem (Ballard and Sloan, 2002), it is clear that the first two post-depressurization PT equilibriums follow the theoretical methane hydrate PT stability curve. The cumulative gas evolved from the cell is plotted against time in Fig. 5.23. As pressure drop increases, the cumulative gas evolved increases.

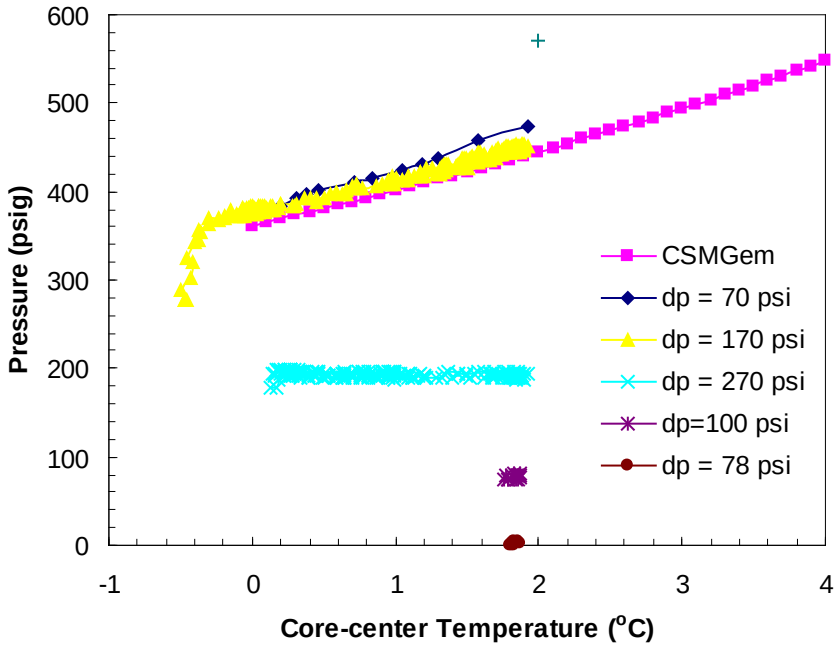

FIG. 5.22. Post-depressurization equilibrium pressure against core-center temperature conditions of methane hydrates in porous media for Run 7. Each plot corresponds to core conditions during thermally induced dissociations after each depressurization step. Equilibrium conditions of bulk methane hydrates were obtained from CSMGem.

The temperatures at the lateral and the radial positions within the sample during dissociation were monitored with thermocouples placed at the outer core surface (T1), half-way radius (T2) and the center of the core (T3). The data in Figure 5.24 confirms that hydrates start to dissociate from the center of the sample towards the walls. This behavior is consistent with earlier observations but differs from observations by Kneafsey et al. (2004) where the dissociation front moved radially inwards from the vessel wall.

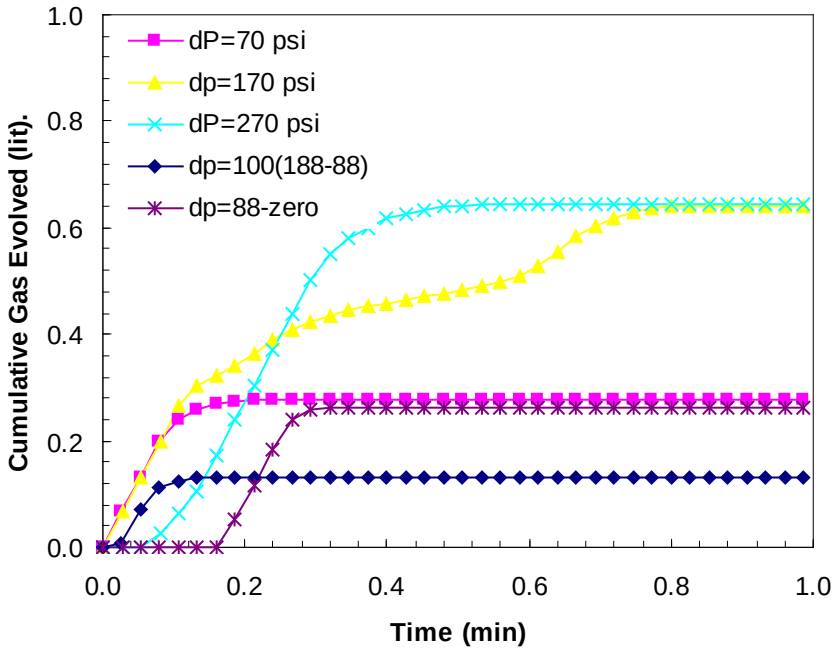

FIG. 5.23. Cumulative gas produced against time for incremental pressure drops during hydrate dissociation in Run 7.

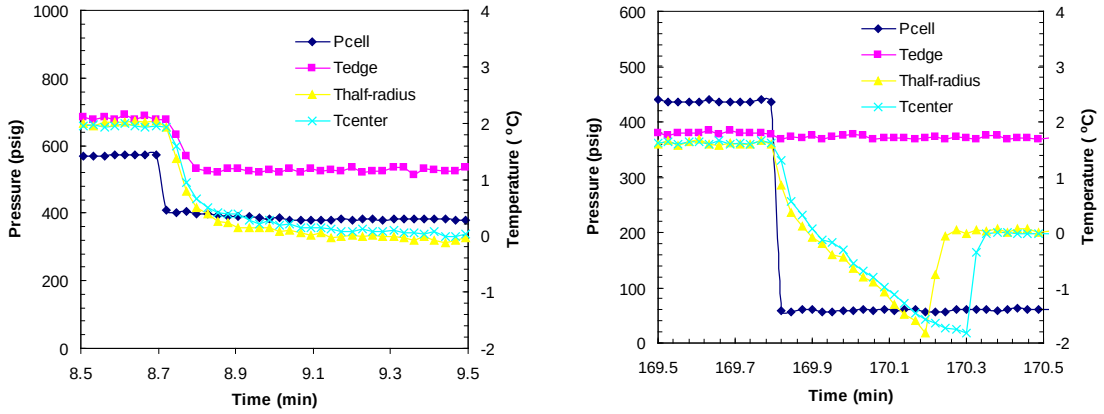

(a) **(b)**

FIG. 5.24. Thermocouple responses at various core locations within the sand-core (edge–T1, half-radius–T2 and center–T3) during dissociation with (a) 70 psi and (b) 400 psi drops below hydrate equilibrium pressure in Run 7 and 6 respectively.

5.2.2 Formation and Dissociation Kinetics of Methane Hydrate Formed by Pressurizing a Sand-core followed by its Cooling

The next set of runs (Runs 8-13) was also performed with the similar water/methane/Ottawa sand-core conditions (Table 5.1) under confining pressure. However, the hydrate formation in these runs was achieved by a single gradual charging of methane through the completely water saturated sand-pack under confining pressure, up to the desired pressure. This was followed by leak checks and cooling the cell down to the experimental temperature with water added to a bath surrounding the core-holder.

Table 5.3. Summary of operational conditions (pressure, temperature, flow) of hydrate formation/dissociation for Runs 8-13 with pure water and methane charging followed by cooling.

Run #	Core conditions P, psig	T,^{o}C	Confining pressure psig	Methane flowrate mL/min	Dissociation ΔP from equilibrium P psig
8	1214	4	1500	<2000	40, 107, 199, 304, 124, 155
9	1311	4	1500	<2000	115, 115, 111, 108, 105, 89, 102, 105, 105, 131
10	1362	4	1500	<2000	182, 159, 152, 139, 166, 147, 99
11	1200	4	1300	<700	85, 168, 277, 338, 132, 112
12	1200	5.5	1300	<2000	79, 171, 267, 329, 130, 138, 103
13	1200	3	1300	<2000	84, 174, 273, 326, 220

5.2.2.a Effect of Pore-pressure/consolidation on the Kinetics of Methane Hydrate Formation (Runs 8-10)

The bath cooling in Run 8 ultimately took the system PT conditions (1129.41 psig, 10.87^{o}C) into a methane hydrate stability region after 8.18 hours in Fig. 5.25(a).

However hydrate formation began at ~12 hours i.e. after 3.8 hours the system entered into hydrate stability region. The sudden pressure drop and exothermic peaks due to the hydrate formation event are shown in Fig. 5.25(b). Upon hydrate formation, system PT conditions followed a pure water-methane stability curve established with CSMGem shown in Fig. 5.26. The temperatures at the outer core surface (T1), half-way radius (T2), and the center of the core (T3) indicate that hydrates may have begun to form around the center and half-way radius of the core.

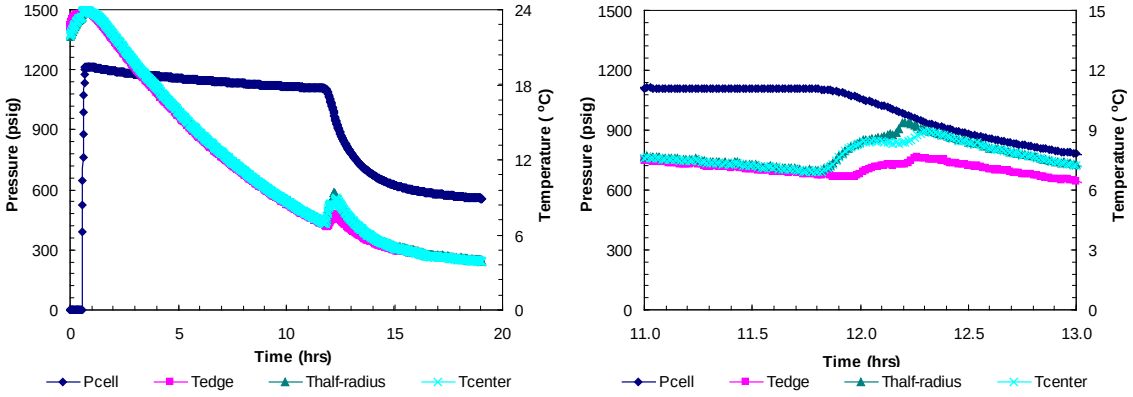

FIG. 5.25. Cell pressure and temperatures within the sand-core (edge–T1, half-radius–T2 and center–T3) against time during (a) methane charging and subsequent hydrate formation for Run 8. A magnified view of core conditions during hydrate formation is shown in plot (b).

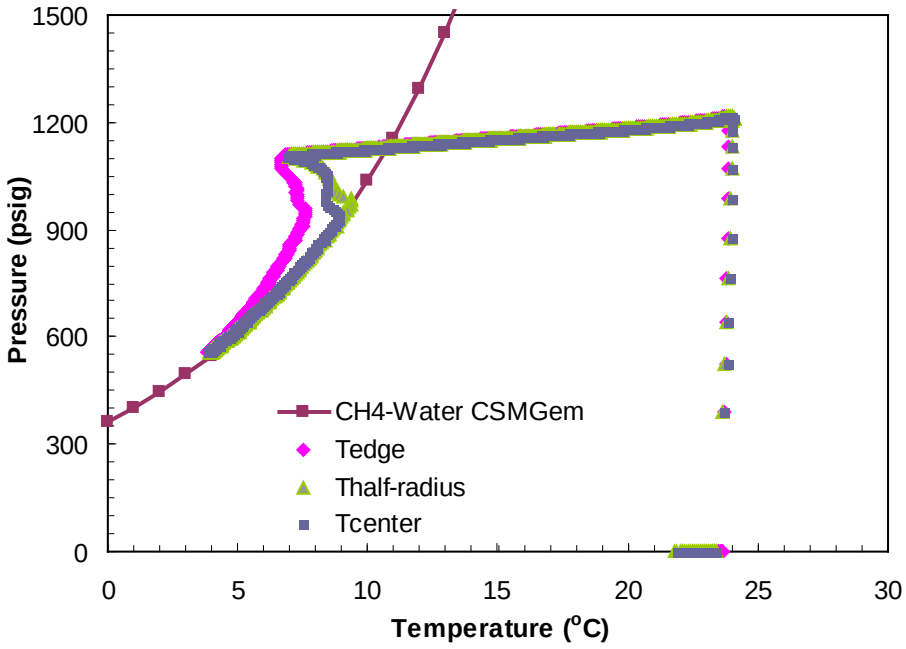

FIG. 5.26. Comparison of cell pressure against temperatures within the sand-core (edge–T1, half-radius–T2 and center–T3) during hydrate formation for Run 8 with a pure water-bulk methane hydrate stability curve obtained from CSMGem.

In a similar experiment (Run 9) where the cell was charged up to 1311 psig and then cooled down to 4°C, the system PT entered into hydrate stability region (11.43°C, 1220.23 psig) ~7.8 hours after cooling (Fig. 5.26(a)). However hydrate formation initiated at ~13.8 hours i.e. ~6 hours after the system entered into hydrate stability region. Once again, hydrate formation was evidenced first around the center and half-way radius of the core (Fig. 5.26(b)). For the 1362 psig charging run (Run 10), hydrate formation began to appear at 12.7 hours i.e. 6.4 hours after system entered into the hydrate stability region at 6.3 hours in Fig. 5.29. The formation was again observed from the center region of the core not from the core-wall.

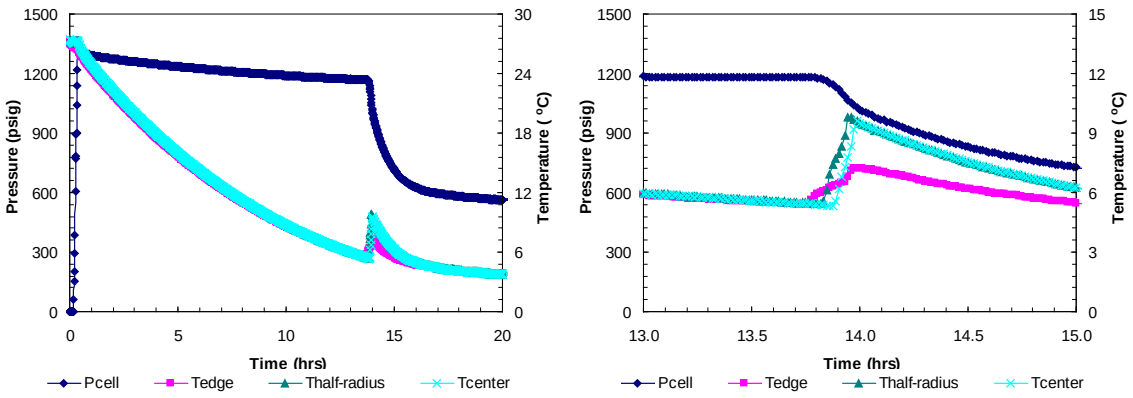

(a) **(b)**

FIG. 5.27. Cell pressure and temperatures within the sand-core (edge–T1, half-radius–T2 and center–T3) against time during (a) methane charging and subsequent hydrate formation for Run 9. A magnified view of cell pressure and exothermic core-temperatures spikes against time during hydrate formation are shown in plot (b).

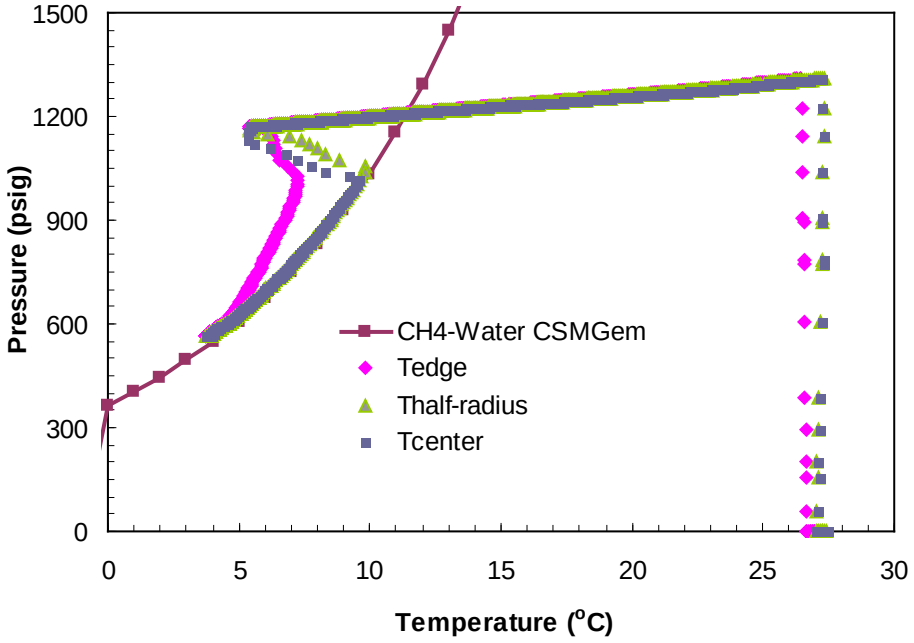

FIG. 5.28. Comparison of cell pressure against temperatures within the sand-core (edge–T1, half-radius–T2 and center–T3) during hydrate formation for Run 9 with a pure water-bulk methane hydrate stability curve obtained from CSMGem.

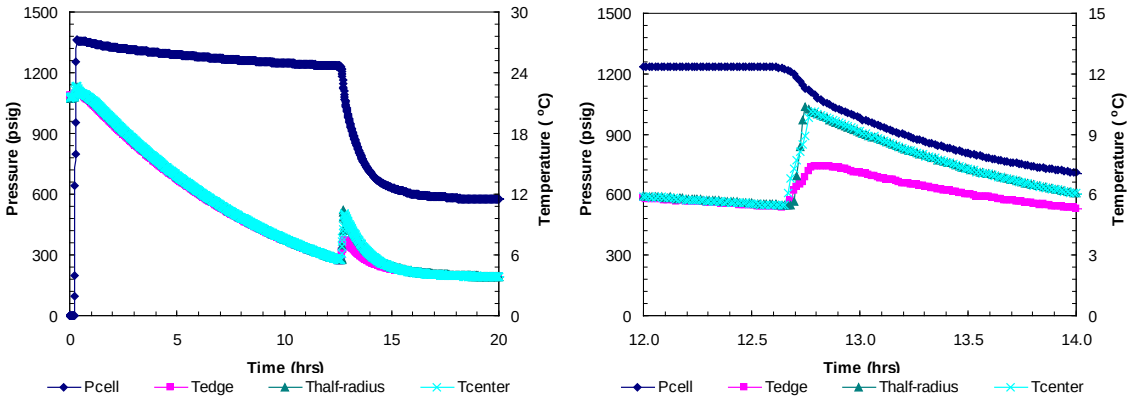

(a) **(b)**

FIG. 5.29. Cell pressure and temperatures within the sand-core (edge–T1, half-radius–T2 and center–T3) against time during (a) methane charging and subsequent hydrate formation for Run 10. A magnified view of cell pressure and exothermic core-temperatures spikes against time during hydrate formation are shown in plot (b).

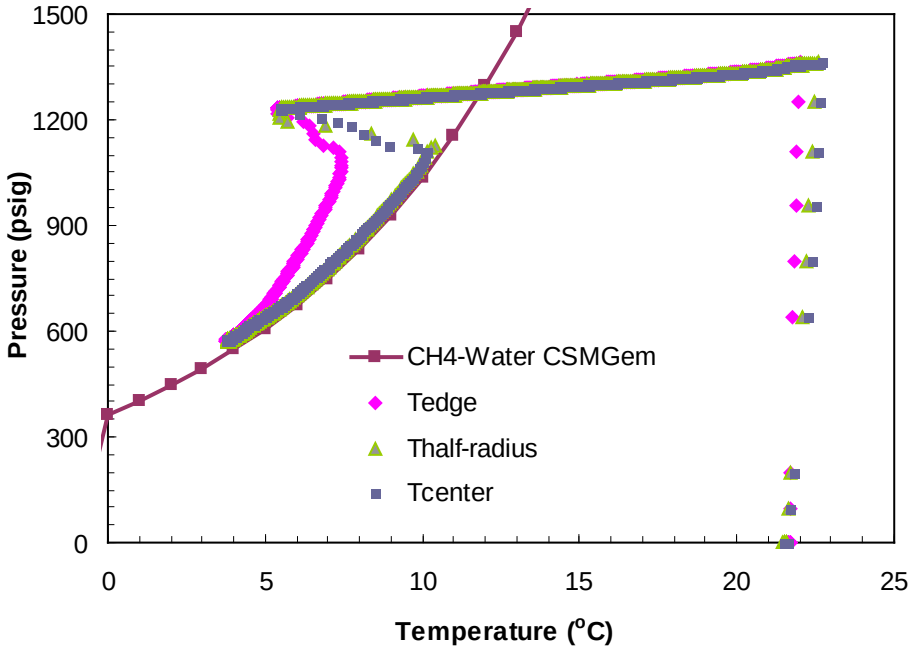

FIG. 5.30. Comparison of cell pressure against temperatures within the sand-core (edge–T1, half-radius–T2 and center–T3) during hydrate formation for Run 10 with a pure water-bulk methane hydrate stability curve obtained from CSMGem.

The hydrate formation times observed from Run 8-10 with varying pore pressures are summarized in Table 5.4. It is evident from Runs 8-10 that as the methane charging pressure increased, the nucleation of hydrates was observed earlier. The higher charging pressure of methane corresponds to higher pore pressure. The excess pore pressure in turn opposed the constant confining pressure (1500 psig) in these runs, relieving the degree of consolidation. In other words, the coefficient of compression/compression index (Cc) is defined as the slope of a plot of void ratio[1] (e) and logarithm of effective stress (σ') as shown in Eq. 4 (Das, 2001). Hence, as the effective stress increases, the coefficient of compression decreases with the degree of consolidation.

$$Cc = \frac{\Delta e}{\log_{10} \frac{\sigma_2'}{\sigma_1'}} \tag{4}$$

The delayed hydrate formation time for the higher degree of consolidation is consistent with earlier finding by Kleinberg et al. (2003). Similarly, Yousif and Sloan (1991) observed lesser and non-homogeneous hydrates with longer formation times (~40 hours) in lower permeability (8.388 x 10^{-2} μm^2) (mean pore radius: 3.5 μm) Berea sandstone investigated at an effective pressure of 145 psi. However, in the most permeable Berea sandstone core, no hydrate formation was seen until the first hour and slow accumulation thereafter over the next 5 hours.

Table 5.4. Summary of the effect of pore-pressure/consolidation on the kinetics of methane hydrate formation runs (8-10) at a constant confining pressure and cooling rate.

Run #	Pore Pressure	Confining Pressure	Effective Pressure	Time for hydrate formation after system PT enters into hydrate stability region
	psig	psig	psig	hrs.
8	1214	1500	286	3.44
9	1311	1500	189	5.48
10	1362	1500	138	6.40

[1] Void ratio (e) is defined as a ratio of unit volume of voids and unit volume of solids. It is expressed in therms of porosity (ø) as ø/(1-ø).

5.2.2.b Kinetics of Dissociation of Methane Hydrates by step-wise Depressurization at a Constant Temperature (Runs 8-10)

The dissociation was achieved with a step-wise depressurization from the hydrate equilibrium pressure at the bath temperature. The entire dissociation event for Run 8 is shown in Fig. 5.31(a). The dissociations at each depressurization step were short lived. As output gas was produced due to the depressurization, sediment temperature dropped due to the endothermic hydrate dissociation and gas expansion. It is evident that the greater the pressure drops during dissociation, the higher the degree of cooling, and a longer time was observed for sediments to reach initial the *in-situ* temperature. The highest pressure drop of 305.9 psi during the dissociation of Run 8 resulted in sediment cooling as low as -0.07^{o}C, close to the water freezing temperature. As the resultant gas output ceased, the cell exit valve was closed after which sediment temperature was allowed to increase up to the bath temperature. This allowed all dissociations at a constant temperature, the bath temperature. Figure 5.31(b) shows post-depressurization PT equilibrium during sediment warm-up to the bath temperature. The post-depressurization dissociation was thermally induced where the system followed hydrate PT equilibrium. However, this effect was seen until hydrates were present within sediments. After the fourth pressure drop (dp4) of 305.9 psi, all hydrates were dissociated and subsequent post-depressurization curves represent methane gas warm-up. The post-depressurization responses for hydrates are slightly shifted towards higher pressure values from the theoretical pure methane hydrate PT stability curve (Fig. 5.31(b)). This is due to the minimal excess pore (pore diameter: 48.28-58.65 μm) pressure generated during subsequent thermally induced dissociations. It is also clear from thermocouple responses that the core boundary experienced a lesser degree of cooling during depressurization than the half-radius and center of the core. This indicates that the hydrates may have been predominantly formed within the interior part of the core. However during thermally induced dissociation, the core boundary warms up at a faster rate, as expected, than at the core half-radius and core center.

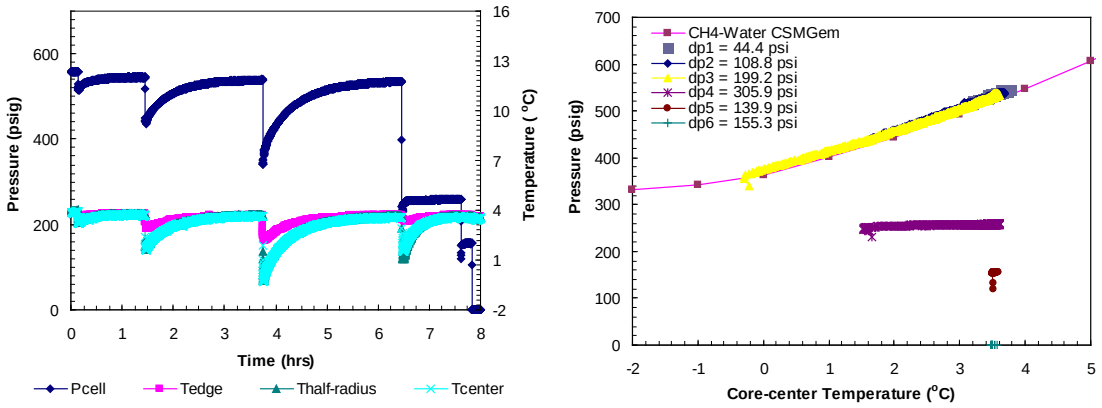

(a) **(b)**

FIG. 5.31. Core pressure and temperatures within the sand-core (edge–T1, half-radius–T2 and center–T3) against time (a) during dissociation with varying pressure drops from equilibrium pressure in Run 8. Post-depressurization equilibrium pressure against core-center temperature conditions of methane hydrates in porous media are shown in plot (b). Each plot corresponds to core conditions during thermally induced dissociations after each depressurization step. Equilibrium conditions of bulk methane hydrates were obtained from CSMGem.

The hydrates formed in Run 9 were dissociated with pressure drops ranging between 106.7 to 115.5 psi from the equilibrium pressure at a bath temperature of ~4^{o}C (Fig. 5.32(a)). Figure 5.33 compares the cumulative gas produced due to successive pressure drops. The first pressure drop (dp1) of 115 psi caused hardly any dissociation, giving out only ~100 mL of gas. This can be also confirmed from Fig. 5.32(a) where a negligible temperature drop was recorded for the first pressure drop. However the second pressure drop (dp2) of 116 psi showed the highest amount of cumulative gas produced (~777 mL) among all dissociations (Fig. 5.33). The subsequent pressure drops (dp3-dp5) not only caused a consistent amount of cumulative gas (Fig. 6.33) but also resulted in a consistent degree of sub-cooling down to 1.67-1.91^{o}C (Fig. 5.32(a)). However, as hydrates dissociate in each step, the resultant sand-gas-water-hydrate mixture took a longer time to warm up to the bath temperature. This may be due to the lower thermal conductivity of resultant methane gas (0.03442 W/m-^{o}K) than that of hydrates (0.45 W/m-^{o}K) (Table 5.5). The pressure drops following the first five did not affect sediment

temperature which confirms the complete hydrate dissociation. The post-depressurization PT equilibrium for the first five pressure drops follow theoretical PT equilibrium for bulk methane hydrates with a minimal effect from excess pore pressure (Fig. 6.32(b)). The post-depressurization PT equilibrium represents thermally induced hydrate dissociation. The enthalpy of hydrate dissociation was computed as a slope of a lnP vs. 1/[TRZ] plot for post-depressurization data (Fig. 5.34). Although the values of the enthalpy of dissociation of hydrates in porous media under the confining pressure of 1500 psig (Fig. 5.34, 60.323 kJ/mol, 60.115 kJ/mol) are consistent with that computed from theoretical PT data for bulk hydrates obtained from CSMGem (62.605 kJ/mol), they are higher than those similarly computed at the confining pressure of 1300 psig (Fig. 5.17, 49.144 kJ/mol, 58.524 kJ/mol, 59.134 kJ/mol). The higher values may be due to a higher effective pressure in case of 1500 psig confining pressure. A higher effective pressure corresponds to lower consolidation (Eq. 4).

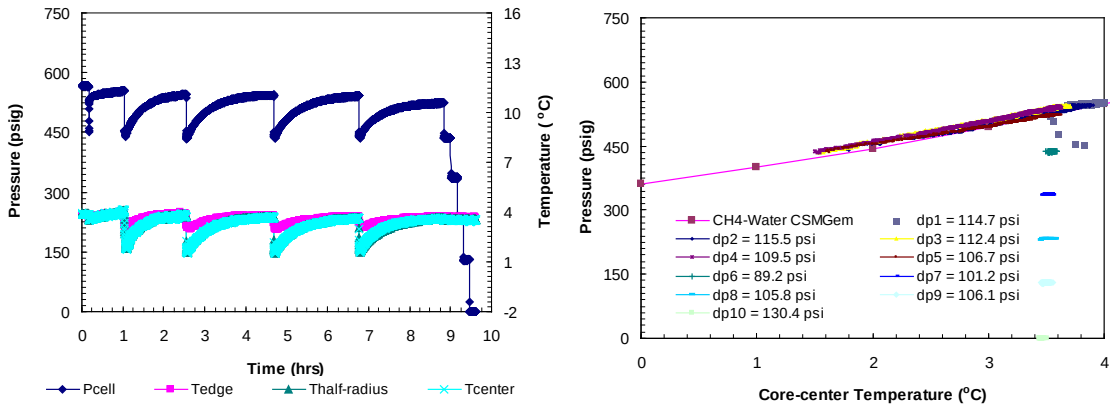

(a) **(b)**

FIG. 5.32. Cell pressure and temperatures within the sand-core (edge–T1, half-radius–T2 and center–T3) against time (a) during dissociation with multiple pressure drops of ~100 psi from equilibrium pressure in Run 9. Post-depressurization equilibrium pressure against core-center temperature conditions of methane hydrates in porous media are shown in plot (b). Each plot corresponds to core conditions during thermally induced dissociations after each depressurization step. Equilibrium conditions of bulk methane hydrates were obtained from CSMGem.

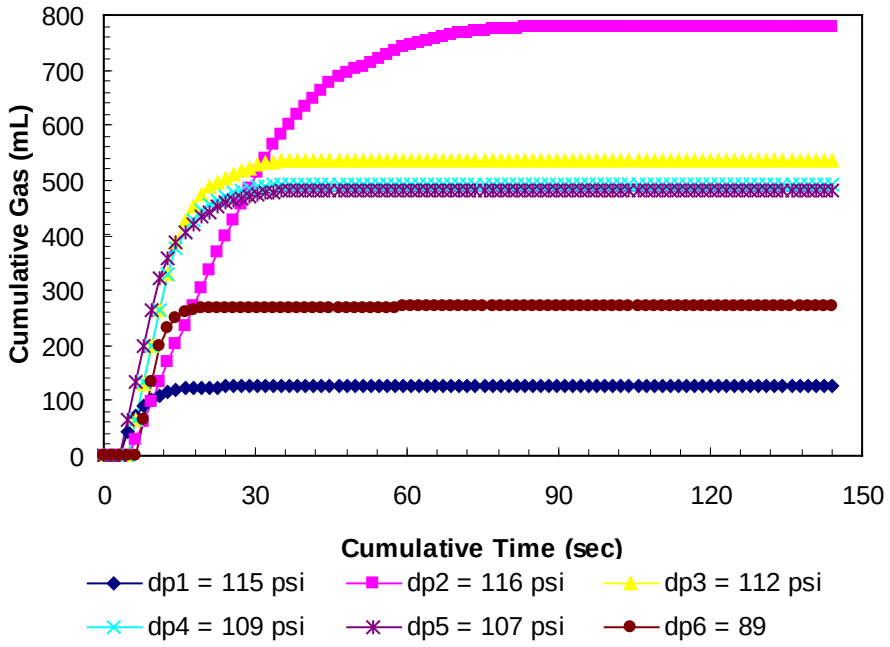

FIG. 5.33. Cumulative gas produced against time for incremental pressure drops during hydrate dissociation in Run 9.

Table 5.5. Thermal conductivities of methane, hydrates, water, ice and Ottawa sand

Phase	**Thermal conductivity (W/m-K)**	**Reference**
Methane	0.03442 @ 0^{o}C, 600 psia	Carmichael, L.T. et al., 1966
Methane hydrate	0.45 @ 0^{o}C	Sloan, 1998
Water	0.565 @ 0^{o}C	Perry and Green, 1984
Ice	2.22 @ 0^{o}C	Pringle, 2004
Ottawa sand	0.33 @ 7^{o}C	Rueff and Sloan, 1985.

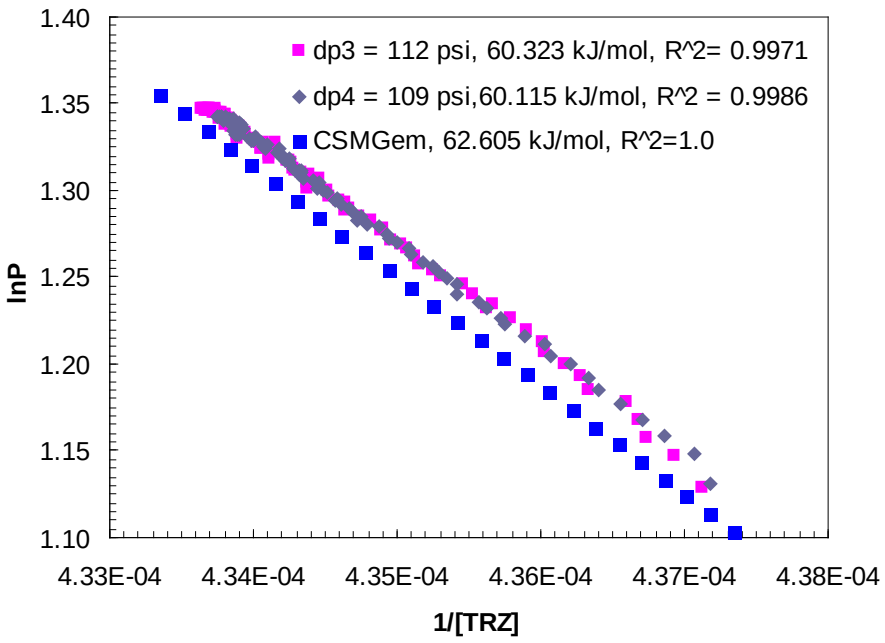

FIG. 5.34. Post-depressurization equilibrium pressure (lnP) against core-center temperature (1/[TRZ]) for Run 9 (dp3 and dp4). The Clausius-Clapeyron equation was used to calculate the enthalpy of dissociation (ΔH_{hyd} in kJ/mol) of methane hydrates in porous media at a confining pressure of 1500 psig. Equilibrium conditions of bulk methane hydrates obtained from CSMGem were used to calculate the theoretical ΔH_{hyd}. The R^2 values indicate the correlation coefficient for the linear regression performed to compute the slope as ΔH_{hyd}.

In Run 10, the dissociation was carried out with pressure drops ~150–180 psi from the hydrate equilibrium pressure at the bath temperature (~4^{o}C) attained the end of the formation. The higher pressure drop as compared to the previous dissociation (106.7 to 115.5 psi in Run 9) led to a lesser number of drops (Fig. 5.35(a)). It is again confirmed from Fig. 5.35(a) that the post-depressurization warm-up gets delayed successively due to the increasing methane gas saturation in the resultant sand-gas-water-hydrate mixture.

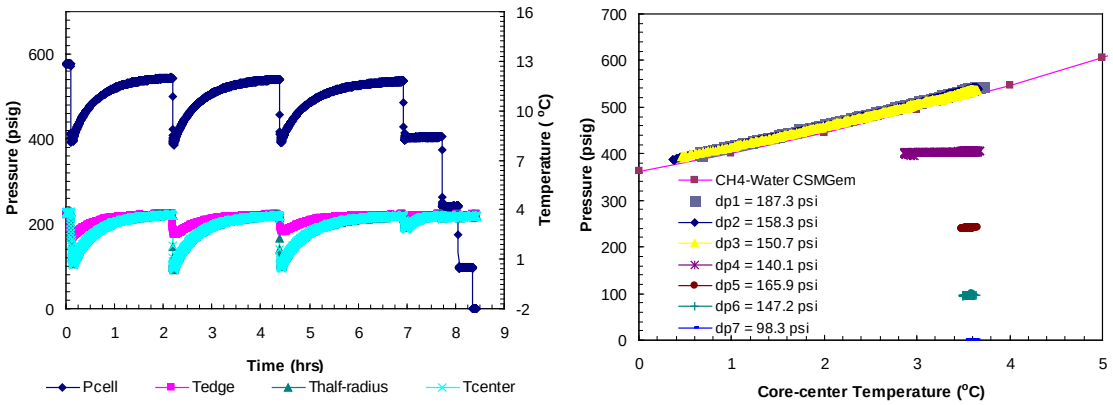

(a) **(b)**

FIG. 5.35. Cell pressure and temperatures within the sand-core (edge–T1, half-radius–T2 and center–T3) against time (a) during dissociation with multiple pressure drops of ~150 psi from equilibrium pressure in Run 10. Post-depressurization equilibrium pressure against core-center temperature conditions of methane hydrates in porous media are shown in plot (b). Each plot corresponds to core conditions during thermally induced dissociations after each depressurization step. Equilibrium conditions of bulk methane hydrates were obtained from CSMGem.

Figure 5.36 compares the thermocouple responses during the second (dp2 = 158.3 psi) and third (dp3 = 150.7 psi) pressure drops to examine the preferential hydrate dissociation due to depressurization. The steep slopes for the core center and half-radius temperatures indicate that the dissociation was found to be preferential in the center part of the core rather than at its boundary.

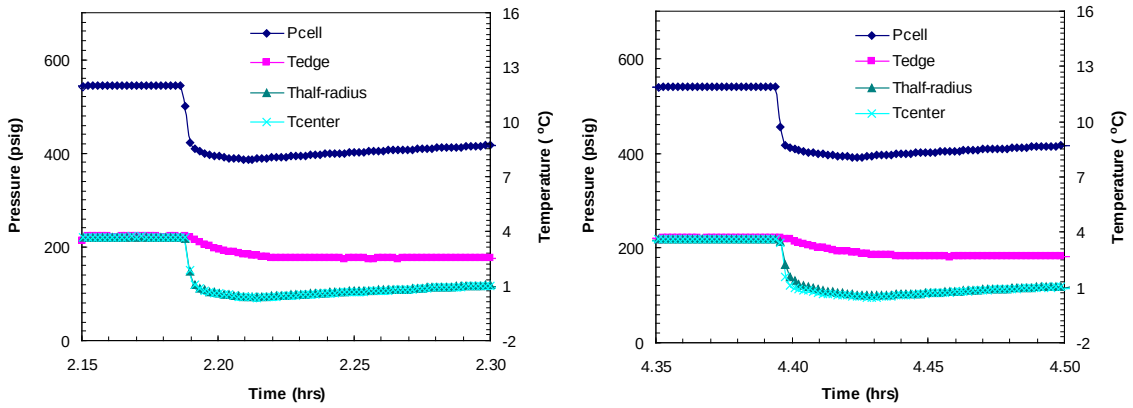

(a) **(b)**

FIG. 5.36. Thermocouple responses at various core locations within the sand-core (edge–T1, half-radius–T2 and center–T3) during dissociation with (a) dp2= 158.3 psi and (b) dp3 = 150.7 psi drops below hydrate equilibrium pressure in Run 10.

5.2.2.c Kinetics of Dissociation of Methane Hydrates by Step-wise Depressurization at different Temperatures (Runs 11-13)

Runs 11-13 were also performed with a formation method similar to one that was utilized for Runs 8-10 i.e. hydrate formation was achieved by a single gradual charging of methane through the completely water saturated sand-pack under confining pressure followed by cooling the cell down to the experimental temperature. However, thermocouple arrangement was altered to have the core-center thermocouple (T3) at the top, followed by the one at the half-radius (T2) and the core boundary (T1) (Fig. 5.37). This arrangement was applied to rule out the effect of gravity on the hydrate dissociation front where hydrates were found in previous runs to dissociate from the center of the sample towards the wall. Moreover, sediment/bath temperature was changed to 4, 5.5 and 3^{o}C in Runs 11, 12, and 13 respectively with a constant initial charging pressure of 1200 psig and confining pressure 1300 psig to investigate the effect of sediment temperature on (a) the degree of sub-cooling during each depressurization step, (b) the cumulative gas produced during each depressurization step, and (c) the time scale for sediments to warm-up to the bath temperature during each depressurization, and (d) to establish methane hydrate PT equilibrium in porous media at temperatures even lower and higher than previous runs (8-10).

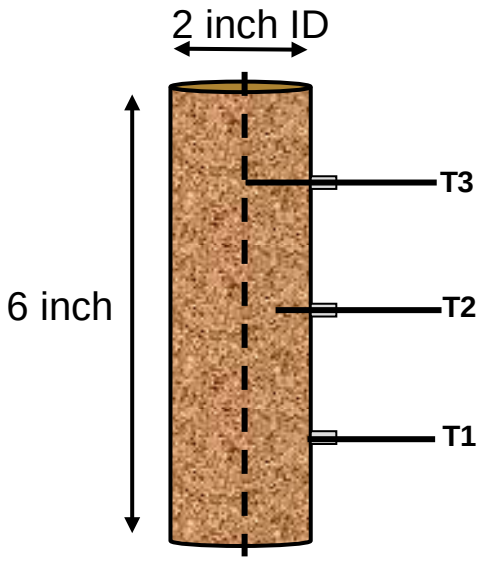

FIG. 5.37. Thermocouple locations (edge-T1, half-radius–T2 and center–T3) within the Ottawa sand-core for hydrate formation/dissociation Runs 11-13 with pure water.

In Runs 11-13, the dissociation was achieved by the increasing series of pressure drops until all hydrates were dissociated. After each pressure drop, the cell temperature dropped and the gas evolved was metered against time. In Run 11, the endothermic cooling responses observed at all thermocouples for only the first four pressure drops of 85, 168, 277 and 338 psi respectively below equilibrium pressure at bath temperature (4^{o}C) confirmed complete dissociation of hydrates in the system (Fig. 5.38 (a)). The presence of hydrates until the fourth pressure drop of 338 psi is also confirmed by the post-depressurization PT shown in Fig. 5.38(b), where plots for dp1 to dp4 follow theoretical methane-water PT curve obtained from CSMGem.

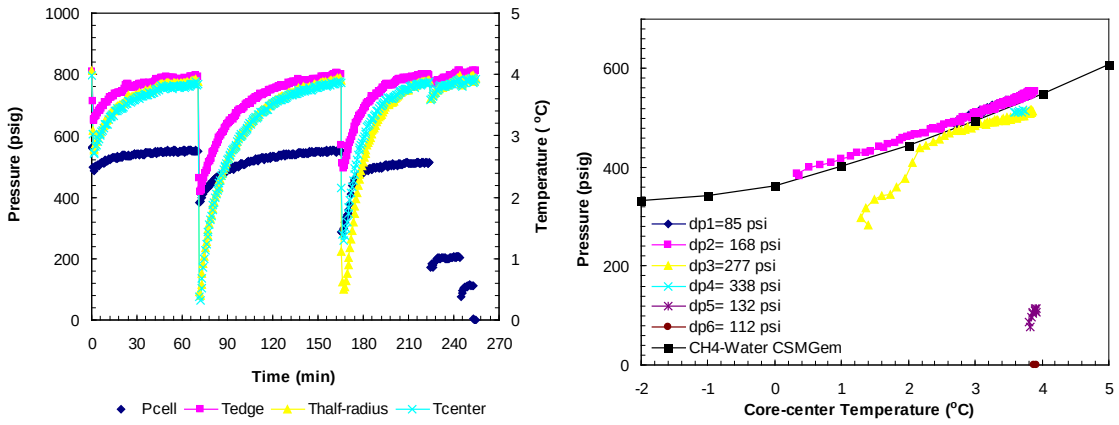

(a) **(b)**

FIG. 5.38. (a) Cell pressure and temperatures within the sand-core (edge–T1, half-radius–T2 and center–T3) against time during dissociation with multiple pressure drops of 85-338 psi in Run 11. Post-depressurization equilibrium pressure against core-center temperature conditions of methane hydrates in porous media are shown in plot (b). Each plot corresponds to core conditions during thermally induced dissociations after each depressurization step. Equilibrium conditions of bulk methane hydrates were obtained from CSMGem.

In Run 12, the dissociating pressure drops were in the order of 79, 171, 267, and 329 psi from equilibrium pressure (~540 psig) at the bath temperature of 5.5^{o}C. From Fig. 5.39 (a) and (b), it is evident that after about three pressure drops, all hydrates appear to have dissociated since the cell pressure did not come back to the hydrate equilibrium pressure. Once gas evolution ceased, the sediments were allowed to equilibrate where the cell pressure gradually rose to the equilibrium pressure as the sediment temperature increased up to the bath temperature (5.5^{o}C).

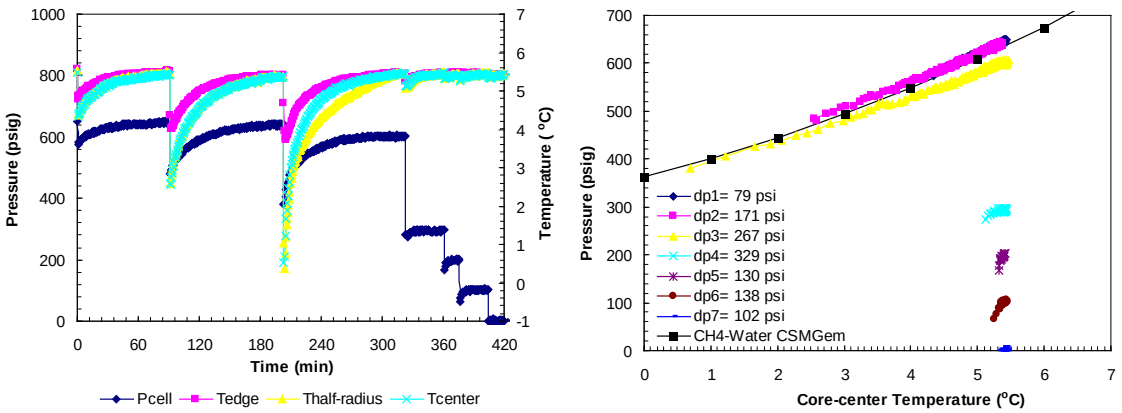

(a) **(b)**

FIG. 5.39. (a) Cell pressure and temperatures within the sand-core (edge–T1, half-radius–T2 and center–T3) against time during dissociation with multiple pressure drops of 79-329 psi in Run 12. Post-depressurization equilibrium pressure against core-center temperature conditions of methane hydrates in porous media are shown in plot (b). Each plot corresponds to core conditions during thermally induced dissociations after each depressurization step. Equilibrium conditions of bulk methane hydrates were obtained from CSMGem.

The dissociation in Run 13 was from an equilibrium pressure at a bath temperature of ~3^{o}C. However, after two pressure drops of 84 and 174 psi, system pressure did not rise up to the equilibrium pressure (Fig. 5.40(a)). This can also be conferred from the post-depressurization PT plot shown in Fig. 5.40(b) where the PT plot for dp3 did not follow the theoretical PT equilibrium curve for a methane-water system. Moreover, subsequent post-depressurization plots move further away on the lower pressure side of the theoretical PT equilibrium curve for a methane-water system.

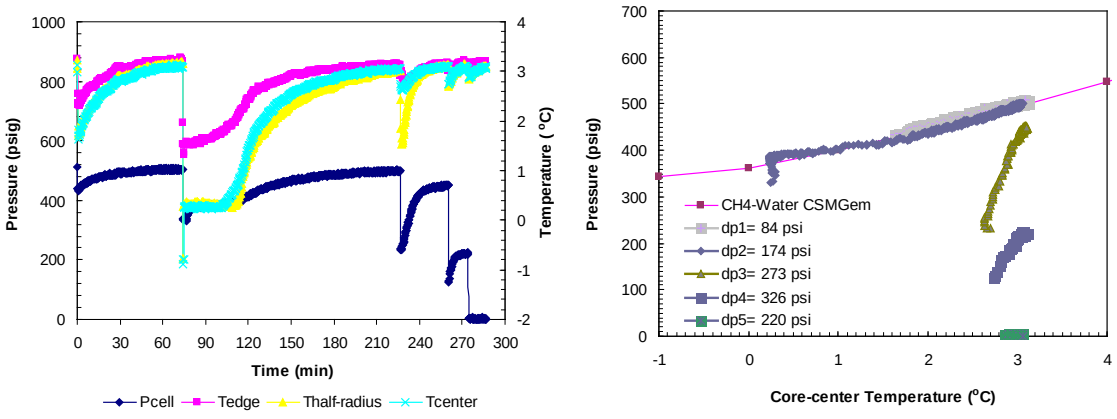

(a) **(b)**

FIG. 5.40. (a) Cell pressure and temperatures within the sand-core (edge–T1, half-radius–T2 and center–T3) against time during dissociation with multiple pressure drops of 74-326 psi in Run 13. Post-depressurization equilibrium pressure against core-center temperature conditions of methane hydrates in porous media are shown in plot (b). Each plot corresponds to core conditions during thermally induced dissociations after each depressurization step. Equilibrium conditions of bulk methane hydrates were obtained from CSMGem.

The post-depressurization sediment temperature at the outer thermocouple (T1) increased quickly towards the bath temperature along with the cell pressure. However, the temperature of the sample center (T3) and the half-way sample radius (T2) rose at a much slower rate. The dissociation was also observed to be preferential in the sample interior than at its boundary in Runs 11-13. This was established from thermocouples responses during short-lived dissociations at each pressure drop (Fig. 5.41). These observations are consistent with earlier experience, despite the changed vertical order of thermocouples from previous runs. This undermines the effect of gravity on the hydrate dissociation front where hydrates were found in previous runs to dissociate from the center of the sample towards the wall.

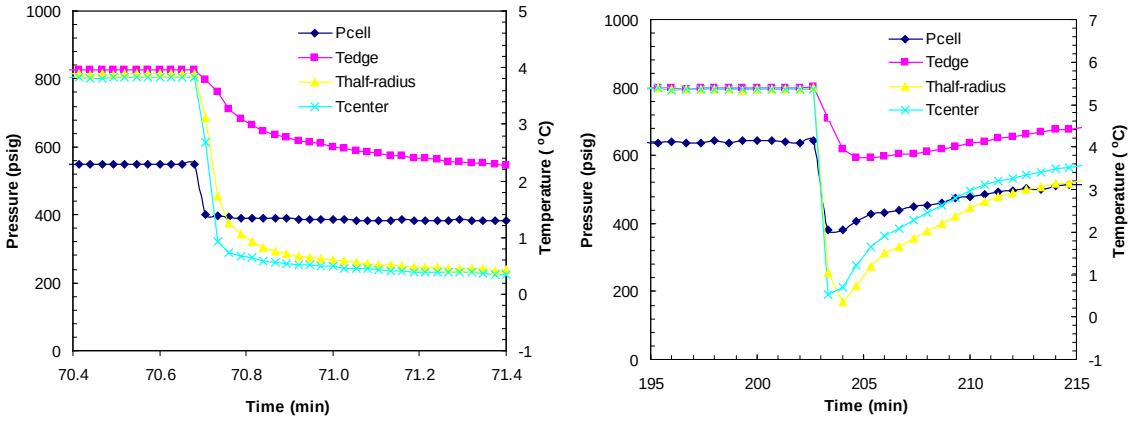

FIG. 5.41. Thermocouple responses at various core locations within the sand-core (edge–T1, half-radius–T2 and center–T3) during dissociation with (a) dp2= 185 psi below hydrate equilibrium pressure in Run 11 and (b) dp3 = 267 psi drops below hydrate equilibrium pressure in Run 12.

It is clear from Run 11-13 that higher pressure drops during dissociation of hydrates at a constant sediment temperature caused a larger degree of sediment-cooling. The higher degree of sediment cooling obviously takes a longer time for sediments to reach the bath temperature. The degree of cooling of the sediment was also found to be dependent upon the sediment temperature for a constant pressure drops. Fig 5.42(a) compares the sediment cooling and subsequent time for warm-up to the bath temperature from Runs 11, 12 and 13 at similar pressure drops. The highest endothermic effect due to hydrate dissociation was observed when sediment temperature dropped as low as -0.88^{o}C at the core-center due to a pressure drop of 174 psi below the equilibrium pressure at ~3^{o}C. Figure 5.42(b) compares the sediment sub-cooling data from Fig. 5.42(a) on a relative dimensionless scale against time. It is obvious that lower sediment temperature caused a higher degree of cooling upon hydrate dissociation and in turn, it took a longer time to warm-up to its initial value.

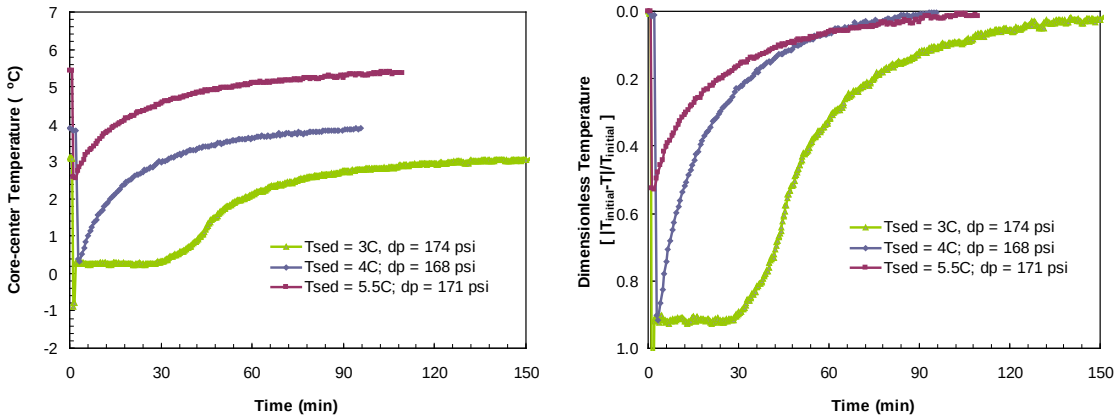

(a) **(b)**

FIG. 5.42. (a) Core-center thermocouple responses during dissociation with similar pressure drops below hydrate equilibrium pressure at sediment temperatures of 4°C (Run 11), 5.5°C (Run 12) and 3°C (Run 13). (b) Dimensionless sediment temperature change [$|T_{initial}-T|/T_{inital}$] against time for similar pressure drops for dissociation from sediments at 4°C (Run 11), 5.5°C (Run 12) and 3°C (Run 13). Runs 11, 12, 13 were performed at a constant confining pressure of 1300 psig.

Figure 5.43 compares the cumulative gas produced due to various pressure drops during hydrate dissociation from sediments at ~4°C and ~3°C from Run 11 and 13 respectively. It is obvious from Figs. 5.43(a) and 5.43(b) that the gas output ceased in less than 30 seconds during dissociation at all pressure drops. The dissociations due to depressurization were found to be consistently short-lived from all previous runs. This observation is consistent with the previous study on sand-pack hydrate dissociation via depressurization by Kneafsey et al. (2007). Figure 5.43 indicates that the first pressure drop in both runs did not produce an appreciable amount of gas. It can also be discerned from Figs 5.38(a) and 5.40(a) where the temperature drop within the core was minimal. This may be due to excess gas from the system that was vented off during the first pressure drop and the minimal hydrate dissociation. Subsequent pressure drops of ~170 and 270 psi from equilibrium conditions resulting in cumulative gas outputs of ~200 mL were observed in Run 11 as well as Run 13.

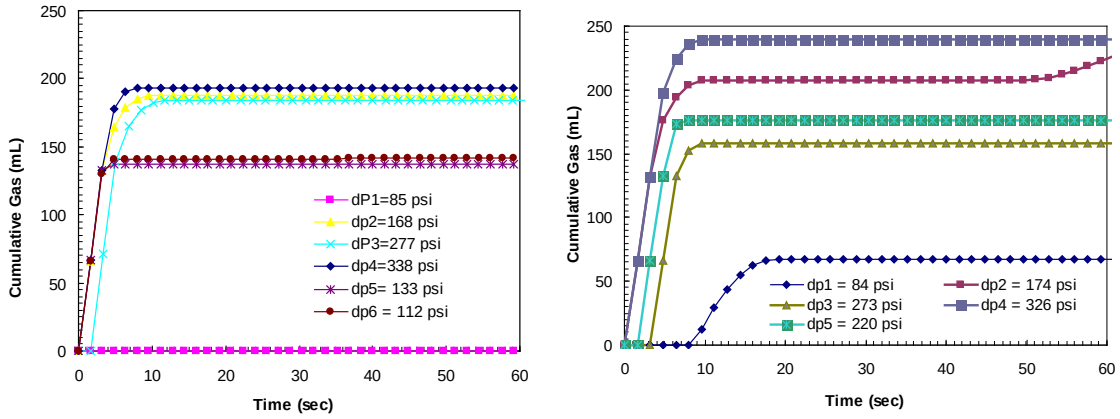

(a) **(b)**

FIG. 5.43. Cumulative gas produced against time for incremental pressure drops during hydrate dissociation at constant sediment temperature of (a) 4°C in Run 11 and (b) 3°C in Run 13.

5.3 Modeling Decomposition Kinetic Behavior for Hydrate Dissociation Constant

The profiles of hydrate dissociation into gas and water by depressurization are analyzed with a model based on work by Kim et al. (1987). The molar generation rate of methane gas (nH_{CH4}) due to hydrate dissociation is related to the dissociation rate constant (k_d), the surface area of hydrates per unit volume (Ap) and the equilibrium (fe) and local (f) fugacity difference.

$$nH_{CH_4} = k_d . Ap(fe - f).t \ . \tag{5}$$

The dissociation rate constant is a function of the intrinsic dissociation constant (k_d^o), the activation energy (ΔE), the gas constant (R), and the temperature (T).

$$k_d \frac{kmol}{Pa.s.m^2} = k_d{}^o \frac{kmol}{Pa.s.m^2} \exp\left(-\frac{\Delta E}{RT} \frac{J}{kmol} . \frac{kmol.K}{J} \frac{1}{K} \right) \tag{6}$$

The total surface area (Ap) of hydrate particles (spherical/non-spherical) is defined in terms of the sphericity factor (ψ), hydrate particle diameter (Do), initial number of moles of methane in the hydrate (no_{CH4}) and the moles of methane in the hydrate (nH_{CH4}).

$$As.m^2 = \left[\frac{6}{\psi.\rho_H \frac{kmol}{m^3}.Do.m}\right](no_{CH4}{}^{1/3}.nH_{CH4}{}^{2/3})kmol \tag{7}$$

The substitution of expressions of As and kd into equation (5) yields

$$nH_{CH_4} \frac{kmol}{s} = k.\frac{1}{s}.t.s(no_{CH4}{}^{1/3}.nH_{CH4}{}^{2/3})kmol \tag{8}$$

where,

$$k.\frac{1}{s} = kd^o.\exp(-\frac{\Delta E}{RT}).\left[\frac{6}{\psi.\rho_H.Do}\right](fe - f) \tag{9}$$

Equation 8 can be rewritten as

$$\sqrt[3]{\frac{nH_{CH4}}{no_{CH4}}} = -\left(\frac{k}{3}\right)t + 1 \tag{10}$$

Liang et al. (2005) studied the decomposition kinetic behavior of methane hydrates formed in 5 mL porous activated carbon from pure free water and an aqueous solution of 650 g/m^3 sodium dodecyl sulfate (SDS), a hydrate promoter. The decomposition rate data were fitted into a model developed for the decomposition kinetic behavior of methane hydrates based on an ice-shielding mechanism in which a porous ice layer was assumed to be formed during the decomposition of hydrates. The model assumes two steps of which the later is assumed to be controlling during dissociation:

1. Destruction of hydrate host lattice at the surface of hydrate particle and desorption of methane molecule from the surface of hydrate particle.
2. Diffusion of methane through ice layer

$$\frac{dn}{dt} = \left[\frac{1}{\frac{1}{k} + \frac{n^b}{D_s}} \right] \left(f_e - f_g \right) \tag{11}$$

where, n – cumulative moles of methane released at time t, moles

k – hydrate dissociation constant, mol./(MPa.sec.g)

b – empirical constant, unitless

Ds – empirical constant, mol(b+1)/(m.MPa.g.sec)

After integrating above equation with limits, t = 0, n = 0 and t = t, n = n,

$$t = \frac{n}{k.(f_e - f_g)} + \frac{1}{(f_e - f_g).D_s(b+1)}.n^{(b+1)} \tag{12}$$

Combining unknowns and re-writing yields,

$$t = \frac{1}{(f_e - f_g)} \left[\frac{n}{K_1} + \frac{1}{D_s.K_3}.n^{K_3} \right] \tag{13}$$

where unknowns are

K_1 = k, hydrate dissociation constant, mol./(MPa.sec.g)

K_3 = b+1

Ds = empirical constant, $mol^{(b+1)}$/(m.MPa.g.sec)

For the present analysis, the number of moles of methane evolved for each pressure drop are plotted against time (red curve in Fig. 5.44) to yield k, hydrate dissociation constant. Equation 13 was used to generate theoretical plot as follows: During Run 9, the pressure drop of 115 psi resulted in changing cell pressure from the equilibrium value, Pe = 555 psig to Pg = 446 psig at the bath temperature of 4.1^{o}C. The pressure values of Pe and Pg were converted into fugacity values viz: fe = 522.5193 psi and fg = 429.5326 psi, respectively using the Redlich-Kwong-Soave equation of state. The experimental data of time (t,sec), cumulative number of moles of methane produced (n) and the fugacity difference (Δf) of 93 psi (0.641 MPa) were iteratively fitted into Eq. 13 to yield the theoretical curve in Fig. 5.44 (blue curve). The computed hydrate dissociation constant (k) was 1.1622 x 10^{-3} mol./(MPa.sec.g). This hydrate dissociation

constant value is about 10,000 times smaller than that observed for the pure water-SDS system by Liang et al. (2005). This may be due to a porous Ottawa sand-pack of pore diameter ranging between 48.28-58.65 µm.

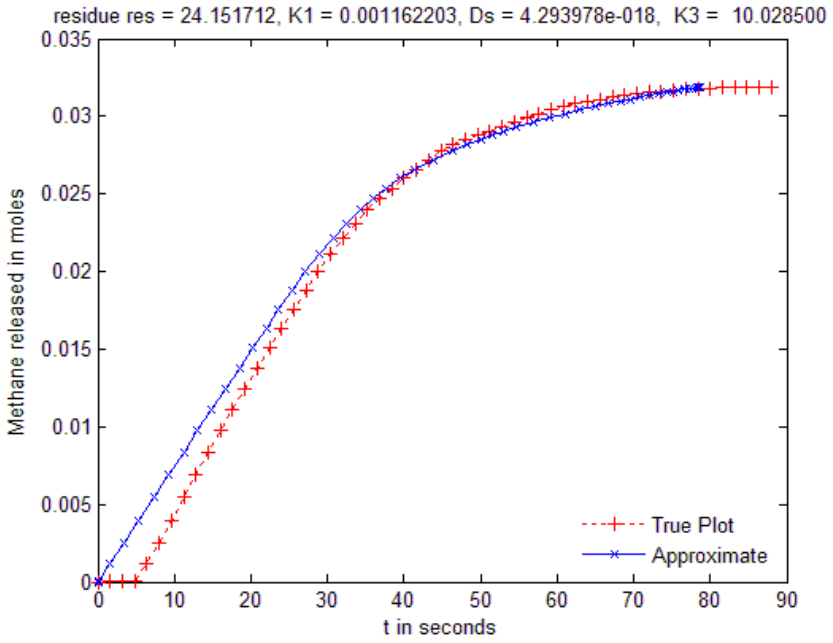

FIG. 5.44. Experimental and model parameters curves for cumulative moles of methane evolved during dissociation due to a depressurization.

Chapter 6

Formation and Dissociation of Methane Hydrates from Seawater in Consolidated Sand: Duplicating Methane Hydrate Dynamics beneath the Seafloor

6.1 Consolidated Core Studies with Seawater – Experimental Conditions

Temco's DCHR-2.0 series hassle-type core holder was used to keep Ottawa sand (110 μm grain diameter) consolidated in a 2 inch diameter and 6 inch length rubber sleeve. Dried and weighed Ottawa sand was loaded into the rubber sleeve after attaching the bottom end-cap assembly. Three ports located at 1, 3 and 5 inches of the core were adapted for thermocouples inserted at different radial locations of the core. Table 6.1 depicts the core holder and sand-core conditions. Figure 6.1 shows the arrangement of thermocouples within core. Two 1/4 inch thick polyethylene filters with a 50 mm diameter and 0.5 μm average pore size installed at the top and bottom of the core prevented sand from slipping out of the rubber sleeve. A constant confining/overburden pressure was applied in small increments on the sleeve with a fluid introduced into an annulus around the sleeve with an Isco syringe pump. The sand-core was saturated with seawater (salinity, S = 28.053%) by flowing it evenly into the core against gravity through lines extending from the top and bottom distributors with another syringe pump. Upon the gradual charging (<2000 mL/min) of methane up to a target pore pressure at

room temperature, hydrate formation was initiated by cooling the system up to an experimental temperature. The cell pressure and three thermocouple responses were monitored until pore pressure asymptoted at hydrate equilibrium pressure at the end of the formation event. During dissociation, the cell was step-wise depressurized (100-200 psi) from equilibrium pressure at the bath temperature. Once the flow of methane produced ceased, the system outlet valve was closed and the sediments were allowed to warm up from cooler temperatures due to an endothermic dissociation of hydrates. This sediment warm-up to the bath temperature after each depressurization allowed investigating hydrate dissociation at a constant temperature. Table 6.2 depicts formation and dissociation conditions employed in each run.

Table 6.1: Ottawa sand-core conditions for hydrate formation/dissociation Runs 14-19 with seawater.

Core holder	Temco DCHR-2.0 w/ 3 temperature ports
Core holder volume	308.9 mL
Core diameter	2 inch
Core length	6 inch
Sediment	520.34 g of Ottawa Sand F110 (average grain diameter – 110 μm)
Sediment bulk density	1.625 g/cc
Volume of a filter	12 mL
Volume of sand	296 mL
Mass of sand packed	520.34 g.
Sediment packing density	1.728 g/cc
Water saturation	~100%

6.2 Results and Discussions

6.2.1 Effect of Pore-pressure/Consolidation on the kinetics of Methane Hydrate Formation (Runs 14-16)

Methane charging pressure, a pore pressure was varied in Runs 14-16 with a constant confining pressure of ~1500 psig and sediment temperature of ~4^{o}C. This allowed a study of methane hydrate formation kinetics at different effective pressure (confining pressure – pore pressure). In Run 14, under the effective pressure of 268.4 psi (1500 – 1231.6), sediment cooling lowered the system pressure gradually (Fig. 6.2(a)). After ~8.8 hours of cooling, the system PT entered into a hydrate stability region shown in Fig. 6.2(b). However, hydrate formation was observed after ~18.2 hours of cooling i.e. after 9.4 hours the system entered into the hydrate stability region. A temperature spike at all thermocouples due to the exothermic nature of hydrate formation and a sudden pressure drop due to methane consumption were evidenced at the same time. Subsequently, the pore pressure asymptoted to equilibrium pressure (~679.4 psig) at the core-temperature (~4.4^{o}C) after 22 hours of operation (Fig. 6.2(a)). This can also be discerned from Fig. 6.2(b) where system PT conditions followed the methane-seawater equilibrium curve obtained from Duan and Sun (2006).

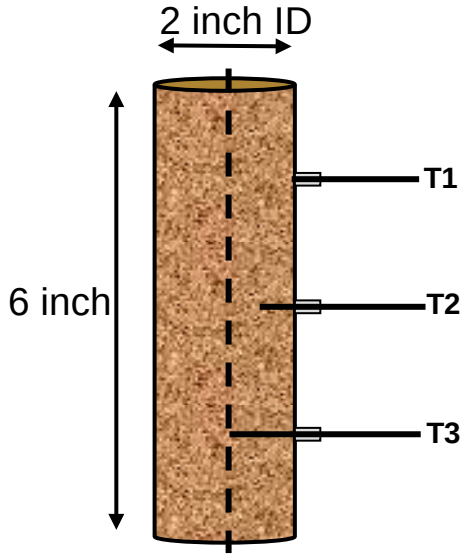

FIG. 6.1. Thermocouple locations (edge-T1, half-radius–T2 and center–T3) within the Ottawa sand-core for hydrate formation/dissociation Runs 14-19 with seawater.

Table 6.2. Summary of the operating conditions of hydrate formation/dissociation runs with seawater and methane charging followed by cooling.

Run #	Core conditions P, psig	T,^{o}C	Confining pressure psig	Methane flowrate mL/min	Dissociation ΔP from equilibrium P psig
14	1231	4	1500	<2000	77, 85, 91, 74, 75, 75, 75, 75, 75, 76, 75, 75, 79, 75, 75, 75, 110
15	1327	4	1500	<2000	100, 99, 146, 100, 100, 100, 99, 94, 104, 103, 100
16	1369	4	1500	<2000	88, 99, 99, 99, 99, 103, 101, 102, 102, 104, 109, 100, 100, 134
17	1300	2	1500	<2000	111, 96, 99, 100, 100, 101, 100, 100, 100, 101, 103, 103, 99, 100, 104, 125
18	1330	6	1500	<2000	82, 126, 95, 100, 103, 102, 110, 102, 104, 102, 102, 103, 103, 103, 101, 102, 101, 128
19	1330	8	1500	<2000	101, 101, 102, 102, 102, 102, 102, 105, 104, 102, 103, 110, 98, 131

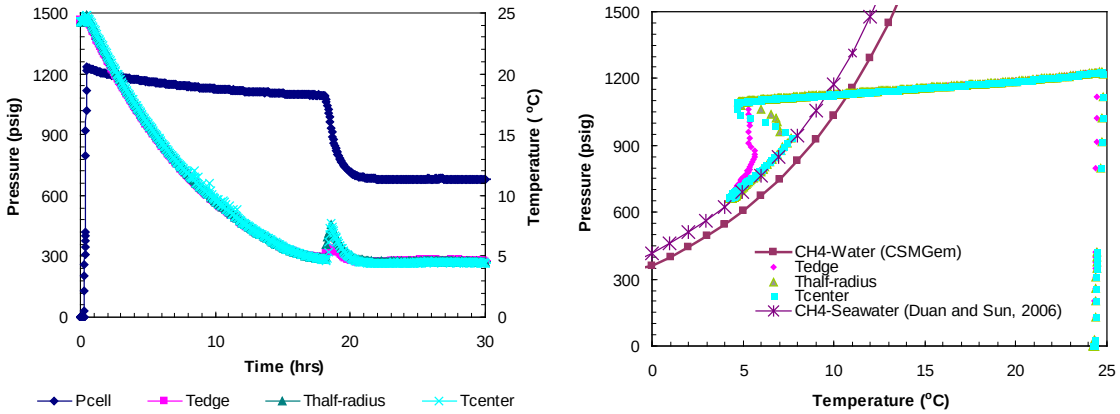

(a) **(b)**

FIG. 6.2. (a) Cell pressure and temperatures within the sand-core (edge–T1, half-radius–T2 and center–T3) against time during methane charging and subsequent hydrate formation for Run 14. (b) Comparison of cell pressure against core-temperature during hydrate formation for Run 14 with a seawater-bulk methane hydrate stability curve.

In a similar experiment (Run 15), with a methane charging pressure of 1327 psig and similar cooling rate as in Run 14, the system PT conditions entered into hydrate stability region after ~10.5 hours of cooling (Fig. 6.3(a)). However, hydrate formation initiated at ~22.4 hours i.e. ~11.9 hours after system PT conditions entered into hydrate stability region. Consequently, the system PT reached to equilibrium conditions (~671 psig, 4.25^{o}C) for a methane-seawater system as shown in Fig. 6.4(b). For the 1369 psig charging run (Run 16), the hydrate formation began to appear at 37.1 hours i.e. 29.3 hours after system entered into the hydrate stability region at 7.9 hours in Fig. 6.4 (a). Figure 6.4(b) shows system PT conditions which follow the theoretical methane-seawater equilibrium (669 psig, 4.16^{o}C) at the end of the formation event in Run 16. Table 6.3 summarizes hydrate formation time measured after the system PT conditions entered into the methane hydrate-seawater stability region for Runs 14-16.

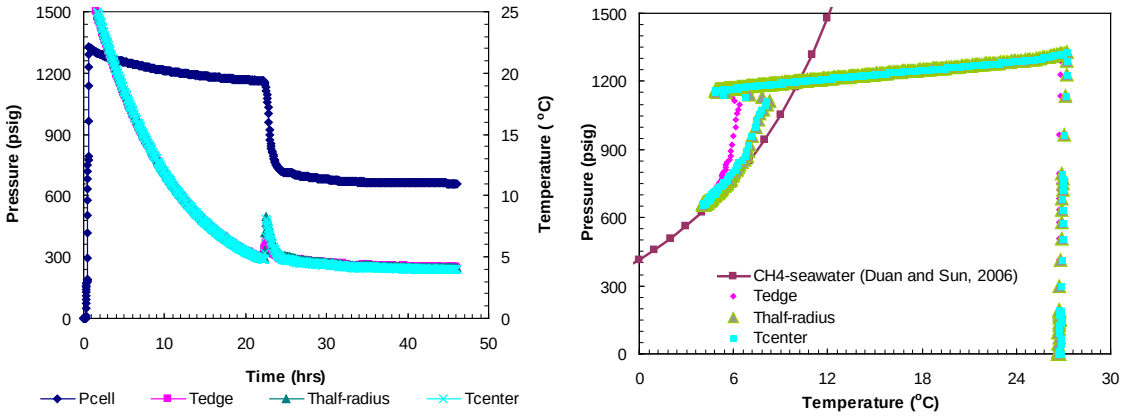

(a) **(b)**

FIG. 6.3. (a) Cell pressure and temperatures within the sand-core (edge–T1, half-radius–T2 and center–T3) against time during methane charging and subsequent hydrate formation for Run 15. (b) Comparison of cell pressure against core-temperature during hydrate formation for Run 15 with a seawater-bulk methane hydrate stability curve.

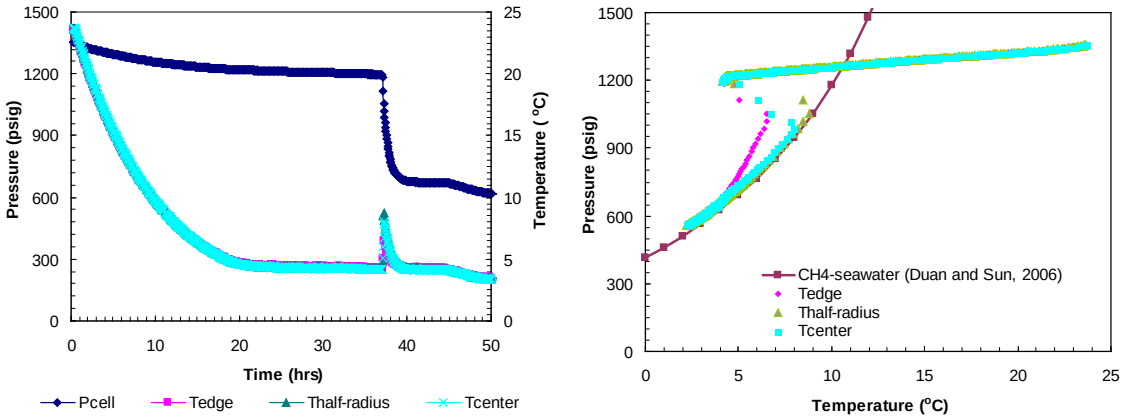

(a) **(b)**

FIG. 6.4. (a) Cell pressure and temperatures within the sand-core (edge–T1, half-radius–T2 and center–T3) against time during methane charging and subsequent hydrate formation for Run 16. (b) Comparison of cell pressure against core-temperature during hydrate formation for Run 16 with a seawater-bulk methane hydrate stability curve.

Table 6.3. Summary of the effect of pore-pressure/consolidation on the kinetics of methane hydrate formation runs (14-16) at a constant confining pressure and cooling rate.

Run #	Pore Pressure	Confining Pressure	Effective Pressure	Time for hydrate formation after system PT enters into hydrate stability region
	psig	psig	psig	hrs.
14	1231.6	1500	268.4	9.39
15	1327.1	1500	172.9	11.86
16	1368.7	1500	131.3	29.27

The effective pressure is inversely related to the coefficient of compression/compression index (Cc), which is defined as the slope of a plot of void ratio[1] (e) and logarithm of effective stress (σ') as shown in Eq. 1 (Das, 2001). Hence, as the effective stress increases, the coefficient of compression decreases with the degree of consolidation.

$$Cc = \frac{\Delta e}{\log_{10} \frac{\sigma_2'}{\sigma_1'}} \quad (1)$$

Clearly, hydrate formation was found to be delayed with increasing pore pressure or consolidation. This is consistent with Kleinberg et al. (2003) where hydrate formation kinetics were studied at sub-seafloor PT conditions mimicked in a 2 inch diameter and 11.8 inch in length Berea sandstone. Yousif and Sloan (1991) also performed similar experiments with lower permeability (8.388×10^{-2} μm^2) (mean pore radius: 3.5 μm) Berea sandstones at a confining pressure of 145 psi where a long formation time (~40 hours) was observed followed by the slow growth of hydrates in the pore space. In the most permeable Berea sandstone core, no hydrate formation was seen until the first hour and slow accumulation thereafter over the next 5 hours.

[1] Void ratio (e) is defined as a ratio of unit volume of voids and unit volume of solids. It is expressed in therms of porosity (ø) as ø/(1-ø).

Hydrate formation was observed through temperature spikes due to the exothermic nature of hydrates during formation. The temperatures at lateral and radial positions within the sample were monitored with thermocouples placed at the outer core surface (T1), half-way radius (T2) and the center of the core (T3). During formation, the uneven temperature spikes at the center, half-radius and boundary of the core indicate that hydrates formed more predominantly inside the core than at the core-boundary (Fig. 6.5).

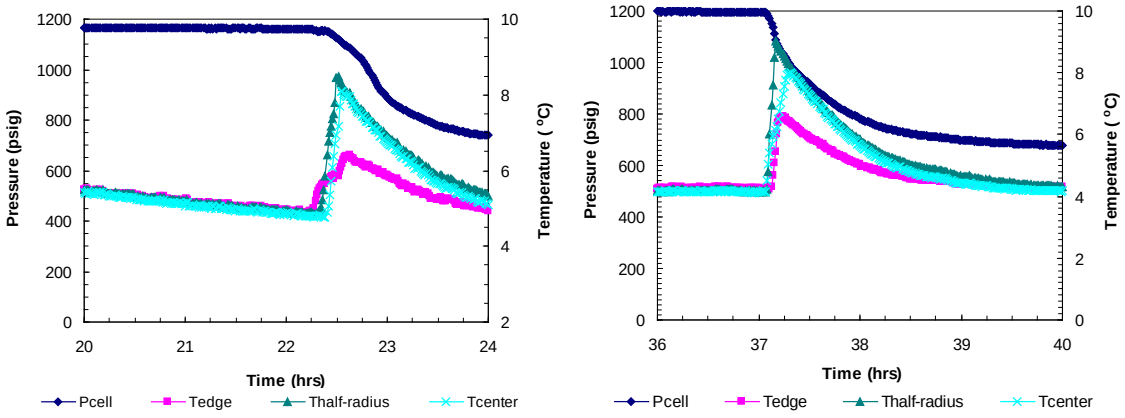

FIG. 6.5. A magnified view of cell pressure and exothermic core-temperatures (edge–T1, half-radius–T2 and center–T3) spikes against time during hydrate formation in (a) Run 15 and (b) Run 16.

6.2.2 Kinetics of Dissociation of Methane Hydrates by Step-wise Depressurization at a Constant Temperature (Runs 14-16)

The dissociation was achieved with a step-wise depressurization from the hydrate equilibrium pressure at a bath temperature. The entire dissociation event for Run 14 is shown in Fig. 6.6(a). The dissociations at each depressurization step were short lived. As output gas was produced due to the depressurization, sediment temperature dropped due to the endothermic hydrate dissociation and gas expansion. It is evident that the greater the pressure drops during dissociation, the higher the degree of cooling, and a longer time period was observed for sediments to reach initial *in-situ* temperature.

The second pressure drop of 139.6 psi during the dissociation of Run 14 resulted in the sediment cooling as low as 3°C. As the resultant gas output ceased, the cell exit valve was closed after which sediment temperature was allowed to increase up to the bath temperature. This allowed all dissociations at a constant bath temperature. Figure 6.6(b) shows post-depressurization PT equilibrium during sediment warm-up to the bath temperature. The post-depressurization dissociation was thermally induced where the system followed hydrate PT equilibrium. However, this effect was seen until hydrates were present within sediments. After the fourth pressure drop (dp4) of 73.8 psi, all hydrates were dissociated and subsequent post-depressurization curves represent methane gas warm-up. The post-depressurization responses for hydrates were slightly shifted towards higher pressure from the theoretical pure methane hydrate-seawater PT stability curve (Fig. 6.6(b)). This was due to the minimal excess pore (pore diameter: 48.28 - 58.65 µm) pressure generated during subsequent thermally induced dissociations.

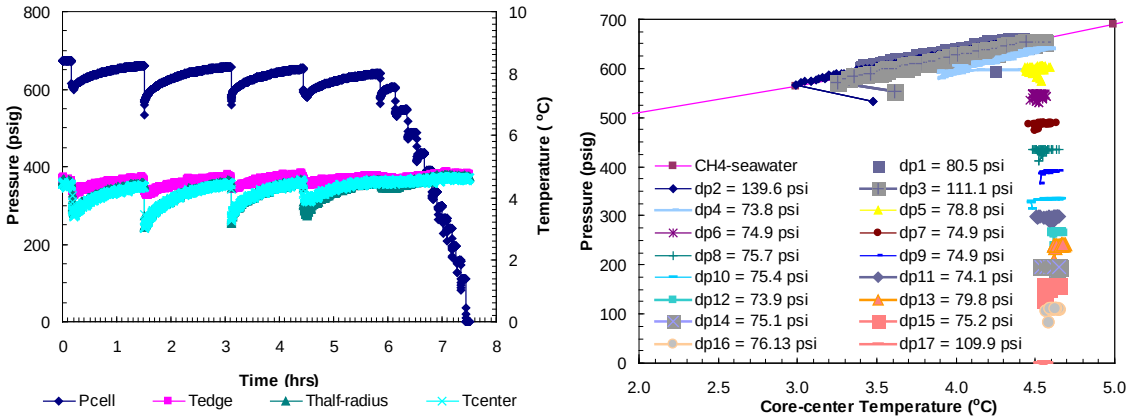

(a) **(b)**

FIG. 6.6. Cell pressure and temperatures within the sand-core (edge–T1, half-radius–T2 and center–T3) against time (a) during dissociation with varying pressure drops from equilibrium pressure in Run 14. Post-depressurization equilibrium pressure against core-center temperature conditions of methane hydrates in porous media are shown in plot (b). Each plot corresponds to core conditions during thermally induced dissociations after each depressurization step. Equilibrium conditions of methane hydrates–seawater were obtained from Duan and Sun (2006).

The hydrates formed in Run 15 were dissociated with pressure drops (dp1-dp5) ranging between 99.5 to 133.9 psi from the equilibrium pressure at bath temperature of ~4^{o}C (Fig. 6.7(a)). The post-depressurization PT conditions shown in Fig. 6.7(b) indicates that the PT equilibrium after each five pressure drops (dp1-dp5) followed theoretical PT stability curve for bulk methane hydrates from seawater with a minimal effect of excess pore pressure (Fig. 6.7(b)). This post-depressurization PT equilibrium also represents thermally induced hydrate dissociation. The pressure drops following the first five do not affect sediment temperature, which confirms complete hydrate dissociation.

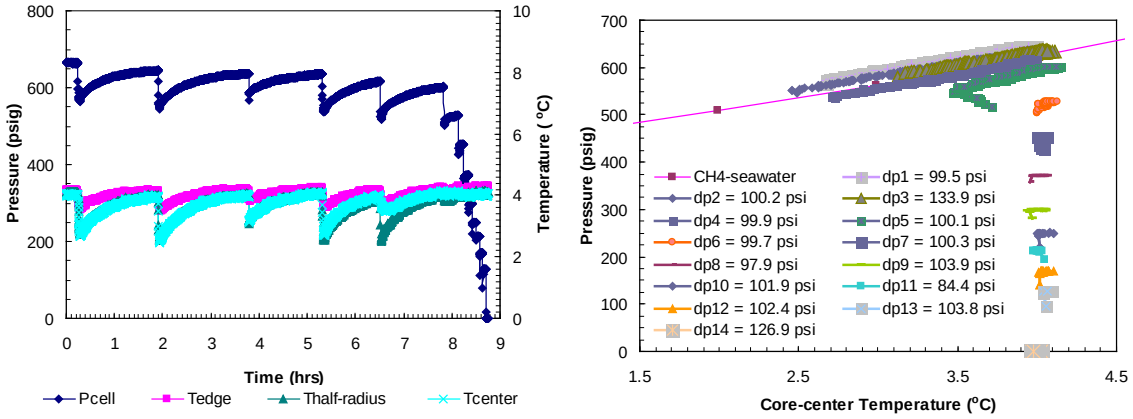

(a) **(b)**

FIG. 6.7. Cell pressure and temperatures within the sand-core (edge–T1, half-radius–T2 and center–T3) against time (a) during dissociation with varying pressure drops from equilibrium pressure in Run 15. Post-depressurization equilibrium pressure against core-center temperature conditions of methane hydrates in porous media are shown in plot (b). Each plot corresponds to core conditions during thermally induced dissociations after each depressurization step. Equilibrium conditions of methane hydrates–seawater were obtained from Duan and Sun (2006).

In Run 16, the dissociation was carried out with a series of pressure drops (dp1-dp7) ~89 – 100 psi from the hydrate equilibrium pressure at the bath temperature (~4^{o}C) attained at the end of the formation. The post-depressurization PT equilibrium (Fig. 6.8(b)) confirms complete hydrate dissociation after the seventh pressure drop (dp7) of

100.7 psi. With an individual pressure drop of similar order in Run 15 (Fig. 6.7(b)) and 16 (Fig. 6.8(b)), the number of pressure drops to dissociate hydrates in Run 16 is higher than that required in Run 15. This may be due to the higher hydrate saturation in Run 16 as a result of the elevated methane charging pressure.

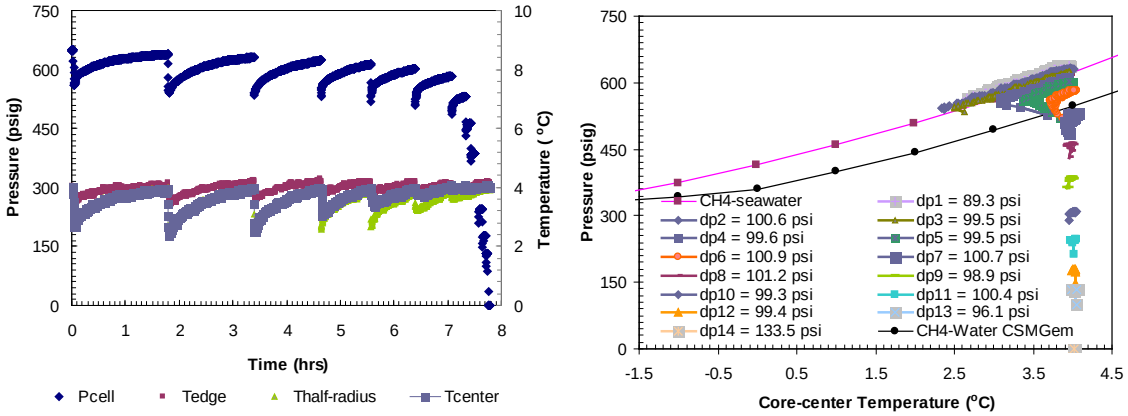

(a) **(b)**

FIG. 6.8. Cell pressure and temperatures within the sand-core (edge–T1, half-radius–T2 and center–T3) against time (a) during dissociation with varying pressure drops from equilibrium pressure in Run 16. Post-depressurization equilibrium pressure against core-center temperature conditions of methane hydrates in porous media are shown in plot (b). Each plot corresponds to core conditions during thermally induced dissociations after each depressurization step. Equilibrium conditions of methane hydrates–seawater were obtained from Duan and Sun (2006).

Figure 6.9 for Run 15 compares the thermocouple responses during dissociation from the first four (dp1-dp4) pressure drops to examine the preferential hydrate dissociation due to depressurization. The steep slopes for the core center and half-radius temperature indicate that the dissociation was found to be preferential in the center part of the core rather than at its boundary. It is also clear from thermocouple responses that the core boundary experiences a lesser degree of cooling during depressurization than half-radius and center of the core. This indicates that the hydrates may have been predominantly formed within the interior part of the core. However, as expected, during

thermally induced dissociation, the core boundary warms up at a faster rate than core half-radius and core center.

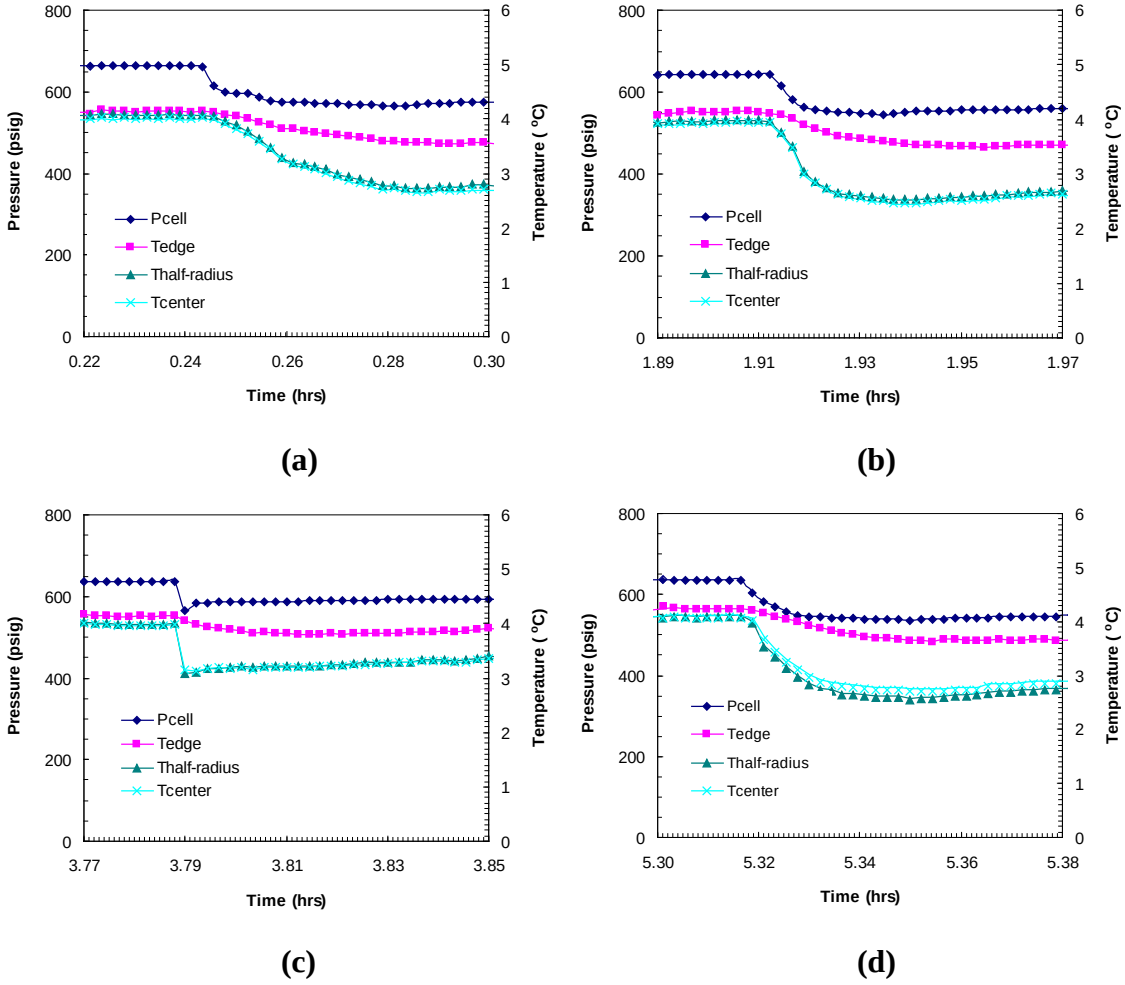

FIG. 6.9. Thermocouple responses at various core locations within the sand-core (edge–T1, half-radius–T2 and center–T3) during dissociation with (a) dp1 = 100 psi, (b) dp2 = 100 psi, (c) dp3 = 134 psi and (d) dp4 = 100 psi drops below hydrate equilibrium pressure in Run 15.

The enthalpy of hydrate dissociation was computed as a slope of a lnP vs. 1/[TRZ] plot for post-depressurization data from Run 14 (Fig.6.10), 15 (Fig. 6.11) and 16 (Fig. 6.12). Note that these values of enthalpy of dissociation of hydrates are from seawater and for an Ottawa sand-core (pore diameter: 48.28-58.65 μm) under a confining pressure of 1500 psig. The computed values are consistent but lower than those computed from theoretical PT data for bulk hydrates obtained from CSMGem (62.605 kJ/mol) and

that from methane-seawater equilibrium data obtained from Duan and Sun (2006). The lower values obtained from post-depressurization data than those for bulk conditions may be due to an excess pore pressure developed during thermally induced dissociation.

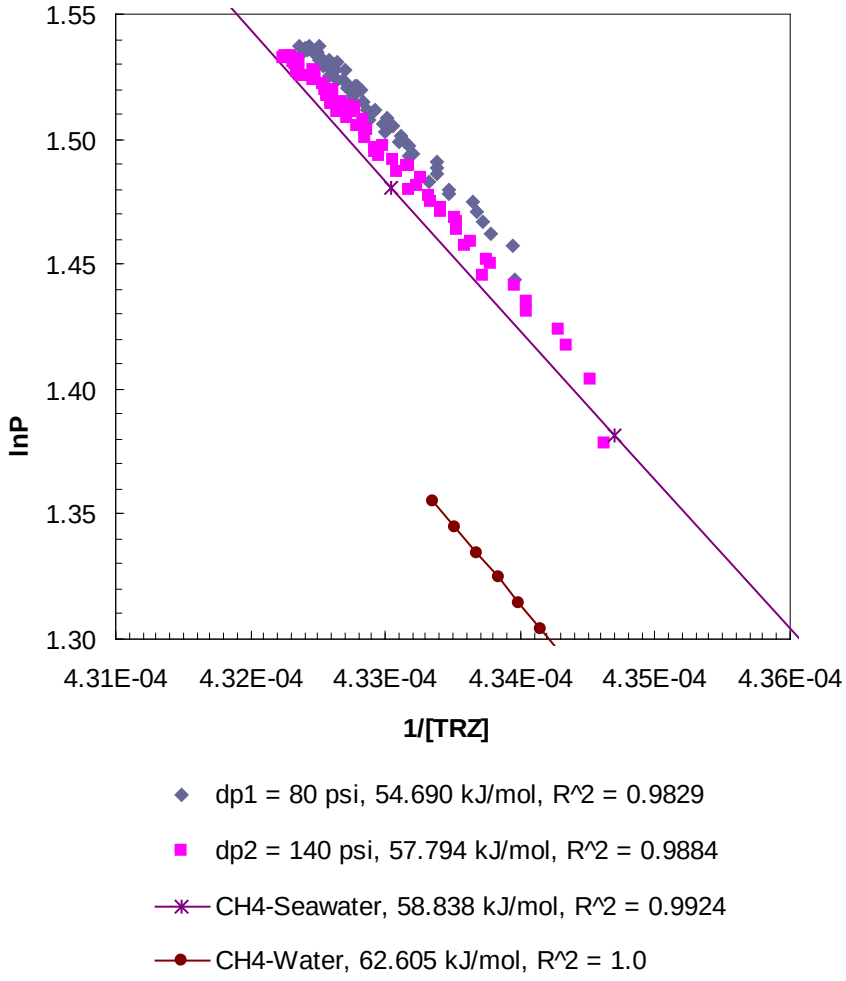

FIG. 6.10. Post-depressurization equilibrium pressure (lnP) against core-center temperature (1/[TRZ]) for Run 14 (dp1 and dp2). The Clausius-Clapeyron equation was used to calculate the enthalpy of dissociation (ΔH_{hyd} in kJ/mol) of methane hydrates from seawater in porous media at a confining pressure of 1500 psig. Equilibrium conditions of bulk methane hydrates-water obtained from CSMGem and those for bulk methane hydrates-seawater obtained from Duan and Sun (2006) were used to calculate the theoretical ΔH_{hyd}. The R^2 values indicate the correlation coefficient for the linear regression performed to compute the slope as ΔH_{hyd}.

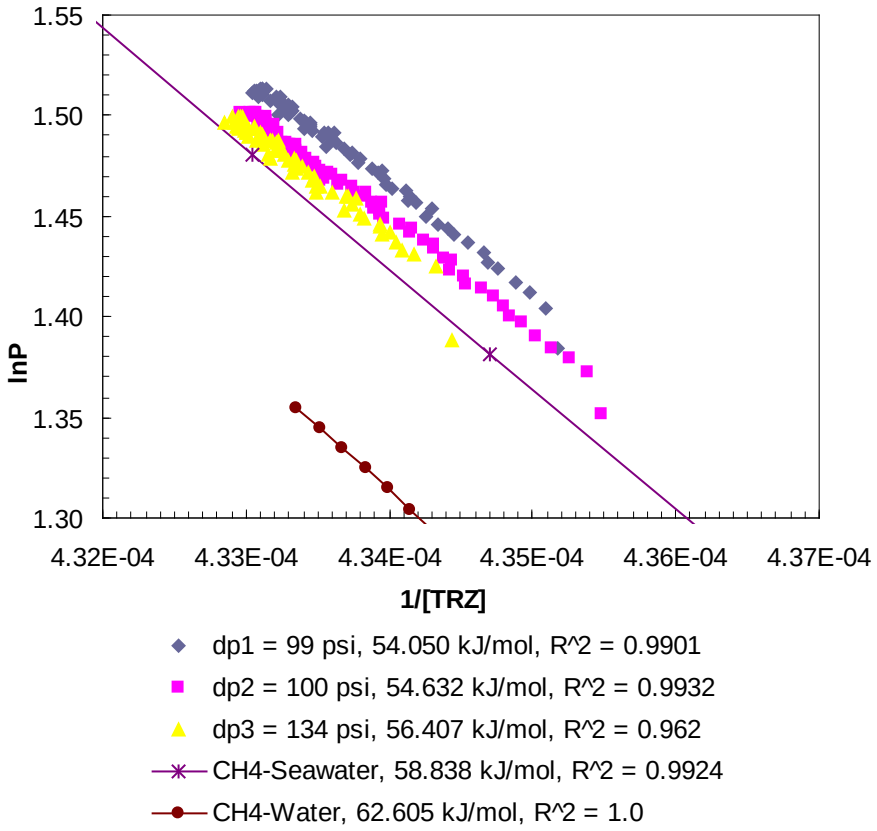

FIG. 6.11. Post-depressurization equilibrium pressure (lnP) against core-center temperature (1/[TRZ]) for Run 15 (dp1-dp3). The Clausius-Clapeyron equation was used to calculate the enthalpy of dissociation (ΔH_{hyd} in kJ/mol) of methane hydrates from seawater in porous media at a confining pressure of 1500 psig. Equilibrium conditions of bulk methane hydrates-water obtained from CSMGem and those for bulk methane hydrates-seawater obtained from Duan and Sun (2006) were used to calculate the theoretical ΔH_{hyd}. The R^2 values indicate the correlation coefficient for the linear regression performed to compute the slope as ΔH_{hyd}.

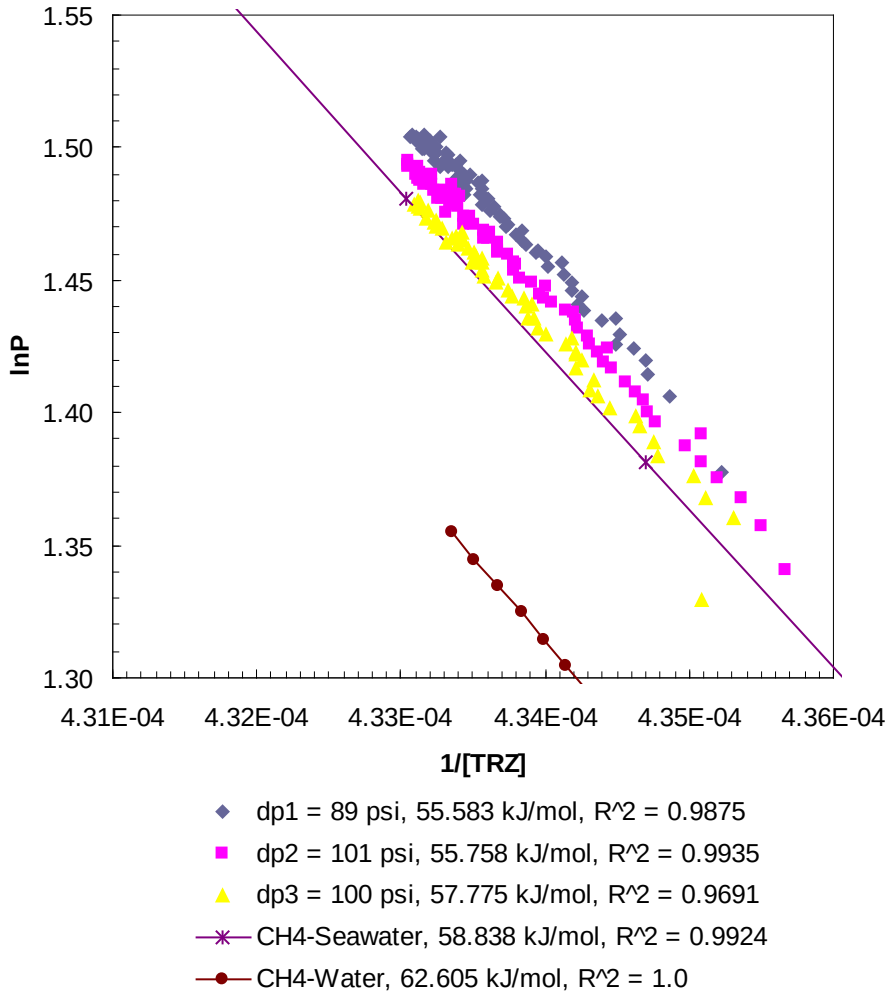

FIG. 6.12. Post-depressurization equilibrium pressure (lnP) against core-center temperature (1/[TRZ]) for Run 16 (dp1-dp3). The Clausius-Clapeyron equation was used to calculate the enthalpy of dissociation (ΔH_{hyd} in kJ/mol) of methane hydrates from seawater in porous media at a confining pressure of 1500 psig. Equilibrium conditions of bulk methane hydrates-water obtained from CSMGem and those for bulk methane hydrates-seawater obtained from Duan and Sun (2006) were used to calculate the theoretical ΔH_{hyd}. The R^2 values indicate the correlation coefficient for the linear regression performed to compute the slope as ΔH_{hyd}.

6.2.3 Kinetics of Dissociation of Methane Hydrates by Step-wise Depressurization at different Temperatures (Runs 17-19)

The Runs 17-19 were also performed with a formation method similar to the one that was utilized for Runs 14-16 i.e. the hydrate formation was achieved by a single gradual charging of methane through the completely seawater saturated sand-pack under confining pressure followed by cooling the cell down to the experimental temperature. However, the sediment/bath temperature was changed to 2, 6 and 8^{o}C in Runs 17, 18, and 19 respectively with a constant initial charging pressure of ~1300 psig and confining pressure of 1500 psig to investigate the effect of sediment temperature on (a) the degree of sub-cooling during each depressurization step and (b) the time scale for sediments to warm-up to the bath temperature after each depressurization and (c) to establish methane hydrate PT equilibrium in porous media at temperatures even lower and higher than previous runs (14-16).

In Runs 17-19, the dissociation of hydrates was achieved by the increasing series of pressure drops of ~100 psi from the equilibrium pressure for the methane hydrates-seawater system at the bath temperature. In Run 17, the endothermic cooling responses observed at all thermocouples for only the first ten pressure drops (dp1-dp10) below equilibrium pressure at bath temperature (~2^{o}C) confirmed complete hydrate dissociation in the system (Fig. 6.13 (a)). The presence of hydrates until the ninth pressure drop of 99.1 is also confirmed by the post-depressurization PT shown in Fig. 6.13(b) where plots for dp1 to dp9 follow theoretical methane-seawater PT curve obtained from Duan and Sun (2006).

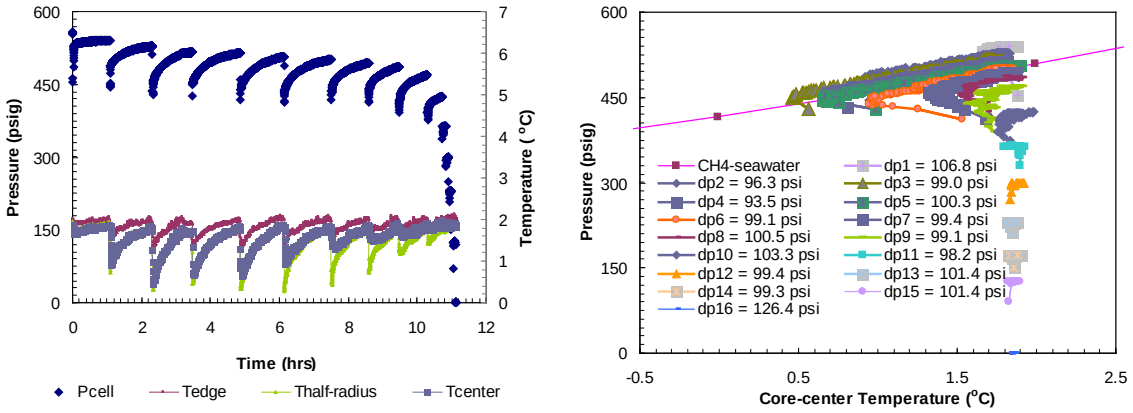

(a) **(b)**

FIG. 6.13. Cell pressure and temperatures within the sand-core (edge–T1, half-radius–T2 and center–T3) against time (a) during dissociation with varying pressure drops from equilibrium pressure in Run 17. Post-depressurization equilibrium pressure against core-center temperature conditions of methane hydrates in porous media are shown in plot (b). Each plot corresponds to core conditions during thermally induced dissociations after each depressurization step. Equilibrium conditions of methane hydrates–seawater were obtained from Duan and Sun (2006).

In Run 18, the dissociating pressure drops were in the order of ~100 psi from equilibrium pressure (~790 psig) at bath temperature of 6^{o}C. Once gas evolution ceased after each depressurization, the sediments were allowed to equilibrate while the cell pressure gradually rose to the equilibrium pressure as the sediment temperature increased up to the bath temperature (6^{o}C). From Fig. 6.14 (a) and (b), it is evident that after about ten pressure drops, all hydrates appear to have dissociated since the cell pressure did not come back to the hydrate equilibrium pressure and no endothermic cooling was observed within core.

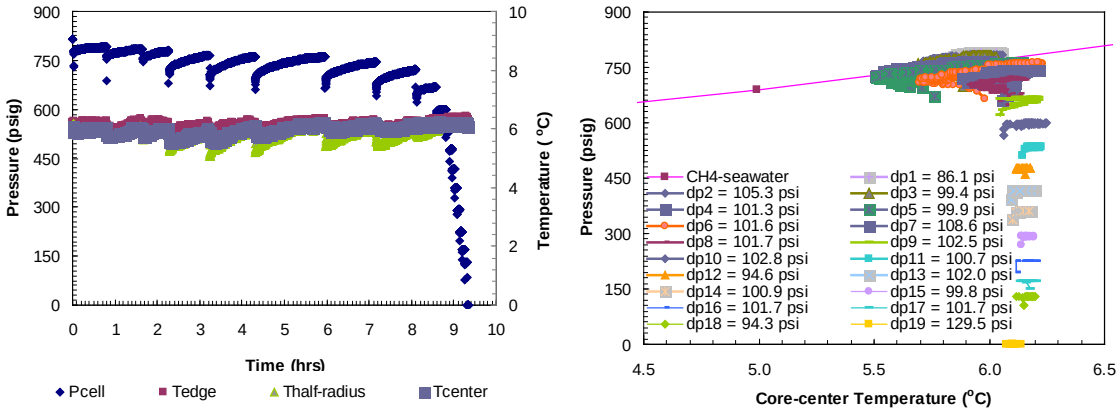

(a) **(b)**

FIG. 6.14. Cell pressure and temperatures within the sand-core (edge–T1, half-radius–T2 and center–T3) against time (a) during dissociation with varying pressure drops from equilibrium pressure in Run 18. Post-depressurization equilibrium pressure against core-center temperature conditions of methane hydrates in porous media are shown in plot (b). Each plot corresponds to core conditions during thermally induced dissociations after each depressurization step. Equilibrium conditions of methane hydrates–seawater were obtained from Duan and Sun (2006).

In Run 19, methane was charged up to 1330 psig and the sediment-seawater-methane system was cooled down to 8^{o}C (Fig. 6.15(a)). The system attained PT conditions of 1241 psig and 10.4^{o}C after ~8.7 hours of cooling to enter into hydrate-seawater stability region shown in Fig. 6.15(b). However no apparent signs of hydrate formation (sudden pressure drop or exothermic temperature profiles) were observed at the end of 140 hours of cooling to equilibrate system PT at 1070.3 psig and 8^{o}C. Dissociation was achieved with a series of pressure drops of ~100 psi from an equilibrium PT for the system. Figure 6.16(a) shows system PT against time during the entire event of dissociation. Figure 6.16(b) compares recorded system PT with methane-seawater equilibrium curve. It is evident from Fig. 6.16(a) that no endothermic cooling was recorded at any thermocouple during an entire dissociation event which indicates negligible hydrate formation in the system.

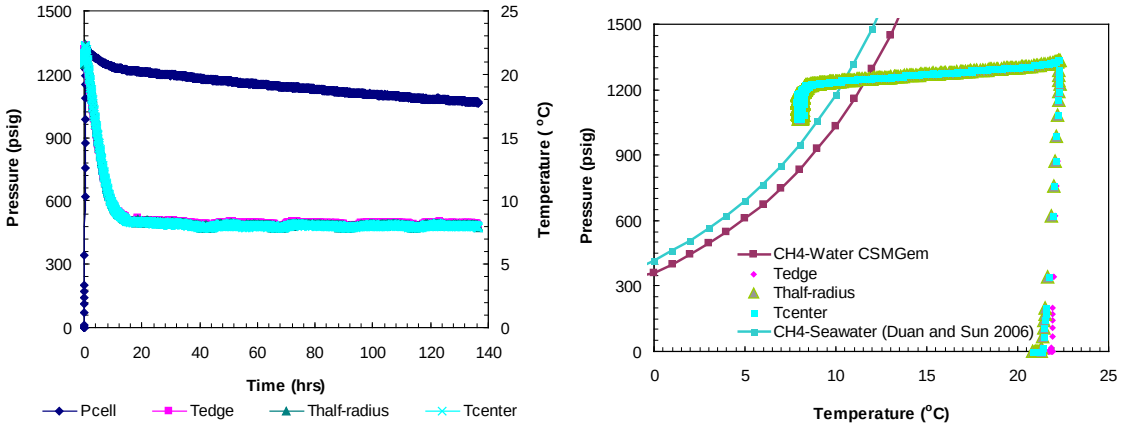

(a) **(b)**

FIG. 6.15. (a) Cell pressure and temperatures within the sand-core (edge–T1, half-radius–T2 and center–T3) against time during methane charging and subsequent hydrate formation for Run 19. (b) Comparison of cell pressure against core-temperature during hydrate formation for Run 19 with a seawater-bulk methane hydrate stability curve.

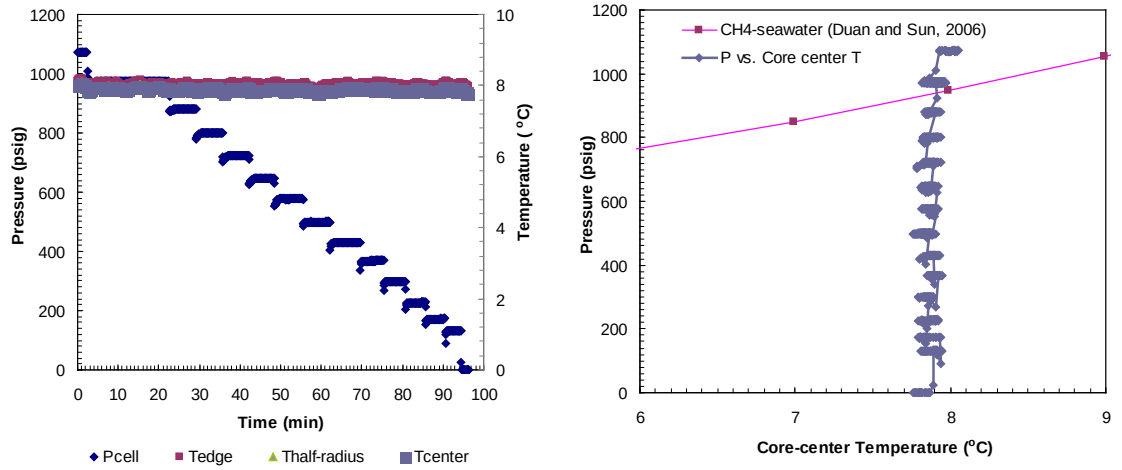

(a) **(b)**

FIG. 6.16. Cell pressure and temperatures within the sand-core (edge–T1, half-radius–T2 and center–T3) against time (a) during dissociation with varying pressure drops from equilibrium pressure in Run 19. Dissociation pressure against core-center temperature conditions are plotted against each other and compared with theoretical PT equilibrium conditions for methane-seawater in plot (b). Equilibrium conditions of methane hydrates–seawater were obtained from Duan and Sun (2006).

The dissociation was found to be preferential from the sample interior than its boundary in Runs 17-19 as well. This was established from thermocouples responses during short-lived dissociations at each pressure drop. Figure 6.17 depicts thermocouple responses due to depressurization during Run 17. The endothermic effect due to hydrate dissociation was recorded with a higher degree of cooling at center and half-radius thermocouples than that at core boundary. These observations are consistent with earlier experiences with a pure water-Ottawa sand system.

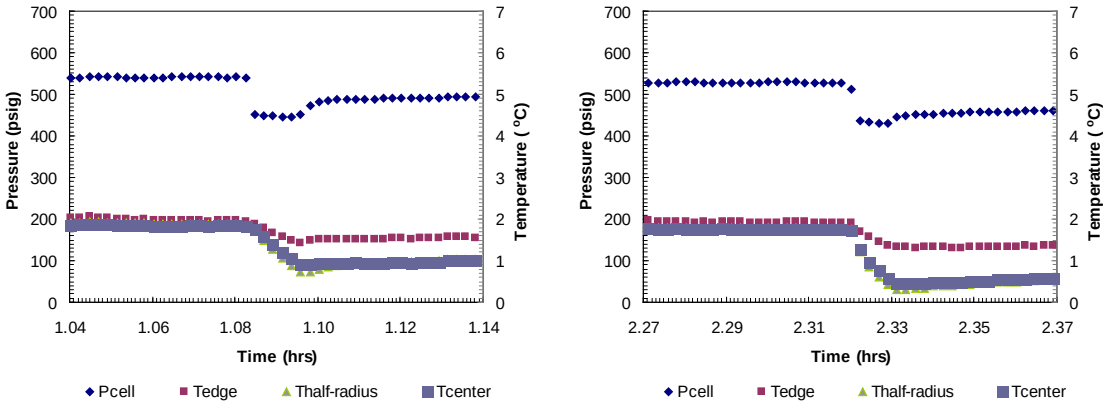

FIG. 6.17. Core-center thermocouple response during dissociation with similar pressure drops (a) dp2 = 96.3 psi and (b) dp3 = 99.0 psi below hydrate equilibrium pressure at sediment temperatures of 2^{o}C in Run 17.

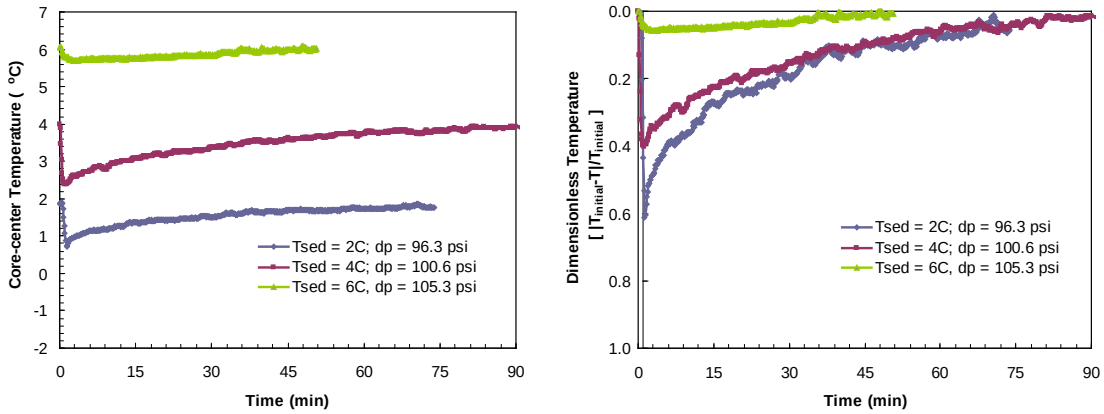

(a) **(b)**

FIG. 6.18. (a) Thermocouple response at half-radius of the core during dissociation with similar pressure drops below hydrate equilibrium pressure at sediment temperatures of 2°C (Run 17), 4°C (Run 16) and 6°C (Run 18). (b) Dimensionless sediment temperature change [$|T_{initial}-T|/T_{inital}$] against time for similar pressure drops for dissociation from sediments at 2°C (Run 17), 4°C (Run 16) and 6°C (Run 18). Runs 16, 17, 18 were performed at a constant confining pressure of 1500 psig.

It is clear from Run 14-19 that higher pressure drops during dissociation of hydrates at constant sediment temperature caused a larger degree of sediment-cooling. The higher degree of sediment cooling obviously requires a longer time for sediments to reach to the bath temperature. The degree of cooling of the sediment was also found to be dependent upon the sediment temperature for a constant pressure drop. Figure 6.18(a) compares the sediment cooling and subsequent time for warm-up to the bath temperature from Runs 16, 17, and 18 at similar pressure drops. The highest endothermic effect due to hydrate dissociation was observed when sediment temperature dropped as low as 0.73°C at core-center due to a pressure drop of 96.3 psi below the equilibrium pressure at ~2°C. Figure 6.18(b) depicts the sediment sub-cooling data from Fig. 6.18(a) on a relative dimensionless scale against time. It is obvious that lower sediment temperature causes a higher degree of cooling upon hydrate dissociation and in turn, takes a longer time to warm-up to its initial value.

Chapter 7

Direct Observations of Three Dimensional Growth of THF Hydrates (sII) Hosted in Porous Media

7.1. Literature Studies

Gas hydrates are known to occur worldwide in locations such as the permafrost regions as well as beneath the seafloor (Makogon, 1981; Sloan, 1998). Methane hydrates are prevalent where high pressure and low temperature conditions naturally coexist. Methane is about 17 times more potent as a greenhouse gas than carbon dioxide (CO_2), the possibility of rapid release of methane through methane-hydrate dissociation is of concern (Kennett, 2003). Therefore, improving our understanding of the geochemical and geotechnical aspects of hydrate formations, including the structure of hydrate in sediments during growth and dissociation is critical. At the grain-size scale, hydrates in sediments are classified as: cementing at grain contacts, grain coating, grain supporting, pore filling, or massive (Jin et al., 2004). The microstructure of sediment-hydrate interaction governs the mechanical strength of the formation or wellbores (Kleinberg et al., 2003), both of which may become unstable in the event of release of methane. Yun et al. (2005) found the greatest impact of hydrate on the skeletal stiffness of the sediments at a hydrate concentration of >40% during a study of the THF hydrate- sediment system.

X-ray computed microtomography (CMT) is well suited to study sediment-hydrate interaction because of its ability to make measurements over a range of size scales. Computed tomography (CT) images of hydrate cores recovered from Amazon Fan[7] indicated nodular structure. Jin et al. (2004) and Freifeld and Kneafsey (2004) characterized the porosity from 2-dimensional (2-D) images of artificial methane hydrate sediments and showed methane hydrate dissociation initiating at the walls of the vessel and progressing inwards. Sato (2005) investigated the density and hydrate saturation distribution of methane hydrates in Toyoura sand (average grain size 0.2 mm) at ~10 MPa and -30^{o}C with CMT.

Though most natural deposits contain methane, which forms structure I hydrates, sites such as the Mississippi Canyon 852/853 in the Gulf of Mexico contain structure II hydrates of mixed (C_1-C_5) hydrocarbons (Milkov and Sasses, 2003). The formation of methane hydrates in the laboratory can be simulated under high pressures (~10 MPa) and low temperatures (~0°C) conditions. However a 19 wt% solution of tetrahydrofuran (THF) and water (stoichiometric mole ratio of THF/H_2O = 1/17) forms structure II hydrate at 4.4^{o}C and atmospheric pressure (Fig. 7.1), making THF a convenient surrogate to understand hydrate growth. Mork et al. (2000) performed NMR imaging of THF hydrate in quartz sand. However the attempts to acquire CT images were unsuccessful due to the negligible density difference between the stoichiometric THF-water mixture (0.978 g/cc) and THF hydrate (0.971 g/cc). Tohidi et al. (2001) visually observed THF hydrate growth in the center of pores with coarse-grained micromodels and encapsulating in finer grained micromodels. Recently, Takeya et al. (2007) used CT at 35 keV to capture 3-dimensional (3-D) image of the THF hydrate crystals grown in a 19 wt% THF solution. However, utilization of the time-resolved CMT technique to monitor the growth of methane or THF hydrate in porous media has not been reported.

7.2 Experimental Conditions

In the present CMT study of THF hydrates in porous media, I focused on visualization of hydrate growth from a 60 wt% THF- 40 wt% H_2O-$BaCl_2$ /glass bead mixture at a micro scale (total volume ~1 mm^3) in a 1 mL polypropylene syringe-cell

fitted within a cooling jacket. The images were recorded using a charge coupled device (CCD) camera (pixel size = 3.93 μm, area = 1340 x 1035 pixels) with 3500-5000 ms exposure in a 0.15^{o} angular increment from angle 0 to 180^{o} at the 24-26 keV X-ray beam line at the National Synchrotron Light Source (NSLS) at Brookhaven National Laboratory (BNL) The particle size distribution of natural sediments typically span a broad range, however a uniform packing of 500 μm sized glass beads was used to remove the uncertainty related to this heterogeneity. The 25 wt% $BaCl_2$ solution was used to enhance the density contrast between aqueous THF and THF-hydrate; it also lowered the freezing point of the $BaCl_2$/Water solution to -6.85^{o}C. To initiate THF-hydrate formation, the solution was cooled with a circulating fluid at -3°C, above the freezing point of solution. Hydrate formation was monitored over 79 hours by scanning 10 tomograms. Of the 10, three were selected with reconstruction for 300 vertical pixels from each tomogram file and then converting them into a stack of jpegs using IDL tomography software. The conversion of each stack of images in to 3-D volume involved Cmtvis (Tomov and McGuigan, 2004) or ImageJ (Rasband, 2005) and volume rendering software, Drishti (Limaye, 2006). The final processing yielded contrasting images in which THF-Water, THF-hydrate, and glass beads could be differentiated based on their attenuation coefficients.

7.3 Results and Discussion

The hydrate formation appeared to start at a few locations in the system before the first images were taken at 28 hours. Figure 7.2 shows the growth pattern of THF hydrate and its interaction with glass beads. Time lapse bead-to-bead matching indicates that the growth of hydrates displaces beads within the unconsolidated pack. Further, the 2-D images show that the hydrate size and shape is independent of container-walls. These observations are consistent with previous NMR (Mork, 2000) and visual observations (Tohidi et al., 2001) and the random nature of the nucleation process.

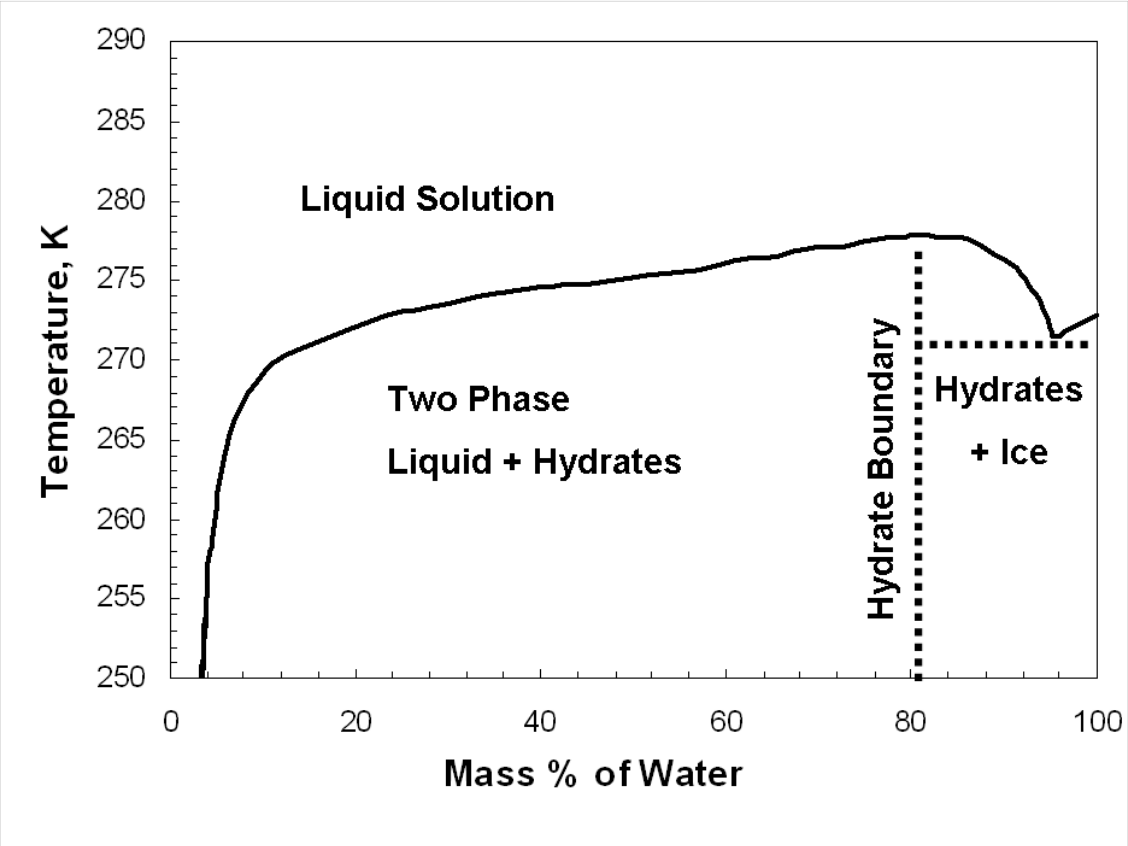

FIG. 7.1. THF-water phase diagram at 1 atmosphere (Yun et al., 2005).

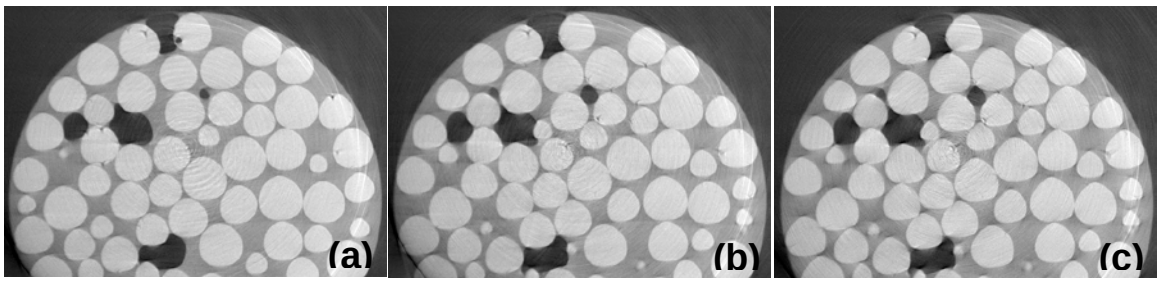

FIG. 7.2. Observation of random THF hydrate (black) growth hosted in glass beads (white spheres) is representative of 2-D cross sections (7 mm diameter). The images are recorded at (a) 54:06 h (b) 70:30 h (c) 74:07 h.

A magnified image of one of the growing hydrates from Fig. 7.2 is shown in Fig. 7.3. Clearly, the hydrates grow in pores in a manner similar to the pore-filling model described by Dvorkin et al (1999). This implies progressive but significant reduction of mechanical strength of the sediment upon dissociation of hydrates by retraction from the

pore walls followed by their shrinkage in the pore space (Kleinberg et al., 2003). The hydrate dissociation in large pores may trap gas within pores until hydrate saturation reaches low values, permitting the flow of gas. Away from grain surfaces, the hydrate surface is convex (Fig. 7.3) indicating that THF, not hydrate, is the wetting phase – presumably in the form of a thin film. This is analogous to ice growth in porous media in which a water film remains unfrozen (Kleinberg and Griffin, 2005; Anderson and Tice, 1971) and consistent with the contact angle arguments of Miller (1980) and Clennell et al. (1999).

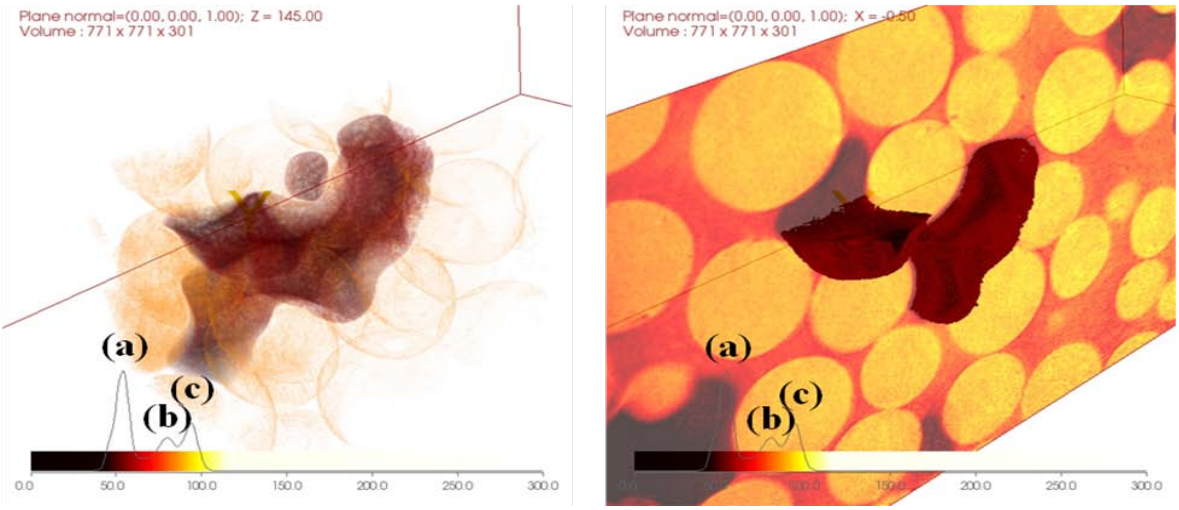

FIG. 7.3. 3-D images of THF-hydrate in glass beads. The image was reconstructed from 300 slices such as those shown in Fig. 7.2. The embedded bar and accompanying graph relates to absorption coefficients that clearly differentiate hydrate (a), liquid THF and water (b), and glass beads seen as faded spheres (c).

Figure 7.4(a) shows an 1119 μm x 1630 μm x 1443 μm volume after 29 hours of cooling. The volume rendering was adjusted to show only the growth of hydrates. Figures 7.4(b) and 7.4(c) reveal continuing hydrate growth in the same volume after 54 hours and 78.5 hours, respectively. Hydrate saturation values were 7.2, 8.1, and 8.8% respectively. The hydrate distribution is patchy even though the THF/H_2O/glass bead system is homogeneous. The patchy growth is consistent with the observation of the weak dependence of sound speed on natural hydrate saturation at low saturation values

(Tserkovnyak and Johnson, 2002). Note that the 60% THF: 40wt % H_2O solution used leaves excess THF.

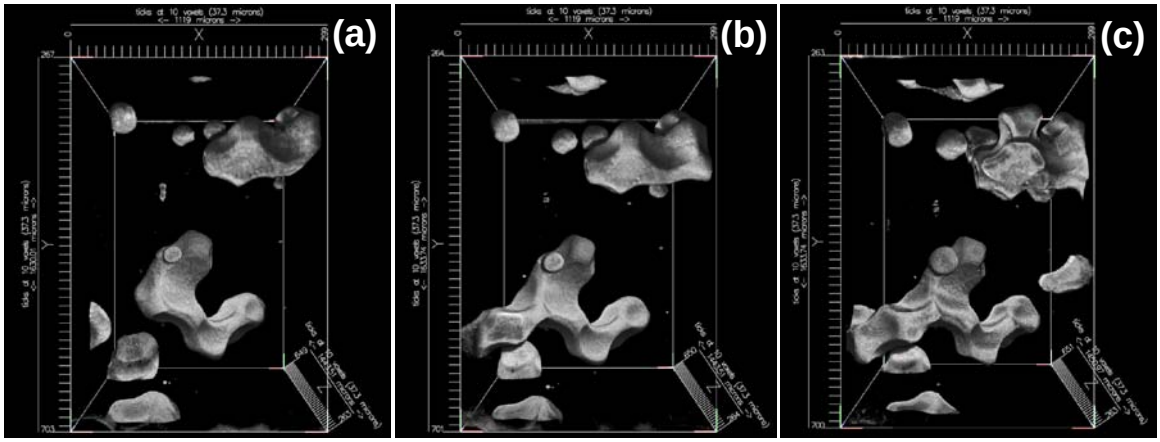

FIG. 7.4. Time resolved THF hydrate growth in glass beads serving as host. The 3-D structures are rendered from tomography scans at cooling times (a) 28:53 h, (b) 54:06 h and (c) 78:39 h. The glass beads are not shown to allow enhancement of the contrast for distinct observation of THF-hydrate growth (shown in grey scale).

The sample porosity was directly determined by segmenting the tomographic data into solid (glass beads) and pore (water) spaces based on the differences in their X-ray attenuation coefficients. The measured porosity value was 34.7%. This value is comparable to 38%, the theoretical porosity of a random dense pack of uniform spheres. The mean pore diameter for the 500 µm diameter (d_g) glass bead sample is calculated using Kozeny's equation (Eq. 1). The experimental porosity (φ) value of 34.7% leads to a pore diameter (d_p) of 177 µm.

$$d_p = \frac{2}{3}\frac{\phi}{1-\phi} d_g \,. \tag{1}$$

The contact angle between hydrate and glass bead is obtainable directly from analysis of cross sections through the volume tomographic data. Typical results are shown in Figs. 7.5(a-c). The value for the contact angle measured in this way was 140.7° averaged over five measurements.

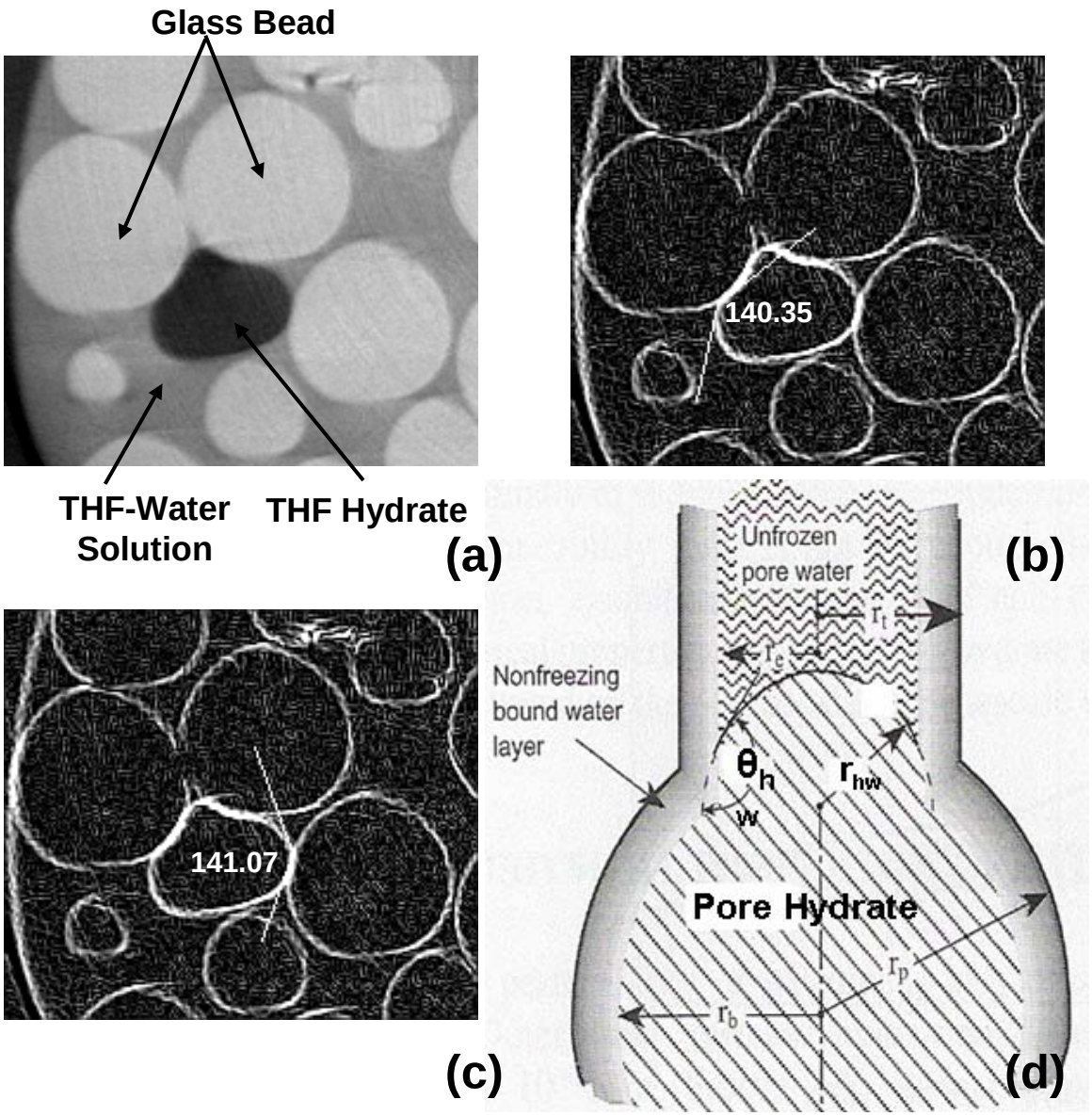

FIG. 7.5 Contact angle measurement and capillary model of hydrate in pores (d) (adapted from Clennell et al. (1999)). A convex contact angle (b), (c) are analyzed with 'angle tool' in ImageJ after processing a 2-D image (a) from a vertical stack with tool such as 'find edges' followed by 'sharpen' in ImageJ.

Fig. 7.5(d) is adapted from Clennell et al (1999) to describe hydrate formation within pores. Upon sufficient temperature depression, a convex hydrate front moves from larger pore (r_b) into a smaller cylindrical channel (r_e) with a nonfreezing layer of

water layer at the pore wall. The Gibbs-Thomson equation (Jallut et al., 1992) can be written for the hydrate-water system within pores as Eq. 2.

$$T_{pore} - T_{bulk} = \frac{2\gamma_{hw} T_{bulk} \cos\theta_{hw}}{\rho_h \Delta H_f r_e} = \frac{\frac{N}{m}.K}{\frac{kg}{m^3}.\frac{J}{kg}.m} \quad , \qquad (2)$$

In Eq. 2, γ_{hw} is the surface energy between hydrate and water, θ_{hw} and ρ_h are the contact angle and density of hydrate respectively and ΔH_f is the enthalpy of melting. The depression of freezing temperature in pores (T_{pore}) below the bulk freezing temperature (T_{bulk}) depends on the pore radii (r_e) and the contact angle for the hydrate. The growth of ice and hydrate is argued to be similar (Kleinberg and Griffin, 2005; Jallut et al., 1992). The surface free energy of the water-ice interface can be approximated for the water-hydrate interface ($\gamma_{hw} = \gamma_{iw} = 0.032$ J/m^2) (Kleinberg and Griffin, 2005). I calculated the dependence of the equilibrium temperature shift on the pore radius for THF hydrates and methane hydrates using the measured contact angles from the reconstructed 2D images (Fig.7.5) and substituting them in Eq. 2. These data were used to plot the temperature depression ratio (T_{pore}/T_{bulk}) versus capillary radius shown in Fig. 7.6. For reference, the ice-water case in which water is assumed to be the wetting phase (contact angle = 180^o) is shown in Fig. 7.6, plot a. The specific enthalpy of dissociation and the density of THF hydrate values of 263.15 kJ/kg (Tombari et al., 2006) and 971 kg/m^3, respectively, were used to construct a plot for THF hydrate (Fig. 7.6, plot c) based on Eq. 2. The summary of parameters used is included in Table 7.1.

Table 7.1. Summary of parameters used to plot the temperature depression ratio (T_{pore}/T_{bulk}) versus capillary radius.

	Ice-Water	Turner et al.[a]	Our Study	Our Study
	----	CH_4HYD	THFHYD	CH_4HYD
γ, N/m	3.20×10^{-2}	2.67×10^{-2} [b]	2.67×10^{-2} [b]	2.67×10^{-2} [b]
θ, deg	180	180	140	140
ρ, kg/m^3	916	910 [a]	971	910 [a]
ΔHf, J/kg	3.34×10^{5} [c]	4.36×10^{5} [a]	2.63×10^{5} [d]	4.36×10^{5} [a]

a. D. J. Turner, R. S. Cherry, E. D. Sloan, Fluid Phase Equilibria, 228-229, 505-510 (2005).

b. M. B. Clennell, M. Hovland, J. S. Booth, P. Henry, W. J. Winters, J Geophysical Res., 104, B10, 22985-23003 (1999).

c. R. M. Rueff, E. D. Sloan, Ind. Eng. Chem. Process Des. Dev., 24, 3, 882-885 (1985).

d. E. Tombari, S. Presto, G. Salvetti, G. P. Johari, J. of Chemical Physics, 124, 154507 (2006).

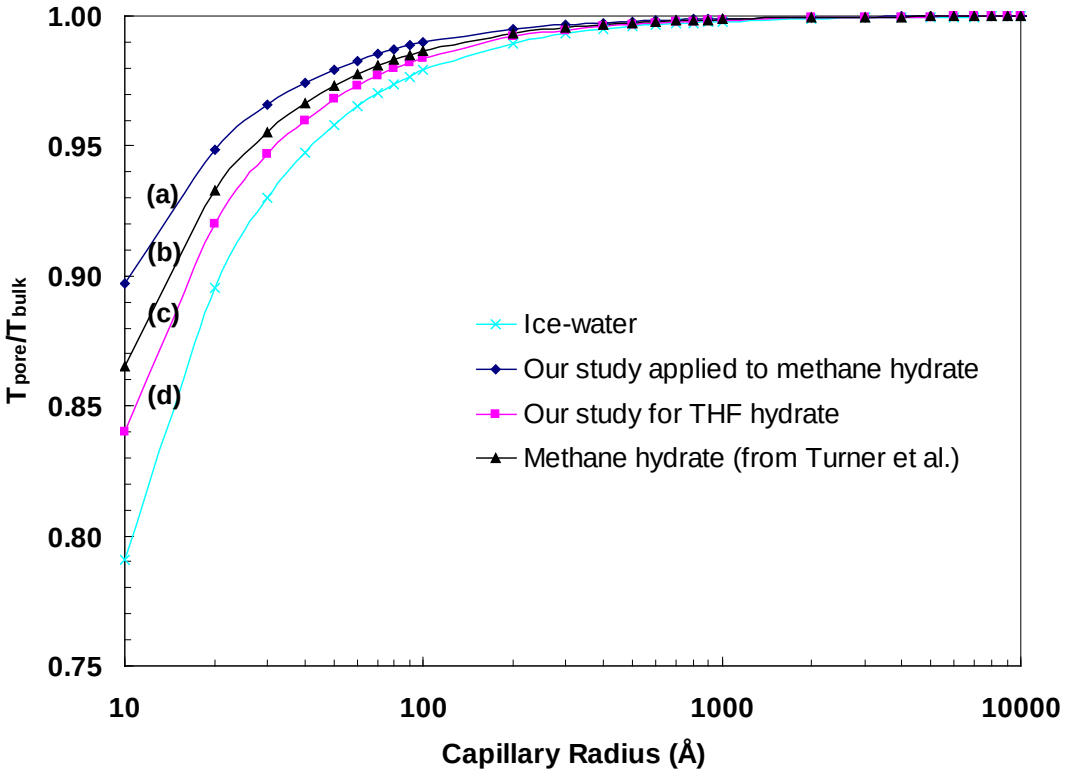

FIG. 7.6. Effect of pore radii and contact angle on equilibrium temperature shift for present THF hydrate analysis, its extension for methane hydrate.

It is apparent from plots a-d in Fig. 7.6 that for capillary radii greater than 1000 Å, the T_{pore}/T_{bulk} value is ~1 suggesting negligible effect of the pore radii and contact angle terms on temperature depression. For the present THF hydrate system, with glass beads of 500 μm uniform diameter and 34.7% porosity, the pore radii was calculated to be 177 μm (1.77×10^6 Å), the value that lies far right of the plot. Fig. 7.6, plot d shows a plot for

the methane hydrate system obtained from the data by Turner et al. (2005). Note that the sign conventions of Turner et al. differ from ours. The right hand side of their Eq. (2) (my Eq. (2)) is preceded by minus sign, and a contact angle of $\theta = 0^o$ indicates perfect wetting by liquid water. In our work, $\theta = 180^o$ corresponds to perfect wetting by liquid water. Using the methane hydrate thermal properties cited by Turner et al. (2005), except for the use of a contact angle of $\theta = 140.7^o$ instead of 180^o, the calculated temperature depression values shown in Fig. 7.6, plot b were obtained, showing significant effect of the contact angle term. For fine host sediments such as those found at hydrate sites like the Gulf of Mexico, the smaller effective pores exhibit higher capillary pressure and increased specific surface energy between solid-liquid interfaces. This results in the liquid phase being thermodynamically favored down to lower temperatures in the smaller pores than that in the bulk.

A uniform distribution of hydrate in sediments has been generally assumed in the prediction of acoustic velocities (Dvorkin et al., 1999). The patchy growth of hydrate observed here radically alters the connection between hydrate saturation and the propagation of sound (Tserkovnyak and Johnson, 2002). The present study involved THF hydrate growing from excess THF in a mono-sized glass bead pack. If the same results extend to natural gas hydrate accumulations in the earth, the interpretation of seismic surveys and sonic well logs would need to be reconsidered.

Chapter 8

Imaging Time-Resolved Methane Hydrates (sI) Grwoth in Porous Media using Synchrotron X-ray CMT

8.1. Literature Studies

Gas hydrates are solid crystalline compounds in which hydrocarbon gases are caged in a lattice structure of water molecules. Numerous studies in the laboratory have established that the stability of this material is imparted through low temperature and high pressure conditions (Sloan, 1998). The common occurrence of methane hydrates in natural settings is now well established at sites such as those below the seafloor in the Gulf of Mexico (GoM) (Milkov, 2000), Blake Ridge (BLR) (Dickens et al., 1997), and Cascadia margin (Suess et al., 2001). Gas hydrates appear abundant within and below permafrost on the North Slope of Alaska (Collett et al., 1983), in the Mackenzie Delta in northern Canada (Bily et al., 1974), and in Russian Siberia (Makogon, 1981). The structural appearance of this sediment-hydrate material is site dependent. Whereas the hydrates at BLR occur as layers up to 15 cm thick of white, crystal-like "bubbles" resembling upside-down ice cream cones (Van Dover et al., 2003), those at the GoM sites are highly dispersed (Kastner et al., 2008). At the grain-size scale, hydrates in sediments are classified as cementing at grain contacts, grain coating (Dvorkin and Nur, 1996), grain supporting, pore filling (Dvorkin et. al., 1999; Helgerud et. al., 1999)., fracture

filling or as nodules (Dai et. al., 2004). The microstructural growth model for hydrates within the sediment matrix governs the elastic properties and the mechanical strength of the host. The sediment-hydrate texture changes that accompany dissociation of hydrates could implicate methane hydrates in seafloor instability and climate change (Kleinberg et al., 2003; Matsumoto et al., 2002).

The elastic properties versus hydrate saturations for the cores recovered from the Mallik 2L-38 well from northern Canada are comparable to the physical model of hydrate supporting grain matrix. On the other hand, gas hydrate coring from the Ocean Drilling Program (ODP) (Booth et.al., 1998) shows that hydrates are usually found as massive bodies, nodules, or layers that spread out as fracture fillings in the shallow shaly sediments. These results are consistent with gas hydrate cores recovered from varying sub-seafloor depths by ODP Leg 204 on the Cascadia margin (Abegg, 2006) imaged using X-ray computed microtomography (CMT). Results indicate that veinlet structures are predominantly found within samples obtained from deeper formations, whereas massive, dispersed, and bubble fabric structures are found at shallower depths. This may be due to lower overburden stress at shallower depths. On the other hand, ice or gas-hydrates from deeper sediments may give off gas without any changes in texture, implying stable gas seepage. However, the connecting pores of the gas hydrate or ice supported texture could fall apart and trap this gas in formations during dissociation (Katsube et. al, 2004). Commonly, seismic surveys are used to detect and estimate hydrates below the seafloor (Dai et al., 2008). Sonic properties are inverted to estimate elastic properties, porosity, and hydrate saturation from sediments. Though proposed models treat gas hydrates as homogeneously spread among the sediment, the natural core samples show these to be heterogeneous with varying hydrate saturations. Hence, it is critical to understand hydrate growth and sediment-hydrate interaction at the grain scale.

X-ray CMT has been used in past studies of hydrate-sediment interactions due to its ability to take images at grain scales. Soh (1997) imaged cores recovered from the Amazon Fan by computed tomography (CT) to show that the dissociation of a large nodule of gas hydrates produced a fluid-like cloud shaped structure with gas bubbles. Mikami et al. (2000) scanned CT images of natural hydrate samples and observed gas hydrates that simultaneously dissociated on exposed surfaces and inside pores. Jin et al.

(2004) defined porosity as the ratio of the area of pore space to the total area from the 2-dimensional (2-D) images of laboratory-formed methane hydrates. Freifeld and Kneafsey (2004) recorded 2-D CT data during methane hydrate dissociations to show that the methane hydrate dissociation front begins near the walls of a pressure vessel and moves inwards to the center. Kneafsey et al. (2007) also recorded CT data during hydrate formation which illustrated that the density of sample increased throughout the formation event, but it increased the most in areas that initially had the smallest densities due to poor packing. Upon dissociation, the density decreased near the pressure vessel walls and spread over time. Upon reforming within the same sediment sample, the hydrates grew in a ring at the center of the cell rather than in places where dissociation had occurred. Sato et al. (2005) also studied density and hydrate saturation variations of methane hydrates with x-ray CMT.

Hydrates of tetrahydrofuran (THF) and methane have similar interfacial tension between water and the hydrate, and both types of hydrates have analogous growth structures in sediments (Lee, 2007). THF-hydrate, due to its formation at ambient pressure, has been a subject of several studies (Gough and Davidson, 1971; Rueff and Sloan, 1985; Yamamuro et al., 1987; Anderson and Suga, 1996; Santamarina and Ruppel, 2008). A 19 wt% solution of THF and water (stoichiometric mole ratio of THF/H_2O = 1/17) forms sII hydrates at 4.4^oC and atmospheric pressure, making THF a convenient surrogate to understand hydrate growth. Mork et al. (2000) used the nuclear magnetic resonance (NMR) technique to establish THF-hydrate formation but were unsuccessful in imaging by CMT since there is the small density difference between the THF-water mixture (0.978 g/cc) and the THF hydrates (0.971 g/cc). Tohidi et al. (2001) visually observed THF-hydrate formation in the pore centers instead of at the grain surface. Takeya et al. (2007) used a phase contrasting method to create density differences between the THF-water and THF-hydrate phase and successfully created 3-dimensional (3-D) CMT images of THF hydrate. Stevens et al. (2009) used magnetic resonance imaging (MRI) with sub-millimeter resolution to analyze hydrate formation in highly permeable sandstone of 125 μm pore size. Kerkar et al. (2009) performed time-resolved CMT of THF-hydrate hosted in 500 μm glass beads and created 3-D images. The formed hydrates fit the pore-filling model which is associated with reduction in mechanical

strength of the sediment upon dissociation (Kleinberg et al., 2003). Kerkar et al. (2009) also measured the contact angle between the hydrate and glass beads. The freezing point depression depends on the hydrate contact angle and the pore radius. For fine sediments such as those from GoM, the smaller effective pores (~2-5 μm) enhance the effect of contact angle on freezing point depression. In this study, we report imaging of the time-resolved growth of methane hydrate in porous media that has not been reported.

8.2 Experimental Conditions

Since the formation of methane hydrates requires high pressures (≥10 MPa), finding an appropriate material to construct the cell of about 10 mL volume has been a challenge. In the present work, a high pressure CMT cell (Fig. 8.1) was fabricated from a seamless aluminum alloy tube (1/4 inch outside diameter, total volume ~3.5 mL) and fitted within a cooling jacket using two bore-through heat-exchanger tees. The bottom of the tube could be plugged or used to insert a thermocouple. The top was connected to a valve and stainless steel quick-connect for loading the sample. Pressure and temperature values were recorded with a pressure transducer and a thermocouple. A safety 3-way relief valve was employed to release pressure from the system at any time during the experiment.

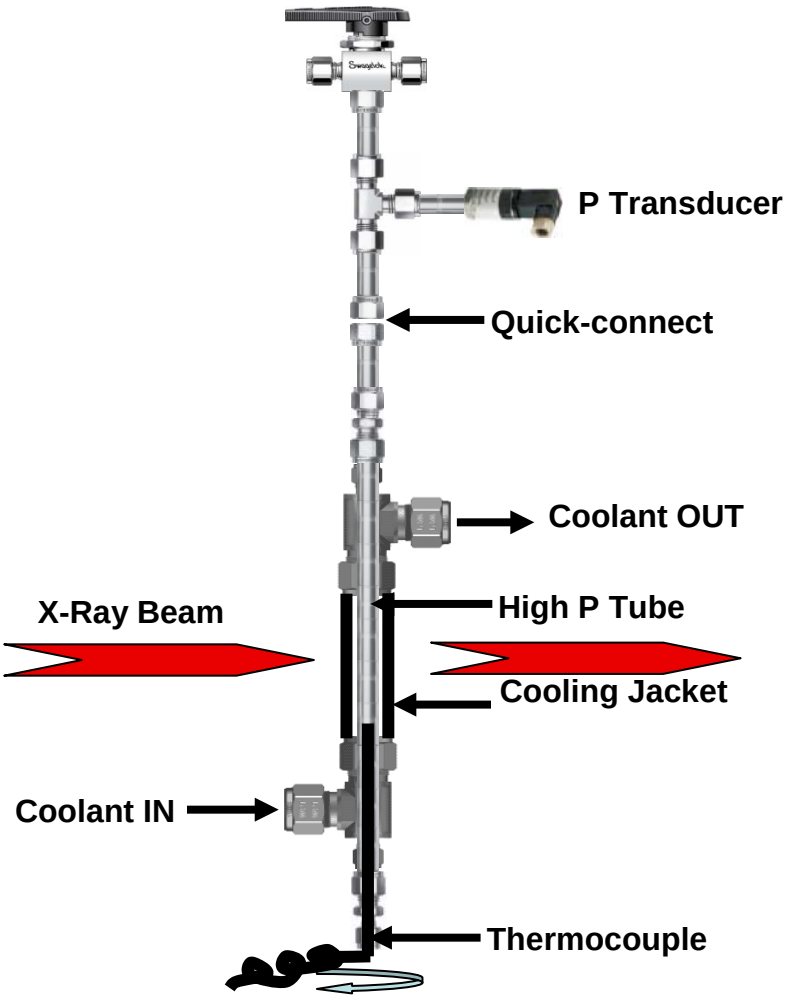

FIG. 8.1. High pressure methane hydrate CMT cell.

Methane hydrates typically nucleate at the gas-liquid (G-L) interface, and their further growth can be significantly reduced due to poor mass transfer across G-L boundary subsequent to initial formation (Sugaya and Mori, 1996). The mass transfer controlled growth of hydrates can be inhibited by reduced sample diameter or G-L interfacial area (Freer et al., 2001). In the present study, the cell was kept in a horizontal orientation throughout the hydrate formation event to maximize the G-L interface. The actual experiment involved flushing the cell with distilled water and compressed air, and then 3 g (bulk volume ~2 mL) of 500 μm uniform diameter glass beads were loaded into the cell. A 5wt% $BaCl_2$ solution (density 1.02 g/cc) was used to enhance the contrast between the hydrates (density 0.92 g/cc) and the aqueous solution. Once the cell was evacuated, methane was slowly charged until the target system pressure (~966 psig) (Fig.

8.2) was achieved. After the cell pressure equilibrated, the cell was transported to beamline X2B, at the National Synchrotron Light Source (NSLS), Brookhaven National Laboratory (BNL). At the NSLS, the cell was submerged horizontally into an ethylene glycol bath pre-chilled to -1^{o}C, just above the freezing point of the 5 wt% $BaCl_2$ solution (-1.4°C). After about 3 hours, the cell pressure dropped and stabilized, corresponding to about 13% conversion of pressurized methane into methane hydrate. Subsequently, the coolant flow regulated by another refrigerated circulator was turned on to maintain the cell temperature at about -1^{o}C. After the beamline parameters such as stage height, beam intensity, and focusing were adjusted, the cell was placed in vertical orientation into the beam for a tomographic run. Several tomograms were acquired with a beam intensity of 27-29 keV and 1200 images (pixel size: 7.42 μm) were taken every 0.15^{o} during the rotation of the sample through 0-180^{o}, with 3.5 sec exposure. The reconstructions were performed for each tomogram with 400 pixels in the y-direction to create a stack of 2-D cross-sectional images of the cell. Each stack of 2-D images was later combined into a raw file (Rasband, 2005) which was converted into a 3-D volume in Drishti (Limaye, 2006). The 3-D volume was rendered for a specific volume and fine tuned to show a specific phase based on its corresponding peak in a histogram.

8.3 Results and Discussion

Figure 8.3 shows the same cross-sectional image of the cell from the stacks of 2-D images created from different tomograms. The glass beads and interstitial aqueous solution are held together on one side of the cell with cementation due to formed hydrate and capillary forces. The images show that hydrates nucleate randomly in pores formed by randomly packed host glass beads, though the nucleation process may or may not involve the cell wall. The time-resolved 2-D growth (Fig. 8.3) indicates methane hydrates as convex and away from the grain. The patchy methane hydrate (sI) distribution seen is consistent with natural hydrate occurrence (Tserkovnyak and Johnson, 2002) and our previous observation of THF hydrates (sII) (Kerkar et al., 2009). The bead-to-bead matching indicates movement of beads during hydrate growth.

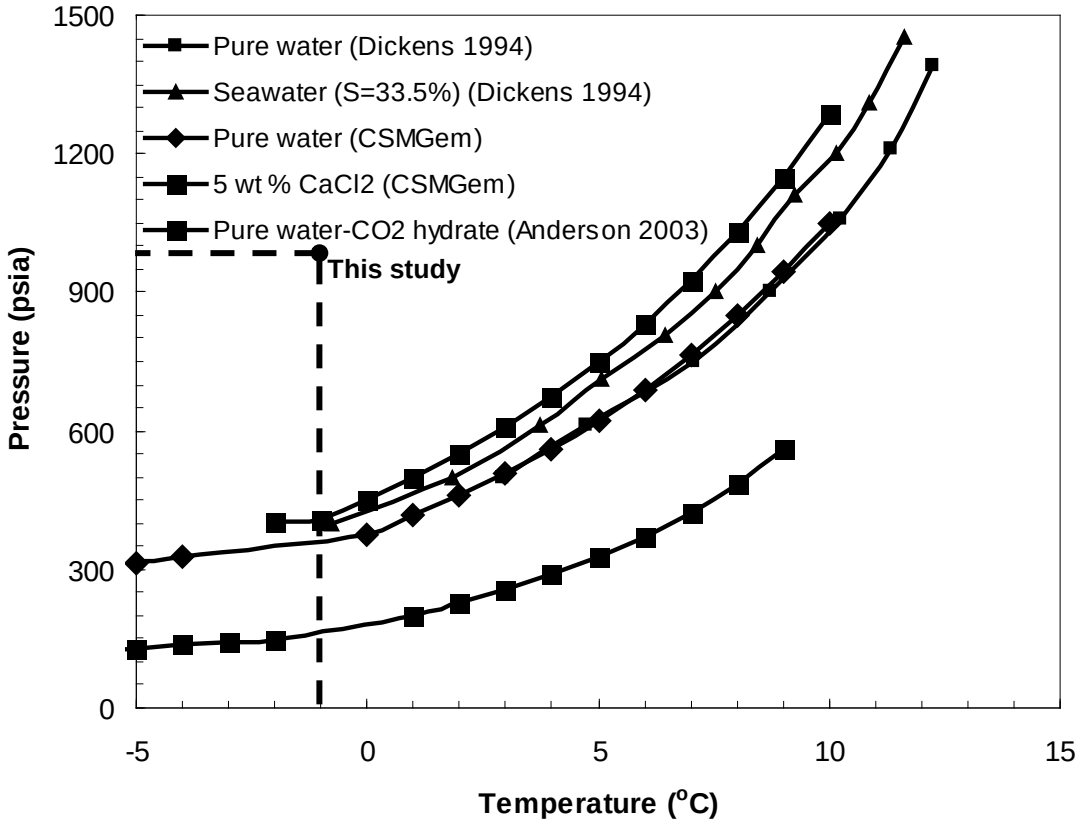

FIG. 8.2. Pressure- temperature stability diagram for formation of methane hydrate in pure water and seawater and CO_2 hydrate formed from pure water.

Figure 8.4 shows (a) 749 x 599 x 972 μm^3 and (b) 4793 x 4793 x 1462 μm^3 volumes after about 49.14 hours of cooling. The cell, beads, aqueous solution, or hydrate could be differentiated in color with their individual transfer functions based on the histogram. Figure 8.4 depicts that hydrates are suspended in an aqueous phase without any contact between them and the glass beads. The presence of an aqueous phase film (shown in yellow) around the glass beads confirms an aqueous phase, not hydrates as a wetting phase. This is also consistent with our previous findings with THF hydrates. This microstructure is categorized as a "pore-filling" according to the microstructural models of gas hydrate bearing sediments proposed by Dvorkin et al. (1999) and Helgerud et al. (1999). The pore-filling hydrates are assumed to change only interstitial fluid density and hence the bulk modulus of the pore fluid. The pore-filling growth of hydrates observed is

in agreement with earlier reported NMR measurements of methane hydrate saturations in Berea sandstones where hydrates were found to grow in the largest pores first (Kleinberg et al., 2003). The findings from this study are also consistent with observations from the cryogenic scanning electron microscopy (SEM) of hydrate cores recovered from the Mount Elbert gas hydrate test well, Milne Point area of the north slope of Alaska (Stern et al., 2009). Moreover, pore-filling hydrates have also been cited at the Mallik 2L-38 well site with hydrate saturations as high as 70-74% (Lee and Collett, 1999), the Nankai Trough offshore Japan (Matsumoto, 2002) and at the Tigershark well in the GoM (Smith et al., 2006).

Figure 8.5 shows time resolved methane hydrate growth. Methane hydrates appear to grow from the direction of the G-L interface, filling the pores formed by close packing of glass beads. As time progressed, hydrate growth was seen predominantly in the center of the cell. The observed time-resolved growth of hydrates into an agglomerate supports the "local-structuring hypothesis" by Hawtin et al. (2008) in which the random collective ordering of methane in the aqueous phase is assumed to induce the re-arrangement of water molecules in the vicinity to nucleate the hydrate network and then expand, forming a more solid structure. Hydrate saturation values estimated for a 4572 x 4572 x 2968 μm^3 volume of a tomogram are 1.5, 3.1, 3.5 and 3.8% after 15:15 h, 19:19 h, 24:54 h and 49:14 h. respectively. The low saturation values may be due to excess water conditions employed in the present analysis.

Based on the capillary model of ice growth in pores described by Clennell et al. (1999), the contact angle measurements were performed on a 2-D image obtained from a stack of images obtained after reconstructions. The image in a colored palette was enlarged (up to 400%) and sharpened and the angle tool in imageJ was utilized to draw and measure the contact angle. Several measurements were performed on different 2-D sections and glass bead-hydrate geometries. Figure 8.6 shows measured values of contact angles between 151.9^o and 156.6^o. These convex values are consistent with our earlier reported values for THF-hydrate but significantly different from the assumption of water as a wetting phase (contact angle = 180^o) in theoretical analyses of methane hydrate phase equilibrium in fine sediments.

The accuracy of the inversion of compressional (Vp) and shear (Vs) wave speeds obtained from well log data into hydrate saturations is significantly affected by the assumed microstructure of gas hydrates in sediments. Dai et al. (2008) used the average background properties of the gas hydrate well, 5L-38 from the Mallik site and plotted compressional and shear wave speeds with hydrate saturations for various microstructural models. The supporting matrix/grain microstructure which treats hydrates as load bearing was found to match hydrate saturations at the Mallik 5L-38 well as well as the BLR drill site. However, the present seismic inversion models consider gas hydrates as uniformly distributed. The patchy nucleation coupled with the pore-filling growth of methane hydrates reported in this paper could significantly change the estimates of hydrate saturations, relative permeabilities and other properties of hydrate zones. The pore-filling model also supports recent field studies at the Keathley Canyon site from the Gulf of Mexico where hydrates were found in the nodular and vertical fracture filling form in the shallow shaly sediments (Cook et al., 2008; Kastner et al, 2008; Lee and Collett, 2008). Moreover, hydrate dissociation from pores suggests more reduction in bulk modulus than that for load bearing hydrate (Waite et al., 2004). This effect could be pronounced during the onset of hydrate dissociation and could have an important impact on seafloor stability. Future studies are focusing on understanding the predictability of host grain size, hydrate saturation, and physical property relationships.

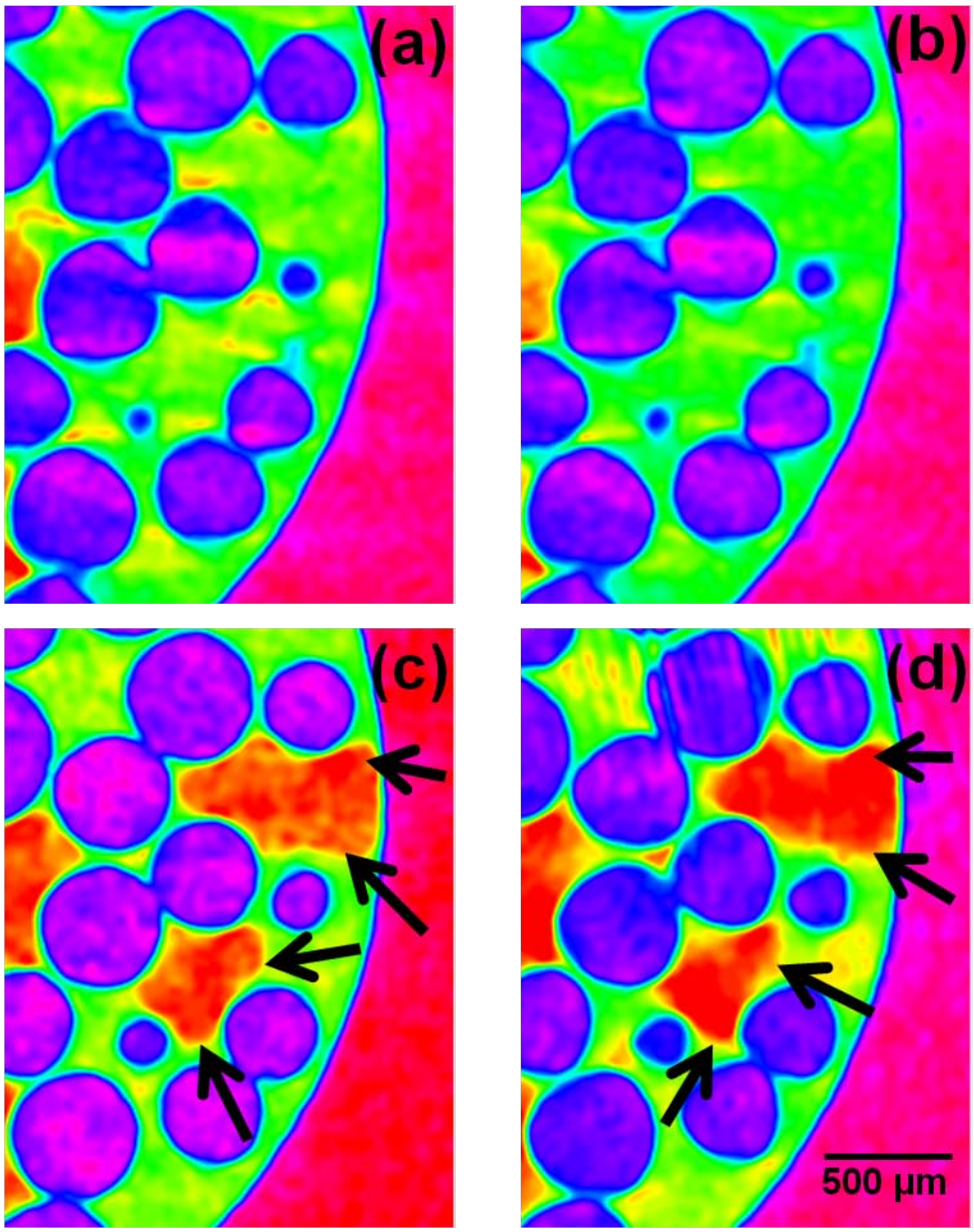

FIG. 8.3. Observation of random methane hydrate growth hosted in glass beads (white spheres) is representative of 2-D cross sections (4.6 mm diameter). The images were recorded at (a) 15:15 h, (b) 19:19 h, (c) 24:54 h and (d) 49:14 h. All images were converted into a colored palette from raw 32-bit images using the Image/Lookup Tables submenu.

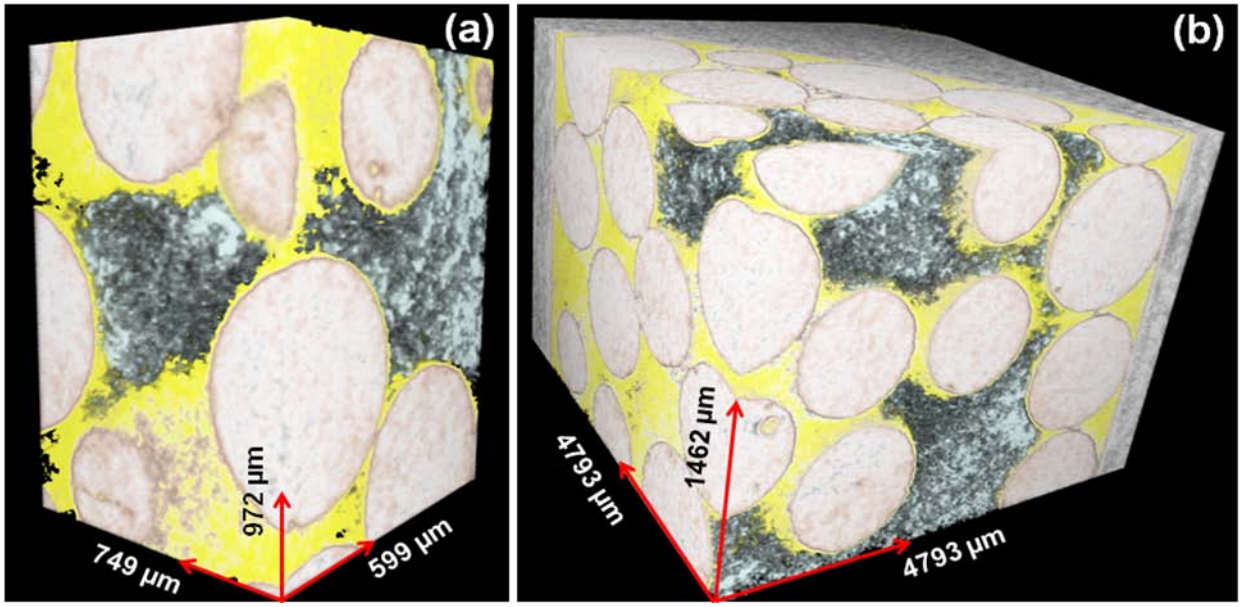

FIG. 8.4. 3-D images of methane hydrate in host glass beads after 49:14 h of cooling. The images were reconstructed from 400 slices such as those shown in Fig. 8.3. An embedded 2-D histogram tool in Drishti and a transfer function for each phase were used to differentiate aluminum cell (white), glass beads (brown), 5wt% aqueous solution (yellow) and methane hydrates (grey).

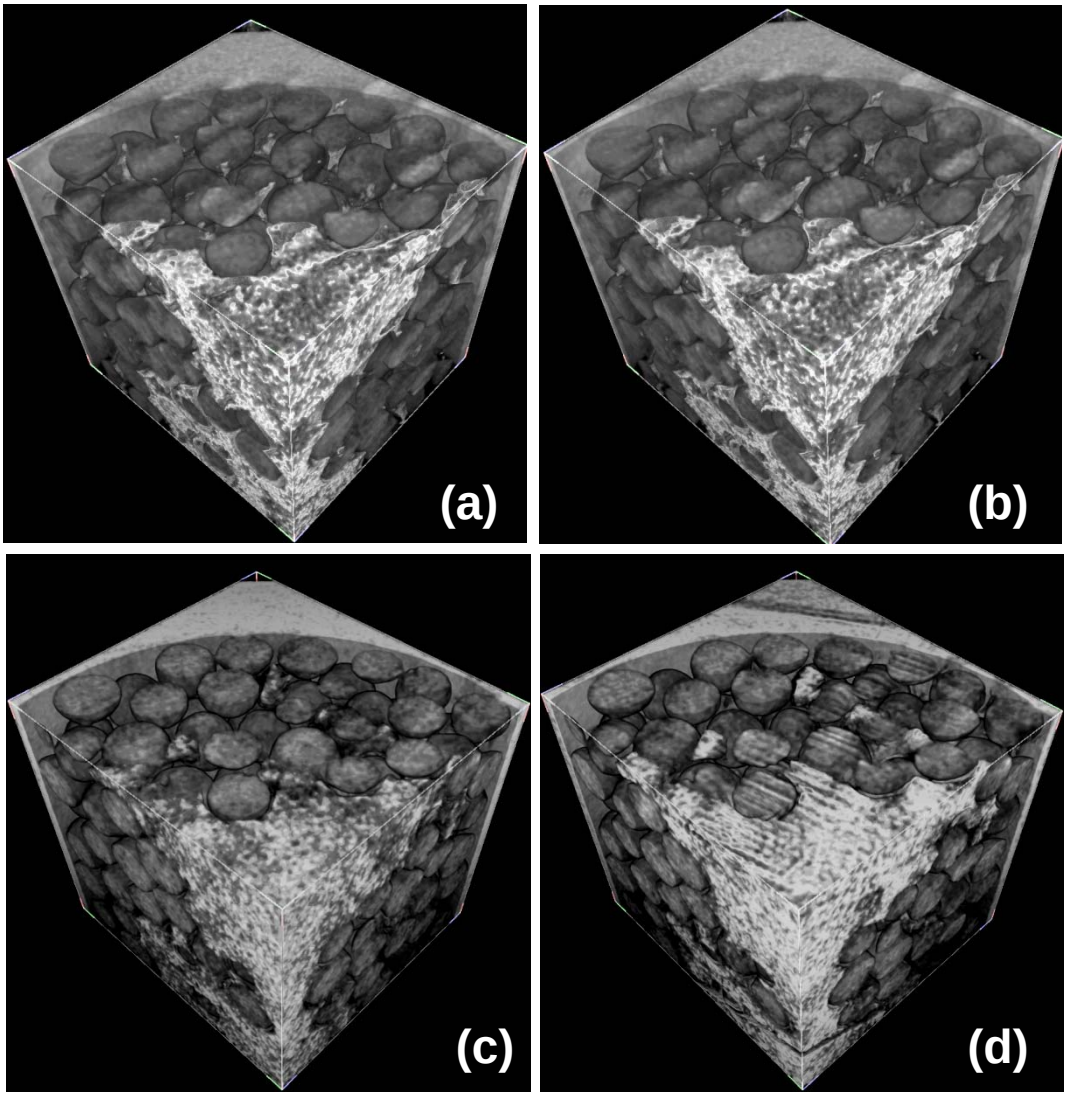

FIG. 8.5. Time resolved methane hydrate growth in host glass beads (500 μm). The 3-D structures are rendered from tomography scans at cooling times (a) 15:15 h, (b) 19:19 h, (c) 24:54 h and (d) 49:14 h. The aqueous solution phase is not shown to allow enhancement of the contrast for distinct observation of methane-hydrate growth (shown in grey scale).

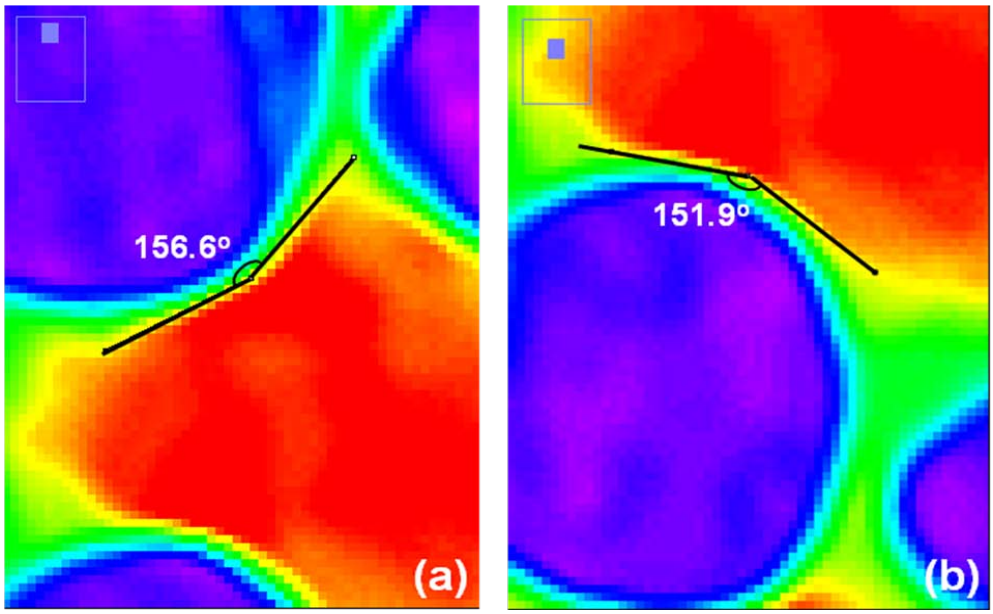

FIG. 8.6. Contact angle measurement of methane hydrates (yellow-orange) around glass beads (blue-pink) from 5wt% $BaCl_2$ solution (green). A raw 32-bit 2-D image was converted into a colored palette, sharpened and magnified up to 400% in imageJ. An "angle tool" in imageJ was utilized to measure contact angles over multiple glass beads and hydrate curvatures.

Chapter 9

Conclusions and Future Work

9.1 Formation and Dissociation of Methane Hydrates from Pure Water in Consolidated Sand

Methane hydrate formation was achieved by gradual and multiple charging of methane through pre-cooled, water saturated, Ottawa sand-pack under a constant confining pressure. After each charging, pore pressure asymptoted to hydrate equilibrium pressure at bath temperature.

a. As the methane charging pressure increased, the nucleation of hydrates was observed in a short period (Runs 8-10). A higher charging pressure of methane corresponds to a higher pore pressure. The excess pore pressure in turn opposes the constant confining pressure (1500 psig) in these runs, relieving the degree of consolidation. The coefficient of compression/compression index (Cc) is defined as the slope of a plot of void ratio[1] (e) and logarithm of effective stress (σ') (Das, 2001). Hence, as the effective stress increases, the coefficient of compression decreases with the degree of consolidation. The delayed hydrate formation time for the higher degree of consolidation is consistent with earlier findings by Kleinberg et al. (2003) and Yousif and Sloan (1991).

[1] Void ratio (e) is defined as a ratio of unit volume of voids and unit volume of solids. It is expressed in therms of porosity (ø) as ø/(1-ø).

b. All dissociations due to pressure drops were short-lived as gas produced from the core ceased quickly. As output gas was produced due to the depressurization, sediment temperature dropped due to the endothermic hydrate dissociation and gas expansion. Once gas output dropped to zero, the outlet valve was closed and the sample was allowed to equilibrate while the cell pressure gradually rose to the equilibrium pressure at the bath temperature. This allowed studying dissociations at a constant bath temperature. The post-dissociation sediment warm-up represented subsequent thermally induced hydrate dissociation. The post-dissociation system pressure-temperature (PT) followed theoretically established methane hydrate-water PT equilibrium but on the higher pressure side. However, this effect was seen until hydrates were present within sediments.

c. The greater the pressure drop during the dissociation of hydrates at constant sediment temperature, the larger the degree of sediment-cooling (Runs 11-13) observed. A higher degree of sediment cooling obviously takes longer for sediments to reach the bath temperature. The degree of cooling of sediment was also found to be dependent upon the sediment temperature for a constant pressure drop. It is obvious from the dissociations from sediment at different temperatures that a lower sediment temperature causes a higher degree of cooling upon hydrate dissociation and in turn takes a longer time to warm-up to its initial value.

d. Post-depressurization PT conditions were observed on the higher pressure side of theoretical PT equilibrium during thermally induced dissociation due to the excess pore pressure generated in the confined core. This excess pore pressure observed for the present Ottawa sand-water-hydrate system (pore radii: 48-58 μm) is minimal when compared to the phase stability of methane hydrates in 14 nm pore radii sized silica gel (Hand and Stupin, 1992).

e. The excess pore pressure data during thermally induced dissociation that occurred until sediments warmed up to the bath temperature was used to estimate the enthalpy of dissociation (ΔH_{hyd}) of methane hydrates hosted in the Ottawa sand-core. The Clausius-Clapeyron equation was applied to estimate ΔH_{hyd} as the slope of a lnP against 1/[TZR] plot. The estimated values of ΔH_{hyd} ranged between 49.14-59.134 kJ/mol, which are consistent but lower than the theoretical enthalpy of dissociation

value (62.6 kJ/mol) computed from equilibrium conditions. The lowered values of the enthalpy of dissociation of methane hydrates are due to the presence of porous media (pore radii: 48-58 μm). Hand and Stupin (1992) found the enthalpy of dissociation of methane hydrates to be 45.19 kJ/mol in porous silica gel with a mean pore diameter of 14 nm.

f. Thermocouple responses at the center (T3), half-radius (T2), and the boundary (T1) of the core were monitored during formation and dissociation as an indicator of hydrate distribution within core. The higher temperature spike during formation and the higher degree of cooling during dissociation observed consistently at the center of the core indicates higher hydrate saturation in the center of the core than at the boundary. Moreover, the steep slopes for the core center and half-radius temperature indicate that the dissociation was found to be preferential in the central part of the core than its boundary. These observations are consistent with earlier experiences despite the changed vertical order of thermocouples from previous runs. This undermines the effect of gravity on the hydrate dissociation front where hydrates were found in previous runs to dissociate from the center of the sample towards the wall.

g. The decomposition rate data were fitted into a model developed by Liang et al. (2005) for the decomposition kinetic behavior of methane hydrates based on an ice-shielding mechanism in which a porous ice layer was assumed to be formed during the decomposition of hydrates. The computed hydrate dissociation constant was 1.1622 x 10^{-3} mol./(MPasecgm). This hydrate dissociation constant value is about 10,000 times smaller than that observed for the pure water system by Liang et al. (2005). This may be due to a porous Ottawa sand-pack of pore diameter ranging between 48.28 - 58.65 μm.

9.2 Formation and Dissociation of Methane Hydrates from Seawater in Consolidated Sand

In methane hydrate formation and dissociation studies from seawater-consolidated Ottawa sand, hydrates were formed by pressurizing the water saturated Ottawa sand-pack

to different pore pressures followed by core cooling. The confining pressure was kept constant in this analysis.

a. Hydrate formation was found to be delayed with increasing pore pressure or consolidation. This is consistent with earlier analysis with pure water-consolidated Ottawa sand system and previous studies by Kleinberg et al. (2003) and Yousif and Sloan (1991).
b. It must be noted that the hydrate formation time is measured after the system PT entered into hydrate stability region. Moreover, the formation times observed for the seawater-consolidated Ottawa sand system were ~9.39, 11.86, and 29.27 hours for the effective pressures of 268.4, 172.9, and 131.3 psi respectively. This longer time observed than that for the pure water-consolidated Ottawa sand system is due to a hydrate inhibition caused by salts from the seawater.
c. The dissociation was achieved by depressurization at a constant sediment temperature in an individual run. However the effect of sediment temperature on dissociation kinetics was studied from multiple runs at varied sediment temperatures. The dissociations due to depressurization were short-lived and caused sediment cooling due to the endothermic nature of hydrate dissociation. The post-depressurization sediment warm-ups to the bath temperature representing thermally induced dissociation were longer and system PT conditions followed theoretical PT equilibrium for a methane hydrate-seawater system on the higher pressure side due to the excess pore pressure generated within a confined core (pore radii: 48-58 μm).
d. The enthalpy of hydrate dissociation was computed as the slope of a lnP vs. 1/[TRZ] plot for post-depressurization data. The computed values (ranging between 54.050 and 58.838 kJ/mole) for a seawater-Ottawa sand core are lower than those computed from theoretical PT data for bulk hydrates from pure water (62.605 kJ/mol). These are also lower than that obtained from bulk methane-seawater equilibrium data due to porous media with pore diameter between 48.28 and 58.65 μm under the confining pressure of 1500 psig.
e. The hydrate formation was observed through temperature spikes due to the exothermic nature of hydrates during formation. The temperatures at lateral and radial positions within sample were monitored with thermocouples placed at the outer core

surface, half-way radius, and the center of the core. During formation, the uneven temperature spikes at the center, half-radius, and boundary of the core indicate that hydrates formed more predominantly inside the core than at the core-boundary.

f. The endothermic effect due to hydrate dissociation was also recorded with a higher degree of cooling at the center and half-radius thermocouples than that at the core boundary. These observations are consistent with earlier experiences with a pure water-Ottawa sand system.

g. The higher pressure drop during the dissociation of hydrates at a constant sediment temperature caused a larger degree of sediment-cooling. The higher degree of sediment cooling obviously results in a longer time for sediments to reach the bath temperature. The degree of cooling of the sediment was also found to be dependent upon the sediment temperature for a constant pressure drop. The lower sediment temperature showed a higher degree of cooling upon hydrate dissociation and in turn, took a longer time to warm-up to its initial value.

9.3 Direct Observations of Three Dimensional Growth of THF Hydrates (sII) Hosted in Porous Media

The visualization of the time-resolved 3-dimensional (3-D) growth of tetrahydrofuran (THF) hydrates with glass spheres of uniform size as porous media was performed using synchrotron X-ray computed microtomography (CMT).

a. Time lapse bead-to-bead matching indicated that the growth of THF hydrates displaces beads within the unconsolidated pack. The 2-dimensional (2-D) images show that the hydrate size and shape is independent of container-walls. These observations are consistent with previous NMR analysis (Mork, 2000), visual observations (Tohidi et al., 2001) and the random nature of the nucleation process.

b. Structure II hydrates were found to grow in pores in a manner similar to the pore-filling model described by Dvorkin et al (1999). This implies a progressive but significant reduction of the mechanical strength of the sediment upon the dissociation of hydrates by retraction from the pore walls followed by their shrinkage in the pore space (Kleinberg et al., 2003). The hydrate surface was found to be convex and away

from grain surfaces, indicating that the THF, not the hydrate, is the wetting phase – presumably in the form of a thin film. This is analogous to ice growth in porous media, in which a water film remains unfrozen (Kleinberg and Griffin, 2005; Anderson and Tice, 1971), and this is consistent with the contact angle arguments of Miller (1980) and Clennell et al. (1999).

c. The hydrate distribution was patchy even though the THF/H_2O/glass bead system was homogeneous. The patchy growth is consistent with the observation of a weak dependence of sound speed on natural hydrate saturation at low saturation values (Tserkovnyak and Johnson, 2002).

d. The contact angle between the hydrate and glass bead was measured as ~140.7° directly from the analysis of the cross sections through the volume tomographic data.

e. The dependence of the pore radius and the temperature shift of THF hydrate and methane hydrate equilibrium were established by substituting the measured contact angles from the reconstructed 2-D images in Gibbs-Thomson equation (Jallut et al., 1992). It is apparent that for capillary radii greater than 1000 Å, the T_{pore}/T_{bulk} value is ~1 suggesting a negligible effect of the pore radii and contact angle terms on the temperature depression. For fine host sediments, such as those found at hydrate sites like the Gulf of Mexico, the smaller effective pores exhibit a higher capillary pressure and increased specific surface energy between solid-liquid interfaces. This results in the liquid phase being thermodynamically favorable down at low temperatures in smaller pores than that in the bulk.

f. A uniform distribution of hydrates in sediments has been generally assumed in the prediction of acoustic velocities (Dvorkin et al., 1999). The patchy growth of the hydrates observed here radically alters the connection between hydrate saturation and the propagation of sound (Tserkovnyak and Johnson, 2002). The present study involved THF hydrates growing from excess THF in a mono-sized glass bead pack. If the same results extend to natural gas hydrate accumulations in the earth, the interpretation of seismic surveys and sonic well logs would need to be reconsidered.

9.4. Imaging Time-Resolved Methane Hydrates (sI) Grwoth in Porous Media using Synchrotron X-ray Computed Microtomography

The synchrotron X-ray CMT technique was utilized to image time-resolved methane hydrate growth in the pore space of a glass bead pack.

a. Hydrates nucleated randomly in pores formed by randomly packed host glass beads, though the nucleation process may or may not involve the cell wall. The time-resolved 2-D growth indicated that methane hydrates are convex and away from the grain. The bead-to-bead matching indicated movement of the beads during hydrate growth.
b. The 3-D images depicted that hydrates are suspended in an aqueous phase without any contact between them and the glass beads. The presence of an aqueous phase film around the glass beads confirmed an aqueous phase, not hydrates, as a wetting phase. This was also consistent with previous findings with THF hydrates. This microstructure was categorized as a "pore-filling" according to the microstructural models of gas hydrate bearing sediments proposed by Dvorkin et al. (1999) and Helgerud et al. (1999).
c. In the time-resolved methane hydrate growth, methane hydrates appeared to grow from the direction of the gas-liquid interface, filling the pores formed by a close packing of glass beads. As time progressed, hydrate growth was seen predominantly in the center of the cell. The observed time-resolved growth of hydrates into agglomerate supports the "local-structuring hypothesis" by Hawtin et al. (2008).
d. Based on the capillary model of ice growth in pores described by Clennell et al. (1999), contact angle measurements were performed on a 2-D image obtained from a stack of images acquired after reconstructions.
e. The measured values of contact angles between 151.9^{o} and 156.6^{o} were convex and consistent with earlier reported values for THF-hydrates but were significantly different from the assumption of water as a wetting phase (contact angle = 180^{o}) in theoretical analyses of methane hydrate phase equilibrium in fine sediments.
f. The present seismic inversion models consider gas hydrates as uniformly distributed. The patchy nucleation coupled with the pore-filling growth of methane hydrates

reported in this study could significantly change the estimates of hydrate saturations. Moreover, hydrate dissociation from pores suggests more reduction in bulk modulus than that for load bearing hydrate (Waite et al., 2004). This effect could be pronounced during the onset of hydrate dissociation and could have an important impact on seafloor stability.

Correlating the nature of hydrate microstructure with host matrix and seafloor stability is critical in the development of an environmentally benign method for the extraction of methane from hydrates. The microstructure of hydrates within sediment can have a profound effect on the mechanical strength of the seafloor. The pore-filling microstructure of hydrates revealed in this study can significantly alter the estimates of hydrate saturations, relative permeabilities and other properties of hydrate zones. Moreover, methane hydrate microstructure is pivotal in understanding carbon dioxide (CO_2) sequestration in the form of hydrates, their formation/dissociation kinetics, wettability, surface energy, and phase saturation. The enthalpy of dissociation of methane hydrates from seawater hosted in a consolidated sand-pack estimated herein from thermally induced dissociation is a principal thermodynamic property which could be significant while exploring methane hydrates using CO_2 sequestration.

9.5 Future Work

The global CO_2 emissions are expected to increase with growing fossil fuel consumption from 24 to 39 billion metric tons in 2025 (Goel, 2006). Over the past one hundred years, the CO_2 atmospheric level has increased from 280 to 370 ppm, further exacerbating global warming. CO_2 sequestration has a potential as an enhanced oil/gas recovery technique and for a simultaneous conversion of methane hydrates into natural gas. The microstructural properties of methane and CO_2 hydrates can greatly affect the elastic properties of their host, the hydrate-bearing matrix. An understanding of the sediment-hydrate interaction, interfacial mass transfer/tension between methane and CO_2, wettability of porous media, saturation of different phases and the role of un/frozen water

during sequestration is important to quantify changes in seafloor stability in the event of a rapid release of methane. The microstructural model of CO_2 hydrates and their growth habit can be established using the synchrotron X-ray computed microtomography or neutron scattering. This study could also be extended to address the variables that can affect formation and dissociation thermodynamics that are important in understanding methane hydrate dissociation and the sequestration of CO_2 hydrates, including pore size distribution, wettability, surface energy and phase saturation.

Geologic sequestration involves taking the CO_2 that has been captured from power plants and other stationary sources and storing it in deep underground geologic formations in such a way that CO_2 will remain permanently stored. Geologic formations such as oil and gas reservoirs, unmineable coal seams, and underground saline formations are potential options for storing CO_2. Storage in basalt formations and organic rich shales is also being investigated. The Carbon Sequestration Program laid out by U.S. Department of Energy (DOE)/National Energy Technology Laboratory (NETL) involves three key elements for technology development: Core R&D, Infrastructure and Global Collaborations. I foresee tremendous potential for laboratory and pilot-scale research in improving the understanding of implications of methane hydrates in the global climate cycle or factors affecting CO_2 storage permanence, capacity, and safety in geologic formations and terrestrial ecosystems with core-flooding cells where *in-situ* conditions can be mimicked to monitor the stored CO_2 and assess the security that the CO_2 will remain permanently sequestered in various geological media.

References

Abegg, F., Bohrmann, G., Kuhs, W., (2006), 21. Data Report: Shapes and Structures of Gas Hydrates imaged by Computed Tomographic Analyses, ODP Leg 204, Hydrate Ridge Proceedings of the Ocean Drilling Program, Scientific Results, 204.

Anderson, D.M. Tice, A.R., (1971), Low Temperature Phases of Interfacial Water in Clay-Water Systems, Proc.-Soil Science Society Am., 35, 47–54.

Anderson, O., Suga, H., (1996), Thermal Conductivity of Normal and Deuterated Tetrahydrofuran Clathrate Hydrates, J. Phys. Chem. Solids, 57, 1, pp. 125-132.

Anderson, R.M. et al., (2001), Experimental Measurement of Gas Hydrate Stability in Porous Media, EAGE 63rdConference & Technical Exhibition, Amsterdam, pp. 567.

Anderson, R., et al., (2003a), Characteristics of Clathrate Hydrate Equilibria in Mesopores and Interpretation of experimental Data, J. Phys. Chem. B, 107, 3500-3506.

Anderson, R. et al., (2003b), Experimental Measurement of Methane and Carbon Dioxide Clathrate Hydrate Equilibria in Mesoporous Silica, J. Phys.Chem. B, *107*, 3507-3514.

Ballard, A.L., Sloan, E.D. Jr., (2002), The next generation of hydrate prediction I. Hydrate standard states and incorporation of spectroscopy, Fluid Phase Equilibria, 194–197**,** pp. 371–383.

Best et al., (2004), Tidal height and frequency dependence of acoustic velocity and attenuation in shallow gassy marine sediments, Journal of Geophysical Research, 109, B08101.

Bily, C., Dick, J.W.L., (1974), Naturally Occurring Gas Hydrates in the Mackenzie Delta, N.W.T., Bulletin of Canadian Petroleum Geology, 22, pp. 320-352.

Booth, J.S. et al., (1998), Laboratory investigation of gas hydrate genesis in sediments--Modes of occurrence, volumes and growth patterns: Gas Hydrates in Nature--

Results from Geophysical and Geochemical Studies, European Geophysical Society, XXIII, General Assembly, Nice, France, p. 425, Spring.

Boswell, R., (2009), Is Gas Hydrate Energy within Reach?, Science, 325, pp. 957-958, August.

Brooks, J.M. et al., (1984), Thermogenic gas hydrate in the Gulf of Mexico, Science, 225, pp.409-411.

Bryant, W.R. et al., (1983), Geotechnical Properties on Intraslope Basin Sediments. Gulf of Mexico, Deep Sea Drilling Project Leg 96, Site 619, Initial Reports of the Deep Sea Drilling Project 96, TAMU ODP, Sept.-Nov.

Carmichael, L.T. et al., (1966), Thermal conductivity of fluids. Methane, Journal of Chemical and Engineering Data, 11, 1, pp. 52-57.

Cherskiy, N.V., Tsarev, V.P., Nikitin, S.P., (1985), Investigation and Prediction of Conditions of Accumulation of Gas Resources in Gas-Hydrate Pools, Petroleum Geology, 21, pp. 65-89.

Clarke, M.A. et al., (1999), A Method to Predict Equilibrium Conditions of Gas Hydrates Formation in Porous Media, Ind. Eng. Chem., 38, pp. 2485-2490.

Clennell, B.M. et al., (1999), Formation of Natural Gas Hydrates in Marine Sediments – Conceptual Model of Gas Hydrate Growth Conditioned by Host Sediment Properties, J Geophysical Res., 104, B10, pp. 22985-23003, October 10.

Clennell, B.M. et al., (2000), Formation of Natural Gas Hydrates in Marine Sediments – Conceptual Model of Gas Hydrate Growth Conditioned by Host Sediment Properties, Analysis of the NY Academy of Scieneces, Vol. 912, pp. 886-896, January.

Collett, T.S., (1993), Natural Gas Hydrates of the Prudhoe Bay and Kuparuk River Area, North Slope, Alaska, AAPG Bulletin, 77.

Collett, T.S., (2004), Gas hydrates as a future energy resource, Geotimes, November.

Collett, T.C., (2000), Natural Gas Hydrates: Resources for the 21st Century?, Proceedings of AAPG Sponsored Wallace C. Pratt Memorial Conference on Petroleum Provinces on the 21st Century, San Diego, pp.64, January 12-15.

Collett, T.S., Dallimore, S.R., (2000), Anonymous, Identification and remediation of gas hydrate induced drilling and production hazards, Annual Meeting, Expanded Abstracts, American Association of Petroleum Geologists, Vol. 30.

Collett, T.S., Ehlig-Economides, C.A., (1983), Detection and Evaluation of the In-Situ Natural Gas Hydrates in the North Slope Region, Alaska, SPE 11673, Presented at the 1983 California Regional Meeting of the Society of Petroleum Engineers of AIME, Ventura, California, March 23-25.

Collett, T.C., Ladd, J., (2000), Detection of Gas Hydrate with Downhole Logs and Assessment of Gas Hydrate Concentrations (Saturations) and Gas Volumes on the Blake Ridge with Electrical Resistivity Log Data, Proceedings of the Ocean Drilling Program, Scientific Results, 164, Vol. 164, pp. 179-191.

Cook, A.E., Goldberg, D., Kleinberg, R.L., (2008), Fracture-controlled gas hydrate systems in the northern Gulf of Mexico, Marine and Petroleum Geology, 25, 9, pp. 932-941, November.

Dai, J. et al., (2004), Detection and Estimation of Gas Hydrates Using Rock Physics and Seismic Inversion: Examples from the Northern Deepwater Gulf of Mexico, The Leading Edge, pp. 60-66, January.

Dai, J. et al., (2008a), Exploration of gas hydrates in the deepwater, northern Gulf of Mexico: Part II. Model validation by Drilling, Marine and Petroleum Geology, 25, pp. 845-859.

Dai, J. et al., (2008b), Exploration of gas hydrates in the deepwater, northern Gulf of Mexico: Part I. A seismic approach based on geologic model, inversion, and rock physics principles, Marine and Petroleum Geology, 25, pp. 830-844.

Dallimore, S.R., Uchida, T., Collett, T.S., (1999), Scientific Results from JAPEX/JNOC/GSC Mallik 2L-38 Gas Hydrate Research Well, Mackenzie Delta, Northwest Territories, Canada, Geological Survey of Canada Bulletin 544, February.

Das, B.M., (2001), Principles of Geotechnical Engineering, Thomson-Engineering; 5th Edition, September 10.

Denison, C., Carlson, W.D., Ketcham, R.A., (1997), Three-dimensional quantitative textural analysis of metamorphic rocks using high-resolution computed X-ray tomography: Part I. Methods and techniques, Journal of Metamorphic Geology, 15, 1, pp. 29–44.

Dickens, G.R., Paull, C.K., Wallace, P., (1997), ODP Leg 164 Scientific Party, Direct Measurement of In-situ Methane Quantities in a Large Gas Hydrate Reservoir, Nature, 385, pp. 426-428.

Dickens, G. R. et al., (1995), Dissociation of Oceanic Methane Hydrate as a Cause of the Carbon Isotope Excursion at the End of the Paleocene, Paleoceanography, 10(6), 965–971.

Dickens, G.R., Quinby-Hunt, M.S., (1994), Methane hydrate stability in seawater, Geophysical Research Letters, 21, 19, pp. 2115-2118.

Dillon et al., (1996), Seismic reflection profiles on the Blake Ridge near sites 994, 995, and 997, Proceedings of the Ocean Drilling Program Initial Report.

Dholabhai, P.D. et al., (1991), Equilibrium conditions for methane hydrate formation in aqueous mixed electrolyte solutions, Canadian Journal of Chemical Engineering, 69, pp. 800-805.

Duan, Z., Sun, R., (2006), A model to predict phase equilibrium of CH_4 and CO_2 clathrate hydrates in aqueous electrolyte solutions, American Mineralogist, 91, pp. 1346-1354.

Dvorkin, J., Nur, A., (1996), Elasticity of high-porosity sandstones: Theory of two North Sea Data Sets, Geophysics.

Dvorkin, J. et al., (1999) Elasticity of Marine Sediments, Geophysical. Res. Letters, 26(12), pp. 1781-1784.

Eaton, M., (2007), Mimicking Marine-Based Natural Systems: A Study of Sediment-Hydrate Interactions under In-Situ Conditions, Ph.D. Thesis, Stony Brook University, December.

Ecker, C., Dvorkin, J., Nur, A., (1998), Sediments with gas hydrates: Internal structure from seismic AVO, Geophysics, 63, 5, pp. 1659-1669, September.

Elwood Madden, M.E. et al., (2006), Hydrate Formation and Dissociation via Depressurization in Simulated and Field Samples, Interim Report, Oak Ridge National Laboratory, June.

Expedition 311 Scientists, (2005), Cascadia Margin Hydrates, IODP Preliminary Report.

Fisher, C.R., (1990), Chemoautotrophic and methanotrophic symbioses in marine invertebrates, Crit. Rev. Aq. Sci., 2, pp. 399–436.

Fleischer, P. et al., (2001), Distribution of free gas in marine sediments: a global overview, Geo-Mar Lett, 21, pp. 103–122.

Flemings, P.B., Liu, X., Winters, W.J., (2003), Critical Pressure and Multiphase Flow in Blake Ridge Gas Hydrates, Geology, 31, 12, pp. 1057-1060, December.

Francisca, F. et al., (2005), Geophysical and Geotechnical Properties of Near-Seafloor Sediments in the Northern Gulf of Mexico Gas Hydrate Province, Earth and Planetary Science Letters, 237, pp. 924-939.

Freer E.M., Selim, M.S., Sloan, E.D. Jr., (2001), Methane hydrate film growth kinetics, Fluid Phase Equilibria, 185, 65-75.

Freifeld, B.M., Kneafsey, T.J., (2004), Investigating Methane Hydrate in Sediment using X-ray Computed Tomography, in Advances in the study of Gas Hydrates, Kluwer Academic/Plenum Publishers, New York.

Ginsburg, G.D. et al., (2000), Sediment Grain-Size Control on Gas Hydrate Presence, ODP Sites 994, 995, 997, Proceedings of the Ocean Drilling Program, Scientific Results, 164, College Station, TX, Vol. 164, pp. 237-246.

Goel, N., (2006), In situ methane hydrate dissociation with carbon dioxide sequestration: Current knowledge and issues, Journal of Petroleum Sci. and Eng., 51, 3-4, pp. 169-187.

Gough, S.R., Davidson, D.W., (1971), Composition of Tetrahydrofuran Hydrate and the Effect of Pressure on the Decomposition, Canadian Journal of Chemistry, 49, pp. 2691-2699.

Guerin G, Goldberg D, Meltser A, (1999), Characterization of in situ elastic properties of gas hydrate-bearing sediments on the Blake Ridge. J Geophys Res 104, pp.17781–17795.

Hammerson, G.A., (2004), Connecticut Wildlife: Biodiversity, Natural History and Conservation, University Press of New England, Lebanon, NH.

Handa, Y.P., (1990), Effect of hydrostatic pressure and salinity on the stability of gas hydrates. Journal of Physical Chemistry, 94, 6, pp. 2652-2657.

Handa, Y.P., Stupin, D., (1992), Thermodynamic Properties and Dissociation Characteristics of Methane, and Propane Hydrates in the 70-Angstrom-Radius Silica Gel Pores, J. Phy. Chem., 96, pp. 8599-8603.

Hangsterfer, A., Driscoll, N., Kastner, M., (2008), Constraining gas hydrate occurrence in the northern Gulf of Mexico continental slope: Fine scale analysis of grain-size in hydrate-bearing sediments, Proceedings of the 6th International Conference on Gas Hydrates (ICGH 2008), Vancouver, BC, Canada, July 6-10.

Hart, B.S., Flemings, P.B., Deshpande, A., (1995), Porosity and pressure: Role of compaction disequilibrium in the development of geopressures in a Gulf Coast Pleistocene basin, Geology, 23,1, pp. 45-48.

Hawtin, R.W., Quigley, D., Rodger P.M., (2008), Gas hydrate nucleation and cage formation at a water/methane interface, Phys. Chem. Chem. Chem. Phys., 10, pp. 4853-4864.

Helgerud, M. et al., (1999), Elastic Wave Velocity in Marine Sediments with Gas Hydrates: Effective Medium Cooling, Geophysical Research Letter, 26, pp.2021-2024.

Henry, P.M. et al., (1999), Formation of Natural Gas Hydrates in Marine Sediments; Part 2: Thermodynamic Calculations of Stability Conditions in Porous Sediments, J. Geophys. Res., 104, pp. 23005-23022.

Myers, B. et al., (1941), Discussion on soil water phenomena, Proceedings of Highway Research Board, 21, pp. 451-470.

Jallut, C. et al., (1992), Thermoporometry : Modeling and simulation of a mesoporous solid, Membrane Science, 68, pp. 271-282.

Jin, S. et al., (2004), Structure, Analyses of Artificial Methane Hydrate Sediments by Microfocus X-ray Computed Tomography, Japanese Journal of Applied Physics, 43, 8A, pp. 5673-5675.

Jones, E., (2006), Characterizing Natural Gas Hydrates in the Deep Water Gulf of Mexico: Applications for Safe Exploration and Production Activities Semi-Annual Report, Semi Annual Report No. 41330R09, Chevron Exploration Production and Technology Company, May.

Jones, K. et al., (2007), Characterization of methane hydrate host sediments using synchrotron-computed microtomography (CMT), Journal of Petroleum Science and Engineering, 56, pp. 136-145.

Kastner, M. et al., (1996), Relation between Pore Fluid Chemistry and Gas hydrates associated with Bottom-Simulating Reflectors at the Cascadia Margin sites 889 and 892, Proceedings of Ocean Drilling Program, Scientific Results, 146, pp. 175-189.

Kastner, M., MacDonald, I., (2006), Controls on Gas Hydrate Formation and Dissociation, Gulf of Mexico: In Situ Field Study with Laboratory Characterization of Exposed and Buried Gas Hydrates, Final Technical Report, USDOE, NETL, June.

Kastner, M., Claypool, G. , Robertson, G., (2008), Geochemical constraints on the origin of the pore fluids and gas hydrate distribution at Atwater Valley and Keathley Canyon, northern Gulf of Mexico, Marine and Petroleum Geology, 25, pp. 860–872.

Katsube, T.J. et al., (2004), Possible Seal Mechanisms in Shallow Sediments and Their Implications for Gas Hydrate Accumulation, Presented at AAPG Hedberg Conference, Vancouver, Canada, September 12-16.

Kennett, J.P. et al., (2003), Methane Hydrates in Quaternary Climate Change, American Geophysical Union Special Publication, 54, Washington, DC.

Kennicutt, M.C. II, Brooks, J.M., Denoux, G.J., (1988), Leakage of deep, reservoired petroleum to the near surface on the Gulf of Mexico continental slope, Mar. Chem., 24, pp. 39–59.

Kerkar, P. et al., (2009), Direct observations of three dimensional growth of hydrates hosted in porous media, Applied Physics Letter, 95, 024102, August.

Kester D.R. et al., (1967), Preparation of artificial seawater, Limnology and Oceanography, 12, 1, 176-179.

Kim, H.C. et al., (1987), Kinetics of methane hydrate decomposition, Chemical Engineering Science, 42, pp. 1645–1653.

Kimura, K., Silver, E., Blum, P., (1998), Leg 170 Scientific Party, Proceedings of the Ocean Drilling Program, Initial Reports, Vol. 170, College Station, TX.

Klapp, S.A., Klein, H., Kuhs, W.F., (2007), First determination of gas hydrate crystallite size distribution using high-energy synchrotron radiation, Geophysical Research Letters, 34, L13608.

Kleinberg, R.L. et al., (2003), Deep Sea NMR: Methane Hydrate Growth Habit in Porous Media and its Relationship to Hydraulic Permeability, Deposit Accumulation, and Submarine Slope Stability, Journal of Geophysical Research (Solid Earth), 108, B10, doi:10.1029/2003JB002389.

Kleinberg, R.L., Griffin, D.D., (2005), NMR measurement of permafrost: Unfrozen water assay, pore scale distribution of ice, and hydraulic permeability of sediments, Cold Regions Science and Technology, 42, 1, pp. 63-77.

Kneafsey, T.J., et al., (2007), Methane Hydrate Formation and Dissociation in a Partially Saturated Sand – Measurement and Observations, Journal of Petroleum Science, 56, pp. 108-126, LBNL-59087.

Knudsen, M., (1900), Eine hydrographische Lehrsatz, Annalen der Hydrographie und Marinen Meteorologie, 28, pp. 316–320.

Kumura, G. et al., Proceedings of the Ocean Drilling Program, Initial Reports, 170, College Station, TX, 1997.

Kunerth, D.C., et al., (2001), Acoustic Laboratory Measurements During the Formation of a THF-Hydrate in Unconsolidated Porous Media, Journal of Seismic Exploration, 9, pp. 337-354.

Kvenvolden, K.A., (1993), Gas hydrates—geological perspective and global change, Rev. Geophys, 31, 2, pp. 173–187.

Kvenvolden, K.A., Lorenson, T.D., (2001), The global occurrence of natural gas hydrate. In: Paull, C.K. and Dillon, W.P., Editors, 2001. Natural Gas Hydrates: Occurrence, Distribution, and DetectionAmerican Geophysical Union, Geophysical Monograph Series**,** Vol. 124, pp. 3–18.

Kvenvolden, K.A., McMenamin, M.A., (1980), Hydrates of Natural Gas: A Review of their Geologic Occurrence, U.S. Geological Survey Circular, 825, pp. 11.

Kvenvolden, K.A., McDonald, T.J., (1985), Initial Reports on Deep Sea Drilling Project Leg 84, pp. 667.

Lee, M.W., (2000), Gas Hydrate amount estimated from acoustic logs at the Blake Ridge, Sites 994, 995, and 997, Proceeding of the Ocean Drilling Program, Scientific Results, Vol. 164, pp. 193-198.

Lee, M.W., Collett, T., (1999), Amount of gas hydrate estimated from compressional- and shear-wave velocities at the JAPEX/JNOC/GSC Mallik 2L-38 gas hydrate research well, in Scientific Results from JAPEX/JNOC/GSC Mallik 2L-38 Gas Hydrate Research Well, Mackenzie Delta, Northwest Territories, Canada, Eds. Dallimore, S.R., T. Uchida, and T.S. Collett, Bulletin - Geological Survey of Canada, 544, 313-322.

Lee, M., Collett, T., (2008), Integrated analysis of well logs and seismic data to estimate gas hydrate concentrations at Keathley Canyon, Gulf of Mexico, Marine and Petroleum Geology, 25, 9, pp. 924-931.

Liang, M.Y. et al., (2005), Experimental and modeling study on decomposition kinetics of methane hydrates in different media, J. Phys. Chem. B. 109, pp. 19034–19041.

Limaye, A., (2006), Drishti – Volume Exploration and Presentation Tool, Poster Presentation, Vis 2006, Baltimore, USA.

Lorenson, T.D., (2000), Microscopic Character of Marine Sediment Containing Disseminated Gas Hydrate – Examples from the Blake Ridge and the Middle America Trench, Annals of NY Academy of Sciences, Vol. 912, Issue: Gas Hydrates: Challenges for the Future, pp. 189-193.

Lu, H. et al., (2007), Complex Gas Hydrate from the Cascadia Margin, Nature, 445, pp. 303-305, January.

Makogon, Y.F. (1981), (Cielewicz, W.J.), Hydrates of Natural Gas, Penn-Well, Tulsa, Oklahoma.

Makogon, Y,F et al., (2000), Dissociation of Natural Gas Hydrates Observed by X-ray CT Scanner, Analysis of the NY Academy of Sciences, 912, January.

Makogon, Y.F., Holditch, S.A., (2001), Experiments illustrate hydrate, Oil and Gas Journal, 45-50, Feb. 12.

Matsumoto,R., Hosein Mahmudy Gharaie, M., Kakuwa, Y., (2002), Was the Late Devonian Mass Extinction caused by massive dissociation of gas hydrate?, Proc. 4th ICGH, 75-79.

Miller, R.D., (1980), Freezing phenomena in soils, Introduction to Soil Physics edited by D. Hillel, 254-299, Academic, San Diego, California.

Mikami, J. et al., (2000), Dissociation of natural gas hydrates observed by X-ray CT scanner, Annals of the NY Academy of Sciences, 912, pp.1011-1020.

Milkov, A.V., Sassen, R., (2001), Estimate of gas hydrate resource, northwestern Gulf of Mexico continental slope, Marine Geology, v. 179, pp. 71-83.

Milkov, A.V., Sassen, R., (2003), Preliminary Assessment of Resources and Economic Potential of Individual Gas Hydrate Accumulations in the Gulf of Mexico Continental Slope, Marine and Petroleum Geology, 20, pp. 111-128.

Milkov, A.V. et al., (2005), Gas Hydrate Systems at Hydrate Ridge offshore Oregon inferred from Molecular and Isotopic Properties of Hydrate-bound and Void gases, Geochimica et Cosmochimica Acta, 69, 4, pp. 1007-1026.

Mork, M. et al., (2000), NMR Imaging Study of Hydrates in Sediments, Annals New York Academy of Sciences, 912(1), pp. 897-905.

Orcutt, B.N. et al., (2004), Life at the edge of methane ice: methane and sulfur cycling in Gulf of Mexico gas hydrates. Chem. Geol., 205, pp. 239–251, May.

Ostergaard, K.K. et al., (2002), Hydrate Phase Equilibria in Porous Media: Effect of Pore Size and Salinity, Terra Nova, 14, pp. 307-312.

Peddireddy, S. et al., (2006), Variable Contact Angle Model for Gas Hydrate Equilibrium in Porous Media, AIChE, 52, 3, pp. 1228-1234, March.

Paull, C.K. et al., (1996), Proceedings of the Ocean Drilling Program, Initial Reports, 164, College Station, TX.

Paull, C.K. et al., (2000), Leg 164 Overview, Proceedings of the Ocean Drilling Program, Scientific Results, 164, College Station, TX.

Perry, R.H., Green, D., (1984), Perry's Chemical Engineering Handbook, 6th Edition, McGraw-Hill, Inc., New York, NY.

Pińero, E., (2007), Gas hydrate disturbance fabrics of southern hydrate ridge sediments (ODP Leg 204): Relationship with texture and physical properties, Geo-Mar Letters, 27, 279-288.

Pitfalls and Uncertainties in Deepwater Production Forecasting, Scotia Group, Inc. Newsletter, December, 2005.

Pringle, D.J., (2004), Thermal Conductivity of Sea Ice and Antarctic Permafrost, School of Chemical and Physical Sciences.

Rasband, W.J., (1997-2005), ImageJ, U. S. National Institutes of Health, Bethesda, Maryland, USA, http://rsb.info.nih.gov/ij/.

Riestenberg, D. et al., (2003), Sediment Surface Effects on Methane Hydrate Formation and Dissociation, Marine Geology, 198, pp. 181-190.

Ripmeester, J.A. et al., (1987), A New Clathrate Hydrate Structure, Nature (London) 325, 135.

Roberts, H.H. et al., (1999), Surficial gas hydrates of the Louisiana continental slope—Initial results of direct observations and in situ data collection: Houston, Texas, Offshore Technology Conference, OTC 10770, p. 259-272.

Rueff, R.M., Sloan, E.D., (1985), Effect of Granular Sediment on Some Thermal Properties of Tetrahydrofuran Hydrate, Ind. Eng. Chem. Process Des. Dev., 24, pp. 882-885.

Santamarina, J. C., Ruppel, C., (2008), The Impact of Hydrate Saturation on the Mechanical, Electrical, and Thermal Properties of Hydrate-Bearing Sand, Silts,

and Clay, in Proceedings of the 6th International Conference on Gas Hydrates (ICGH '08), Vancouver, Canada, July.

Sassen, R., Macdonald, I.R., (1997), Hydrocarbons of experimental and natural gas hydrates, Gulf of Mexico Continental Slope, Organic Geochemistry, 26, 3-4, pp. 289-293, February.

Sato, M. et al., (2005), Distribution of Hydrate Saturation Ratios in Artificial Methane Hydrate Sediments Measured by High-Speed X-ray Computerized Tomography, Japanese Journal of Applied Physics, 44, 1A, pp. 473-475.

Sayers, C.M., den Boer, L.D., (2006), Method and system for pore pressure prediction, USPTO Patent 20080033704.

Seshadri, K., Wilder, J. W., Smith, D. H., (2001), Measurements of equilibrium pressures and temperatures for propane hydrate in silica gels with different pore-size distributions, J. Phys. Chem. B 105, pp. 2627-2631.

Sugaya, M., Mori, Y.H., (1996), Behavior of clathrate hydrate formation at the boundary of liquid water and a fluorocarbon in liquid or vapor state, Chemical Engineering Science, 51, 3505.

Sloan, E.D. Jr., (1998), Clathrate Hydrates of Natural Gases, Marcel Dekker Inc., New York.

Smith, D.H. et al., (2002), Methane Hydrate Equilibria in Silica Gels with Broad Pore-Size Distributions, AIChE Journal, 48, 2, pp. 393-400, February.

Smith, D.H. et al., (2004), Thermodynamics of Methane, Propane, and Carbon Dioxide in Porous Glass, AIChE Journal, 50, 7, pp. 1589-1598, July.

Smith, S. et al., (2006), Alaminos Canyon Block 818: a documented example of gas hydrate saturated sand in the Gulf of Mexico, Fire in the Ice: Methane Hydrate Newsletter, Fall 2006, 12-13, Natl. Energy Technol. Lab., U. S. Dept. of Energy, Morgantown, W. Va.

Snyder, F. et al., (2004), Seismic Analysis and Characterization of Gas Hydrates in the Northern Deepwater Gulf of Mexico, Presented at the AAPG Annual Convention, Dallas, Texas, April 18-21.

Soh, W., (1997), Computed Tomography Scan Analysis of Site 941 Cores, Western Mass-Transport Deposit, Amazon Fan, Proceedings of the Ocean Drilling Program, Scientific Results, 155, pp. 465-475.

Staykova, D.K. et al., (2003), Formation of Porous Gas Hydrates from Ice Powders: Diffraction Experiments and Multi-Stage Model, Journal of Physical Chemistry B, 107, pp. 10299-10311.

Stern, L.A., Lorenson, T.D., Pinkston, J.C., (2009), Gas-hydrate characterization and grain-scale imaging of recovered cores from the BPXA–DOE–USGS Mount Elbert Gas-Hydrate Stratigraphic Test Well, Milne Point, Alaska, Marine and Petroleum Geology, In Press, Corrected Proof, Available online 12 August.

Stevens, J. et al., (2008), Measurements of hydrate formation in sandstone, Petrophysics-Houston, 49**,** 1, pp. 67–73.

Stock, S.R., (1999), X-ray Microtomography of Materials, International Materials Reviews. 44, 4, pp. 141-164.

Suess, E. et al., (2001), Sea Floor Methane Hydrates at Hydrate Ridge, Cascadia Margin, In C.K. Paull and W.P. Dillon: Natural Gas Hydrates: Occurrence, Distribution, and Detection. Geophysical Monograph, 124, pp. 87-98.

Sugaya, M., Mori, Y.H., (1996), Behavior of clathrate hydrate formation at the boundary of liquid water and a fluorocarbon in liquid or vapor state, Chemical Engineering Science, 51, pp. 3505-3517.

Sung, W. et al., (2003), Experimental Investigation of Production Behaviors of Methane Hydrate Saturated in Porous Rock, Energy Sources, 25, pp. 845-856.

Takeya et al., (2007), Imaging and Density Mapping of Tetrahydrofuran Clathrate Hydrates by Phase-Contrast X-ray Computed tomography, Applied Physics Letters, 90, 081920-1.

Terzaghi, K., Peck, R.B., Mesri, G., (1996), Soil Mechanics in Engineering Practice,_3rd Edition, Wiley-IEEE, pp. 20.

Tserkovnyak, Y., Johnson, D.L., (2002), Can one hear shape of saturation patch?, Geophysical Research Letters, 29, 7, 1108.

Tohidi B. et al., (2001), Visual Observation of Gas Hydrate Formation and Dissociation in Synthetic Porous Media by Means of Glass Micromodels, Geology, 29, 9, pp. 867-870.

Tombari, E. et al., (2006), Heat capacity of tetrahydrofuran clathrate hydrate and of its components, and the clathrate formation from supercooled melt, J. of Chemical Physics, 124,15, 154507.

Tomov, S., McGuigan, M., (2004), Interactive visualization of higher dimensional data in a multiview environment, arXiv:cs.GR/0405048, http://arxiv.org/PS_cache/cs/pdf/0405/0405048v1.pdf

Torres, M.E. et al., (2002), Fluid and Chemical Fluxes in and out of Sediment hosting Methane Hydrate deposits on Hydrate Ridge, OR, I: Hydrological Provinces, Earth and Planetary Sciences Letters, 201, pp. 525-540.

Turner, D.J., Cherry, R.S., Sloan, E.D., (2005), Sensitivity of Methane Hydrate Phase Equilibria to Sediment Pore Size, Fluid Phase Equilibria, V. 228-229, pp.505-510, February.

Uchida, T., Ebinuma, T., Ishizaki, T., (1999), Dissociation Condition Measurements of Methane Hydrate in Confines Small Pores of Porous Glass, Journal of Physical Chemistry B, 103, pp. 3659-3662.

Uchida, T. et al., (2002), Effects of Pore Sizes on Dissociation Temperatures and Pressures of Methane, Carbon dioxide and Propane Hydrate in porous media, J. Phys. Chem. B., 106, pp. 820-826.

Uchida, T., et al., (2004), Decomposition of Methane Hydrates in Sand, Sandstone, Clays and Glass Beads, Journal of Geophysical Research, Vol. 109, B05206.

U.S. Silica. "Ottawa Sand" Ottawa_sand_-US_Silica_Results.pdf

van der Waals, J.H., Platteeuw, J.C., (1959), Validity of Clapeyron's Equation for Phase Equilibria involving Clathrates, Nature, 183, 462, 14 February.

Van Dover, C.L. et al., (2003), Blake Ridge methane seeps: characterization of a soft sediment, chemosynthetically based ecosystem, Deep Sea Research Part I: Oceanographic Research Papers, 50, 2, pp. 281-300, February.

von Stackelber, M., Müller, H.R., (1954), Z. Electrochem, Feste Gashydrate II. Structur und Raumchemie, 58, pp. 25-39.

Waite, W.F., Winters, W.J., Mason, D.H., (2004), Methane Hydrate Formation in Partially Water-Saturated Ottawa Sand, American Mineralogist, 89, pp. 1202-1207.

Westbrook, G.K. et al., (1994), Proceedings of , Ocean Drilling Program, Initial Reports, Vol. 146, Ocean Drilling Program, College Station, TX.

White, K., (2004), Fore sighting Future Fuel Technology: Backgrounder on Methane Gas Hydrates, Discussion Draft, National Science and Technology Development Agency, Krabi, Thailand, December, 13-15.

Wilder, J.W. et al., (2001), Modeling Hydrate Formation in Media with Broad Pore Size Distributions, Langmuir, 17, pp. 6729-6735.

Winters, W.J., Dugan, B., Collett, T.S., (2008), Physical properties of sediments from Keathley Canyon and Atwater Valley JIP Gulf of Mexico gas hydrate drilling program, Marine and Petroleum Geology, 25, pp. 896-905.

Wong, R.C.K., Maini, B.B., (2007), Gas bubble growth in heavy oil-filled sand packs under undrained unloading, J. of Petroleum and Engineering, 55, pp. 259-270.

Wood, D.M., (1990), Soil Behavior and Critical State Soil Mechanics, Cambridge University Press, New York.

Wood, W.T., Ruppel, C., (2000), Seismic and Thermal Investigations of the Blake Ridge Gas Hydrate Area: A Synthesis, Proceedings of the Ocean Drilling Program, Scientific Results, 164, pp. 253-263.

Wright, J.F., Dallimore, S.R., (2004), Pressure-Temperature-Salinity Influences on Gas Hydrate Stability in Sediments of the Mallik Gas Hydrate Reservoir, Mackenzie Delta, Canada, Presented at the AAPG Hedberg Conference, Vancouver, BC, Canada, September 12-16.

Yamamuro, O., (1987), Heat Capacity and Phase Transition of Tetrahydrofuran Clathrate Hydrate, Solid State Communications, 62, 4, pp. 289-292.

Yousif, M.H. et al., (1991), Experimental and Theoretical Investigation of Methane-Gas-Hydrate Dissociation in Porous Media, SPE 18320, SPE Reservoir Engineering, February.

Yun, T.S., Narsilio, G.A., Santamarina, J.C., (2006), Physical characterization of core samples recovered from Gulf of Mexico, Marine and Petroleum Geology, 23, pp. 893-900.

Zhu, T., McGrail, P.B., (2004), Injection of CO_2 for Recovery of Methane from Gas Hydrate Reservoirs, Federal Assistance Program/Project Status Report, DE-FC26-01NT41248; April 1st – June 30th.